

UNCLASSIFIED



Australian Government
Department of Defence
Defence Science and
Technology Organisation

Magnetic Test Facility - Sensor and Coil Calibrations

Justin Peter Dinale

Maritime Division
Defence Science and Technology Organisation

DSTO-RR-0396

ABSTRACT

This report details the areas in which signal processing techniques have enabled DSTO Sydney to enhance its existing magnetic testing capability, and present viable data processing options for their implementation. This entails not only accurate sensor calibration, but also calibration of the excitation coils used within the magnetic test system. Reduction of external noise influences through the use of high permeability shielding and filtering are detailed, presenting modelling of coil-shield interactions, and experimental tests for various filter characteristics. Various magnetic coil designs, including DSTO's previously undocumented "Ternan" coil, are also investigated, leading to the design of a new magnetic coil, the "ELFcage" coil, being developed. Field uniformity measurements for the "Ternan" magnetic coil are also presented.

RELEASE LIMITATION

Approved for public release

UNCLASSIFIED

UNCLASSIFIED

Published by

Maritime Division

DSTO Defence Science and Technology Organisation

506 Lorimer St

Fishermans Bend Victoria 3207 Australia

Telephone: 1300 DEFENCE (1300 333 362)

Fax: (08) 7389 6567

© Commonwealth of Australia 2013

AR-015-690

August 2013

APPROVED FOR PUBLIC RELEASE

UNCLASSIFIED

Magnetic Test Facility - Sensor and Coil Calibrations

Executive Summary

This report contains the author's Master of Sciences (Defence Signals and Information Processing) thesis, completed as part of the DSTO Continuing Education Initiative.

This thesis investigates the coil geometries of the Australian Defence Science and Technology Organisation's previously undocumented "Ternan" magnetic coil facility. Computational modelling has been conducted to investigate the extent of the usable volume of uniform magnetic field generated by the magnetic coils, as well as modelling of an enhanced coil design named "ELFcage". Experimental measurements have found the Ternan coil to have a very large area of uniformity, permitting the testing of objects previously deemed too large to be easily investigated.

Also, this paper investigates the impact high permeability magnetic shielding material has on an enclosed magnetic coil. Computational modelling has shown the shielding material enhanced the magnitude and the uniformity of the magnetic flux density within the coil.

Finally this paper investigates methods used for calibrating magnetic sensors and triaxial magnetic coil systems, to enable the development of an automated calibration procedure for triaxial magnetic coils. Since existing magnetic coil calibration techniques found in literature do not fully account for secondary errors such as orthogonality, the TWOSTEP magnetometer calibration algorithm is recast to enable its use to calibrate triaxial magnetic coils. Experimental measurements have found the procedure enables an accurate coil calibration to be conducted with 90 s of measurement data, significantly reducing the error in the generated magnetic field when using theoretically derived calibration parameters

Given the DSTO magnetic test facility is already built and available for use it is recommended that the existing Ternan coil configuration be kept, and be used for characterisation of ranging system sensors, and measurement of magnetic signatures of bulky equipment. It is also recommended a small 2-axis ELCage coil be built for y-axis and z-axis field stimulation of small sensors within a shielded laboratory environment, for use in the design and development of future ranging systems, and that an additional removable solenoid be built to stimulate the x-axis field.

UNCLASSIFIED

Authors



Justin Peter Dinale
Maritime Division

Justin Dinale was born in Sydney, Australia [REDACTED] He received a B.Sc (Physics, Mathematics) and a B.Eng (Honours Electrical) degrees from the University of New South Wales in 2006; and in 2013 he received a M.Sc (Defence Signals and Information Processing) from the University of Adelaide. He has been working for DSTO since 2006, in the areas of modelling & simulation, battle-labs (2006-2010), and mine countermeasures (2010-present).

-

UNCLASSIFIED

Magnetic Test Facility

-

Sensor and Coil Calibrations

by

Justin Peter Dinale

Bachelor of Engineering (Honours Electrical)
Bachelor of Science (Physics, Mathematics)
University of New South Wales, 2006

Thesis submitted for the degree of

Master of Sciences

(Defence Signals and Information Processing)

in

The School of Electrical and Electronic Engineering
University of Adelaide

2013



Australian Government
Department of Defence
Defence Science and
Technology Organisation

© 2013

Commonwealth Of Australia
All Rights Reserved



ADELAIDE
UNIVERSITY
AUSTRALIA

Contents

| | |
|--------------------------------------|----------|
| Contents | iii |
| Abstract | ix |
| Acknowledgements | xi |
| Conventions | xiii |
| List of Figures | xv |
| List of Tables | xxi |
| Chapter 1. Introduction | 1 |
| Chapter 2. Literature Review | 5 |
| 2.1 Sensors | 5 |
| 2.1.1 Vector magnetometers | 6 |
| 2.1.2 Scalar magnetometers | 8 |
| 2.1.3 Sources of error | 9 |
| 2.1.4 Sensor calibration | 9 |
| 2.1.5 Attitude correction | 13 |
| 2.1.6 Summary | 14 |
| 2.2 Coils | 15 |
| 2.2.1 Coil uniformity | 16 |
| 2.2.2 Coil calibration | 17 |
| 2.2.3 Coil limitations | 19 |
| 2.3 Noise and Shielding | 21 |

| | | |
|--|--|-----------|
| 2.3.1 | High magnetic permeability (μ) shields | 21 |
| 2.3.2 | Self-shielding coils | 22 |
| 2.3.3 | Superconducting shields | 22 |
| 2.3.4 | Signal filtering | 22 |
| 2.3.5 | Summary | 23 |
| Chapter 3. Coil Design | | 25 |
| 3.1 | Coil Definitions and Derivations | 25 |
| 3.1.1 | Coil designs | 26 |
| 3.1.2 | Approximation of \mathbf{B} for $\cos(\theta)$ coils at centre of coil | 28 |
| 3.1.3 | Engineering considerations | 33 |
| 3.2 | Simulation | 36 |
| 3.2.1 | Volume calculations | 36 |
| 3.2.2 | Comparison of coil designs | 52 |
| Chapter 4. Effect of Magnetic Shielding on Field Uniformity | | 55 |
| 4.1 | Solenoid | 55 |
| 4.1.1 | Anomalies | 58 |
| 4.2 | ELFcage | 61 |
| 4.3 | Summary | 62 |
| Chapter 5. Calibration Estimators | | 67 |
| 5.1 | TWOSTEP | 67 |
| 5.1.1 | Model | 67 |
| 5.1.2 | Parameter re-definition | 68 |
| 5.1.3 | Sensor “error measurement” & “error measurement noise” | 69 |
| 5.1.4 | Vectorisation | 70 |
| 5.1.5 | Noise distribution | 71 |
| 5.1.6 | Likelihood function | 72 |

| | | |
|--|--|------------|
| 5.1.7 | Centering | 73 |
| 5.1.8 | Fisher information matrix | 75 |
| 5.1.9 | Center term correction | 78 |
| 5.1.10 | Converting to \mathbf{b} and D | 79 |
| 5.1.11 | Implementation | 80 |
| 5.2 | Geometric Approach - Ellipsoid Calibration | 82 |
| 5.2.1 | Model | 82 |
| 5.3 | Estimator Selection | 84 |
| 5.3.1 | First order performance | 86 |
| 5.3.2 | Reference frame selection | 86 |
| 5.3.3 | Performance for noisy data | 90 |
| 5.3.4 | Performance for large data-sets | 95 |
| 5.3.5 | Summary | 96 |
| Chapter 6. Calibration Methods | | 101 |
| 6.1 | Coil Calibration Estimation | 101 |
| 6.1.1 | Model | 101 |
| 6.1.2 | Manipulation to enable use of TWOSTEP | 102 |
| 6.1.3 | Driving the coil | 103 |
| 6.1.4 | Implementation issues in TWOSTEP | 103 |
| 6.2 | Sensor in Coil Estimation | 104 |
| 6.2.1 | Model | 104 |
| 6.2.2 | Bias issues | 105 |
| Chapter 7. Experimental Results | | 107 |
| 7.1 | Introduction | 107 |
| 7.1.1 | Experimental setup | 107 |
| 7.1.2 | Stimulation signals | 109 |

| | | |
|---|---|------------|
| 7.2 | Magnetometer Spin Calibration | 111 |
| 7.3 | Calibration Experiments | 113 |
| 7.3.1 | Coil calibration | 113 |
| 7.3.2 | B field predictions | 117 |
| 7.3.3 | Analog filter impacts | 120 |
| 7.4 | Coil Property Measurements | 134 |
| 7.4.1 | Coil frequency response | 134 |
| 7.4.2 | Uniformity | 135 |
| Chapter 8. Conclusions | | 147 |
| 8.1 | Recommendations | 147 |
| Appendix A. Additional Definitions and Derivations | | 149 |
| A.1 | Moments of a Gaussian random variable | 149 |
| A.1.1 | Fourth moment of noise amplitude | 151 |
| A.2 | Sum of centre and centred pseudo-covariance | 152 |
| A.3 | Expectations of centre and centred variables | 153 |
| A.3.1 | Centre variables | 153 |
| A.3.2 | Centered variables | 154 |
| A.4 | Geometric Approach Auxiliary Formulae | 155 |
| A.4.1 | Least squares estimate | 155 |
| A.4.2 | Maximum likelihood estimate | 156 |
| Appendix B. Ancillary Results | | 159 |
| B.1 | AC calibration | 159 |
| B.1.1 | Model | 159 |
| B.1.2 | Parameter re-definition | 160 |
| B.1.3 | Sensor error measurement & sensor error measurement noise . . | 160 |
| B.1.4 | Noise distribution | 161 |

| | | |
|-------------------------|--|------------|
| B.1.5 | Likelihood function | 162 |
| B.1.6 | Fisher information matrix | 163 |
| B.1.7 | Converting to D | 164 |
| B.1.8 | Implementation | 165 |
| B.2 | Amplifier linearity | 166 |
| Appendix C. Code | | 177 |
| C.1 | TWOSTEP estimator | 177 |
| C.1.1 | 'TWOSTEP_estimate.m' | 177 |
| C.2 | Geometric Approach estimator | 182 |
| C.2.1 | 'ellipsoid_estimate.m' | 182 |
| C.2.2 | 'ellipsoid_first_estimate.m' | 185 |
| C.2.3 | 'normcol.m' | 187 |
| C.2.4 | 'mult_k.m' | 187 |
| C.2.5 | 'kron_k.m' | 189 |
| C.3 | AC calibration estimator | 191 |
| C.3.1 | 'AC_estimate.m' | 191 |
| C.4 | Parameter recovery | 193 |
| C.4.1 | 'recover_angles.m' | 193 |
| C.4.2 | 'ql.m' | 194 |
| Bibliography | | 195 |

Abstract

This thesis investigated the methods used for calibrating magnetic vector sensors and triaxial magnetic coils, to enable the development of an automated calibration procedure, as well as investigating the coil geometries of the previously undocumented “Ternan” coil, as part of its ongoing refurbishment.

Since existing magnetic coil calibration techniques found in literature did not fully account for secondary errors such as orthogonality, a magnetometer calibration algorithm was extended to enable its use to calibrate triaxial magnetic coils.

Computational modelling was also conducted to investigate the extent of the usable volume of uniform magnetic field generated by the magnetic coils, and the impact high permeability materials would have on it, if used to shield the system from external magnetic influences.

The extended calibration algorithm was found to be effective at determining the magnetic coil fabrication errors, allowing them to be counteracted by the use of a calibration matrix within the control software of the system.

The Ternan coil was found to have a very large area of uniformity, permitting the testing of objects previously deemed too large to be easily investigated; and the volume of magnetic uniformity was found to be extendable if appropriate shielding was placed around the system.

Statement of Originality

This work contains no material that has been accepted for the award of any other degree or diploma in any university or other tertiary institution and, to the best of my knowledge and belief, contains no material previously published written by another person, except where due reference has been made in the text.

I give consent to this copy of the thesis, when deposited in the University Library, being available for loan, photocopying and dissemination through the library digital thesis collection.

Signed

Date

Acknowledgements

The author would firstly like to thank his God and savior Jesus the Christ for everything in his life; and to thank his wife Christine and daughters Abigail and Miriam for their ongoing support and understanding over many years of study. Many special thanks go to Dr Julian Vrbancich, for the many long hour spent verifying derivations, and revising the thesis. Thanks go to Dr James Smelt for supplying sections of code implementing Biot-Savart; Dr David Clarke, Dr John Barnes and Dr Andrew Bailey for assistance in understanding the operation of the Ternan $\cos(\theta)$ coil; Mr Neil Tavener and Mr Garry Harris for assistance taking validation measurements for the Ternan $\cos(\theta)$ coil; and Mr Adam Fairley and Mr Timothy Dell for taking the spin calibration measurements used to calibrate the reference sensor. Thanks go to Dr Rastko Zivanovic (Adelaide University) for supporting this project and constructive comments. Thanks also go to Dr José Vasconcelos for his assistance in implementing the TWOSTEP code. Thank also go to the family and colleagues who assisted me in the editing of the thesis.

Conventions

This thesis is typeset using the L^AT_EX2e software. WinEdt build 5.5 was used as an interface to L^AT_EX (T. Oetiker and Schlegl 2000). Harvard style is used for referencing and citation in this thesis.

Acronyms

APF All-Pass Filter

DSAD Defence Systems Analysis Division

ELF Extremely Low Frequencies

FFT Fast Fourier Transform

HPF High-Pass Filter

IEEE Institute of Electrical and Electronic Engineers

JOD Joint Operations Division

LPF Low-Pass Filter

MAGFAC Magnetic Test Facility

MATLAB Matrix Laboratory software developed by Mathworks Pty Ltd.

MLE Maximum Likelihood Estimator

MOD Maritime Operations Division

PID Proportional Integration Differentiation - A type of control system with fast response and small errors.

RAN Royal Australian Navy

Conventions

RF Radio Frequency

SI International System of Units

SNR Signal to Noise Ratio

SQUID Superconducting Quantum Interference Device

Units

A Ampere - SI unit of electric current

C Celsius Centigrade - a scale and unit of measurement for temperature

Hz Hertz - SI unit of frequency

K Kelvin - SI unit of temperature

m Metre - SI unit of length

T Tesla - SI unit of magnetic flux density

V Volt - SI unit of electric potential (Voltage)

Metric Prefixes

M mega - 10^6

k kilo - 10^3

m milli - 10^{-3}

μ micro - 10^{-6}

n nano - 10^{-9}

p pico - 10^{-12}

f femto - 10^{-15}

List of Figures

| | | |
|-------|---|----|
| 1.1 | Ternan coil magnetic volume as delivered to Sydney in 2004. | 2 |
| <hr/> | | |
| <hr/> | | |
| 3.1 | Circular Helmholtz design | 26 |
| 3.2 | Square Helmholtz design | 27 |
| 3.3 | Barker design | 27 |
| 3.4 | Ternan $\cos(\theta)$ design | 28 |
| 3.5 | Coil filaments as they travel along the boundary of the circular base of the Ternan coil. | 29 |
| 3.6 | ELFcage design | 29 |
| 3.7 | Generic coil pair | 30 |
| 3.8 | ELFcage coil | 31 |
| 3.9 | Laboratory model of Ternan coil. At the coil boundary the wire forms an arc on the surface of the cylindrical former. | 31 |
| 3.10 | Laboratory model of Ternan coil. | 34 |
| 3.11 | B_y , B_z and B_x field variations in Square Helmholtz coil | 38 |
| 3.12 | B_y , B_z and B_x field variations in Circular Helmholtz coil | 39 |
| 3.13 | B_y , B_z and B_x field variations in Barker coil | 40 |
| 3.14 | B_y , B_z and B_x field variations in Ternan coil | 41 |
| 3.15 | B_y , B_z and B_x field variations in ELFcage coil | 42 |
| 3.16 | Helmholtz $\pm 1\%$ uniformity | 44 |
| 3.17 | Helmholtz $\pm 1\%$ uniformity | 44 |
| 3.18 | Barker $\pm 1\%$ uniformity | 45 |

List of Figures

| | | |
|-------|--|----|
| 3.19 | Ternan $\pm 1\%$ uniformity | 46 |
| 3.20 | ELFcage $\pm 1\%$ uniformity | 47 |
| 3.21 | Helmholtz $\pm 3\%$ uniformity | 48 |
| 3.22 | Helmholtz $\pm 3\%$ uniformity | 48 |
| 3.23 | Barker $\pm 3\%$ uniformity | 49 |
| 3.24 | Ternan $\pm 3\%$ uniformity | 50 |
| 3.25 | ELFcage $\pm 3\%$ uniformity | 51 |
| 3.26 | Comparison of usable volume as a function of the percentage field uniformity | 52 |
| 3.27 | Comparison of usable area as a function of the percentage field uniformity | 53 |
| <hr/> | | |
| 4.1 | Illustration of μ -metal shielding container. | 56 |
| 4.2 | Magnetic field generated by solenoid in air | 57 |
| 4.3 | Magnetic field generated by solenoid in open μ -metal container | 57 |
| 4.4 | Magnetic field generated by solenoid in closed μ -metal container | 58 |
| 4.5 | Total field strength along solenoid axis of rotational symmetry. | 59 |
| 4.6 | Total field strength along the radial direction from the axial centre of solenoid. | 59 |
| 4.7 | Total field strength variation along solenoid axis of rotational symmetry. | 60 |
| 4.8 | Total field strength variation along the radial direction from the axial centre of solenoid. | 60 |
| 4.9 | Magnetic field generated by infinitely long ELFcage in air. | 62 |
| 4.10 | Magnetic field generated by infinitely long shielded ELFcage. | 62 |
| 4.11 | Total field strength along horizontal (y) axis of ELFcage. | 63 |
| 4.12 | Total field strength along vertical (z) axis of ELFcage. | 63 |
| 4.13 | Normalised total field strength variation along horizontal (y) axis of ELFcage. | 64 |

| | | |
|-------|--|----|
| 4.14 | Normalised total field strength variation along vertical (z) axis of ELFcage. | 64 |
| <hr/> | | |
| 5.1 | Simulated “true” (green) and “measured” (blue) magnetic field components of \mathbf{B} . | 85 |
| 5.2 | TWOSTEP and Geometric Approach $ \mathbf{B} $ - 80 Samples | 87 |
| 5.3 | TWOSTEP and Geometric Approach $ \mathbf{B} $ - 8000 Samples | 88 |
| 5.4 | TWOSTEP and Geometric Approach $ \mathbf{B} + noise $ Errors - 80 Samples. | 88 |
| 5.5 | TWOSTEP and Geometric Approach $ \mathbf{B} + noise $ Errors - 8000 Samples. | 89 |
| 5.6 | Coordinate framework for lower-triangular matrix | 90 |
| 5.7 | TWOSTEP (blue), Geometric Approach (red), and TS + GA (magenta): processing time vs noise. | 91 |
| 5.8 | Number of TWOSTEP (blue), Geometric Approach (red), and TS + GA (magenta): iterations required for convergence vs noise. | 92 |
| 5.9 | TWOSTEP (blue), Geometric Approach (red), and TS + GA (magenta): RMS of $(\mathbf{B} + noise - \mathbf{B}_{estimate})$ vs noise. | 93 |
| 5.10 | TWOSTEP and Geometric Approach: angle errors vs noise. | 94 |
| 5.11 | TWOSTEP and Geometric Approach: sensitivity errors vs noise. | 94 |
| 5.12 | TWOSTEP (blue), Geometric Approach (red), and TS + GA (magenta): processing time vs sample size. | 96 |
| 5.13 | Number of TWOSTEP (blue), Geometric Approach (red), and TS + GA (magenta): iterations required for convergence vs sample size. | 97 |
| 5.14 | TWOSTEP (blue), Geometric Approach (red), and TS + GA (magenta): RMS of $(\mathbf{B} + noise - \mathbf{B}_{estimate})$ vs sample size. | 98 |
| 5.15 | TWOSTEP and Geometric Approach: angle errors vs sample size. | 98 |
| 5.16 | TWOSTEP and Geometric Approach: sensitivity errors vs sample size. | 99 |

| | | |
|------|---|-----|
| 7.1 | Experimental setup used throughout the experiments. | 108 |
| 7.2 | Array of Bartington MAG3-SM sensors used to measure field uniformity. | 109 |
| 7.3 | Ideal distribution of data-points forming the calibration test signal. . . . | 111 |
| 7.4 | Ideal stimulation signals applied to the coils. | 112 |
| 7.5 | Calibration data obtained by spinning the reference sensor about it axes in a uniform magnetic field. | 113 |
| 7.6 | Coil factors converging to a stable value as sample-set-size is increased. | 117 |
| 7.7 | Coil factors normalised with respect to the values estimated by the 90 s dataset. | 118 |
| 7.8 | Orthogonality errors converging to stable values as set-size is increased. Convergence is not as rapid as that of the coil factors. | 119 |
| 7.9 | Estimated system resistance viewed from the amplifier output as sample- set-size is increased. | 120 |
| 7.10 | RMS error of field prediction using theoretical and estimated calibration matrices. | 121 |
| 7.11 | $ \mathbf{B}_{centre} - \mathbf{B}_{estimated} $ using theoretical and estimated calibration matri- ces. 4 second calibration. | 122 |
| 7.12 | $ \mathbf{B}_{centre} - \mathbf{B}_{estimated} $ using theoretical and estimated calibration matri- ces. 40 second calibration. | 123 |
| 7.13 | RMS error of field prediction using estimated voltage and current refer- enced calibration matrices. | 124 |
| 7.14 | $ \mathbf{B}_{centre} - \mathbf{B}_{estimated} $ using voltage and current referenced calibration matrices. 4 second calibration. | 125 |
| 7.15 | $ \mathbf{B}_{centre} - \mathbf{B}_{estimated} $ using voltage and current referenced calibration matrices. 40 second calibration. | 126 |
| 7.16 | Unexpected step increase in the current flowing in the x -axis coil. | 126 |
| 7.17 | Estimated orthogonality errors within the Ternan coil system, using a variety of analog filters. | 127 |
| 7.18 | Estimated coil factors within the Ternan coil system, using a variety of analog filters. | 128 |

| | | |
|------|---|-----|
| 7.19 | Recorded $ \mathbf{B}_{centre} $ data, using a variety of analog filters. | 129 |
| 7.20 | Estimated orthogonality errors within the Ternan coil system, using an all-pass-filter and some low-pass-filters. | 130 |
| 7.21 | Estimated coil factors within the Ternan coil system, using an all-pass-filter and some low-pass-filters. | 131 |
| 7.22 | Recorded $ \mathbf{B}_{centre} $ data, using an all-pass-filter and some low-pass-filters. | 131 |
| 7.23 | Filter-induced deviation from the unfiltered (APF) magnetic signal. . . . | 132 |
| 7.24 | Filter-induced temporal delay of signals. | 132 |
| 7.25 | Coil factors for Ternan coil system as frequency is increased from 1 Hz to 90 Hz. Coil factors are with respect to the amplifier drive signal. . . . | 135 |
| 7.26 | Attenuation of generated magnetic field for the Ternan coil system as frequency is increased from 1 Hz to 90 Hz. | 136 |
| 7.27 | Phase delays in the Ternan coil system as frequency is increased from 1 Hz to 90 Hz. | 137 |
| 7.28 | Trolley and array of sensors at end of coil. | 137 |
| 7.29 | Total Field strength for 3Hz \mathbf{B}_x signals, sensors placed parallel to y -axis (Table 7.1) and moved along x -axis. | 138 |
| 7.30 | Total Field strength for 3Hz \mathbf{B}_y signals, sensors placed parallel to y -axis (Table 7.1) and moved along x -axis. | 139 |
| 7.31 | Total Field strength for 3Hz \mathbf{B}_z signals, sensors placed parallel to y -axis (Table 7.1) and moved along x -axis. | 140 |
| 7.32 | Total Field contour plot for 3 Hz \mathbf{B}_x , \mathbf{B}_y and \mathbf{B}_z coil signals. Sensors were placed parallel to y -axis (Table 7.1) and moved along x -axis. | 141 |
| 7.33 | Total Field error contour plot for 3 Hz \mathbf{B}_x , \mathbf{B}_y and \mathbf{B}_z coil signals. Sensors were placed parallel to y -axis (Table 7.1) and moved along x -axis. | 142 |
| 7.34 | \mathbf{B}_x , \mathbf{B}_y and \mathbf{B}_z contour plot for 3 Hz \mathbf{B}_x coil signals. Sensors were placed parallel to y -axis (Table 7.1) and moved along x -axis. | 143 |
| 7.35 | \mathbf{B}_x , \mathbf{B}_y and \mathbf{B}_z contour plot for 3 Hz \mathbf{B}_y coil signals. Sensors were placed parallel to y -axis (Table 7.1) and moved along x -axis. | 144 |

| | | |
|-------------|--|-----|
| 7.36 | \mathbf{B}_x , \mathbf{B}_y and \mathbf{B}_z contour plot for 3 Hz \mathbf{B}_z coil signals. Sensors were placed parallel to y -axis (Table 7.1) and moved along x -axis. | 145 |
| <hr/> <hr/> | | |
| B.1 | Coil factors estimated by the AC Calibration algorithm compared to the coil factors estimated by the TWOSTEP algorithm. | 167 |
| B.2 | Orthogonality errors estimated by the AC Calibration algorithm compared to the orthogonality errors estimated by the TWOSTEP algorithm. | 168 |
| B.3 | Measured Welch power spectral density of the reference sensor x -axis when the coil x -axis is energised. | 169 |
| B.4 | Measured Welch power spectral density of the reference sensor y -axis when the coil y -axis is energised. | 170 |
| B.5 | Measured Welch power spectral density of the reference sensor z -axis when the coil z -axis is energised. | 171 |
| B.6 | Measured Welch power spectral density of current flowing in the x -axis coil. | 172 |
| B.7 | Measured Welch power spectral density of current flowing in the y -axis coil. | 173 |
| B.8 | Measured Welch power spectral density of current flowing in the z -axis coil. | 174 |
| B.9 | Measured power spectral density of the Kepco amplifiers used to drive the Ternan coil system. | 175 |

List of Tables

| | | |
|-----|---|-----|
| 3.1 | Field normalisations, where i, j, k are unit vectors along the x, y, z axes. . | 37 |
| 5.1 | Mapping E indexed elements ' E_m ' and matrix E elements ' $E_{i,j}$ '. | 77 |
| 5.2 | Measurement errors used in the simulation. | 86 |
| 7.1 | Sensor array serial numbers (S/N) and placement. | 110 |
| 7.2 | Bartington sensor sensitivity errors. | 114 |
| 7.3 | Bartington sensor orthogonality errors. | 115 |
| 7.4 | Bartington sensor bias errors. | 116 |
| 7.5 | Bartington SCU-1 filter settings (3dB) used in experiment. | 122 |

Chapter 1

Introduction

Mines/Torpedoes¹ were first used against ships in late Dec 1777 - early Jan 1778, in the Delaware River at Philadelphia; kegs filled with gunpowder which were set to explode when a flintlock trigger fired on contact with targets that drifted into them once they were released down a river (Hartmann 1979). Since then mines progressively evolved to include more complicated triggering mechanisms, providing both greater safety during deployment and better target discernment. Contact mines such as these were used throughout the First World War, and more recently by countries such as Iran.

The Second World War saw the development of magnetic, pressure, and acoustic mines. Their evolution has led to the development of mines capable of detecting and classifying vessels based on increasingly more detailed characteristics of their signatures, i.e., the physical characteristics of the platform for the purpose of detection and classification. Consequently military organisations and scientists globally were and are endeavoring to minimise signatures as far as possible, whilst concurrently researching other methods to counter the continually changing mine threat. The determination of these signatures is called “ranging”; and this can be performed on a variety of platforms, varying from large vessels down to smaller platforms such as autonomous underwater vehicles (AUVs) or diving gear.

The drive to accurately measure vessel signatures has led to the use of more accurate sensors able to detect absolute pressure signals to part-per-billion resolutions (Schaad 2009). Acoustic sensors have progressed to the point where they are limited by environmental noise (Stansfield 1991) and magnetic sensors are capable of detecting changes

¹Mines were initially called Torpedoes

in the sub nano-Tesla (nT) ranges (Lenz and Edelstein 2006). Because these resolutions are so small, even slight errors in magnetometer manufacture, such as a misalignment of 0.1 degrees, could lead to several tens of nT errors in the readings, which can easily swamp the signals being measured.

The three main sensors used in ranging are acoustic, pressure and magnetic. DSTO MOD currently has the ability to test acoustic sensors at Woronora Dam (Sydney) and pressure sensors in-house. However magnetic sensors have not been able to be properly characterised since the shutdown of the Maritime Operations Division of DSTO Maribyrnong (Melbourne) began in 2004, during which time the magnetic testing and calibration equipment was relocated into storage in Sydney. In this project the pre-existing magnetic coil system from Maribyrnong (referred to as the Ternan coil magnetic volume, shown in Figure 1.1) has since been thoroughly modelled to gain a comprehensive understanding of the coil and magnetic-field topology, prior to being reinstated as a fully-operational magnetic-field calibration facility. Furthermore an alternative magnetic coil design (referred to as the ELFcage) was also thoroughly investigated and was shown to exhibit a higher degree of magnetic field uniformity compared to the Ternan magnetic volume. This was a significant finding.

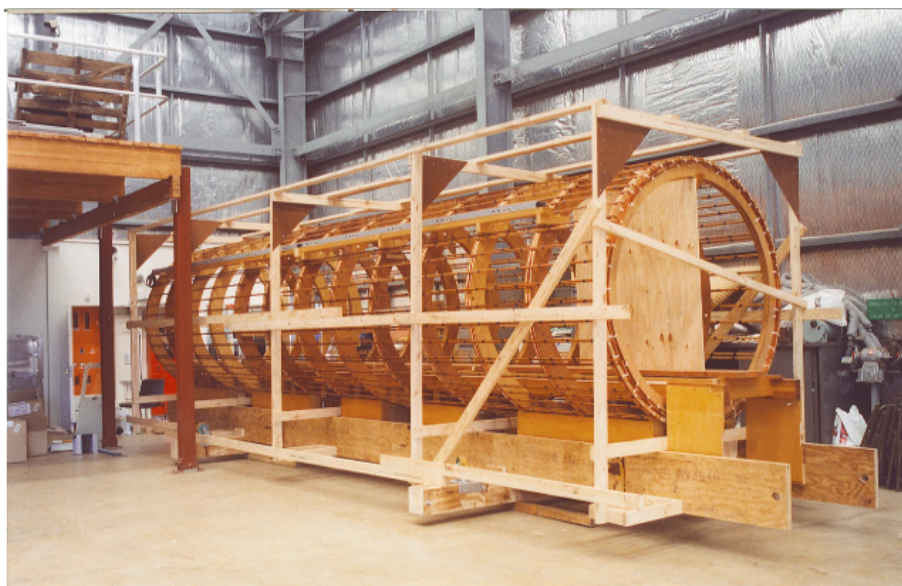


Figure 1.1: Ternan coil magnetic volume as delivered to Sydney in 2004 (Coil length = 8 m, coil diameter = 2 m).

This thesis project will present the signal processing techniques which are being used in the re-establishment of a large-volume magnetic testing and calibration facility using the Ternan coil, and their implementation for use in a small scale coil located within a magnetically noisy laboratory.

The thesis will commence with an overview of the types of sensors available, their sources of error, and calibration techniques used to calibrate them. An overview of magnetic coils will then introduce the advantages of using the non-standard coil design utilised in the Ternan coil system, as well as the expected sources of errors and limitations of calibration techniques available within the literature. Noise sources and the effectiveness of magnetic shielding will then be addressed, before assessing suitability of two estimators (the “TWOSTEP” and “Geometric Approach” methods) and their performance. In this context the TWOSTEP formulation was re-derived to verify the equations and was coded in MATLAB, enabling processing performance to be tested under various noise levels and sample-set sizes. Finally a series of field measurements will be presented for both sensors and coils.

Chapter 2

Literature Review

2.1 Sensors

Magnetic sensors can be divided into two classes, scalar magnetometers and vector magnetometers.

As the name indicates, scalar magnetometers measure the total field strength at a point, whilst vector magnetometers provide the 3D components making up the field. Vector magnetometers generally have higher sensitivity and enable higher sampling frequencies than their scalar counterparts, with the exception of SQUIDs (Superconducting Quantum Interference Devices), which are bound to low sampling frequencies. Vector magnetometers are also smaller than the scalar sensor, since they do not require volumes of liquids or gases to excite.

Scalar magnetometers are less sensitive, bulkier and provide lower sampling frequencies than vector magnetometers, but their use becomes apparent once fabrication errors (e.g. sensor orthogonality and bias voltage) within vector sensors are taken into consideration.

Selection of the magnetic sensor for a system will often have a major impact on the system's final errors and capabilities; as such it is important to identify the most appropriate sensor for its intended purpose(s).

Lenz and Edelstein (2006) and Tumanski (2007) provide good overviews of existing and emerging vector and scalar magnetic sensors, a few of which are summarised in Sections 2.1.1 and 2.1.2.

2.1.1 Vector magnetometers

2.1.1.1 Search-coil magnetometers

Search-coils consist of a conducting wire wound around a core commonly made of high permeability materials. The response is governed by Faraday's law of induction, where a voltage is generated proportional to the change of flux through a coil. Signals in the tens of fT have been detected with these sensors, but search-coils can also be designed to detect extremely strong signals, which are orders of magnitude stronger (i.e., > 1 mT). The typical frequency of operation is 1 Hz to 1 MHz, dependent on the inductance, stray capacitance and resistance of the system. These sensors are unlikely to be useful in the measurement of sub 1 Hz signals due to the small amplitude of signals induced into the sensor.

2.1.1.2 Fluxgate magnetometers

Fluxgate sensors consist of a ferromagnetic core, around which drive and sense coils are wound. They use magnetic induction coupled with the change of permeability of the core as it goes into saturation at high fields caused by the applied drive signal, to induce even-numbered harmonics of the drive signal into the sense coil. The amplitude of the second harmonic is proportional to the ambient field strength in the axial direction of the coil. Sensitivity range is from ≈ 10 pT to ≈ 10 mT. The sampling frequency of these sensors is limited by the driving signal, which is in turn limited to ≈ 10 kHz by the response time of the core, thereby enabling flux variations in the kHz range to be measured. Fluxgate magnetometers do not have a lower limit to their frequency response, and hence can be used to measure frequencies all the way down to DC fields.

2.1.1.3 SQUID magnetometers

The SQUID sensor consists of a small superconducting loop in which a quantized current passes, dependent on the flux density passing through the loop. Superconductivity is achieved at low temperatures, requiring liquid Helium — referred to as low

temperature superconductivity (< 4 K), or liquid nitrogen — referred to as high temperature superconductivity (77 K), dependent on the superconductive material used. The current is measured by observing the pattern of the oscillating current passing through a “weak link”², allowing information to be inferred, due to its similarity to interference patterns in light, but in this case related to flux quantization. Sensitivity is limited by magnetic field noise to ≈ 10 fT. The devices can easily be set to null out static fields, making them well suited for anomaly detection. Frequency response is from DC to ≈ 1 Hz. SQUIDs can be configured to act as gradiometers, but at the expense of resolution. The requirement of a supply of liquid Nitrogen or Helium is a major impediment to their widespread use in the field.

2.1.1.4 Hall Effect magnetometers

These sensors work on the Hall effect, a property of conductors and semiconductors by which a strong magnetic field perpendicular to the plane of a rectangle of conductive material with current passing along its length will generate, due to the Lorentz force, a voltage across the width of the rectangle, proportional to the field strength. Sensitivity typically ranges from ≈ 100 nT to ≈ 0.1 T, and can sample signals up to 1 MHz.

2.1.1.5 Other vector magnetometers

A variety of other vector magnetometers are available, including MEMS (Micro Electro Mechanical Systems) devices, magneto-resistive devices (which exploit the change in resistance of certain materials in a magnetic field), magneto optical sensors (which rotate the plane of a polarised light passing through a field), and magneto-strictive sensors (which use the physical change of size of materials as the applied field changes).

Most vector magnetometers exhibit $1/f$ noise and are susceptible to errors introduced by rotational vibrations.

²a thin layer of insulator, or a thinning of the superconducting loop

2.1.2 Scalar magnetometers

Scalar sensors are insensitive to rotational vibrations, and will reliably measure the total field strength at a point but, due to the physical processes involved in these devices, they are only usable for sampling frequencies below $\approx 10\text{Hz}$, and require the total field strength to be above a minimum level.

2.1.2.1 Optically pumped magnetometers

These sensors detect the splitting of spectral lines when Cesium and Rubidium atoms, for example, are placed in a magnetic field. Detection is achieved by tracking the frequency of a variable radio frequency (RF) source, which is used to release excited electrons from their high energy state; this is achieved via a feedback loop involving a photo-sensor to keep the RF source tuned to produce maximum light intensity. Sensitivity typically ranges from 1 pT to 100 μT . These devices exhibit “dead zones”, requiring multiple sensors to obtain a full omnidirectional spherical response.

2.1.2.2 Nuclear precession magnetometers

Also known as proton precession magnetometers, nuclear precession magnetometers temporarily align protons in a hydrocarbon fluid to a magnetic field generated by a coil. When the induced field is removed, the protons precess about the ambient field, creating a signal in the coil, the frequency of which is dependent on the ambient field strength. Sensitivity typically ranges from 0.1 nT to 100 μT . Nuclear precession magnetometers have no dead zones.

2.1.2.3 Overhauser magnetometers

These sensors are an evolution of the nuclear precession magnetometers, which use a coupling between the electron spins and the protons, to get a factor of 1000 increase in the nuclear polarisation, hence providing better noise levels, as low as $15\text{ pT}/\sqrt{\text{Hz}}$ at 1 Hz.

2.1.3 Sources of error

Small instrumentation errors are generally introduced into the magneto-sensing device by the fabrication process itself. For vector magnetometers these errors include sensor bias/offset, sensor drift, sensor orthogonality and coordinate system misalignment. Obviously a scalar magnetometer cannot experience orthogonality or coordinate system errors, since it does not contain coordinate information, but as mentioned earlier it can suffer from other errors, including the “dead zone”, due to which the sensitivity response of the sensor is not a spherical beam pattern.

Reduction of many of these errors can be achieved through sensor calibration, a process which initially involved direct measurement of offset and the linear approximation of sensitivities, but which has matured to utilise a swathe of signal processing techniques including Kalman filters, neural networks, maximum likelihood estimators and least mean square estimators, as well as image processing techniques such as ellipsoid fitting. What follows is an overview of techniques used in recent papers, the most relevant of which will be further investigated for implementation in the Ternan & ELFcage coil systems. This technique can be extended for use with other coil designs.

2.1.4 Sensor calibration

IEEE standards propose several ways of calibrating a sensor (Frix *et al.* 1994, Mirzaeva *et al.* 2012), namely using a single square coil as a reference source, using a Helmholtz coil as a reference source, and calibrating against a reference sensor. While from a general perspective this is accurate, the necessary data processing algorithms are not detailed for the calibration estimations. Hence, suitable estimators need to be developed for each particular application or sourced from other literature.

Lassahn and Trenkler (1995) investigate the calibration of sensors with a set of three orthogonal Helmholtz coil pairs. Two methods for orthogonality detection are presented. In the first a calibrated reference sensor is used in conjunction with an interferometer to detect the orthogonality of a Helmholtz coil system. Once this has been done the

2.1 Sensors

sensor under test is also run through the same steps, with the difference in field components indicating the orthogonality errors. In the second method a 180° rotation is used to cancel out bias components, providing a two-datapoint measurement for each axis. The procedure has weaknesses in the requirement for accurate sensor placement, and physical rotation of the sensor.

2.1.4.1 Minimum variance analysis

Auster *et al.* (2002) perform a scalar calibration³ using a minimum variance analysis (MVA) estimation. The authors outline the parameters which can be inferred by rotations about a single axis, or two or three axes, proving a complete parameter estimation can be achieved by performing a scalar calibration by rotating about two or more axes. The introduction section also suggests that it may be possible to calibrate a static sensor, comparing it to another stationary calibrated vector magnetometer, using the variations in earth's field to perform the calibration. Whilst this may be possible, data acquisition is most likely time consuming, and best done only for estimating the relationship between two pre-calibrated sensors when they cannot be moved due to their use, such as when using a sensor as a reference for compensating earth's reference field within a coil.

2.1.4.2 Least squares fit

Merayo *et al.* (2000) present a scalar calibration, using linear and non-linear least squares fits. Residual field strength due to sensor offsets (bias) is found to cause errors for estimating sensitivity. These errors are addressed through an iterative re-calibration leading to the non-linear least squares fit. Data needs to be evenly distributed on the surface of a sphere (representing 3D space) to achieve an unbiased estimate, since there is no weighting to account for the angular distribution density of samples. The calibration process appears resistant to zero mean Gaussian noise. Petrucha and Kaspar (2009) re-implement the procedure of Merayo *et al.* (2000), with three additional attitude correction parameters for the sensor's calibration referencing frame. Additionally

³A scalar calibration uses an accurately measured total magnetic field as a reference signal.

they extend the calibration technique to accelerometers. Their results show the necessity of calibrating in the absence of any ferromagnetic or high permeability materials, in order to avoid degradation of the estimated calibration coefficients. The developed system has an angular positioning resolution of only 1° , hence the system cannot be used for vector calibrations. Scalar calibrations are acceptable since the errors in angular position can be viewed as Gaussian noise.

2.1.4.3 Kalman filtering

Huang and Jing (2008) design an “Extended” Kalman filter, which characterises the drag, position and velocity of a satellite, and the orthogonality, bias and sensitivity of the onboard sensor. The model generates errors in the order of nT for bias estimates, and $\sim 10\%$ errors in the sensitivity and orthogonality calculations. Similarly Soken and Hajiye (2011) design an “Unscented” Kalman filter, including sensor attitude (but not sensor orthogonality) estimation in the filter, with sensitivity calculations separated as an extension to the filter. Whilst possibly suitable for a pico-satellite, the large variations in the sensitivity estimation and lack of orthogonality estimation make this technique unsuitable for our purposes.

2.1.4.4 TWOSTEP maximum likelihood estimator

Alonso and Shuster introduce the TWOSTEP algorithm (Alonso and Shuster 2002a, Alonso and Shuster 2003), initially developed to estimate bias voltages with no attitude information, but extended to include sensitivity and orthogonality (Alonso and Shuster (2002c)). To begin with, a maximum likelihood estimator (MLE) is used to calculate an estimate of the magnetometer errors using centred data. This estimate is then used as a first guess for a non-centred MLE calculation, allowing the Gauss-Newton method to select the global maxima instead of a local maxima. The TWOSTEP method can be used to estimate the zero and first order terms of a calibration (bias and sensitivity respectively), but it does not provide a computational advantage for higher order terms. Fortunately, for the majority of sensors of interest, a first order approximation of the response is all that is required. Kim and Bang (2007) use a genetic algorithm to generate an initial estimate of bias for the TWOSTEP method. Whilst there is no

improvement evident in the final results, their method provides an alternative method for defining a first guess for the estimation of bias.

Wang (2008) presents a neural network configuration using a linearised model for the orthogonality correction, assuming fabrication errors of less than 1 degree. The paper reproduces work by Olsen *et al.* (2001) as an introduction to scalar calibration, using a linearised least squares approach, before defining the Wang (2008) neural network design. Experimental results are not compared with the Olsen *et al.* (2001) implementation or any other technique; and with the final calibrated results varying up to 55 nT, the approach seems suitable only as an initial estimate of calibration coefficients.

2.1.4.5 Ellipsoid fitting

Camps *et al.* (2009) perform a scalar calibration for sensors, which minimises the errors using the Levenberg-Marquadt algorithm to fit the results onto an ellipsoid. Initially only sensitivity and bias are modelled (Model 1), then orthogonality is included (Model 2). Results for the two models are compared, performing three runs for each sensor, but are not compared to any other estimators. Between the calibration runs there appear to be a variation of 0.1% in sensitivity, 10% in orthogonality and 2% in bias, but since the results are derived from experimental data instead of simulation the true errors in the estimation may be unknown.

Vasconcelos *et al.* (2011) present the “Geometric Approach”, in which they view the sampled data as the surface of an ellipsoid. Ellipsoid parameters are estimated using a MLE, and magnetometer calibration coefficients are then derived from these parameters. A pseudo-linear least squares estimate provides a first guess of the parameters, followed by the MLE of the ellipsoid, and coefficient extraction. The paper painstakingly defines the error framework, starting with a description of the physical sources of errors, such as hard and soft iron (which generate permanent and induced magnetic fields), orthogonality of the sensors, electronic bias voltages, wide-band noise, body frame alignment and a catch-all “other” category; it then couples the errors back into sensitivity, orthogonality and bias errors. Whilst the algorithm does not provide for the alignment of the sensor due to the lack of a suitable reference frame, a method

for the alignment of the sensor to a second vector magnetometer is supplied. Simulated results comparing the Geometric Approach to the TWOSTEP method presented in Alonso and Shuster (2002c) show good agreement between the techniques.

Zhang and Gao (2009) present a model in which the sensitivity and orthogonality are combined into a single matrix, effectively acting more as a cross-coupling representation. Measurements taken by performing mechanical sensor rotations in a uniform field are used to obtain a least-squares estimate of the parameters for the ellipsoid, described by the data, similar to the estimation method used by Vasconcelos *et al.* (2011). Simulated results show a variance of approximately 1 nT in calibrated total field, 10% errors in the estimation of bias, 0.001% error in the sensitivity and 0.5% errors in the orthogonality correction.

2.1.5 Attitude correction

As mentioned above, Vasconcelos *et al.* (2011) present a simple attitude correction procedure, as a solution to the Procrustes problem (Mathworks 2012). Bracken *et al.* (2005) and Vcelak (2006), as part of their gradiometer calibration, re-align individual sensors to the first sensor in their gradiometer array. As part of estimating the alignment rotation matrix, Bracken *et al.* (2005) minimise the dot product of each newly calibrated sensor to the first sensor. In the case of a scalar calibration this is obviously not possible, since the reference sensor only provides a total field, but if it is assumed that the sensor is rotated about a single axis, and the body of the sensor is aligned to the plane perpendicular to this axis, then the alignment coefficients can be obtained to enable alignment to the rotation axis. The estimator would minimise the variance on the spin axis signal and the variance of the sum of the squares of the other two components. If additionally the sensor is rotated on another orthogonal axis, the complete alignment matrix to the sensor body should be able to be derived.

2.1.6 Summary

Estimation of the magnetometer calibration coefficient can be performed by a range of techniques, which generally place the sensor in an absolute field of known magnitude and relatively low noise. These techniques involve rotating the sensor on various axes, and measuring the field strength detected on each sensor. Recorded data is then processed through a variety of techniques to calculate sensor properties such as sensitivity (nT/V), and orthogonality of sensor outputs to each other, and bias. Sensors have been rotated in a variety of ways: with mechanical systems devised to physically rotate a sensor; placing the sensor on a rotating table; or using the motion of a satellite through space.

Based on the review of the above-mentioned algorithms, the TWOSTEP method by Alonso and Shuster (2002a, 2002c) and the Geometric Approach method by Vasconcelos *et al.* (2011) appear the most suitable for implementation. This project focuses on the full implementation of the TWOSTEP and Geometric Approach methods using MATLAB code in order to calibrate the magnetic sensors and magnetic volume generated within the Ternan and ELFcage systems.

2.2 Coils

As seen in Section 2.1.4, magnetic coils are used to generate a magnetic field for calibration and excitation. This section will provide a brief overview of a few coils, their advantages and coil calibration techniques found in literature.

Caprari (1995) compares the uniformity of several common coil designs: the Helmholtz, Maxwell, Garrett, Barker and Braunbek coils. In each of these coils the wire is wound into circular coaxial loops, of varying spacing-to-radii ratios, with the aim of achieving the maximum field uniformity possible within the centre of the coil setup. The coil most often referred to in literature is the Helmholtz coil, in which the two circular coils are spaced a radius apart. Whilst the easiest coils to construct (and the first invented), the Helmholtz design also produces the smallest volume of homogeneity. The Rubens coil provides an improvement on the Helmholtz coil, but should not be used where precise controls of the field and field gradient are required (Kirschvink 1992). The Barker and Braunbek coils, on the other hand, produce uniform volumes much larger than the Helmholtz, at the cost of more complex manufacture and excitation current requirements.

Square coil implementations of the Helmholtz design have also been built, with a slightly larger spacing between coils, resulting in a larger volume of magnetic field uniformity (Kirschvink 1992).

The “Ternan $\cos(\theta)$ ” coil used in the DSTO MOD system is based on the approximation of a $\cos(\theta)$ current density distribution on the surface of a cylinder. This concept is discussed in detail in Section 3.1.1. Specific examples of this implementation could not be found in the literature, but the following two related designs were found:

- Zlobin *et al.* (2001) present the design of a coil for the “Very Large Hadron Collider”, based on Nb_3Sn superconducting wire, a $\cos(\theta)$ coil and iron yokes. Cross sectional fields are very similar to those modelled in the Ternan coil. Coils are fabricated in two halves which are then epoxy-impregnated together; the accuracy of this alignment is not stated.

- Hayes *et al.* (1985) presents a high-frequency coil for use in magnetic resonance imaging (referred to as the “Birdcage” resonator coil), in which the complex impedance at a specific frequency is used to force a $\cos(\theta)$ current-density distribution on the coil surface. A method by which such a coil could be reproduced for low-frequency use is also presented in Section 3.1, including modeling of the **B** field homogeneity.

Everett and Osemeikhian (1966) describe the construction of a “spherical coil”, which is very closely related to the $\cos(\theta)$ coil. As the name indicates, the “spherical coil” is wound on the surface of a sphere, but the current density on the surface is still in a $\cos(\theta)$ distribution. Due to the coil being wound on a sphere instead of a cylinder, there should be a slight difference in the axial field gradient.

The distribution of the coil winding in the $\cos(\theta)$ coils enables the generation of a volume of magnetic field uniformity that extends along the cylindrical axis with height and width limited by the radius of the cylinder, thereby allowing objects which had previously not been able to be inserted into a magnetic volume to be tested.

2.2.1 Coil uniformity

Field uniformity is extremely important for accurate sensor and hence coil calibration, but its impact on sensors is often not well understood. Frix *et al.* (1994) compare IEEE standard calibration coil options (single coil, circular and square Helmholtz coil pairs), as well as sensor misalignment, showing that the rapid degradation of the field uniformity leads to several percent error in the expected calibration field.

Nissen and Paulsson (1996) investigated the impact of field non-uniformity of the coil on the calibration of sensors, finding the deviation from the true coil calibration factor (defined as the proportionality constants between the excitation currents and the induced magnetic fields), as a function of sensor and coil diameter ratios. Interestingly, for the Helmholtz coil, a sensor must be smaller than a fifth the diameter of the coils to achieve less than 0.1% error.

Carter (1976) associates different coil design methodologies with the Taylor, Chebyshev and Lagrange polynomial approaches, with the Taylor polynomial representing a “maximally flat” field, and with the other two polynomial methods introducing a ripple in the volume of field uniformity. This approach is similar to electronic filter design. Whilst in many cases ripple within a volume may be an acceptable tradeoff for larger uniform volume, our desired magnetic volume may be used for gradiometer calibrations, and hence must have a maximally flat uniform field.

Bronaugh (1995) noted the lack of understanding concerning the limitations of the Helmholtz coil, its available field uniformity and the impact of the size of a device under test on the calibration accuracy. Bronaugh needed to achieve the most effective use of space in a laboratory environment, similar to DSTO’s requirements. Coil calibration was performed by Bronaugh using the “ruler” approach (i.e. physical measurements of coil dimensions are fed into an analytical model to calculate the predicted magnetic field). A rigorous approach to verifying other coil parameters necessary for theoretical modelling, such as the number of turns, is also provided. Finally, Bronaugh also comments on the impact of loading on the coil: if too large an object is inserted within the coil volume, the coil excitation current requirements may be altered, compromising the field uniformity due to mutual inductive coupling to the object.

2.2.2 Coil calibration

Drake (1994) presents an overview of sensor and coil calibrations within the National Physical Laboratory in the United Kingdom. Coil factors are calculated theoretically, and validated against search coils using a known 20 Hz signal. Orthogonality and bias are not considered.

Klymovych and Pajunpaa (2004) present a triaxial coil system made of three sets of four square coils. Coil orthogonality is measured using a theodolite with built-in magnetic sensor, presumably placed within the system during orthogonality measurements. Coil factors are measured by zeroing earth’s field on two axes, and applying large positive and negative signals on the third axis. Background noise is reduced through the use of a remote reference sensor. Accurate current control is achieved by

characterising the response of reference resistors to temperature, during coil excitation. Over the life of the system (years), it was claimed that the coil factors varied by 0.01% and orthogonality varied by 20 arc-seconds.

Piergentili *et al.* (2011) design an earth-field simulator for space applications using a triaxial square Helmholtz system. The system is validated against computer simulations for the field uniformity and coil factors, but orthogonality is not measured, and hence not compensated for.

Kuberry (1967) measures coil factors by zeroing out earth's field using a fluxgate magnetometer, then using a scalar sensor to detect field strength increases due to a subsequent increase in driving current. Error bounds arising from coil and sensor misalignment, as well as sensor bias are estimated in the order of 0.02%, but are not compensated for. Orthogonality between axes is not addressed, as the paper only examines the calibration of single-axis coils.

Youguang *et al.* (2006) built a triaxial yoke system for testing magnetic properties of materials. Search coils are used for field sensing, and are calibrated following a manual alignment in a solenoid of known magnetic field strength. Sensor-coil misalignment is considered, and accounted for by a rotational transformation, but coil orthogonality is assumed to be accurate due to the mechanical fabrication of the triaxial yoke. Desired field strength is obtained using a feedback control system. Field uniformity in the air gap does not appear to have been fully considered.

Schill and Hoff (2001) present work in experimentally measuring the coil factor for a Helmholtz coil. The coil under calibration is placed within a larger triaxial coil which is used in conjunction with a fluxgate magnetometer to cancel earth's field at the centre of the coil. A proton resonance magnetometer is then used to measure the fields generated by the coil under calibration. This procedure contains several shortcomings which Schill and Hoff point out. Firstly, the earth-nulling coil must be larger than the coil under calibration. Secondly, due to the temperature-dependence of the wire-resistance in the offset-coil, changes in temperature will lead to a change in offset field strength, and hence introduce a bias in the calibration. Finally, the fluxgate sensor used in offsetting the earth's field will introduce a bias error dependent on its own internal

errors. The temperature dependence of the coils on the signal amplitude applied to the coils was measured, and temperatures of $\approx 25^{\circ}\text{C}$ to $\approx 80^{\circ}\text{C}$ were achieved after the coil magnetic field strength had stabilised for a set voltage amplitude.

Mirzaeva *et al.* (2012) designed a single axis calibration system for fields of the order of 1 T. A step function is applied to a drive coil wound upon a yoke, and the increasing magnetic field is monitored on a sense coil. Linear regression analysis is used to fit the coil's response. The resulting coil factor was then used to drive the system without feedback, generating fields within 0.76% of expected values.

Shifrin *et al.* (2000) present a four-square-coil-per-axis system, calibrated with a scalar sensor. Sensor orthogonality is measured using methods presented in the Russian literature. Unfortunately, an English translation of the paper could not be obtained in order to provide insight into the techniques used.

2.2.3 Coil limitations

Crotti and Giordano (2004) and Crotti *et al.* (2006) investigate a coil's frequency response, and how it is impacted by inter-winding inductance and capacitance and the skin effect, using a multi-conductor transmission line approach. Coil factors are found to change by $\approx 1\%$ between DC and 250 kHz, or less than 0.1% for frequencies below 50 kHz. Hence for our frequencies of interest (≤ 1 kHz) constant coil factors with respect to frequency can be assumed, but if the coils are driven at higher frequencies, the coil factor variation and the impact on coil orthogonality should be addressed.

Bronaugh (1995) identifies three primary frequency limiting characteristics of the coil:

- The highest frequency limit (and hence the least impact), is when wires are longer than $\approx 0.15\lambda$, and are hence comparable to λ , where λ is the wavelength in the conductor .
- The middle frequency limit is caused by the induced field in the windings.

2.2 Coils

- The lowest and dominant limiting characteristic is the self-resonance of the coil, occurring at frequency $f_0 = \frac{1}{2\pi\sqrt{LC}}$, where L and C are inductance and capacitance of the coil.

Practically the excitation coil will be operated well below resonance, and is more likely to be limited by the response of the driving power supply.

2.3 Noise and Shielding

Two principal noise sources are likely to impact the system: Geomagnetic noise and local transient noise sources. Geomagnetic noise is spatially correlated over distances of several kilometers, due to the large physical size of its sources (Lenz and Edelstein (2006)), and can therefore be compensated for by using a remote reference sensor to feed a compensating signal to the coil. Localised transient noise sources on the other hand are not correlated, and will require shielding.

2.3.1 High magnetic permeability (μ) shields

Mager (1968, 1970) presents work on shielding with high permeability materials to “pull” magnetic fields away from a specified area, with greatest effectiveness when there is a large permeability within the shielding material. Using small nested shields, shielding factors of 6×10^6 have been measured (Donley *et al.* (2007)).

Tashiro *et al.* (2011) experimentally characterise the effect of shielding materials and their impact on the fields. They show how small gaps in the shield endplates can introduce significant fields. The impact of shielding material on the coil factor of a coil within the shield is also briefly discussed.

Kim *et al.* (2007) perform computer modeling on the effectiveness of μ -metal and aluminium shields, to provide low reluctance paths for the magnetic field and hence generating opposing magnetic fields through induced eddy-currents respectively. The effectiveness of the μ -metal shield drops off at ≈ 10 Hz and above, while aluminium on the other hand begins to improve in effectiveness for frequencies above 1 Hz. A combination of the two shielding materials allows a high shielding factor to be maintained over a broad range of frequencies.

Lee and Romalis (2008) investigate the noise sources introduced by shielding. Lee and Romalis (2008) also define an analytical model for calculating the Johnson noise caused by the μ -metal shielding for a variety of geometries. Based on this analytical model, for the in-lab shielded system at DSTO, noise from the shield amounts to ≈ 5 fT, an insignificant amount unlikely to impact on results.

2.3.2 Self-shielding coils

Yoda (1990) presents self shielded coils, which are designed to reduce the external field created by a coil system by placing coils to counteract its field. Whilst this could provide reduced coupling to external structures, there is no guarantee that the magnetic field uniformity within the system being shielded is not compromised. On the other hand Boyvatn and Hafner (2012) present a similar system, using meta-materials, with significant reduction of field strength of ≈ 40 dB. Such a material would likely provide excellent shielding for a small coil, but appears limited to specific frequencies.

2.3.3 Superconducting shields

Aaroe *et al.* (2009) and Claycomb and Miller (2006) present superconducting shields which, whilst providing excellent shielding factors, have the major drawback of requiring liquid Helium or Nitrogen cooling to attain superconductivity.

2.3.4 Signal filtering

Mengchun *et al.* (2010) add digital filtering to a calibration method referred to as a “double adaptive algorithm” taken from Chinese literature, to improve performance in noisy environments. Whilst the core idea is commendable, the paper exhibits several flaws in reasoning⁴, detracting from the core idea of removing noise components from the signal before feeding it into the calibration algorithm. In principle, a band-pass filter, fast Fourier transform (FFT) or an estimator could be used to select specific frequencies which have low background noise, using the alternating signal amplitude to perform a sensitivity and orthogonality calibration as a substitute for the total field

⁴Noise is apparently reduced by applying a low-pass finite impulse response (FIR) filter to signals (which do not appear to be adequately pre-conditioned), removing much of the higher frequency noise (some of which was likely introduced through aliasing) before performing the calibration. The filtering provides an improvement to the calibration, but the paper then proceeds to claim that a filtering post-calibration provides improvements over pre-calibration filtering, presumably mistaking the reduction in signal variance due to filtering for the reduction in signal variance caused by proper calibration.

measurements. This procedure provides improved signal to noise ratios (SNR), and hence a better estimate. The FFT frequency estimators presented by Liao (2011) would serve this purpose. Care should be taken when filtering, as the total $|\mathbf{B}|$ field will contain higher order harmonics of the AC signal.

2.3.5 Summary

High permeability materials used for magnetic shielding can affect the field uniformity within the volume of the magnetic field generated by the coil system. This effect is important because magnetic shielding is necessary for sensor calibration. However, the literature review failed to identify any substantial studies addressing this effect and as such, numerical modelling was conducted to approximately model the impact of high permeability shields on magnetic field uniformity (Section 4).

Chapter 3

Coil Design

3.1 Coil Definitions and Derivations

The existing magnetic coil system from Maribyrnong is modelled as well as alternate designs for comparison of magnetic field uniformity. Four coil designs were selected for modelling:

- The Helmholtz coil design using both circular and square coils is modelled as a benchmark for comparison as it is the typical coil design used in many research environments.
- The Barker coil design is modelled because a similar coil design is in use at the RAN MAGFAC facility located at Steele Point (Sydney Harbour), to quantify the areas of field homogeneity (*Fleet Command - RAN Ranges and Assessing Unit* 2009).
- The coil setup at the Maribyrnong facility was a custom design for DSTO developed by Dr John Ternan (retired); a literature search was conducted to identify the exact name of the coil design, but none was found, as such the coil is here referred to as the “Ternan $\cos(\theta)$ coil”. Modelling is required to provide a comprehensive understanding of the coil’s capabilities.
- A low frequency version of the Birdcage resonator coil system (Hayes *et al.* 1985), was modelled and constructed because of its similarity to the Ternan $\cos(\theta)$ coil design. To avoid confusion with the actual Birdcage resonator design, this coil will be referred to as the “ELFcage” coil (Extremely Low Frequency birdcage coil).

3.1.1 Coil designs

Coil setups were modelled in increasing complexity:

- Circular Helmholtz - two identical circular coils placed symmetrically one on each side of the experimental area along a common axis, and separated by a distance ($2L_s$) equal to the radius (R) of the coil. Each coil carries an equal electrical current flowing in the same direction. See Figure 3.1.

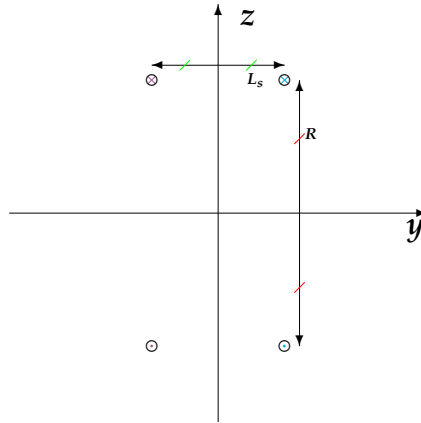


Figure 3.1: Cross section of circular Helmholtz coil design, showing relative spacing of wires.

- Square Helmholtz - two identical square coils (side length $2L$) placed symmetrically one on each side of the experimental area along a common axis, and separated by a distance ~ 0.5445 times the height of the coil (i.e. $L_s = 0.5445L$). Each coil carries an equal electrical current flowing in the same direction. See Figure 3.2.
- Barker - four circular coils placed symmetrically two on each side of the experimental area. The two outer coils have ~ 2.26044 times the current to the inner coils. Inner coils are spaced about ~ 0.23186 times their radii from the centre of the experimental area, whilst the outer coils are ~ 0.940733 times their radii from the centre of the experimental area (Barker 1949, Caprari 1995)⁵. See Figure 3.3.

Where $L_{small} = 0.23186R$ and $L_{med} = 0.940733R$.

⁵Values are taken directly from Barker and Caprari papers

- Ternan $\cos(\theta)$ - the Ternan $\cos(\theta)$ coil consists of N_{cp} coil pairs spaced uniformly with respect to $\cos(\theta)$ on the curved surface of a cylinder whose base is in the yz plane and length is along the x axis; each coil has N_t turns, which is rounded to the closest integer. The same current is passing through each coil turn. At the extremities of the coil the filaments travel along the curved boundary of the circular base of the cylinder, in the yz plane. See Figures 3.4 - 3.5. The configurations of loops shown in Figures 3.4 and 3.6, is designed to provide a uniform field within the cylinder parallel to the y -axis (i.e. \mathbf{B}_y). These sets of coils are referred to as y -axis coils. Furthermore, a uniform field \mathbf{B}_z , orthogonal to \mathbf{B}_y can be generated by a rotation of the set of coil windings by 90 degrees about the x -axis.

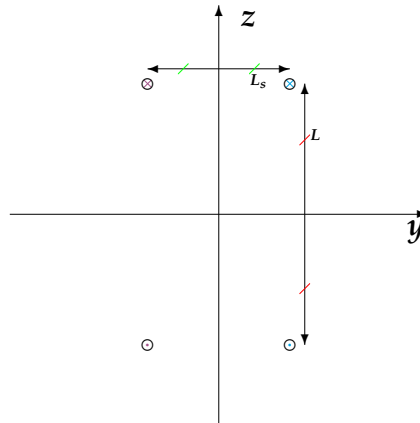


Figure 3.2: Cross section of square Helmholtz coil design, showing relative spacing of wires.

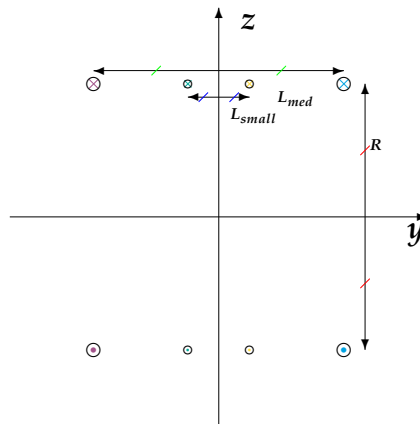


Figure 3.3: Cross section of Barker coil design, showing relative spacing of wires.

3.1 Coil Definitions and Derivations

These sets of coils are referred to as z -axis coils. These two orthogonal sets of coil pairs therefore generate a uniform field parallel to the y and z axes. A third coil (e.g. solenoid) is wound around the cylinder to provide a uniform field along the x -axis, and this coil is referred to as the x -axis coil.

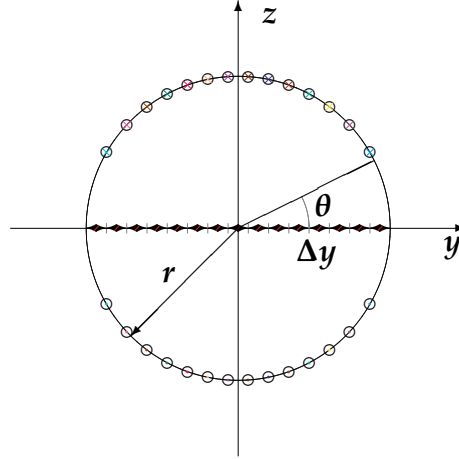


Figure 3.4: Cross section of Ternan $\cos(\theta)$ coil design, showing relative spacing of wires for $N_{cp} = 7$. Each coil on the right hand side of the z axis is associated with a corresponding coil on the left hand side of the z axis, thus forming a coil pair.

- ELFcage - the Birdcage-resonator-like coil consists of N_{cp} coil pairs spaced uniformly with respect to θ on the curved surface of a cylinder whose base is in the yz plane and length is along the x axis, each coil has $||[N_t \sin(\theta)]||$ turns, and the same current passing through each turn. At the extremities of the coil the filaments travel along the curved boundary of the circular base of the cylinder, in the yz plane. See Figure 3.6.

3.1.2 Approximation of B for $\cos(\theta)$ coils at centre of coil

Modelling shows that the magnetic field for $\cos(\theta)$ coils, which are at least three times in length as in diameter, is equivalent to the magnetic field based on Ampere's law for an infinitely long wire given in equation (3.1). This equation can be used to calculate the approximate field in the centre of the coil to within an underestimation of $\sim 5\%$, by summing the B_y components from every line segment (parallel to the x -axis) of the

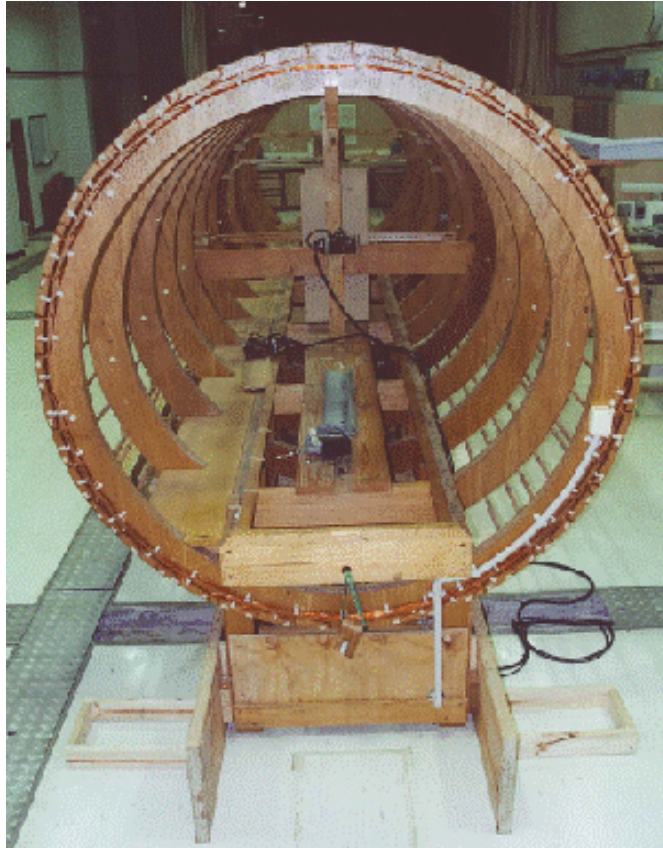


Figure 3.5: Coil filaments as they travel along the boundary of the circular base of the TERNAN coil.

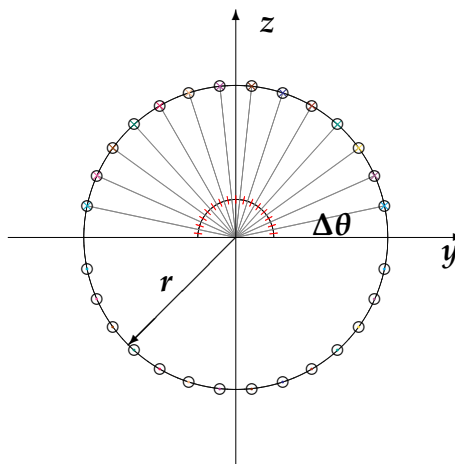


Figure 3.6: Cross section of ELFcage coil design, showing relative spacing of wires for $N_{cp} = 7$.

3.1 Coil Definitions and Derivations

coil filaments for each coil pair. The four wire filaments that lie parallel to the x -axis, and form a coil pair are shown in Figure 3.7.

$$B = \frac{\mu_0 I}{2\pi a} \quad (3.1)$$

where I is the current in the wire and a is the distance from the wire.

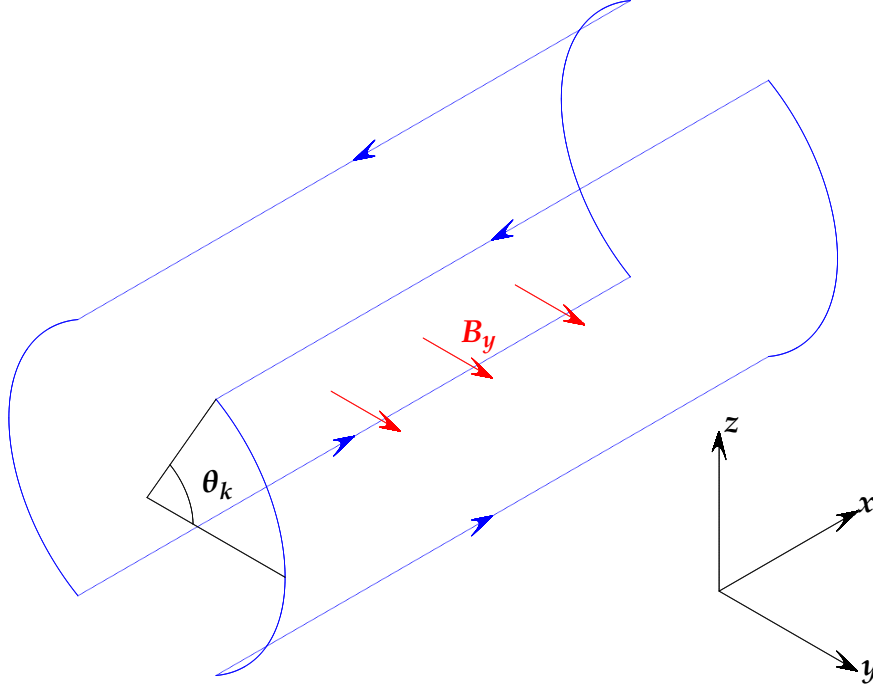


Figure 3.7: Generic coil pair for Ternan and ELFcage designs.

Another method which can be used for shorter coils is obtained by using the Biot-Savart law to calculate the contribution to the field from each loop in the coil (Cheng 1989, Griffiths 1999). For single straight sections of wire, equation (3.2) can be used. Cheng (1989) to calculate the field, a distance r perpendicular to the centre of the wire; and wire length $2L$.

$$B = a_\phi \frac{\mu_0 I L}{2\pi r \sqrt{L^2 + r^2}} \quad (3.2)$$

Note that for $L \rightarrow \infty$ equation (3.2) collapses to (3.1). For the arc at the end of the cylinder, equation (3.3) can be used to calculate its y contribution to the field at the centre of the coil. The z component is ignored as it will be cancelled due to symmetry. Equation (3.3) is derived from the Biot-Savart law applied to a section of a ring which

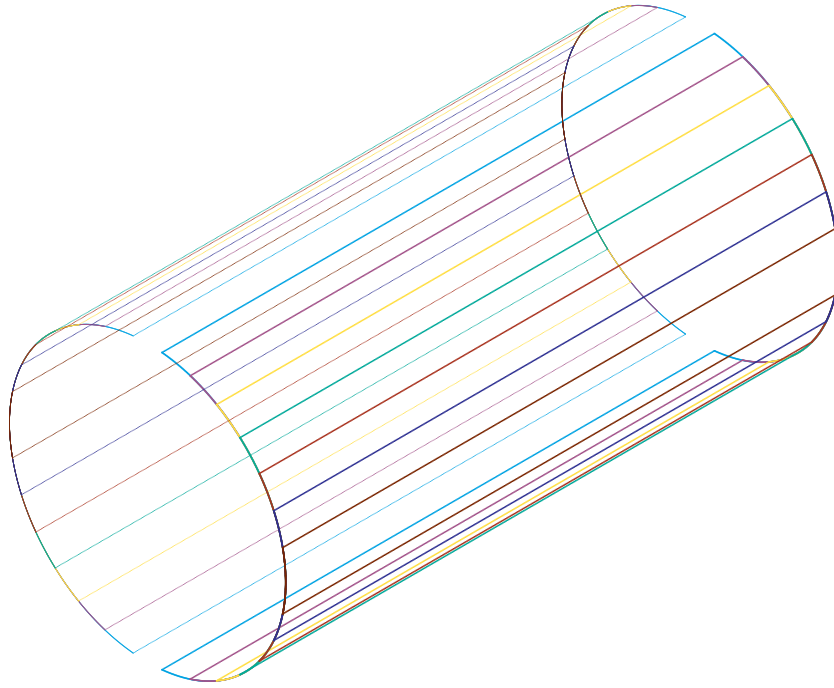


Figure 3.8: Coil winding for ELFcage design.

represents the curved boundary (arc) at the end of the cylinder. For each coil pair, there are four arc segments as shown in Figures 3.7 and 3.9.

$$B = a_y \frac{\mu_0 I L r}{2\pi(L^2 + r^2)^{3/2}} \sin(\theta) \quad (3.3)$$

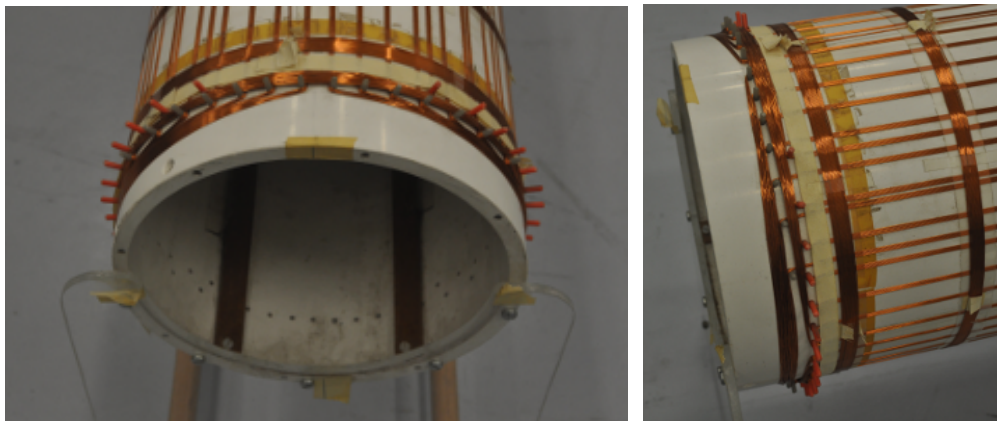


Figure 3.9: Laboratory model of Ternan coil. At the coil boundary the wire forms an arc on the surface of the cylindrical former.

Hence the contribution to the total field at the centre B_y from a single loop which consists of two arc and two line segments is as shown in equation (3.4), generating a field

3.1 Coil Definitions and Derivations

as shown in the right half of Figure 3.7, an equal contribution is provided by the matching coil on the left half of the figure.

$$\mathbf{B} = a_y \frac{\mu_0 I L}{\pi \sqrt{L^2 + r^2}} \left(\frac{r}{L^2 + r^2} + \frac{1}{r} \right) \sin(\theta) \quad (3.4)$$

For a series of N_c single turn loops, as illustrated in Figure 3.8, this becomes equation (3.5).

$$\mathbf{B} = a_y \frac{\mu_0 I L}{\pi \sqrt{L^2 + r^2}} \left(\frac{r}{L^2 + r^2} + \frac{1}{r} \right) \sum_{k=1}^{N_c} \sin(\theta_k) \quad (3.5)$$

3.1.2.1 Ternan $\cos(\theta)$ coil

Since the Ternan $\cos(\theta)$ coil has the same number of turns N_t for each loop, we multiply equation (3.5) by the number of turns, and set θ_k to $\arccos(1 - \frac{2k}{N_c+1})$, because coils are spaced uniformly with respect to $\cos(\theta)$, giving equation (3.6) for the y -component of the magnetic field at the centre of the coil. The field would appear to be more uniform if coils were spaced at the midpoints of current positions, but this introduces the additional constraint of N_t being even to maintain left-right symmetry for the arc sections of the loops at $\theta = \frac{\pi}{2}$, or else the B_z cancelation assumptions leading to equations (3.3) - (3.5) are void.

$$\mathbf{B} = a_y \frac{\mu_0 I N_t L}{\pi \sqrt{L^2 + r^2}} \left(\frac{r}{L^2 + r^2} + \frac{1}{r} \right) \sum_{k=1}^{N_c} \sin(\arccos(1 - \frac{2k}{N_c+1})) \quad (3.6)$$

where $N_c = 2N_{cp}$, and N_{cp} is the number of coil pairs as defined in Section 3.1.1.

In the case of the Ternan $\cos(\theta)$ coil from Maribyrnong, an empirical formula was supplied, which takes into consideration the effects of the conductors as they form a non overlapping arc on the yz plane at the extremities of the coil (Clarke 2011).

$$B = \frac{\mu_0 K I}{r} \quad (3.7)$$

where $K = 22.71$, and $r = 1.003$ m

If we set $I = 1$ A in the case of $N_{cp} = 7$ and $N_t = 6$; $L = 4$ m and $r = 1$ m:

- Equation (3.7) gives $B = 28.4529 \times 10^{-6}$ T;

- Equation (3.6) gives $B = 28.51651 \times 10^{-6}$ T; and
- MATLAB modelling⁶ gives $B = 28.51676 \times 10^{-6}$ T.

There was found to be agreement to within 1% (See Section 7.3.1) between the values calculated by modelling (MATLAB), and equations (3.6) and (3.7); and the magnetic field measured when the coil was tested. This level of agreement is to be expected, since the winding at the coil boundary did not follow the perfect arc assumed in (3.4), and sensors were not properly calibrated. The above expressions for the coil factors refer to the y and z -axis coils. The analogous empirical formula for the x -axis solenoidal coil is equation (3.7), with $K = 20.6$ and $r = 0.99$ m, giving $B = 26.148 \times 10^{-6}$ T.

3.1.2.2 ELFcage coil

Since the ELFcage coil has the number of turns in each loop related to $\cos(\theta)$, we multiply equation (3.5) by $||N_t \sin(\theta_k)||$, and set θ_k uniformly spaced at $\frac{\pi}{N_c+1}$ intervals. $||N_t \sin(\theta_k)||$, is rounded to the nearest integer, representing the number of turns at θ_k .

$$B = a_y \frac{\mu_0 I L}{\pi \sqrt{L^2 + r^2}} \left(\frac{r}{L^2 + r^2} + \frac{1}{r} \right) \sum_{k=1}^{N_c} \sin\left(\frac{\pi k}{N_c + 1}\right) ||N_t \sin\left(\frac{\pi k}{N_c + 1}\right)|| \quad (3.8)$$

where $N_c = 2N_{cp}$, and N_{cp} are defined in Section 3.1.1.

For large N_{cp} the Ternan $\cos(\theta)$ coil approaches a perfect $\cos(\theta)$ current distribution; and if N_t is sufficiently large so will the ELFcage, as such it can be stated that the Ternan and ELFcage coils are simply two different approximations of the $\cos(\theta)$ coil.

3.1.3 Engineering considerations

Selection of N_{cp} and N_t values will affect cost, ease of fabrication, as well as the uniformity of the magnetic field within the coil. Intuitively the most uniform field will be achieved using a Ternan $\cos(\theta)$ coil with an large value of N_{cp} and $N_t = 1$, as it will provide the closest approximation to the field generated by a cylinder with a $\cos(\theta)$ current distribution along its surface.

⁶Full coil was modelled using Biot-Savart law to compute magnetic field throughout the volume within the coil.

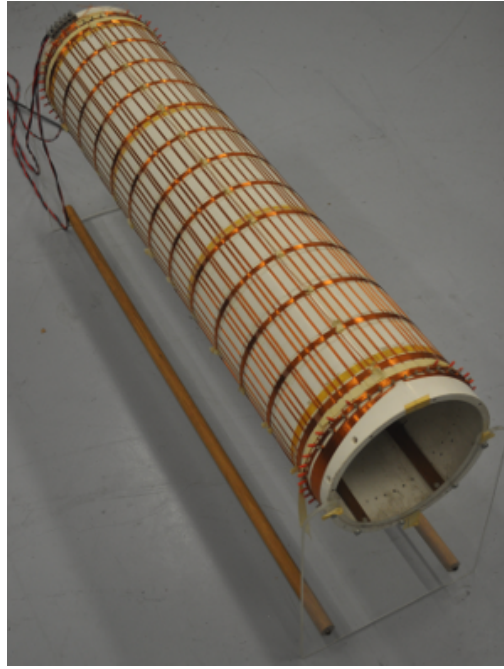


Figure 3.10: Laboratory model of Ternan coil.

A major disadvantage to this approach is that the construction of the coils becomes quite complicated and prone to errors in the placement of wires, due to strict requirements in their positioning, and the sheer number of separate loops to be wound (See Figures 3.9, 3.10); hence wires need to be grouped together either by increasing N_t whilst decreasing N_{cp} , or by moving to the ELFcage design with a lower value of N_{cp} , and higher N_t . This complication is compounded by the addition of a complete set of orthogonal coil pairs required to produce a magnetic field uniformity parallel to the z-axis.

The the estimated wire requirements outlined in equations (3.9) and (3.10). The Ternan $\cos(\theta)$ coil in the DSTO magnetic test facility has values: $N_{cp} = 7$ and $N_t = 6$; $L = 4$ m and $r = 1$ m. The ELFcage was designed with $N_{cp} = 7$ and $N_t = 14$; $L = 4$ m and $r = 1$ m. Hence the Ternan and ELFcage coils require $\sim 1.4\text{km}$ and $\sim 2.1\text{km}$ of wire respectively. The differing wire requirements do not directly impact on manufacture cost, since differing wire gauges would be required, but the process of winding an

ELFcage would most likely be more time-consuming than the winding of a Ternan coil.

$$l_{w_{Ternan}} \approx 2\pi r + 4LN_c N_t + 8N_t r \sum_{k=1}^{N_c/2} \arccos\left(1 - \frac{2k}{N_c + 1}\right) \quad (3.9)$$

$$l_{w_{ELFcage}} \approx 2\pi r + 8L \sum_{k=1}^{N_c/2} \left| \left[N_t \sin\left(\frac{\pi k}{N_c + 1}\right) \right] \right| + 8 \sum_{k=1}^{N_c/2} \left| \left[N_t \sin\left(\frac{\pi k}{N_c + 1}\right) \right] \right| \frac{\pi k}{N_c + 1} r \quad (3.10)$$

The advantage of the Ternan $\cos(\theta)$ coil with a lower N_{cp} , but higher N_t is that fabrication becomes much easier: all loops have the same number of turns, are spaced further apart than for large N_{cp} , and the maximum field strength increases linearly with N_t ; but uniformity is lost near the boundaries of the coil along the y -axis.

The advantage of the ELFcage coil that for the same value of N_{cp} and sufficiently large N_t , a better uniformity is achieved near the y -axis, due to the uniform spacing of coils with respect to θ . Uniformity very close to the boundary is reduced compared to a perfect $\cos(\theta)$ coil, but not as much as for the Ternan approximation.

3.2 Simulation

3.2.1 Volume calculations

MATLAB code was written to reproduce each of the modelled coils as a series of straight line segments defining the path the wire would follow when actually winding the coil. In the case of the Helmholtz, Barker and Ternan $\cos(\theta)$ coils, the increased number of turns in the coil was modelled by a linear increase of current passing through a single wire; whereas in the case of the ELFcage coil each winding was individually included. The BiotSavart law was then used to calculate the contribution from each segment to our area of interest.

3.2.1.1 Field strength at centre of coil

From the field strengths B_x , B_y and B_z calculated in MATLAB, B_{centre} was defined to be the field strength at the centre of the coil as shown in equation (3.11). B_x and B_z were found to be zero at the centre of the coil.

$$B_{centre} = |B_{y_{centre}}| \quad (3.11)$$

3.2.1.2 Field normalisation

Since coils were designed to generate a field in the y direction, fields were normalised as shown in Table 3.1, to provide a clear representation of the variation of the field with respect to the centre.

Results for the cross section at the centre of each coil are in Figures 3.11, 3.12, 3.13, 3.14 and 3.15, where all variations greater than 5% have been clipped to allow visibility of small changes.

| Field Component axis | Normalisation | Reason |
|----------------------|--|---|
| $\Delta B_{x\%}$ | $100 \left \frac{B_x}{B_{centre}} \right i$ | Calculate % variation from zero |
| $\Delta B_{y\%}$ | $100 \left \frac{B_y - B_{centre}}{B_{centre}} \right j$ | Calculate % variation from B_{centre} |
| $\Delta B_{z\%}$ | $100 \left \frac{B_z}{B_{centre}} \right k$ | Calculate % variation from zero |

Table 3.1: Field normalisations, where i, j, k are unit vectors along the x, y, z axes.

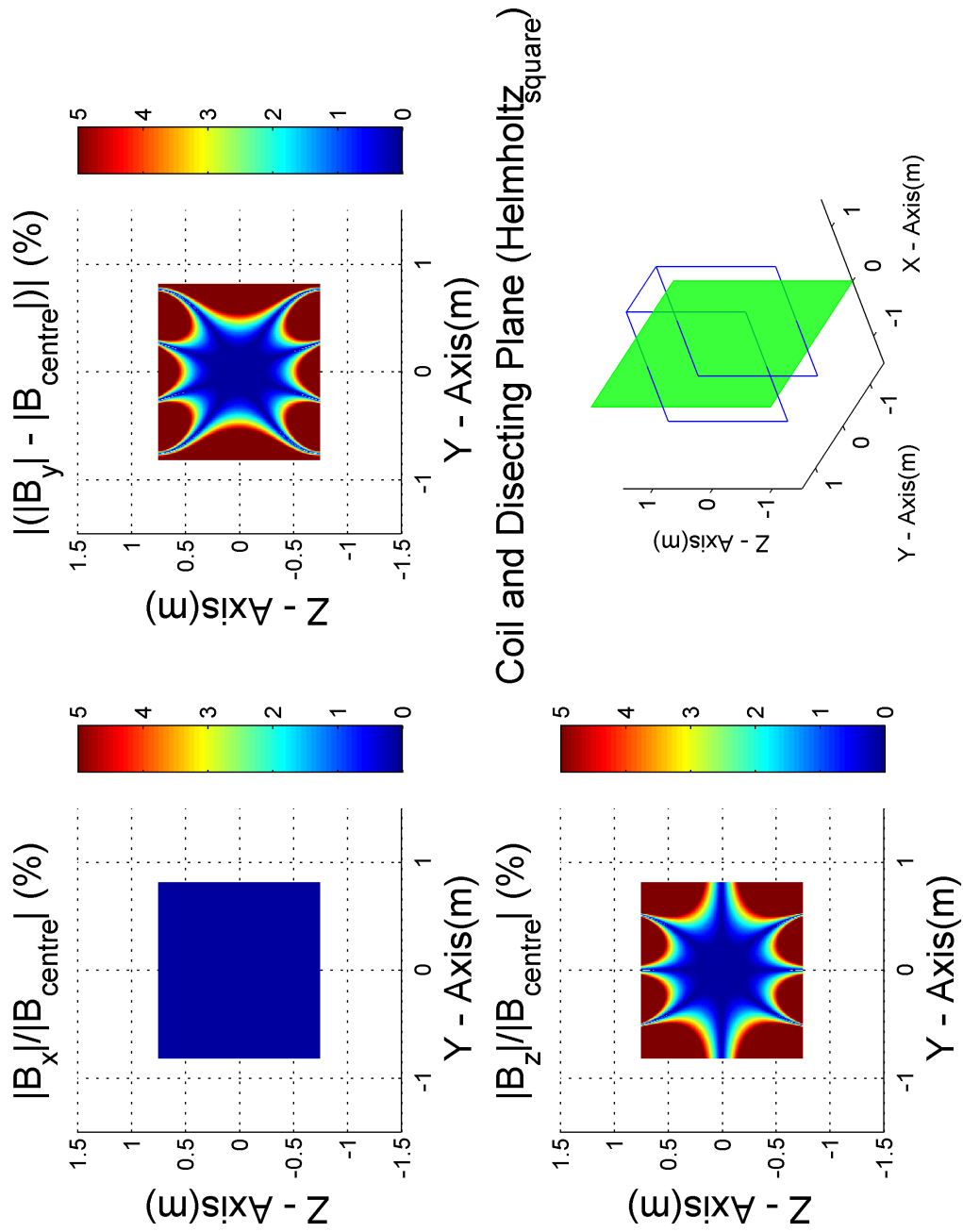


Figure 3.11: Representation of B_y , B_z and B_x fields components mapped in the yz -plane at $x = 0$, for the square Helmholtz coil configuration (side length of 2 m).

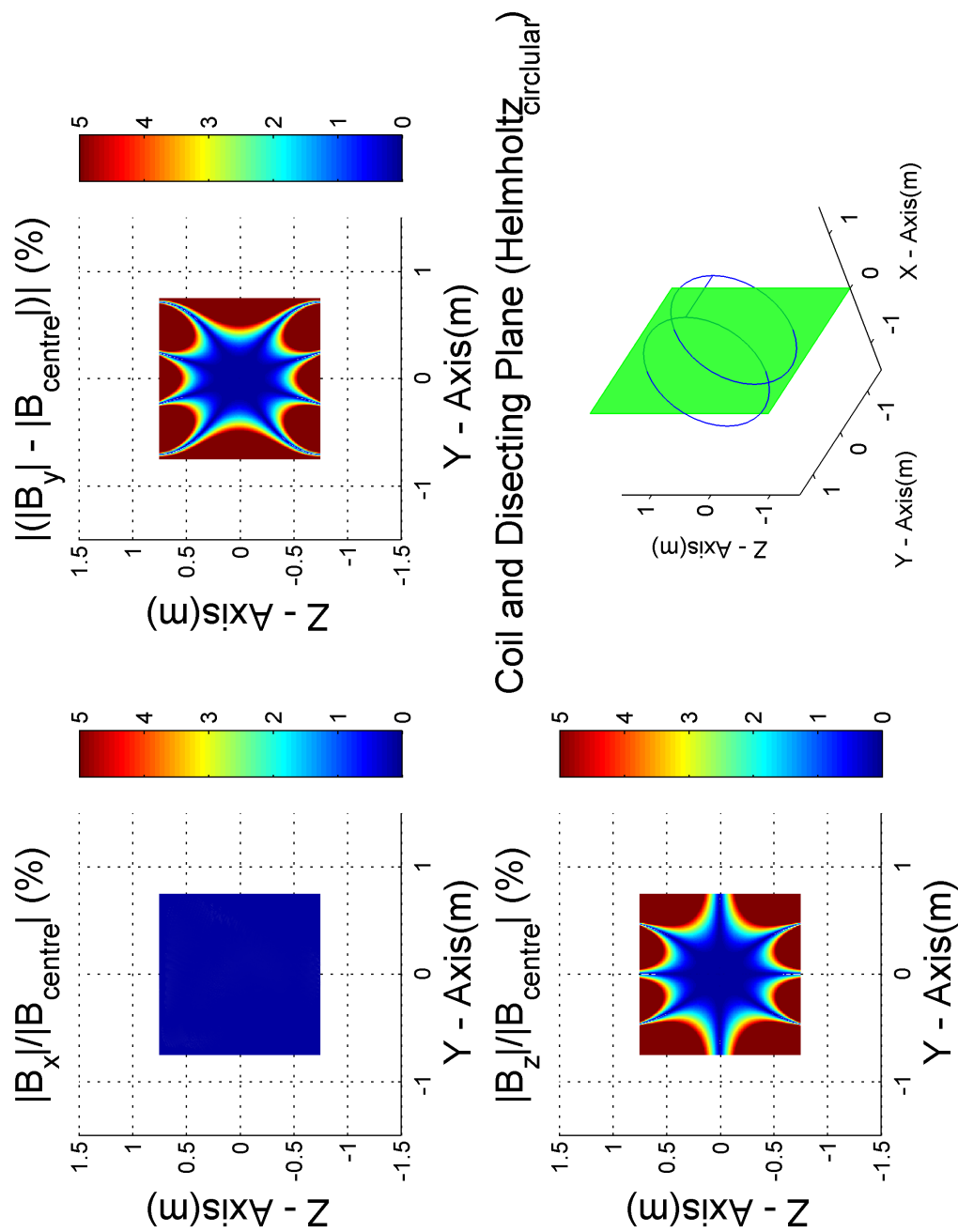


Figure 3.12: Representation of B_y , B_z and B_x fields components mapped in the yz -plane at $x = 0$, for the circular Helmholtz coil configuration (radius 1 m).

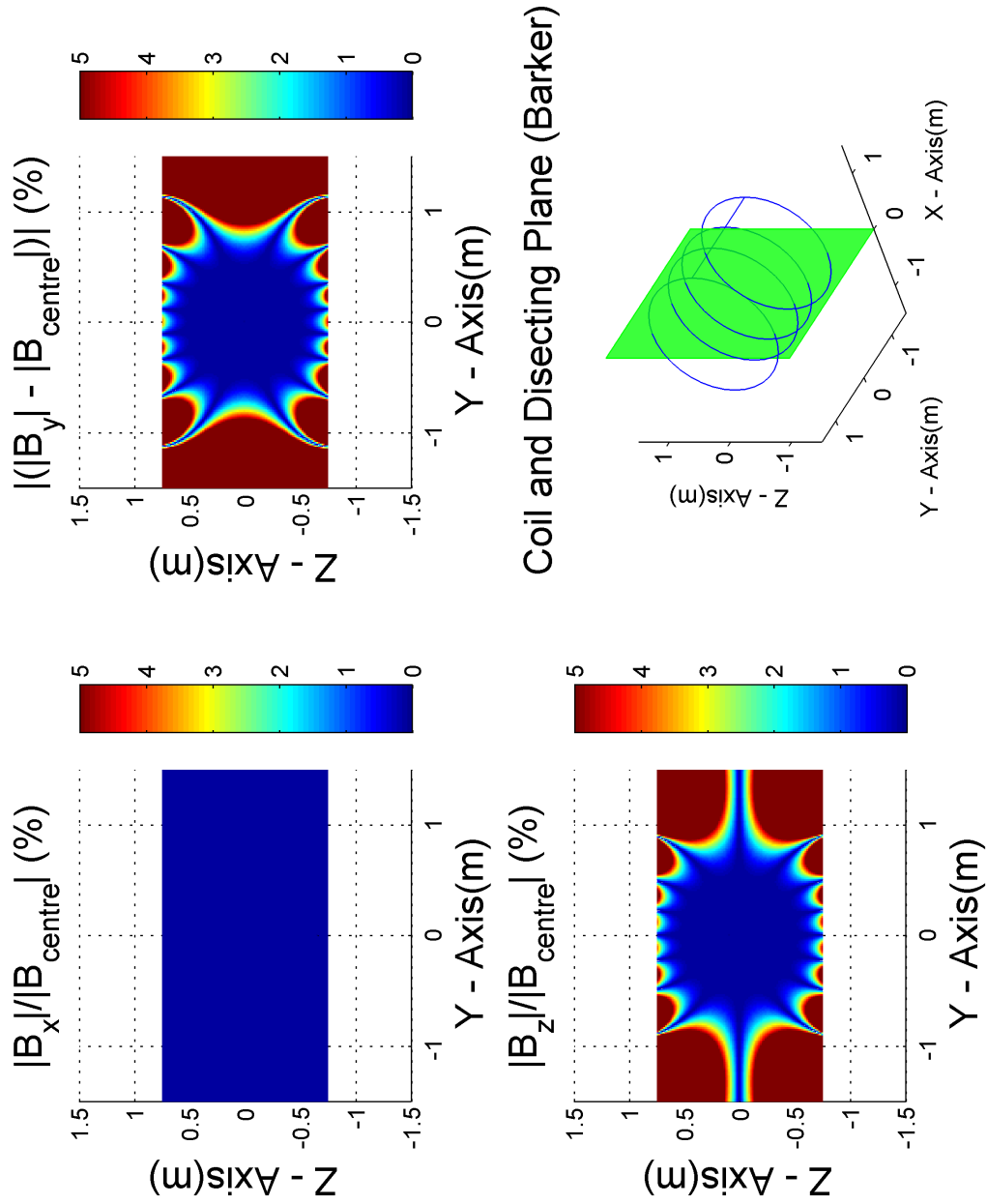


Figure 3.13: Representation of B_y , B_z and B_x fields components mapped in the yz -plane at $x = 0$, for the Barker coil configuration (radius 1 m).

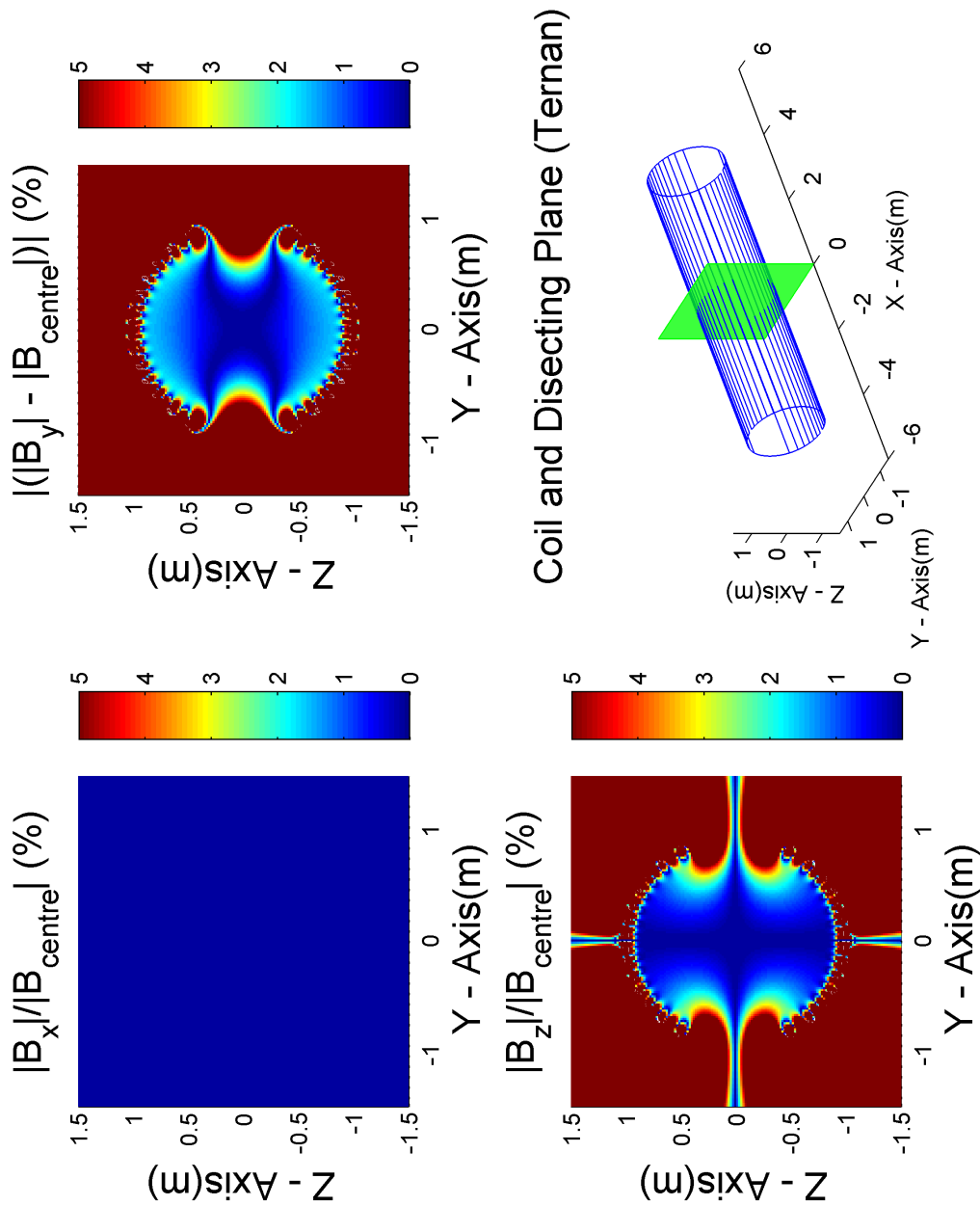


Figure 3.14: Representation of B_y, B_z and B_x fields components mapped in the yz -plane at $x = 0$, for the Ternan $\cos(\theta)$ coil configuration (radius 1 m, side length of 8 m).

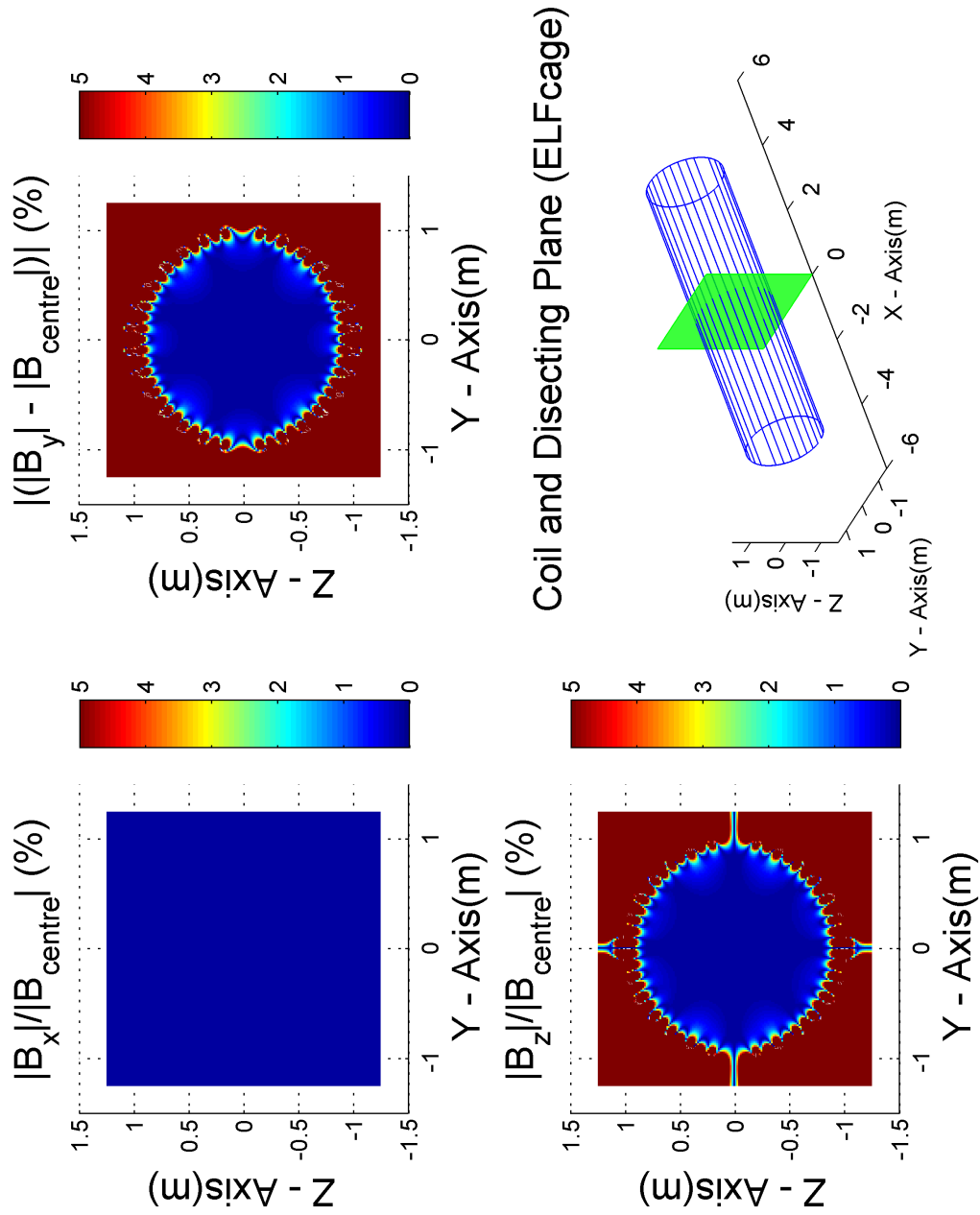


Figure 3.15: Representation of B_y , B_z and B_x fields components mapped in the yz -plane at $x = 0$, for the ELFCage coil configuration (radius 1 m, side length of 8 m).

Note that in Figures 3.11 - 3.15, in the lower right panel, at the furthest points of the coil in the x - z plane, the coils appear connected by a wire parallel to the y axis. This wire is in fact a pair of wires with current running in opposite directions, and was included to faithfully represent how the coils are wound in real life. The wire-pair does not contribute to the total magnetic field as the wires cancel out each other's field.

3.2.1.3 Volume surface

Data points were considered to be part of the uniform volume if they met three conditions:

- $\Delta B_{total\%}$ was less than desired uniformity error bounds (see equation (3.12)). Equation (3.12) represents the absolute value of the sum of the column vectors $\Delta B_{x\%}$, $\Delta B_{y\%}$, $\Delta B_{z\%}$.
- The point was within a radius $0.85r$ from the x -axis, to reject the filaments of $\Delta B_{total\%} \sim 0$ field error which appear between closely spaced wires. These filaments are clearly shown as the ripple in the field uniformity in Figures 3.14 and 3.15.
- Starting from the point's projection on the x -axis, all points to the centre of the coil along the x -axis are within the volume.

$$\Delta B_{total\%} = |\Delta B_{x\%} + \Delta B_{y\%} + \Delta B_{z\%}| \quad (3.12)$$

Figures 3.16 - 3.20 show the $\pm 1\%$ $\Delta B_{total\%}$ volumes for the Helmholtz, Barker, Ternan $\cos(\theta)$ and ELFcage coils; Figures 3.21 - 3.25 show the $\pm 3\%$ equivalents. What appear to be steps along the x -axis, are in fact caused by the discrete number of samples taken along said axis.

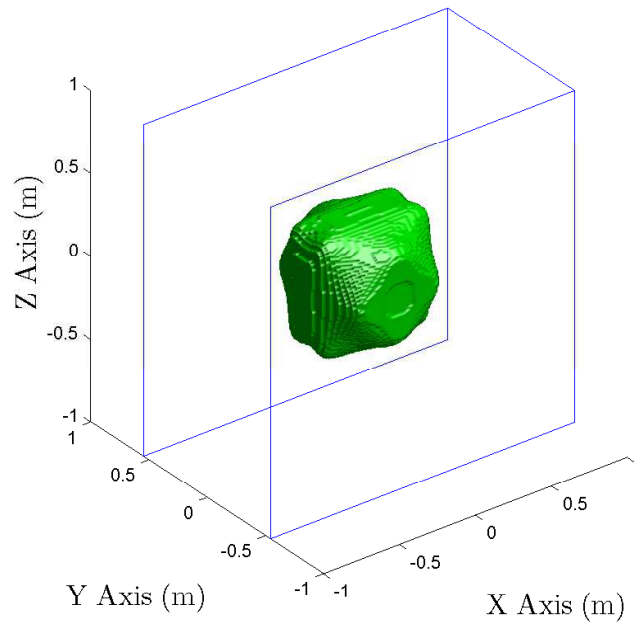


Figure 3.16: Volume bounded by a $\pm 1\%$ variation from B_{centre} within Square Helmholtz coil.

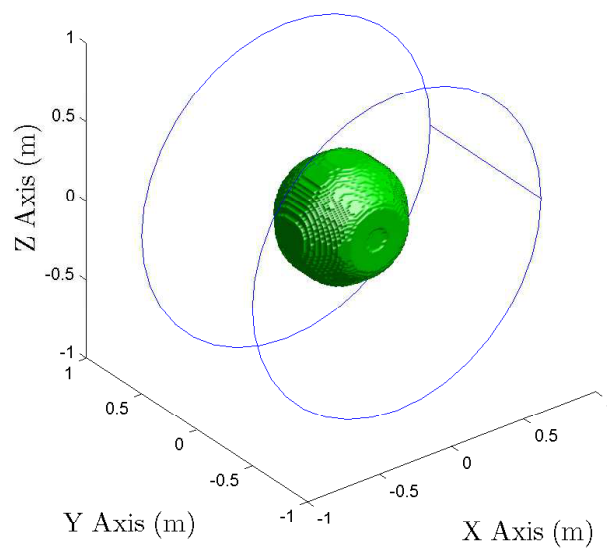


Figure 3.17: Volume bounded by a $\pm 1\%$ variation from B_{centre} within Helmholtz coil.

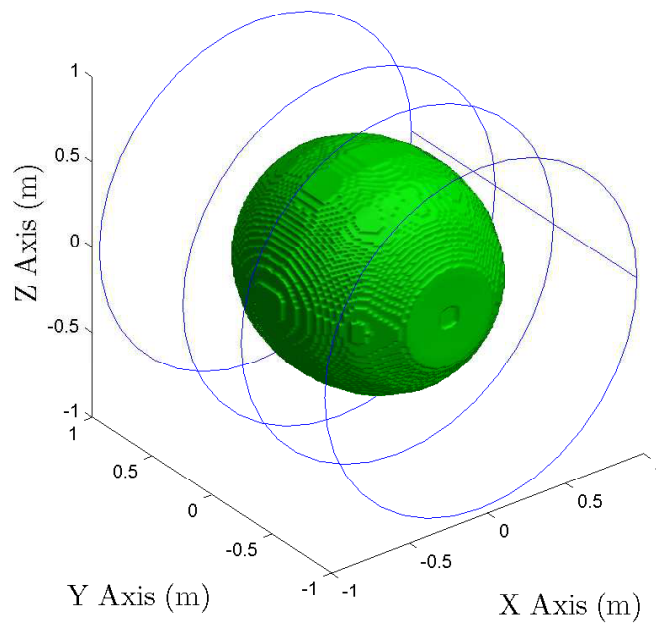


Figure 3.18: Volume bounded by a $\pm 1\%$ variation from B_{centre} within Barker coil.

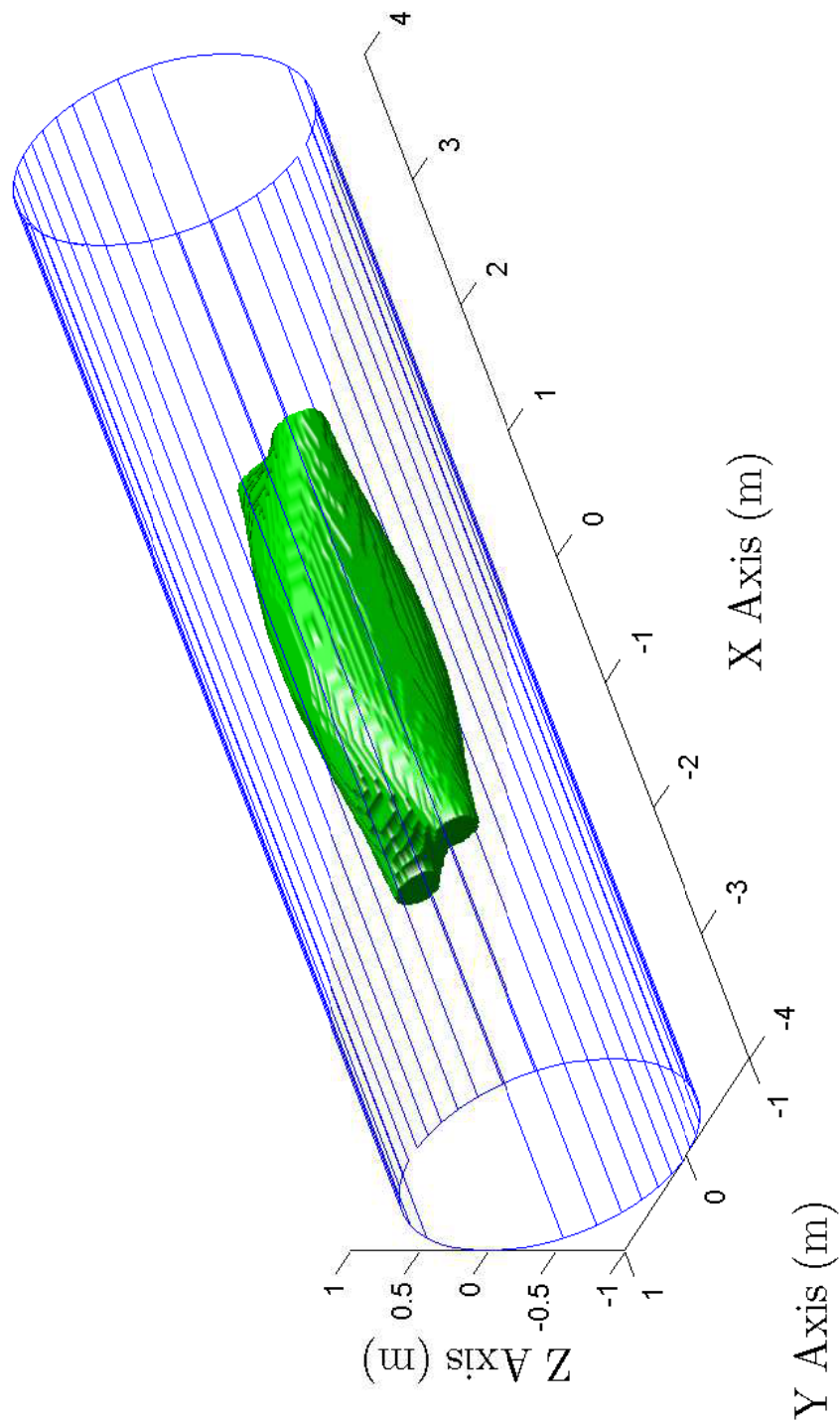


Figure 3.19: Volume bounded by a $\pm 1\%$ variation from B_{centre} within Terman $\cos(\theta)$ coil.

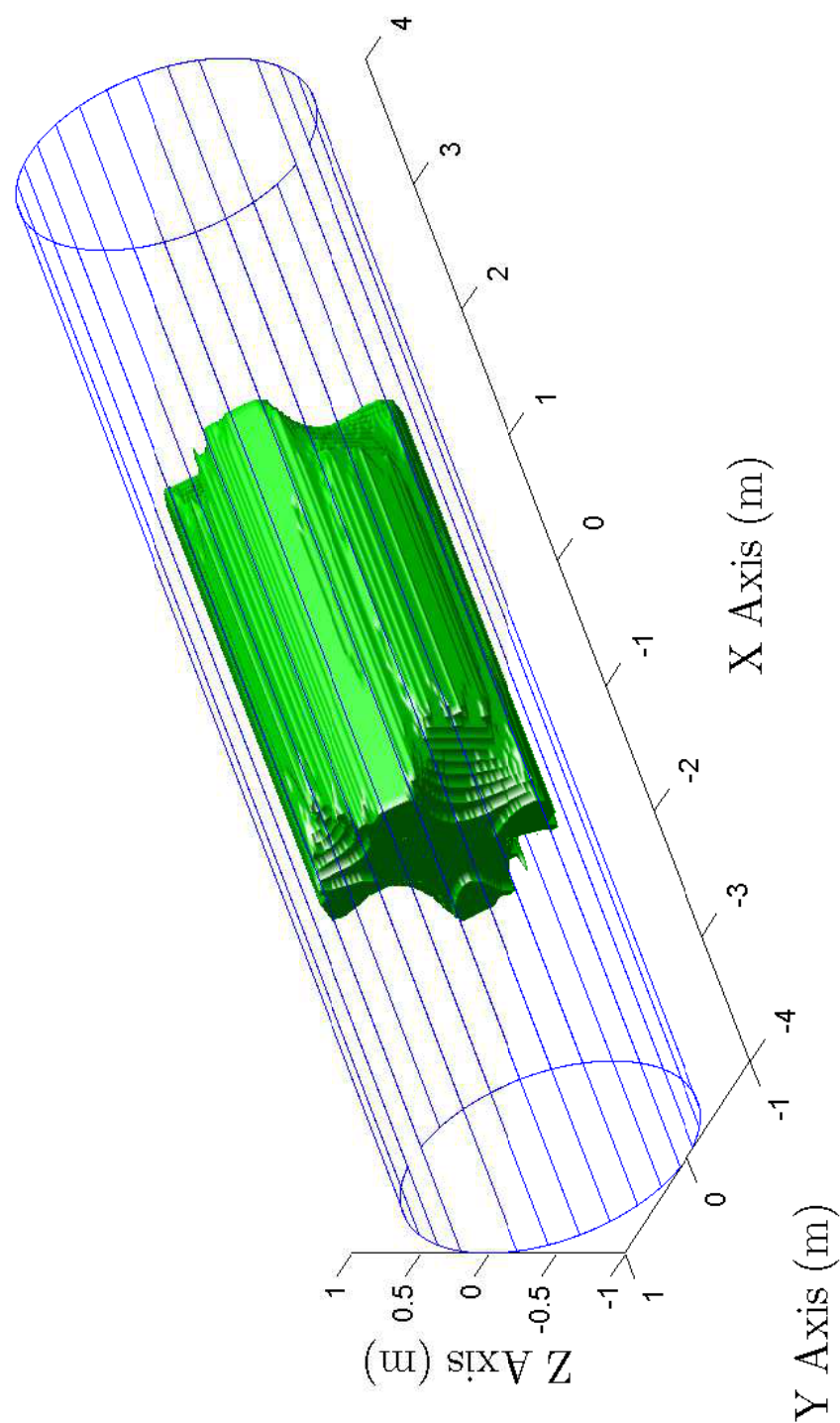


Figure 3.20: Volume bounded by a $\pm 1\%$ variation from B_{center} within ELFcage coil.

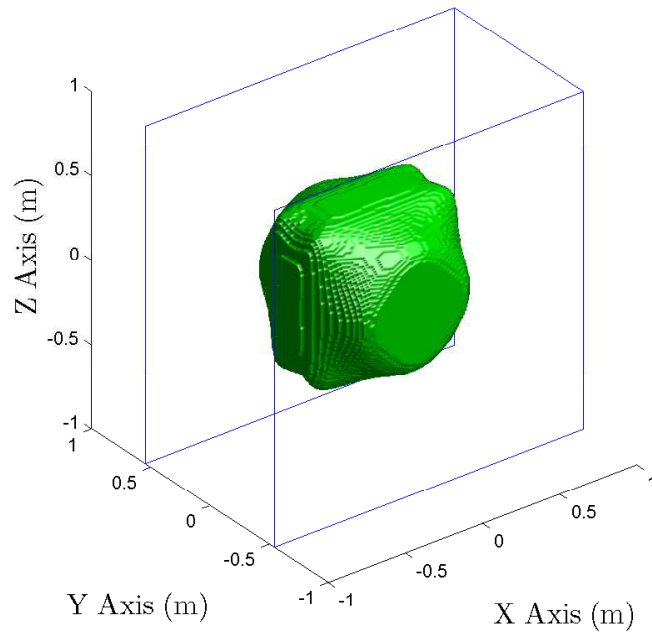


Figure 3.21: Volume bounded by a $\pm 3\%$ variation from B_{centre} within Square Helmholtz coil.

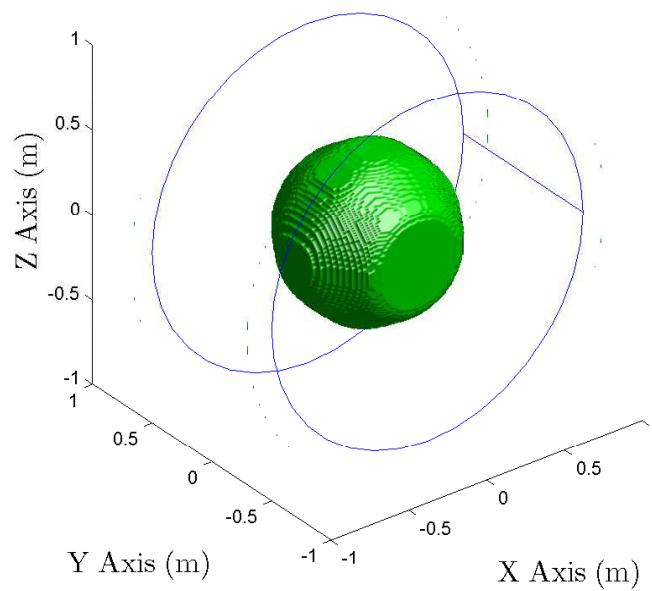


Figure 3.22: Volume bounded by a $\pm 3\%$ variation from B_{centre} within Helmholtz coil.

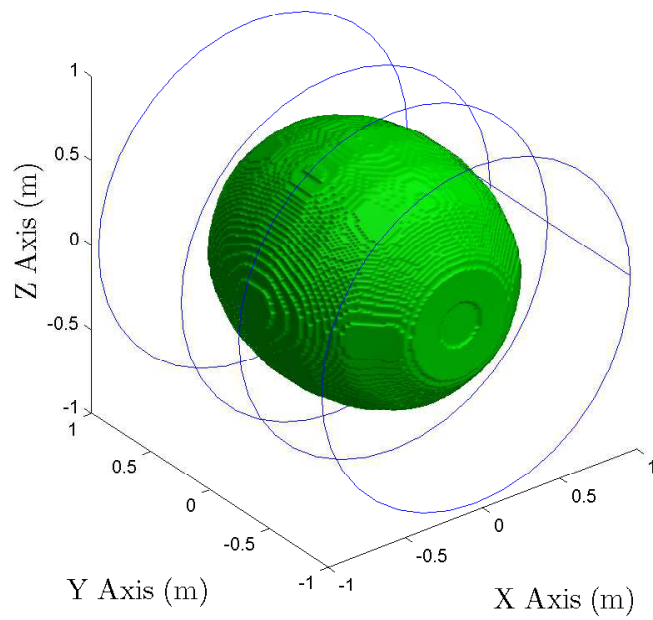


Figure 3.23: Volume bounded by a $\pm 3\%$ variation from B_{centre} within Barker coil.

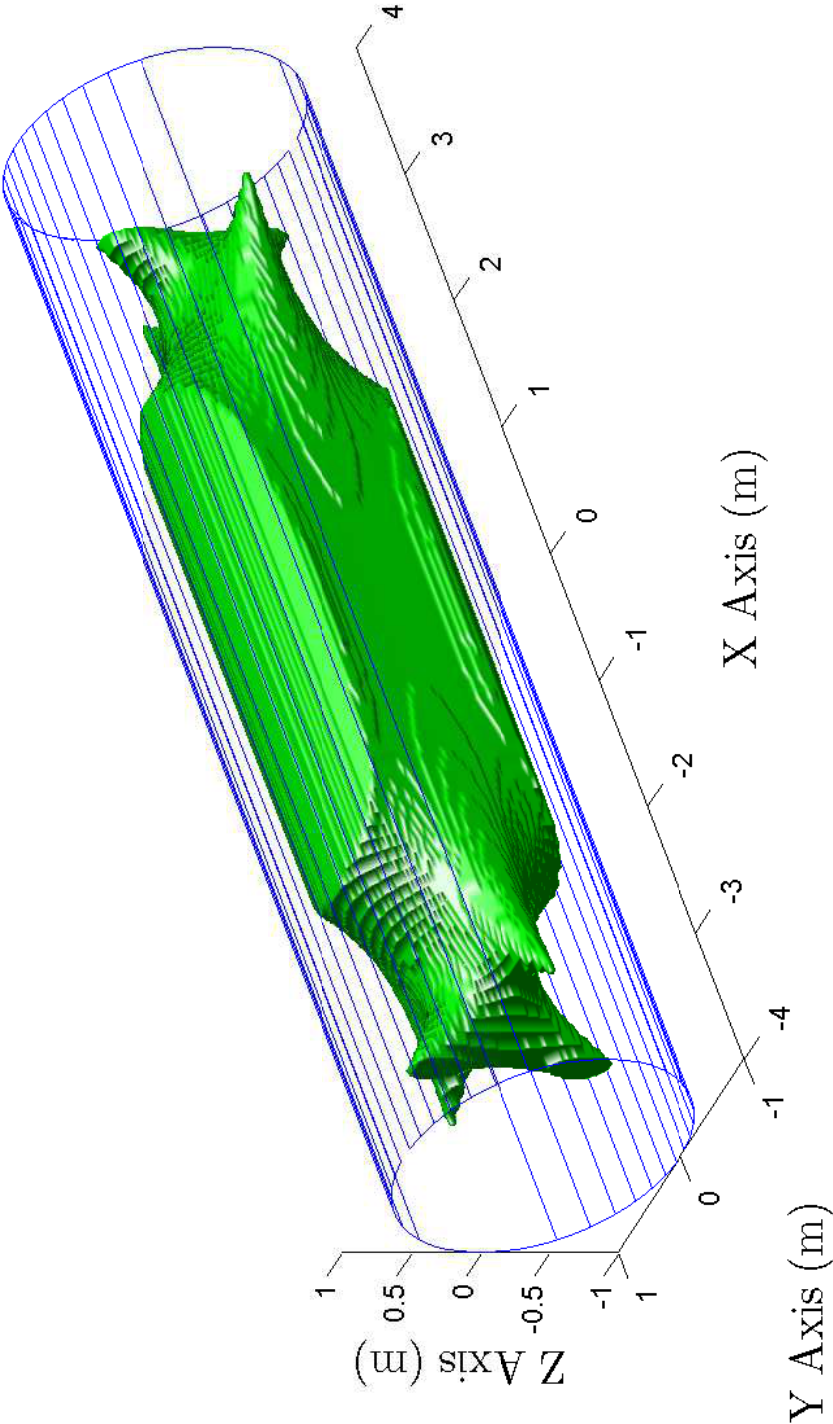


Figure 3.24: Volume bounded by a $\pm 3\%$ variation from B_{centre} within Ternan $\cos(\theta)$ coil.

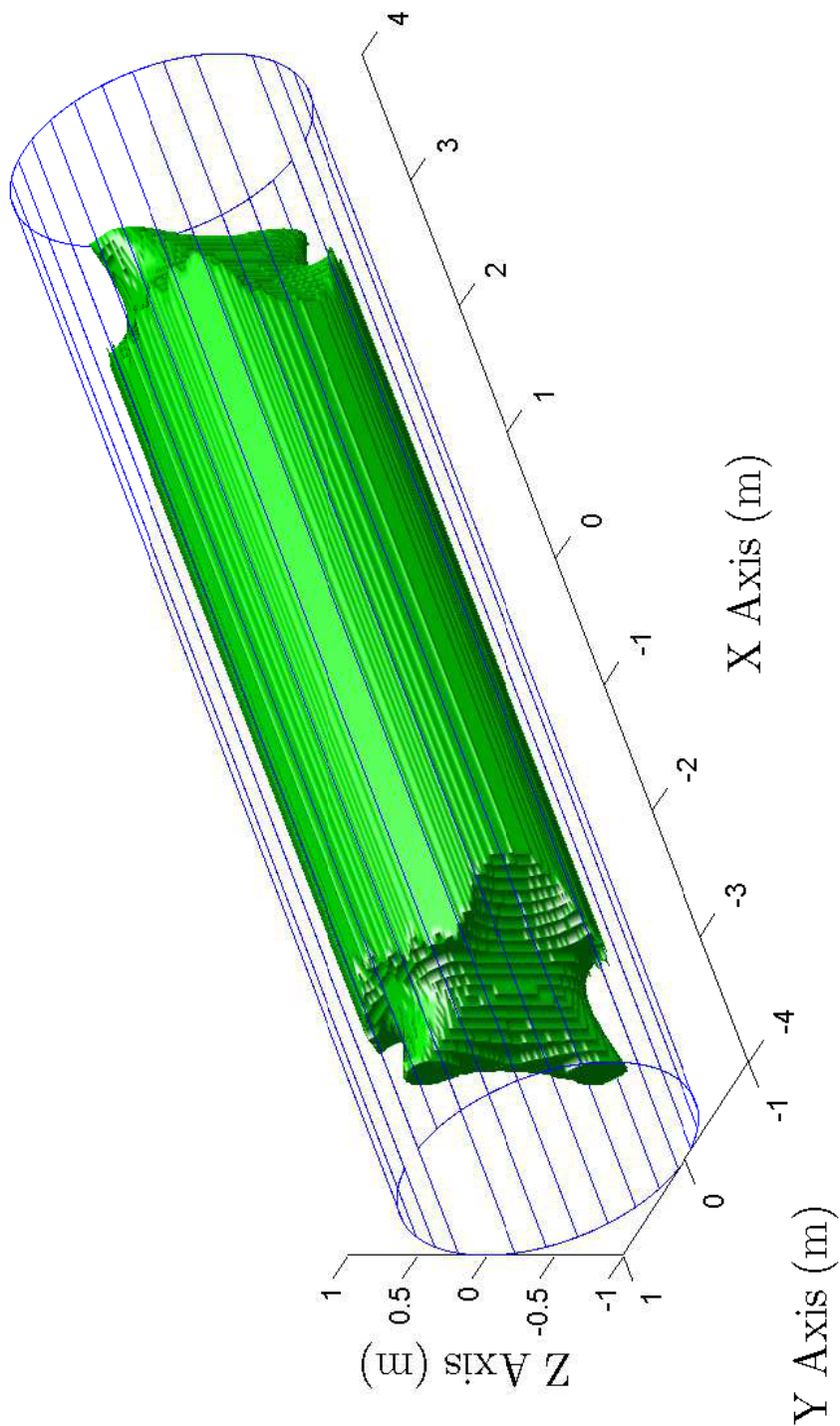


Figure 3.25: Volume bounded by a $\pm 3\%$ variation from B_{center} within ELFcage coil.

3.2.2 Comparison of coil designs

As a measure for comparing the effectiveness of each coil, the ratios of the uniform volume to the total volume bounded by the coil and of the uniform area to the total area in the yz -plane are shown in Figures 3.26 and 3.27 respectively. Usable volume and area were calculated using the method defined in Section 3.2.1.3.

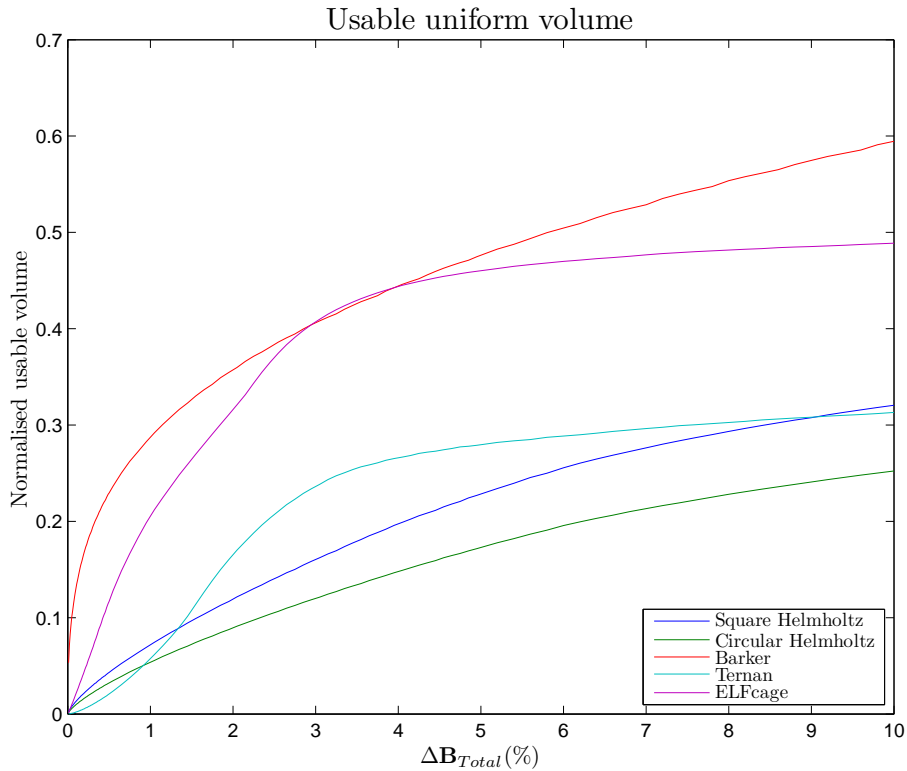


Figure 3.26: Comparison of usable volume as a function of the percentage field uniformity ($\Delta B_{total\%}$ (3.12): 0 – 10%).

As shown in Figure 3.26, the Ternan $\cos(\theta)$ and ELFcage coils provide a large uniform volume to work with for any set uniformity requirements, with reasonably steep increases in usable volume as the requirements are relaxed. The ELFcage exhibits strong radial growth at the centre as values are relaxed from 0 to 1% (See Figure 3.27), making it ideal for ranging of short objects with large diameters to a high degree of accuracy. The ELFcage and Ternan $\cos(\theta)$ coil are superior to the Helmholtz and Barker designs only under specific uniformity values. Their performance could be improved by an

increase of N_{cp} for both coils, and an increase in N_t for the ELFcage. Preliminary simulations indicate the ELFcage can generate a more uniform field than the Barker coil when both N_{cp} and N_t are increased to values of ~ 10 and ~ 16 respectively.

Note that the Barker coil appears to be the most suitable given that it has the highest usable volume and area ratios. However the Barker coil has a lower diameter to length ratio compared to the $\cos(\theta)$ coils for creating a uniform field. For example for 3% field uniformity Figure 3.23 shows that 2 m diameter coils are required to generate a uniform \mathbf{B}_y field that extends approximately 1 m in length along the x -axis. Therefore a longer prolate object, e.g. 6 m in length, would require a coil diameter of approximately 12 m, which is impractical. However, Figures 3.24 and 3.25 show that the field uniformity for the Ternan and ELFcage coils extends to approximately 6 m.

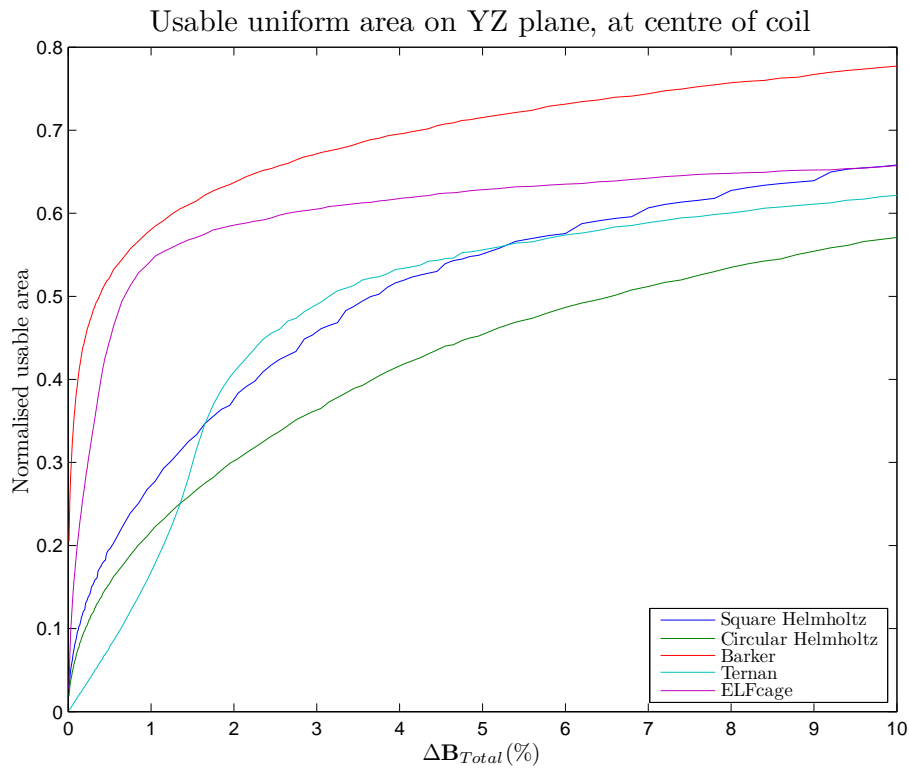


Figure 3.27: Comparison of usable area as a function of the percentage field uniformity ($\Delta B_{total\%}$ (3.12): 0 – 10%).

Chapter 4

Effect of Magnetic Shielding on Field Uniformity

The “Finite Element Method Magnetism 4.2” package (Meeker 2010), is used to investigate the impact μ -metal shielding would have on the field uniformity of a small triaxial magnetic coil system.

A solenoidal field was modeled in free air, inside a cylindrical shield with one open end, and inside a closed cylindrical shield with a small gap in the junction between the body of the shield and the lid. An infinitely long ELF cage coil was also modeled with and without shielding.

4.1 Solenoid

The solenoid has the following physical dimensions: radius 0.28 m, length 0.66 m, with 340 turns of 2 mm diameter wire, having 0.1 A flowing through them. The μ -metal shield is in the form of a can, and is 2 mm thick with an internal radius of 0.320 m, and is 0.684 m deep. The lid provides an additional 0.058 m of space above the shield body. The lid is 2 mm thick, and is modeled as having an outside diameter that is 6 mm larger than the outside diameter of the shield body, leading to a 1 mm gap in the overhang between the lid and the body (See Figure 4.1), this gap is a worst-case scenario for incorrect lid placement, and in real life is expected to be of the order of 0.1 mm.

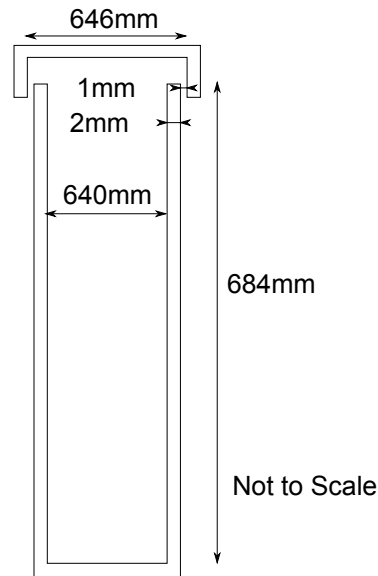


Figure 4.1: Illustration of μ -metal shielding container.

Figures 4.2, 4.3, and 4.4 illustrate how the magnetic field lines are pulled toward the shielding material, with angles of incidence close to 90° , and the magnetic field lines in Figure 4.4 are visibly straightened by the end-fire shielding from the lid. Note that the contour lines are not an indication of field strength, since they were plotted using an auto-scale function. Figures 4.3, 4.5 and 4.6 show the effect of removing the shielding lid (located at approximately -0.4 m in Figures 4.5 and 4.6), causing the field at the coil boundary to be pulled radially outward toward the shield body, creating a greater field-gradient than in the in-air coil. The cross sections in Figures 4.7, and 4.8 show the extent to which field uniformity is broadened by the gradual increase in shielding.

Figure 4.5, shows the effect of the gap between the shield lid and the coil (at approximately -0.4 m) compared to the shield base and the coil (at approximately $+0.4$ m), leading to a slight reduction in field strength. Compare right and left hand sides of the “green” curve in Figure 4.5.

The spike in magnetic field strength at approximately $+0.4$ m (Figure 4.5) from the centre is due to the boundary between air and the shield, followed by a the final extracted data-point being set to zero for plotting purposes; this glitch is also present in Figure 4.7, and to a lesser extent in the other figures. The asymmetry in the in air coil in Figure 4.5 (“red” curve) is caused by the coil and shield not being co-centred, that is the field

lines are computed to the edge of the can on the right hand side, and to the edge of the lid on the left hand side, hence causing the air-gap to the left of the solenoid to be included.

Shielding will tend to increase the uniformity of the generated field.

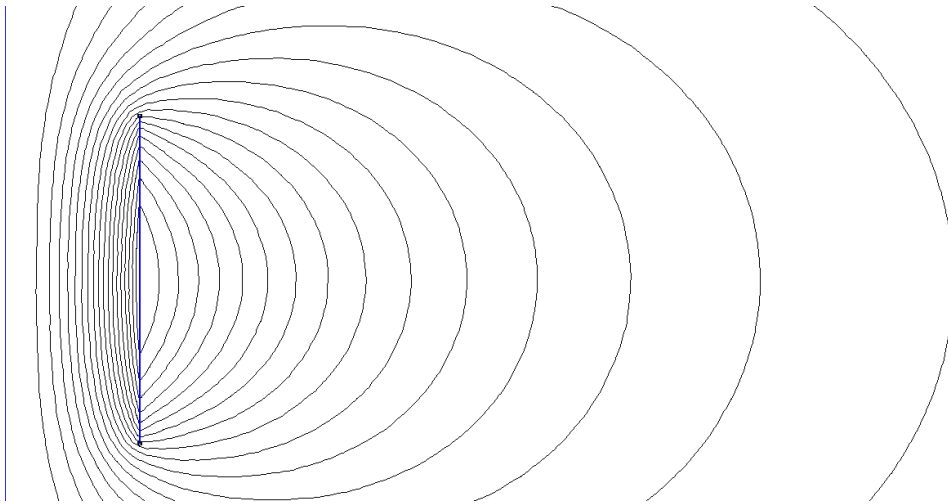


Figure 4.2: Magnetic field generated by solenoid in air. Diagram shows right hand side of field lines. The leftmost line represents the solenoid axis of symmetry.

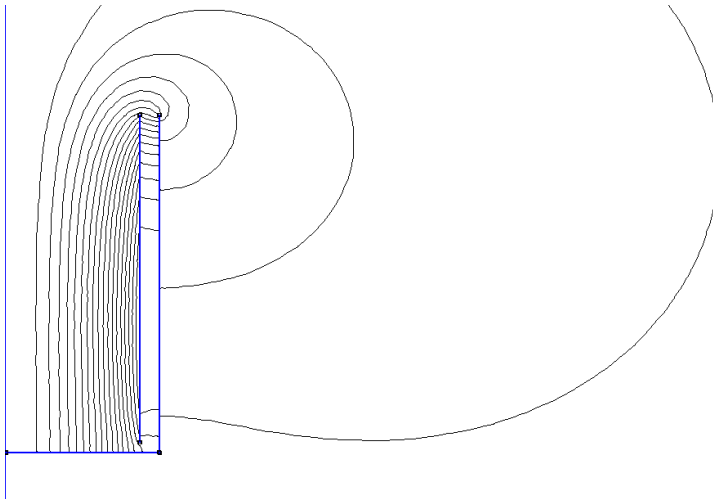


Figure 4.3: Magnetic field generated by solenoid in open μ -metal container. Diagram shows right hand side of field lines. The leftmost line represents the solenoid axis of symmetry.

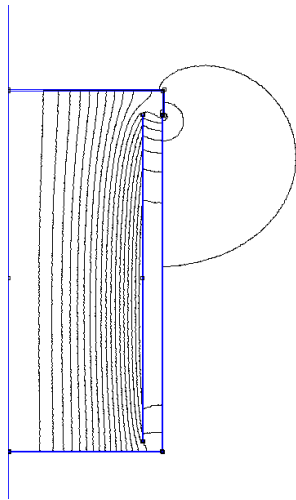


Figure 4.4: Magnetic field generated by solenoid in closed μ -metal container. Diagram shows right hand side of field lines. The leftmost line represents the solenoid axis of symmetry.

4.1.1 Anomalies

Figures 4.6 and 4.8 exhibit a sharp drop in the field at the origin, this is due to FEMM not calculating the field at the simulation boundary, whence when interpolating the cross section plot near the boundary a straight line is generated linking the closest data-point within the finite element mesh and the boundary. As the mesh density is increased⁷, the drop becomes steeper, since the data-points are closer to the origin.

⁷The mesh resolution was increased as more details were added to the geometry

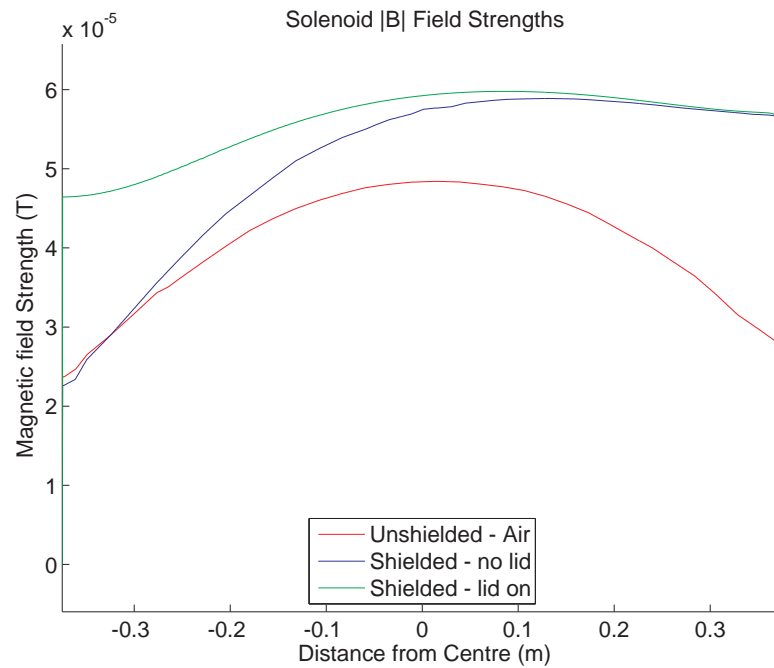


Figure 4.5: Total field strength along solenoid axis of rotational symmetry. The lid is located at -0.4 m, and the base is located at $+0.4$ m.

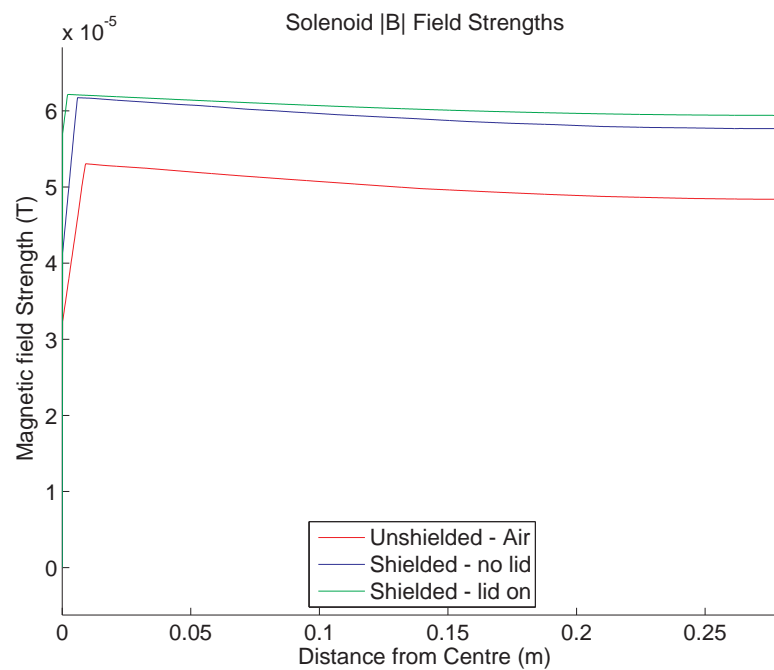


Figure 4.6: Total field strength along the radial direction from the axial centre of solenoid.

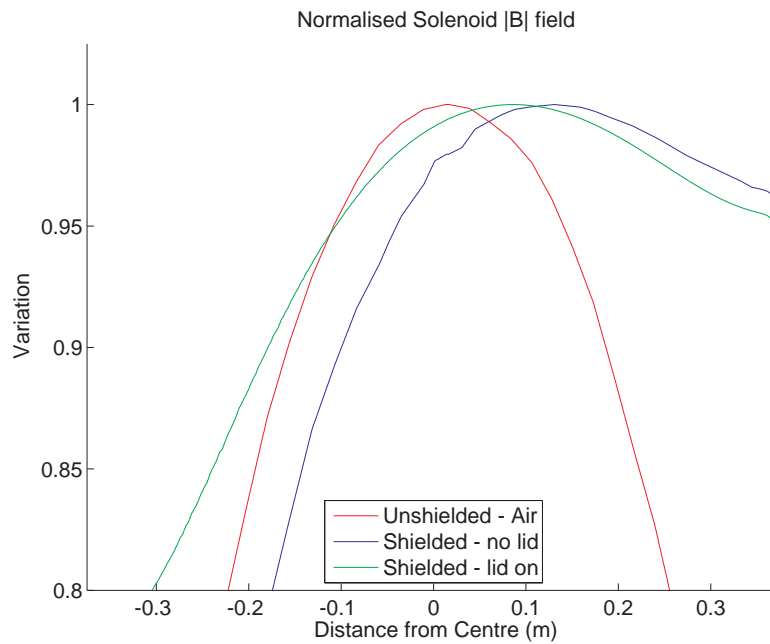


Figure 4.7: Total field strength variation along solenoid axis of rotational symmetry. The lid is located at -0.4 m, and the base is located at $+0.4$ m.

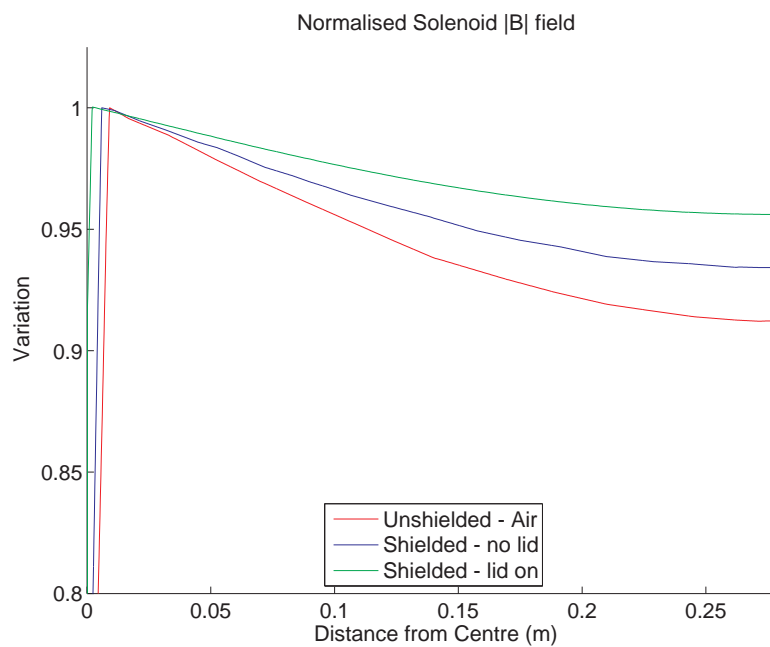


Figure 4.8: Total field strength variation along the radial direction from the axial centre of solenoid.

4.2 ELFcage

The simulated ELFcage had the following physical properties: Shield radius is 0.32 m, ELFcage radius is 0.28 m, $N_T = 11$, and $N_{cp} = 4$, with a current of 0.01 A running through the coil filaments.

Figures 4.9 and 4.10 seem to indicate the shielding does not significantly improve uniformity within the ELFcage coil, however it does show qualitatively the increase in field strength with shielding compared to an in-air coil. In Figure 4.9 the blue circular boundary represent the fictitious boundary of the shield. In Figure 4.10 the blue circular boundary represent the boundary of the shield.

Similar to the case of the shielded solenoid, Figures 4.11 and 4.12 show how the magnetic field strength is amplified by the presence of shielding; the generated field strength is increased by a factor of two, while the induced currents in the shields slightly improve uniformity, as shown in Figures 4.13 and 4.14. Figures 4.11 to 4.14 represent the fields along the two orthogonal axes matching the y and z axes in Figure 3.7 in Section 3.1.2.

The currents in the shield are only a slightly better approximation to a $\cos \theta$ current density distribution than the wires, hence if a better approximation of a $\cos \theta$ current density coil (large N_{cp}) were simulated, the shield would only negligibly improve the magnetic field uniformity.

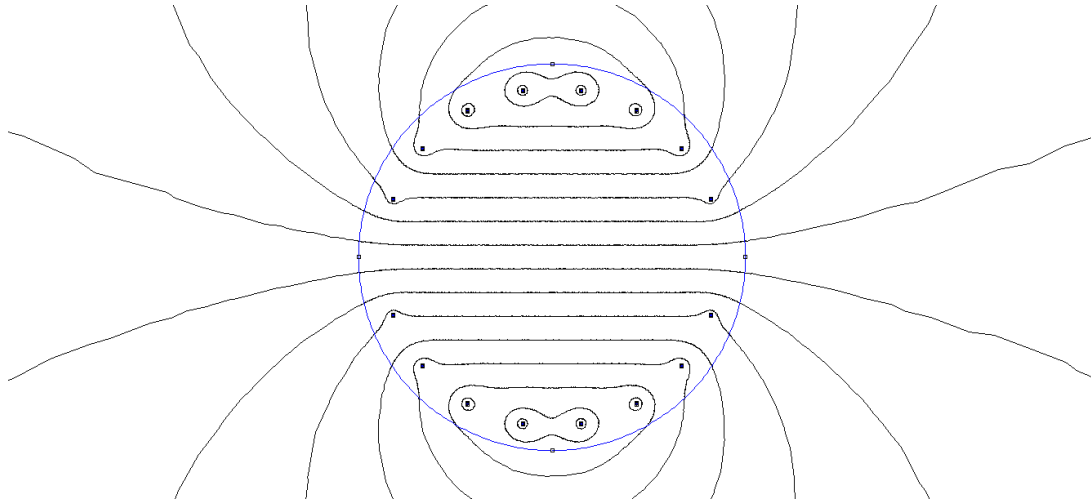


Figure 4.9: Magnetic field generated by infinitely long ELF cage in air.

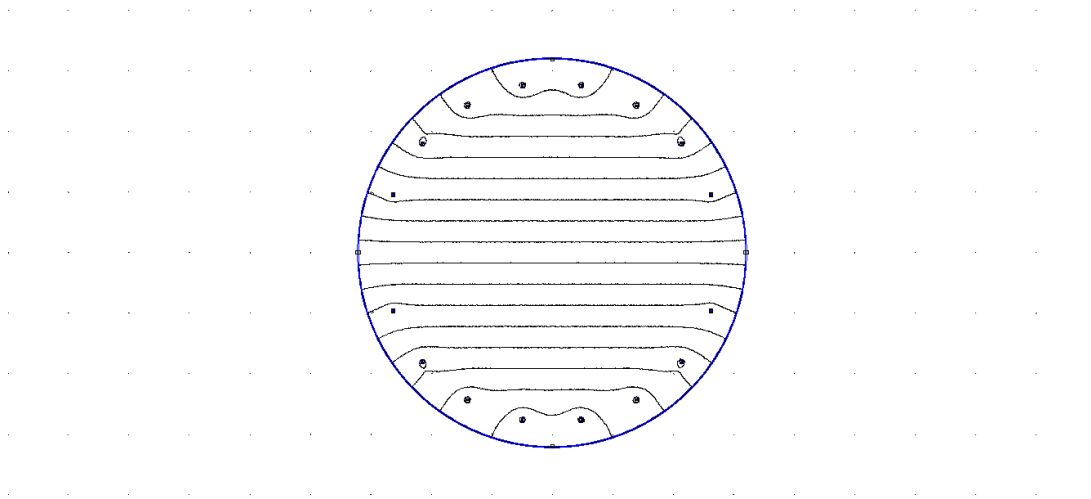


Figure 4.10: Magnetic field generated by infinitely long shielded ELF cage.

4.3 Summary

Modelling shows a μ -metal shield will increase both the uniformity and the field strength of solenoidal and ELF cage coils. In solenoidal coils the relative distance between the circular shield lids/endcaps to the coil's end-fire boundary compared to the shield body to coil end-fire boundary has a strong impact on field uniformity. For best uniformity, the shield end-caps must be as close as possible to the solenoid's end-fire boundary.

A finite length ELF cage has field-distorting currents running at the coil boundaries, in the same location as and flowing in the same plane as the solenoid end-fire boundary.

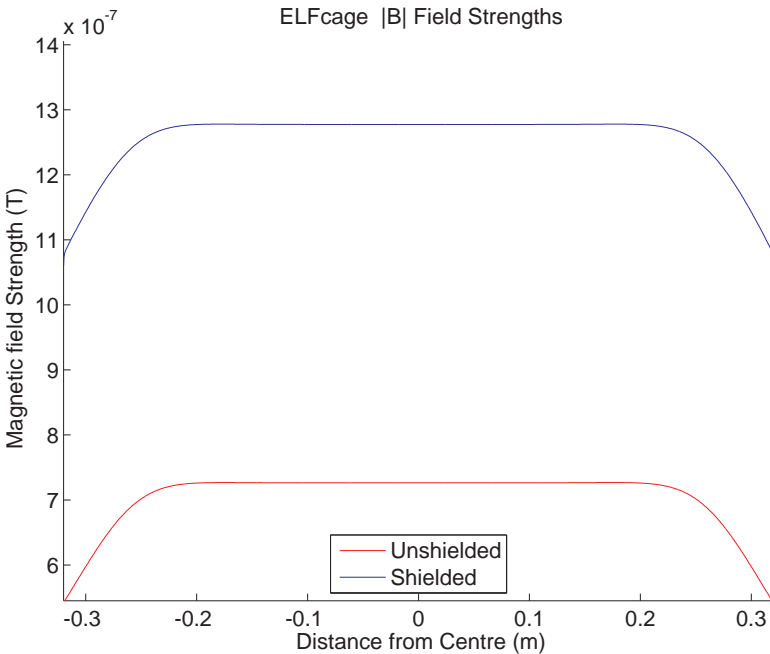


Figure 4.11: Total field strength along horizontal (y) axis of ELF cage.

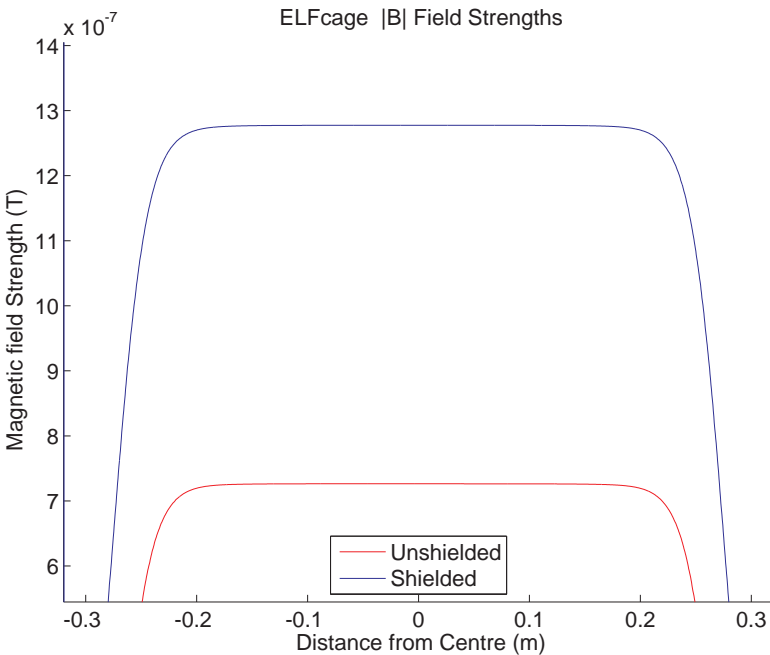


Figure 4.12: Total field strength along vertical (z) axis of ELF cage.

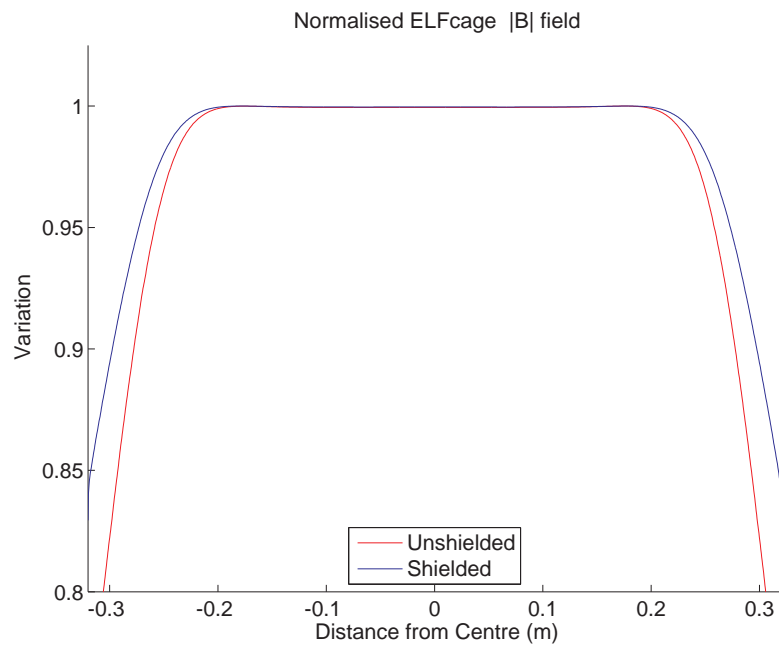


Figure 4.13: Normalised total field strength variation along horizontal (y) axis of ELF cage.

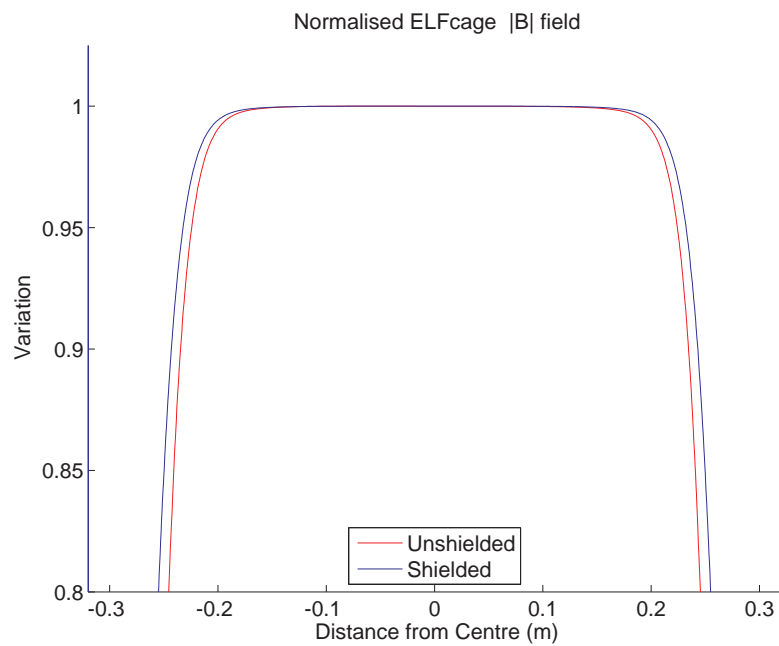


Figure 4.14: Normalised total field strength variation along vertical (z) axis of ELF cage.

Shield end-plates are expected to pull associated field-lines away from the main body of the ELFcage, significantly improving field uniformity.

High permeability shielding is expected to improve magnetic field uniformity for solenoid and ELFcage coil designs, whilst concurrently attenuating external magnetic noise, hence μ -metal shielding is ideal for isolating laboratory setups in noisy environments.

Chapter 5

Calibration Estimators

5.1 TWOSTEP

This section “walks through” the derivation of the complete TWOSTEP method in greater detail than presented in Alonso and Shuster (2002c). Latter sections address re-defining the coil and sensor-within-coil calibration models so as to match the TWOSTEP algorithm, enabling it to be used to estimate their properties. For ease of comparison to the Alonso and Shuster papers, cross-references to the relevant papers are included. References $[\{x\}]$ and $[(x)]$ indicate the x^{th} equation as marked in Alonso and Shuster (2002a) and Alonso and Shuster (2002c) respectively, where both papers contain the same equation both will be referred to, as $[\{x\},(x)]$.

5.1.1 Model

We define the sensor model as follows [(45)]:

$$\mathbf{B}_k = (\mathbf{I} + \mathbf{D})^{-1}(\vartheta^T \mathbf{A}_k \mathbf{H}_k + \mathbf{b} + \boldsymbol{\varepsilon}_k) \quad (5.1)$$

where \mathbf{B}_k is the k^{th} sensor reading, \mathbf{H}_k is earth’s field at that reading, \mathbf{b} is sensor bias, $\boldsymbol{\varepsilon}_k$ is the measurement noise. \mathbf{D} is a fully populated symmetric matrix representing sensitivity and orthogonality errors when added to the identity matrix \mathbf{I} . \mathbf{A}_k is an attitude correction matrix (rotation) used to put \mathbf{H}_k in the same reference frame as \mathbf{B}_k , and ϑ is a rotational error within the sensor, hence another rotation matrix. Since only $|\mathbf{H}_k|$ is expected to be known during the calibration (\mathbf{A}_k and ϑ are not known or estimated), (5.1) is manipulated to eliminate the rotations (which are singular orthogonal matrices), and use only magnitude data [(19)].

Thus:

$$(I + D)\mathbf{B}_k = \vartheta^T A_k \mathbf{H}_k + \mathbf{b} + \boldsymbol{\varepsilon}_k \quad (5.2a)$$

$$(I + D)\mathbf{B}_k - \mathbf{b} - \boldsymbol{\varepsilon}_k = \vartheta^T A_k \mathbf{H}_k \quad (5.2b)$$

$$((I + D)\mathbf{B}_k - \mathbf{b} - \boldsymbol{\varepsilon}_k)^T ((I + D)\mathbf{B}_k - \mathbf{b} - \boldsymbol{\varepsilon}_k) = |\mathbf{H}_k|^2 \quad (5.2c)$$

5.1.2 Parameter re-definition

$|\mathbf{H}_k|^2$ is re-arranged and a better set of basis functions is selected for improved model stability (Barker *et al.* 2007), hence:

$$|\mathbf{H}_k|^2 = ((I + D)\mathbf{B}_k - \mathbf{b} - \boldsymbol{\varepsilon}_k)^T ((I + D)\mathbf{B}_k - \mathbf{b} - \boldsymbol{\varepsilon}_k) \quad (5.3a)$$

$$\begin{aligned} &= \mathbf{B}_k^T (I + D)^T (I + D) \mathbf{B}_k - \mathbf{B}_k^T (I + D)^T \mathbf{b} - \mathbf{B}_k^T (I + D)^T \boldsymbol{\varepsilon}_k \\ &\quad - \mathbf{b}^T (I + D) \mathbf{B}_k + \mathbf{b}^T \mathbf{b} + \mathbf{b}^T \boldsymbol{\varepsilon}_k \end{aligned} \quad (5.3b)$$

$$\begin{aligned} &- \boldsymbol{\varepsilon}_k^T (I + D) \mathbf{B}_k + \boldsymbol{\varepsilon}_k^T \mathbf{b} + \boldsymbol{\varepsilon}_k^T \boldsymbol{\varepsilon}_k \\ &= \mathbf{B}_k^T (I + 2D + D^2) \mathbf{B}_k - 2\mathbf{B}_k^T \mathbf{c} - 2\mathbf{B}_k^T (I + D)^T \boldsymbol{\varepsilon}_k \\ &\quad + 2\mathbf{b}^T \boldsymbol{\varepsilon}_k + |\boldsymbol{\varepsilon}_k|^2 + |\mathbf{b}|^2 \end{aligned} \quad (5.3c)$$

$$\begin{aligned} &= |\mathbf{B}_k|^2 + \mathbf{B}_k^T E \mathbf{B}_k - 2\mathbf{B}_k^T \mathbf{c} \\ &\quad - (2[(I + D)\mathbf{B}_k - \mathbf{b}] \cdot \boldsymbol{\varepsilon}_k - |\boldsymbol{\varepsilon}_k|^2) + |\mathbf{b}|^2 \end{aligned} \quad (5.3d)$$

$$= |\mathbf{B}_k|^2 + \mathbf{B}_k^T E \mathbf{B}_k - 2\mathbf{B}_k^T \mathbf{c} - \nu_k + |\mathbf{b}|^2 \quad (5.3e)$$

Where for ease of estimation we removed the non-linear dependence on parameter D , defining matrix E and vector \mathbf{c} as shown in (5.4) [(46)], and the scalar ν_k is explicitly defined in (5.7b).

$$E = 2D + D^2 \quad (5.4a)$$

$$\mathbf{c} = (I + D)\mathbf{b} \quad (5.4b)$$

As we can see \mathbf{c} is simply the bias recast through sensitivity and orthogonality errors.

Manipulating (5.4) as shown in (5.5) and (5.6) expresses \mathbf{b} in terms of \mathbf{c} and E , therefore $\mathbf{b} \equiv \mathbf{b}(\mathbf{c}, E)$, (5.6c).

$$E = 2D + D^2 \quad (5.5a) \quad \mathbf{c} = (I + D)\mathbf{b} \quad (5.6a)$$

$$D^{-1}E = 2I + D \quad (5.5b) \quad (I + D)^{-1}\mathbf{c} = \mathbf{b} \quad (5.6b)$$

$$D^{-1}E - I = I + D \quad (5.5c) \quad (D^{-1}E - I)^{-1}\mathbf{c} = \mathbf{b} \quad (5.6c)$$

5.1.3 Sensor “error measurement” & “error measurement noise”

We work with scalar measurement z_k and scalar measurement noise ν_k , as defined in [(23a, 24)]; which is the nomenclature used in the Alonso and Shuster papers. z_k and ν_k should not be confused with ε_k and \mathbf{B}_k being measurement noise and the k^{th} sensor measurement respectively. As shown in (5.3d) and (5.3e), ν_k holds all the ε_k noise elements present in $|\mathbf{H}_k|^2$, and z_k could be considered a scalar measurement of the sensor errors we are trying to estimate. z_k and ν_k are defined in (5.7).

$$z_k = |\mathbf{B}_k|^2 - |\mathbf{H}_k|^2 \quad (5.7a)$$

$$\nu_k = 2[(I + D)\mathbf{B}_k - \mathbf{b}] \cdot \varepsilon_k - |\varepsilon_k|^2 \quad (5.7b)$$

Using (5.3e) the scalar measurement z_k is expressed as follows [(47)]:

$$z_k = |\mathbf{B}_k|^2 - |\mathbf{H}_k|^2 \quad (5.8a)$$

$$= -\mathbf{B}_k^T E \mathbf{B}_k + 2\mathbf{B}_k^T \mathbf{c} + \nu_k - |\mathbf{b}|^2 \quad (5.8b)$$

5.1.4 Vectorisation

For ease of derivation and coding, E and \mathbf{c} are vectorised, rearranging to remove the symmetric 3×3 matrix E and to use 6×1 vector \mathbf{E} instead, as done in (5.9) [(48)].

$$\mathbf{B}_k^T E \mathbf{B}_k = \begin{pmatrix} B_{1k} & B_{2k} & B_{3k} \end{pmatrix} \begin{pmatrix} E_{11} & E_{12} & E_{13} \\ E_{12} & E_{22} & E_{23} \\ E_{13} & E_{23} & E_{33} \end{pmatrix} \begin{pmatrix} B_{1k} \\ B_{2k} \\ B_{3k} \end{pmatrix} \quad (5.9a)$$

$$= E_{11}B_{1k}^2 + E_{22}B_{2k}^2 + E_{33}B_{3k}^2 + E_{12}(2B_{1k}B_{2k}) + E_{13}(2B_{1k}B_{3k}) + E_{23}(2B_{2k}B_{3k}) \quad (5.9b)$$

$$= \begin{pmatrix} B_{1k}^2 & B_{2k}^2 & B_{3k}^2 & 2B_{1k}B_{2k} & 2B_{1k}B_{3k} & 2B_{2k}B_{3k} \end{pmatrix} \begin{pmatrix} E_{11} \\ E_{22} \\ E_{33} \\ E_{12} \\ E_{13} \\ E_{23} \end{pmatrix} \quad (5.9c)$$

$$= \mathbf{K}_k \mathbf{E} \quad (5.9d)$$

Where \mathbf{K}_k [(49a)] and \mathbf{E} [(49b)] are defined as follows:

$$\mathbf{E} = \begin{pmatrix} E_{11} & E_{22} & E_{33} & E_{12} & E_{13} & E_{23} \end{pmatrix}^T \quad (5.10a)$$

$$\mathbf{K}_k = \begin{pmatrix} B_{1k}^2 & B_{2k}^2 & B_{3k}^2 & 2B_{1k}B_{2k} & 2B_{1k}B_{3k} & 2B_{2k}B_{3k} \end{pmatrix} \quad (5.10b)$$

Applying this simplification to z_k in (5.11) [(50)] and merging \mathbf{E} and \mathbf{c} , z_k is expressed in terms of variables L_k and $\boldsymbol{\theta}'$ shown in (5.12) [(51)].

$$z_k = -\mathbf{B}_k^T E \mathbf{B}_k + 2\mathbf{B}_k^T \mathbf{c} + \nu_k - |\mathbf{b}|^2 \quad (5.11a)$$

$$= -\mathbf{K}_k \mathbf{E} + 2\mathbf{B}_k^T \mathbf{c} + \nu_k - |\mathbf{b}(\mathbf{c}, \mathbf{E})|^2 \quad (5.11b)$$

$$= \begin{pmatrix} 2\mathbf{B}_k^T & -\mathbf{K}_k \end{pmatrix} \begin{pmatrix} \mathbf{c} \\ \mathbf{E} \end{pmatrix} - |\mathbf{b}(\mathbf{c}, \mathbf{E})|^2 + \nu_k \quad (5.11c)$$

$$= L_k \boldsymbol{\theta}' - |\mathbf{b}(\boldsymbol{\theta}')|^2 + \nu_k \quad (5.11d)$$

L_k is 1×9 row vector dependent on sensor measurements B_k , and θ' is a 9×1 column vector dependent on the redefined sensor errors E and c , hence on D and b .

$$L_k = \begin{pmatrix} 2B_k^T & -K_k \end{pmatrix} \quad (5.12a)$$

$$\theta' = \begin{pmatrix} c \\ E \end{pmatrix} \quad (5.12b)$$

The use of θ' as opposed to θ , reflects the need to recover b and D from θ' . $\theta = (\mathbf{b} \ D)^T$ can be derived from θ' as is shown later in Section 5.1.10. A re-arrangement of (5.11) represents v_k in terms of L_k and θ' as shown in (5.13).

$$v_k = z_k - L_k \theta' + |\mathbf{b}(\theta')|^2 \quad (5.13)$$

5.1.5 Noise distribution

As part of the MLE process the noise in the system needs to be characterised. ε_k is assumed to be white and Gaussian distributed with zero mean. Since $\varepsilon_k \sim \mathcal{N}(\mathbf{0}, \Sigma_k)$ [$\{5\},(4)$] then $v_k \sim \mathcal{N}(\mu_k, \sigma_k^2)$ as shown in (5.14a) [$\{7a\},(5a)$] and (5.15a) [$\{7b\},(5b)$].

Calculation of μ_k is shown below:

$$\mu_k \equiv E \{v_k\} \quad (5.14a)$$

$$= E \{2[(I + D)B_k - \mathbf{b}] \cdot \varepsilon_k\} - E \{|\varepsilon_k|^2\} \quad (5.14b)$$

$$= 0 - E \{(\sqrt{\varepsilon_k \cdot \varepsilon_k})^2\} \quad (5.14c)$$

$$= -tr(\Sigma_k) \quad (5.14d)$$

where Σ_k is the covariance matrix for sample k is $\begin{pmatrix} \varepsilon_{k,1}^2 & 0 & 0 \\ 0 & \varepsilon_{k,2}^2 & 0 \\ 0 & 0 & \varepsilon_{k,3}^2 \end{pmatrix}$, and $tr(\Sigma_k) = (\varepsilon_{k,1}^2 + \varepsilon_{k,2}^2 + \varepsilon_{k,3}^2)$

5.1 TWOSTEP

Calculation of σ_k^2 requires the use of Gaussian random variable moments presented in Appendix A.1.

$$\sigma_k^2 \equiv E \left\{ \nu_k^2 \right\} - \mu_k^2 \quad (5.15a)$$

$$= 4E \left\{ \left[(I + D)\mathbf{B}_k - \mathbf{b} \right]^T \boldsymbol{\varepsilon}_k \right\}^2 - 2E \left\{ \left[(I + D)\mathbf{B}_k - \mathbf{b} \right]^T \boldsymbol{\varepsilon}_k \right\} E \left\{ |\boldsymbol{\varepsilon}_k|^2 \right\} + E \left\{ |\boldsymbol{\varepsilon}_k|^4 \right\} - \text{tr}(\Sigma_k)^2 \quad (5.15b)$$

$$= 4E \left\{ \left[(I + D)\mathbf{B}_k - \mathbf{b} \right]^T \boldsymbol{\varepsilon}_k \boldsymbol{\varepsilon}_k^T \left[(I + D)\mathbf{B}_k - \mathbf{b} \right] \right\} + E \left\{ |\boldsymbol{\varepsilon}_k|^4 \right\} - \text{tr}(\Sigma_k)^2 \quad (5.15c)$$

$$= 4 \left[(I + D)\mathbf{B}_k - \mathbf{b} \right]^T \Sigma_k \left[(I + D)\mathbf{B}_k - \mathbf{b} \right] + 5\text{tr}(\Sigma_k^2) - 3\text{tr}(\Sigma_k)^2 \quad (5.15d)$$

$$= 4 \left[(I + D)\mathbf{B}_k - \mathbf{b} \right]^T \Sigma_k \left[(I + D)\mathbf{B}_k - \mathbf{b} \right] + 2\text{tr}(\Sigma_k^2) \quad (5.15e)$$

where $3\text{tr}(\Sigma_k^2) = [\text{tr}(\Sigma_k)]^2$ (See equation (A.13)).

5.1.6 Likelihood function

Having characterised the noise, the likelihood (5.16a) and negative log-likelihood (5.17a) [(6)] functions are obtained:

$$f_{N|\boldsymbol{\Theta}'=\boldsymbol{\theta}'}(\boldsymbol{\theta}') = \prod_{k=1}^N \frac{1}{\sqrt{2\pi\sigma_k^2}} e^{-(\nu_k - \mu_k)^2 / 2\sigma_k^2} \quad (5.16a)$$

$$= \prod_{k=1}^N \frac{1}{\sqrt{2\pi\sigma_k^2}} e^{-(z_k - \mathbf{L}_k \boldsymbol{\theta}' + |\mathbf{b}(\boldsymbol{\theta}')|^2 - \mu_k)^2 / 2\sigma_k^2} \quad (5.16b)$$

$$J(\boldsymbol{\theta}') = -\ln f_{N|\boldsymbol{\Theta}'=\boldsymbol{\theta}'}(\boldsymbol{\theta}') \quad (5.17a)$$

$$= \sum_{k=1}^N \left[\left(z_k - \mathbf{L}_k \boldsymbol{\theta}' + |\mathbf{b}(\boldsymbol{\theta}')|^2 - \mu_k \right)^2 / 2\sigma_k^2 + \frac{1}{2} \ln(2\pi\sigma_k^2) \right] \quad (5.17b)$$

$$= \frac{1}{2} \sum_{k=1}^N \left[\frac{1}{\sigma_k^2} \left(z_k - \mathbf{L}_k \boldsymbol{\theta}' + |\mathbf{b}(\boldsymbol{\theta}')|^2 - \mu_k \right)^2 + \ln(2\pi\sigma_k^2) \right] \quad (5.17c)$$

5.1.7 Centering

As part of the TWOSTEP method, $J(\theta')$ will be split into a centred and centre component, keeping the non-linear components in the centre component. (5.18), and (5.19) define the centre variables and (5.20) defines the centred variables [(7, 8, 9, 52)].

$$\frac{1}{\bar{\sigma}^2} \equiv \sum_{k=1}^N \frac{1}{\sigma_k^2} \quad (5.18)$$

$$\bar{z} \equiv \bar{\sigma}^2 \sum_{k=1}^N \frac{1}{\sigma_k^2} z_k \quad \bar{B} \equiv \bar{\sigma}^2 \sum_{k=1}^N \frac{1}{\sigma_k^2} B_k \quad \bar{L} \equiv \bar{\sigma}^2 \sum_{k=1}^N \frac{1}{\sigma_k^2} L_k \quad (5.19)$$

$$\bar{v} \equiv \bar{\sigma}^2 \sum_{k=1}^N \frac{1}{\sigma_k^2} v_k \quad \bar{\mu} \equiv \bar{\sigma}^2 \sum_{k=1}^N \frac{1}{\sigma_k^2} \mu_k$$

$$\begin{aligned} \tilde{z}_k &= z_k - \bar{z} & \tilde{B}_k &= B_k - \bar{B} & \tilde{L}_k &= L_k - \bar{L} \\ \tilde{v}_k &= v_k - \bar{v} & \tilde{\mu}_k &= \mu_k - \bar{\mu} \end{aligned} \quad (5.20)$$

Hence $\tilde{z}_k = \tilde{L}_k \theta' + \tilde{v}_k$ and $\bar{z} = \bar{L} \theta' - |\mathbf{b}(\theta')|^2 + \bar{v}$.

$J(\theta')$ can be split into centre and centred terms as shown in (5.21) [(10)].

$$J(\theta') = -\ln f_{N|\theta'=\theta'}(\theta') \quad (5.21a)$$

$$= \frac{1}{2} \sum_{k=1}^N \left[\frac{1}{\sigma_k^2} (v_k - \mu_k)^2 + \ln 2\pi\sigma_k^2 \right] \quad (5.21b)$$

$$= \frac{1}{2} \sum_{k=1}^N \left[\frac{1}{\sigma_k^2} (\tilde{v}_k + \bar{v} - \tilde{\mu}_k - \bar{\mu})^2 + \ln 2\pi\sigma_k^2 \right] \quad (5.21c)$$

$$= \frac{1}{2} \sum_{k=1}^N \left[\frac{1}{\sigma_k^2} ((\tilde{v}_k - \tilde{\mu}_k)^2 + (\bar{v} - \bar{\mu})^2 + 2(\tilde{v}_k - \tilde{\mu}_k)(\bar{v} - \bar{\mu})) + \ln 2\pi\sigma_k^2 \right] \quad (5.21d)$$

$$= \tilde{J}(\theta') + \bar{J}(\theta') + \frac{1}{2} \sum_{k=1}^N \frac{1}{\sigma_k^2} [2(\tilde{v}_k - \tilde{\mu}_k)(\bar{v} - \bar{\mu})] \quad (5.21e)$$

$$= \tilde{J}(\theta') + \bar{J}(\theta') \quad (5.21f)$$

5.1 TWOSTEP

Where \tilde{J} (5.22) is the centred measurement component and \bar{J} (5.23) is the centre measurement component [(56, 58)], and $\sum_{k=1}^N \frac{1}{\sigma_k^2} (2(\tilde{v}_k - \tilde{\mu}_k)(\bar{v} - \bar{\mu})) = 0$ as shown in Appendix A.2.

$$\tilde{J}(\theta') = \frac{1}{2} \sum_{k=1}^N \frac{1}{\sigma_k^2} ((\tilde{v}_k - \tilde{\mu}_k)^2 + \ln 2\pi\sigma_k^2) \quad (5.22a)$$

$$= \frac{1}{2} \sum_{k=1}^N \frac{1}{\sigma_k^2} (\tilde{z}_k - \tilde{\mathbf{L}}_k \theta' - \tilde{\mu}_k)^2 + \text{terms independent of } \theta' \quad (5.22b)$$

$$\bar{J}(\theta') = \frac{1}{2} \sum_{k=1}^N \frac{1}{\sigma^2} (\bar{v} - \bar{\mu})^2 \quad (5.23a)$$

$$= \frac{1}{2\bar{\sigma}^2} \left(\bar{z} - \bar{\mathbf{L}}\theta' + |\mathbf{b}(\theta')|^2 - \bar{\mu} \right)^2 \quad (5.23b)$$

5.1.7.1 Centered estimator

Estimator for the centred measurement is found by setting $\frac{\partial}{\partial \theta'} \tilde{J} = 0$ [(57a)].

$$\frac{\partial}{\partial \theta'} \tilde{J} = \frac{\partial}{\partial \theta'} \left(\frac{1}{2} \sum_{k=1}^N \frac{1}{\sigma_k^2} (\tilde{z}_k - \tilde{\mathbf{L}}_k \theta' - \tilde{\mu}_k)^2 + \text{terms independent of } \theta' \right) \quad (5.24a)$$

$$= \frac{1}{2} \sum_{k=1}^N \frac{-2\tilde{\mathbf{L}}_k^T}{\sigma_k^2} (\tilde{z}_k - \tilde{\mathbf{L}}_k \theta' - \tilde{\mu}_k) \quad (5.24b)$$

$$= \sum_{k=1}^N \frac{-1}{\sigma_k^2} (\tilde{z}_k - \tilde{\mu}_k) \tilde{\mathbf{L}}_k^T + \sum_{k=1}^N \frac{\tilde{\mathbf{L}}_k^T \tilde{\mathbf{L}}_k}{\sigma_k^2} \theta' = 0 \quad (5.24c)$$

$$\therefore \sum_{k=1}^N \frac{\tilde{\mathbf{L}}_k^T \tilde{\mathbf{L}}_k}{\sigma_k^2} \theta' = \sum_{k=1}^N \frac{1}{\sigma_k^2} (\tilde{z}_k - \tilde{\mu}_k) \tilde{\mathbf{L}}_k^T \quad (5.24d)$$

We multiply both sides by the inverse of $\sum_{k=1}^N \frac{\tilde{\mathbf{L}}_k^T \tilde{\mathbf{L}}_k}{\sigma_k^2}$ to obtain the centred estimate $\tilde{\theta}'^*$ [(57a)], where * indicates the value is an estimate.

$$\therefore \tilde{\theta}'^* = \left(\sum_{k=1}^N \frac{\tilde{\mathbf{L}}_k^T \tilde{\mathbf{L}}_k}{\sigma_k^2} \right)^{-1} \sum_{k=1}^N \frac{1}{\sigma_k^2} (\tilde{z}_k - \tilde{\mu}_k) \tilde{\mathbf{L}}_k^T \quad (5.25a)$$

$$= [\tilde{\mathcal{J}}(\theta')]^{-1} \sum_{k=1}^N \frac{1}{\sigma_k^2} (\tilde{z}_k - \tilde{\mu}_k) \tilde{\mathbf{L}}_k^T \quad (5.25b)$$

Where $\tilde{\mathcal{J}}(\theta')$ is the centred Fisher Information Matrix and is derived in Section 5.1.8.

5.1.8 Fisher information matrix

The Fisher Information Matrix \mathfrak{J} is the expectation of the Hessian matrix - the square matrix of the second order partial derivatives of the negative log likelihood function $J(\theta')$. The fisher matrix is defined by Poor (1994) as (5.26):

$$\mathfrak{J}(\theta') = E_{X|\Theta'=\theta'} \left\{ \left(\frac{\partial \ln f_{X|\Theta'=\theta'}(X)}{\partial \theta'} \right) \left(\frac{\partial \ln f_{X|\Theta'=\theta'}(X)}{\partial \theta'} \right)^T \right\} \quad (5.26)$$

The Fisher matrix can also be represented as (5.27), as shown in White (2012).

$$\mathfrak{J}(\theta') = -E_{X|\Theta'=\theta'} \left\{ \left(\frac{\partial^2 \ln f_{X|\Theta'=\theta'}(X)}{\partial \theta'^2} \right) \right\} \quad (5.27)$$

5.1.8.1 Centered Fisher Information Matrix

Using (5.27) the Fisher Information Matrix for $\tilde{J}(\theta')$ is derived⁸, as shown in (5.28) [(57b)].

$$\tilde{\mathfrak{J}}(\theta') = E \left\{ \left(\frac{\partial^2 \tilde{J}(\theta')}{\partial \theta'^2} \right) \right\} \quad (5.28a)$$

$$= E \left\{ \left(\frac{\partial^2}{\partial \theta'^2} \frac{1}{2} \sum_{k=1}^N \frac{1}{\sigma_k^2} (\tilde{z}_k - \tilde{\mathbf{L}}_k \theta' - \tilde{\mu}_k)^T (\tilde{z}_k - \tilde{\mathbf{L}}_k \theta' - \tilde{\mu}_k) \right) \right\} \quad (5.28b)$$

$$= E \left\{ \frac{\partial}{\partial \theta'} \sum_{k=1}^N \frac{-1}{\sigma_k^2} \tilde{\mathbf{L}}_k^T (\tilde{z}_k - \tilde{\mathbf{L}}_k \theta' - \tilde{\mu}_k) \right\} \quad (5.28c)$$

$$= E \left\{ \sum_{k=1}^N \frac{1}{\sigma_k^2} \tilde{\mathbf{L}}_k^T \tilde{\mathbf{L}}_k \right\} \quad (5.28d)$$

$$= \sum_{k=1}^N \frac{1}{\sigma_k^2} \tilde{\mathbf{L}}_k^T \tilde{\mathbf{L}}_k \quad (5.28e)$$

5.1.8.2 Center Fisher Information Matrix

As stated in (5.26) and (5.27), there are two ways of calculating the Fisher matrix, for the centre log-likelihood function $\tilde{J}(\theta')$ [(59)], we will use (5.26).

⁸Due to the differentiation $\tilde{\mathfrak{J}}(\theta')$ is no longer dependent on θ' . θ' is nonetheless maintained in the notation to distinguish $\tilde{\mathfrak{J}}(\theta')$ from $\tilde{\mathfrak{J}}(\cdot)$

$$\tilde{J}(\theta') = E_{X|\Theta=\theta} \left\{ \left(\frac{\partial \bar{J}(\theta')}{\partial \theta'} \right)^T \left(\frac{\partial \bar{J}(\theta')}{\partial \theta'} \right) \right\} \quad (5.29a)$$

$$= E_{X|\Theta=\theta} \left\{ \left(\frac{1}{\bar{\sigma}^2} \right)^2 \left(-\bar{L} + \frac{\partial |\mathbf{b}(\theta')|^2}{\partial \theta'} \right)^T (\bar{v} - \bar{\mu})^T (\bar{v} - \bar{\mu}) \left(-\bar{L} + \frac{\partial |\mathbf{b}(\theta')|^2}{\partial \theta'} \right) \right\} \quad (5.29b)$$

$$= \left(\frac{1}{\bar{\sigma}^2} \right)^2 \left(-\bar{L} + \frac{\partial |\mathbf{b}(\theta')|^2}{\partial \theta'} \right)^T E_{X|\Theta=\theta} \{ (\bar{v} - \bar{\mu})^2 \} \left(-\bar{L} + \frac{\partial |\mathbf{b}(\theta')|^2}{\partial \theta'} \right) \quad (5.29c)$$

$$= \frac{1}{\bar{\sigma}^2} \left(\bar{L} - \frac{\partial |\mathbf{b}(\theta')|^2}{\partial \theta'} \right)^T \left(\bar{L} - \frac{\partial |\mathbf{b}(\theta')|^2}{\partial \theta'} \right) \quad (5.29d)$$

Where $E_{X|\Theta=\theta} \{ (\bar{v} - \bar{\mu})^2 \}$ is derived in Appendix A.3, and the derivative of $|\mathbf{b}(\theta')|^2$ with respect to θ' is shown below.

$|\mathbf{b}(\theta')|^2$ is presented in terms of \mathbf{c} and E [(54)]:

$$|\mathbf{b}(\theta')|^2 = \mathbf{b}(\theta')^T \mathbf{b}(\theta') \quad (5.30a)$$

$$= \mathbf{c}^T ((I + D)^{-1})^T (I + D)^{-1} \mathbf{c} \quad (5.30b)$$

$$= \mathbf{c}^T (I + D)^{-2} \mathbf{c} \quad (5.30c)$$

$$= \mathbf{c}^T (I + 2D + D^2)^{-1} \mathbf{c} \quad (5.30d)$$

$$= \mathbf{c}^T (I + E)^{-1} \mathbf{c} \quad (5.30e)$$

Splitting θ' into sub-vectors:

$$\frac{\partial}{\partial \theta'} |\mathbf{b}(\theta')|^2 = \begin{bmatrix} \frac{\partial}{\partial \mathbf{c}} |\mathbf{b}(\theta')|^2 \\ \frac{\partial}{\partial \mathbf{E}} |\mathbf{b}(\theta')|^2 \end{bmatrix} \quad (5.31a)$$

$|\mathbf{b}(\theta')|^2$ is then differentiated element by element with respect to \mathbf{c} and E [(55)]:

$$\frac{\partial}{\partial c_l} |\mathbf{b}(\theta')|^2 = \frac{\partial}{\partial c_l} \mathbf{c}^T (I + E)^{-1} \mathbf{c} \quad (5.32a)$$

$$= ((I + E)^{-1} \mathbf{c} + \mathbf{c}^T (I + E)^{-1})_l \quad (5.32b)$$

$$= (2(I + E)^{-1} \mathbf{c})_l \quad (5.32c)$$

| m | (i, j) | E element | E element | θ' element |
|-----|----------|-------------|-------------|-------------------|
| 1 | (1, 1) | E_{11} | E_1 | θ'_4 |
| 2 | (2, 2) | E_{22} | E_2 | θ'_5 |
| 3 | (3, 3) | E_{33} | E_3 | θ'_6 |
| 4 | (1, 2) | E_{12} | E_4 | θ'_7 |
| 5 | (1, 3) | E_{13} | E_5 | θ'_8 |
| 6 | (2, 3) | E_{23} | E_6 | θ'_9 |

Table 5.1: Mapping E indexed elements ' E_m ' and matrix E elements ' $E_{i,j}$ '.

$$\frac{\partial}{\partial \mathbf{E}_m} |\mathbf{b}(\theta')|^2 = \frac{\partial}{\partial \mathbf{E}_m} \mathbf{c}^T (I + E)^{-1} \mathbf{c} \quad (5.33a)$$

$$= \mathbf{c}^T \frac{\partial}{\partial \mathbf{E}_m} (I + E)^{-1} \mathbf{c} \quad (5.33b)$$

$$= -\mathbf{c}^T (I + E)^{-1} \frac{\partial (I + E)}{\partial \mathbf{E}_m} (I + E)^{-1} \mathbf{c} \quad (5.33c)$$

$$\frac{\partial}{\partial E_{i,j}} |\mathbf{b}(\theta')|^2 = -(2 - \delta_{i,j}) (\mathbf{c}^T (I + E)^{-1})_i ((I + E)^{-1} \mathbf{c})_j \quad (5.34a)$$

$$= -(2 - \delta_{i,j}) ((I + E)^{-1} \mathbf{c})_i ((I + E)^{-1} \mathbf{c})_j \quad (5.34b)$$

Where $\delta_{i,j}$ is the Kronecker delta function, and i & j take on the values shown in Table 5.1.

Consideration of (5.21) and (5.27) implies the complete Fisher matrix can be obtained by adding the centre and centred components as in (5.35).

$$\mathfrak{J}(\theta') = \tilde{\mathfrak{J}}(\theta') + \tilde{\mathfrak{J}}(\theta') \quad (5.35)$$

5.1.9 Center term correction

The Gauss-Newton method is used to iteratively bring the estimate θ'_i closer to the true value θ' . Starting with $\theta'^*_0 \equiv \tilde{\theta}'^*$, we iterate (5.36) until η_i in (5.37) reaches a predetermined small quantity, or i reaches an upper limit [(14a, 14b)].

$$\theta'_{i+1} = \theta'_i - \mathfrak{J}(\theta'_i)^{-1} \frac{\partial}{\partial \theta'} J(\theta'_i) \quad (5.36)$$

$$\eta_i \equiv (\theta'_i - \theta'_{i-1})^T \mathfrak{J}(\theta'_{i-1}) (\theta'_i - \theta'_{i-1}) \quad (5.37)$$

5.1.9.1 Log-likelihood gradient

Section 5.1.9 required the gradient of $J(\theta')$ to be evaluated at $\tilde{\theta}'^*$. Equation (5.21) is used to derive the $\frac{\partial J}{\partial \theta'}$ gradient by evaluating components $\frac{\partial \tilde{J}}{\partial \theta'}$ and $\frac{\partial \bar{J}}{\partial \theta'}$ separately. $\frac{\partial}{\partial \theta'} \tilde{J}$ was derived in (5.24) and refined in (5.38). $\frac{\partial}{\partial \theta'} \bar{J}$ is fully derived in (5.39).

$$\frac{\partial}{\partial \theta'} \tilde{J} = \sum_{k=1}^N \frac{-1}{\sigma_k^2} (\tilde{z}_k - \tilde{\mu}_k) \tilde{\mathbf{L}}_k^T + \sum_{k=1}^N \frac{\tilde{\mathbf{L}}_k^T \tilde{\mathbf{L}}_k}{\sigma_k^2} \theta' \quad (5.38a)$$

$$= \sum_{k=1}^N \frac{-1}{\sigma_k^2} (\tilde{z}_k - \tilde{\mu}_k) \tilde{\mathbf{L}}_k^T + \tilde{\mathfrak{J}}(\theta') \theta' \quad (5.38b)$$

$$\frac{\partial}{\partial \theta'} \bar{J} = \frac{\partial}{\partial \theta'} \left[\frac{1}{2} \sum_{k=1}^N \frac{1}{\sigma_k^2} (\bar{v} - \bar{\mu})^2 \right] \quad (5.39a)$$

$$= \frac{\partial}{\partial \theta'} \left[\frac{1}{2\bar{\sigma}^2} \left(\bar{z} - \bar{\mathbf{L}}\theta' + |\mathbf{b}(\theta')|^2 - \bar{\mu} \right)^2 \right] \quad (5.39b)$$

$$= -\frac{1}{\bar{\sigma}^2} \left(\bar{\mathbf{L}}\theta' - \frac{\partial}{\partial \theta'} |\mathbf{b}(\theta')|^2 \right) \left(\bar{z} - \bar{\mathbf{L}}\theta' + |\mathbf{b}(\theta')|^2 - \bar{\mu} \right) \quad (5.39c)$$

5.1.10 Converting to \mathbf{b} and D

Estimate $\boldsymbol{\theta}^*$ is in terms of \mathbf{E}^* and \mathbf{c}^* , as opposed to the desired D^* and \mathbf{b}^* . \mathbf{E}^* can be changed back into matrix form E^* by using its definition in (5.10a). To compute D^* we write [(60)]:

$$E^* = USU^T \quad (5.40)$$

where U is orthogonal and S is a 3×3 diagonal matrix with elements s_i [(61)], and both matrices are obtained by the Eigen-decomposition of symmetric matrix E^* .

We define diagonal matrix W , satisfying $S = 2W + W^2$ [(62)], hence using the quadratic formula the elements are⁹ [(63)]:

$$w_j = -1 + \sqrt{1 + s_j} \quad (5.41)$$

The maximum likelihood estimate for D can hence be calculated by [(64)]:

$$D^* = UWU^T \quad (5.42)$$

Bias vector \mathbf{b}^* can be calculated as shown in (5.6c) [(65)]:

$$\mathbf{b}^* = (I + D^*)^{-1} \mathbf{c}^* \quad (5.43)$$

5.1.10.1 Covariance Matrix

To obtain the covariance matrix we need to transform $\mathcal{J}(\boldsymbol{\theta}')$ to $\mathcal{J}(\boldsymbol{\theta})$, where $\boldsymbol{\theta} = \begin{pmatrix} \mathbf{b} \\ D \end{pmatrix}$ and D is defined with respect to D , the same way as \mathbf{E} was defined in (5.10a) [(67)]. Explicit derivation of this process is not shown [(66, 68, 69)].

$$\mathcal{J}(\boldsymbol{\theta})^{-1} = \left(\frac{\partial \boldsymbol{\theta}}{\partial \boldsymbol{\theta}'} \right) \mathcal{J}(\boldsymbol{\theta}')^{-1} \left(\frac{\partial \boldsymbol{\theta}}{\partial \boldsymbol{\theta}'} \right)^T \quad (5.44a)$$

$$= \left(\frac{\partial(\mathbf{b}, D)}{\partial(\mathbf{c}, \mathbf{E})} \right) \mathcal{J}(\boldsymbol{\theta}')^{-1} \left(\frac{\partial(\mathbf{b}, D)}{\partial(\mathbf{c}, \mathbf{E})} \right)^T \quad (5.44b)$$

⁹ $w_j = -1 - \sqrt{1 + s_j}$, is not used as it would give negative sensitivity values, implying the sensor was facing the wrong way. This is not possible since it would have been accounted for by attitude rotations, and manufacture quality control is expected to capture such major sensitivity errors

5.1 TWOSTEP

Element by element differentiation of $\left(\frac{\partial(\mathbf{b}, \mathbf{D})}{\partial(\mathbf{c}, \mathbf{E})}\right)$ can be represented as $\left(\frac{\partial\theta'}{\partial\theta}\right)_{i,j} = \frac{\partial\theta'_j}{\partial\theta_i}$

$$\left(\frac{\partial(\mathbf{b}, \mathbf{D})}{\partial(\mathbf{c}, \mathbf{E})}\right) = \left(\frac{\partial(\mathbf{c}, \mathbf{E})}{\partial(\mathbf{b}, \mathbf{D})}\right)^{-1} \quad (5.45a)$$

$$= \begin{bmatrix} (I + D) & M_{cD}(\mathbf{b}) \\ 0_{6 \times 3} & 2I + M_{ED}(D) \end{bmatrix}^{-1} \quad (5.45b)$$

with

$$M_{cD}(\mathbf{b}) = \begin{bmatrix} b_1 & 0 & 0 & b_2 & b_3 & 0 \\ 0 & b_2 & 0 & b_1 & 0 & b_3 \\ 0 & 0 & b_3 & 0 & b_1 & b_2 \end{bmatrix} \quad (5.46)$$

and

$$M_{ED}(D) = \begin{pmatrix} 2D_1 & 0 & 0 & 2D_4 & 2D_5 & 0 \\ 0 & 2D_2 & 0 & 2D_4 & 0 & 2D_6 \\ 0 & 0 & 2D_3 & 0 & 2D_5 & 2D_6 \\ D_4 & D_4 & 0 & D_1 + D_2 & D_6 & D_5 \\ D_5 & 0 & D_5 & D_6 & D_1 + D_3 & D_4 \\ 0 & D_6 & D_6 & D_5 & D_4 & D_2 + D_3 \end{pmatrix} \quad (5.47)$$

5.1.11 Implementation

Begin by assuming $|\mathbf{H}_k|$, \mathbf{B}_k , and Σ_k are known.

- Calculate $\mu_k = -tr(\Sigma_k)$
- Calculate z_k using (5.7a).
- Calculate L_k using (5.12)
- Set $\theta' = 0$, and calculate σ_k^2 using (5.15a).
- Calculate centre components $\bar{\sigma}^2$, $\bar{\mathbf{B}}$, \bar{z} , \bar{L}_k and $\bar{\mu}$ using (5.18), and (5.19).
- Calculate centred components $\tilde{\mathbf{B}}_k$, \tilde{z}_k , \tilde{L}_k , and $\tilde{\mu}_k$, using (5.20).
- Calculate centred Fisher Information Matrix $\tilde{\mathcal{J}}(\theta'^*)$ using (5.28).

- Estimate $\tilde{\theta}'^*$ using (5.25).
- Calculate log likelihood gradients using (5.38) and (5.39).
- Calculate centre Fisher Information Matrix $\tilde{\mathcal{J}}(\theta'^*)$ using (5.29).
- Iterate centre term correction as described in Section 5.1.9, updating $\tilde{\mathcal{J}}(\theta'^*)$ at each iteration.
- Recover desired values \mathbf{b} and D as shown in Sections 5.1.10 and 5.1.10.1.

An optimised implementation of the code can be found in Appendix C.1. I gratefully acknowledge Dr José Vasconcelos for providing his implementation of the TWOSTEP code for debugging and validating this implementation.

5.2 Geometric Approach - Ellipsoid Calibration

This section briefly summarises the model and estimator presented in Vasconcelos *et al.* (2011), along with a minor correction to their first-guess estimation. The model was implemented for comparison with TWOSTEP, but not taken beyond the calibration of sensors in constant magnetic fields, as the model struggled with large data-sets, even when code was optimised.

5.2.1 Model

The sensor model is defined as follows:

$$\mathbf{h}_{ri} = \mathbf{C}^B \bar{\mathbf{h}}_i + \mathbf{b} + \mathbf{n}_{mi} \quad (5.48)$$

where \mathbf{h}_{ri} is the i^{th} vector reading from the sensor; $\mathbf{C} = \mathbf{S}_M \mathbf{C}_{NO} \mathbf{C}_{SI} \parallel {}^E \bar{\mathbf{h}} \parallel$ is a fully-populated matrix built from diagonal scaling matrix \mathbf{S}_M , lower-triangular non-orthogonality matrix \mathbf{C}_{NO} , and fully populated soft-iron transformation matrix \mathbf{C}_{SI} ; $\mathbf{b} = \mathbf{S}_M \mathbf{C}_{NO} \mathbf{b}_{HI} + \mathbf{b}_M$ is sensor bias, with hard-iron bias \mathbf{b}_{HI} and null-shift \mathbf{b}_M ; \mathbf{n}_{mi} is noise on the i^{th} reading; and ${}^B \bar{\mathbf{h}}_i = {}^B_E \mathbf{R}_i {}^E \bar{\mathbf{h}}_i$ is the true magnetic field rotated from the earth's field reference frame to the sensor-body frame.

Vasconcelos *et al.* (2011) show the calibration parameters can be inferred from the centre, orientation and radii a 3D ellipsoid, the surface of which is defined by the best fit of acquired sensor data.

Initially a least squares estimation is used to obtain a first guess \mathbf{p} , a 9×1 vector, which is the solution to the least squares problem (5.49):

$$\begin{bmatrix} h_{r1x}^2 & h_{r1x}h_{r1y} & h_{r1x}h_{r1z} & h_{r1y}^2 & h_{r1y}h_{r1z} & h_{r1x} & h_{r1y} & h_{r1z} & 1 \\ \vdots & \vdots & \vdots & \vdots & \vdots & \vdots & \vdots & \vdots & \vdots \\ h_{rnx}^2 & h_{rnx}h_{rny} & h_{rnx}h_{rnz} & h_{rny}^2 & h_{rny}h_{rnz} & h_{rnx} & h_{rny} & h_{rnz} & 1 \end{bmatrix} \mathbf{p} = \begin{bmatrix} h_{r1z}^2 \\ \vdots \\ h_{rnz}^2 \end{bmatrix} \quad (5.49)$$

where $\mathbf{p} = \begin{bmatrix} A & B & C & D & E & G & H & I & J \end{bmatrix}^T$ and h_{rix} , h_{riy} , and h_{riz} are the i^{th} x , y , and z components of recorded data \mathbf{h}_{ri} . \mathbf{p} is converted to the initial estimate of calibration parameters T_0 ¹⁰ (5.50) and \mathbf{b}_0 (5.51):

$$T_0 = \begin{bmatrix} \frac{1}{a} & 0 & 0 \\ -\frac{1}{a} \tan(\rho) & +\frac{1}{b} \sec(\rho) & 0 \\ -\frac{1}{a} (\tan(\rho) \tan(\lambda) \sec(\phi) - \tan(\phi)) & -\frac{1}{b} \sec(\rho) \tan(\lambda) \sec(\phi) & \frac{1}{c} \sec(\lambda) \sec(\phi) \end{bmatrix} \quad (5.50)$$

$$\mathbf{b}_0 = \frac{1}{2\alpha_1} \begin{bmatrix} \beta_1 \\ \beta_2 \\ \beta_3 \end{bmatrix} \quad (5.51)$$

Parameters a , b , c , ρ , λ and ϕ are numerically calculated in Appendix A.4.1, and defined in Section 5.3.

In the second stage the vectorised¹¹ initial estimate $\mathbf{x}_0 = \begin{bmatrix} T_0 \\ \mathbf{b}_0 \end{bmatrix}$ calculated above is used to place the first guess of the MLE close to the estimator's peak. The Gauss-Newton approach is used to bring the solution close to the true maxima:

$$\begin{bmatrix} T_{k+1} \\ \mathbf{b}_{k+1} \end{bmatrix} = \begin{bmatrix} T_k \\ \mathbf{b}_k \end{bmatrix} - (\nabla^2 f|_{x_k})^{-1} \nabla f|_{x_k} \quad (5.52)$$

where $\nabla f|_{x_k}$ and $\nabla^2 f|_{x_k}$ are the gradient and Hessian matrices of the log-likelihood function $f(\mathbf{x})$, and are re-produced in A.4.2.

¹⁰ The sign of the term at the centre of the T_0 matrix has been changed from that presented in Vasconcelos *et al.* (2011).

¹¹ T_k is the vector defined by the stacked column elements of T_k .

5.3 Estimator Selection

In this section processing time and accuracy of the Geometric Approach and TWOSTEP estimators are compared, and one is selected for further use. The key measures of effectiveness will be accuracy, processing time, estimator stability and algorithm performance for large data-sets. Un-calibrated “measured” and “true” data is initially compared with their calibrated total field measurement for data-sets of 80 and 8000 samples. Performance of the two estimators then is tested over a range of noise levels and sample sizes. Throughout all the simulations the sensor is stimulated from random directions, describing the surface of a sphere, as is illustrated in Figure 5.1. A Geometric Approach calibration on pre-calibrated TWOSTEP data is also performed, in an attempt to reduce total processing time when using Geometric Approach. This method is referred to the “TS + GA” method.

Stimulation data, as illustrated in Figure 5.1 was generated using the MATLAB “rand” function to assign random θ and ϕ spherical coordinates to the magnetic field direction, for a constant magnitude of one, forming the surface of a sphere. Normally distributed noise is then added to the magnetic field amplitude of each axis, with noise variance dependent on simulation parameters, consequently moving data-points above and below the surface of the sphere.

Referring to Figure 5.1, note that:

- Assuming perfect orthogonality, good sensitivity equates to the magnitude of the semi-principal axes of the measurement ellipsoid being equal to each other and also to the magnitude of the field component being measured, thereby creating a unit sphere, which may be displaced from the origin, dependent on bias.
- Assuming perfect sensitivity, good sensor orthogonality equates to alignment of the measurement ellipsoid’s axes to the cartesian axes. A non-orthogonality of the sensor will cause the measurement ellipsoid axes to be rotated, and a slight deformation from the shape of a sphere.
- Good bias equates to the origin of the measurement ellipsoid and the sphere being coincident.

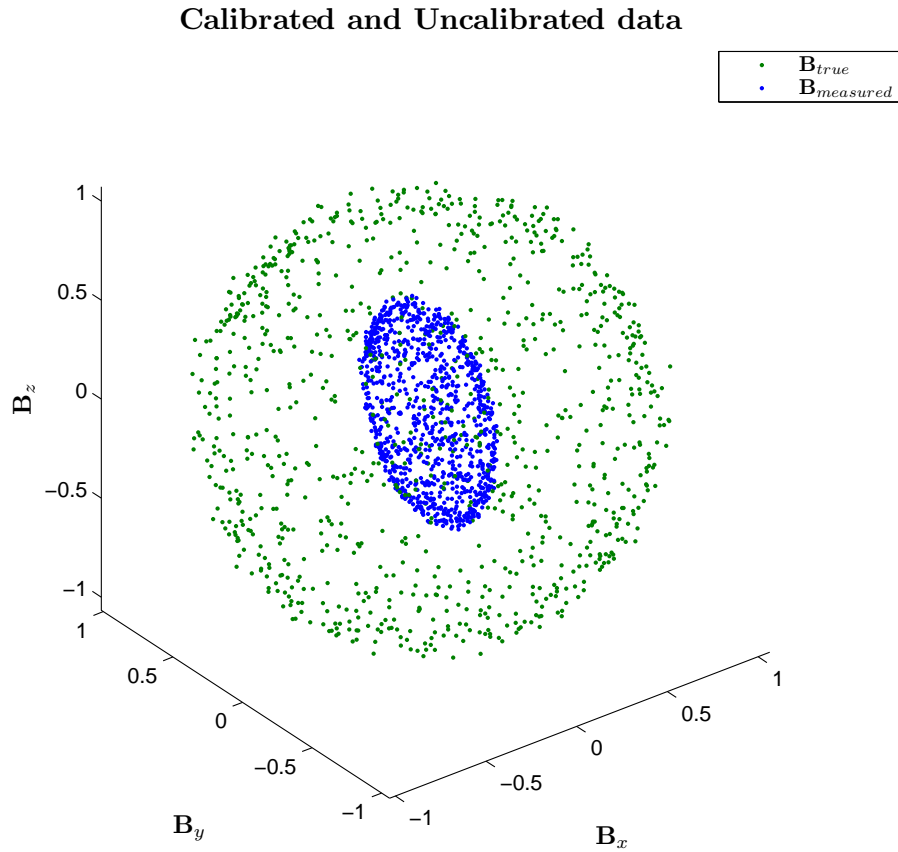


Figure 5.1: Simulated “true” (green) and “measured” (blue) magnetic field components of \mathbf{B} .

Large sensitivity (K_x , K_y and K_z) and orthogonality (ρ , λ and ϕ) errors were selected to represent a badly built sensor or coil, and bias (b_x , b_y and b_z) was included in the simulation, but is not presented in the results since the Geometric Approach and TWOSTEP models place it in differing locations, of their respective models, meaning that moving either bias from one model’s framework to the other’s would couple sensitivity and orthogonality estimation errors into the resulting bias, thereby influencing the result; hence the RMS value of $|\mathbf{B} + \text{Noise}| - |\mathbf{B}_{Estimated}|$ is used instead. Numerical values of the errors are shown in Table 5.2.

5.3 Estimator Selection

| K_x | K_y | K_z | ρ | λ | ϕ | b_x | b_y | b_z |
|--------|--------|--------|---------|-----------|---------|--------|--------|--------|
| 3.9589 | 2.9243 | 2.2485 | -2.0608 | -19.4292 | 16.5846 | 0.0055 | 0.0137 | 0.0235 |

Table 5.2: Measurement errors used in the simulation. Units of K_x , K_y , K_z , b_x , b_y , and b_z are arbitrary, and ρ , λ , ϕ are in units of degrees.

5.3.1 First order performance

The “true” total field strength in the following section is unity with isotropic noise of variance of 1.25×10^{-3} added to the dataset¹². Total fields for two datasets of 80 and 8000 samples are compared to get a first order understanding of the performance of the estimators.

Figures 5.2 and 5.3 show the true, un-calibrated and calibrated total field $|\mathbf{B} + noise|$ data, for the TWOSTEP and Geometric Approach estimates. The data calibrated using the two estimates closely follows the simulated total field and magnetic noise, along with what appears to be a slight estimator bias in the sensitivity and bias error estimates, leading to an underestimate of the total field. As sample size is increased the total-field bias appears to reduce, as would be expected since MLEs are asymptotically unbiased.

Figures 5.4 and 5.5 show the difference between $|\mathbf{B} + noise|$ and $|\mathbf{B}_{estimate}|$. The estimator bias alluded to above is evident. The TWOSTEP bias appears to be slightly larger than that in the Geometric Approach, with both approaching zero as sample size is increased.

5.3.2 Reference frame selection

TWOSTEP and Geometric Approach impose different restrictions on the calibration matrices, which impacts on the way sensitivity orthogonality errors are represented. The sensitivity and orthogonality correction in the TWOSTEP process can be expressed symbolically as shown in equation (5.53).

$$\mathbf{H} = \mathbf{KB} \tag{5.53}$$

¹² $\epsilon_1 = \epsilon_2 = \epsilon_3 = 1.25 \times 10^{-3}$. Measurements are relative to each other, not absolute.

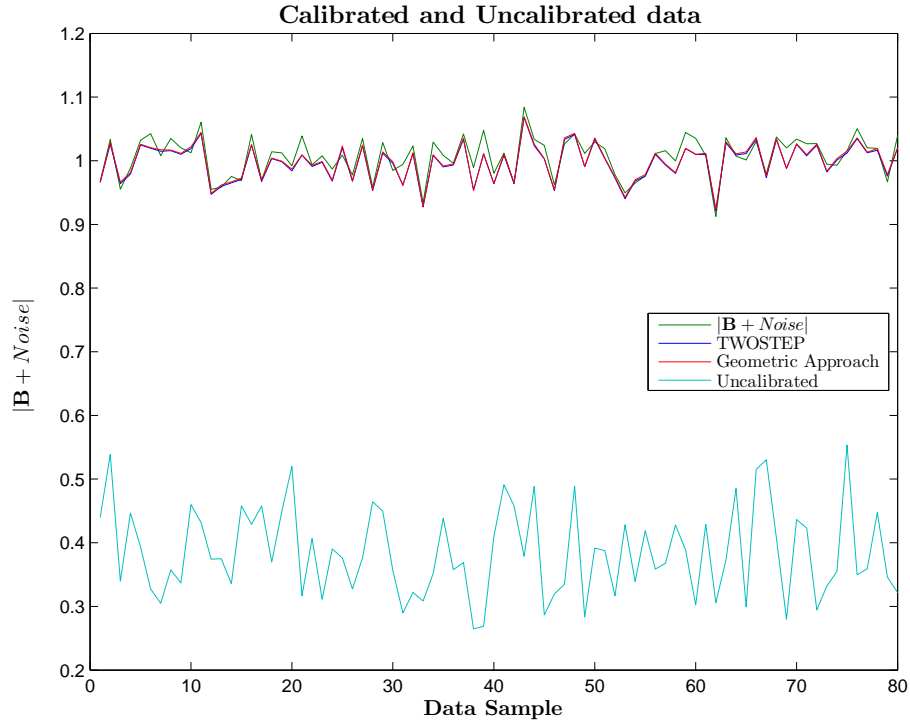


Figure 5.2: Comparison between uncalibrated data with noise (pale blue) and true (known magnetic field data) with noise (green), calibrated (estimated) $|\mathbf{B}_{estimate}|$ using TWOSTEP (blue) and Geometric Approach (red) methods. 80 Samples.

where $\mathbf{H} = [H_x, H_y, H_z]^T$ is the calibrated signal, $\mathbf{B} = [B_x, B_y, B_z]^T$ is the raw measured signal, and $K = \begin{bmatrix} K_x & a & b \\ a & K_y & c \\ b & c & K_z \end{bmatrix}$ is the calibration matrix.

$$\mathbf{H}_x = K_x \mathbf{B}_x + a \mathbf{B}_y + b \mathbf{B}_z \quad (5.54a)$$

$$\mathbf{H}_y = a \mathbf{B}_x + K_y \mathbf{B}_y + c \mathbf{B}_z \quad (5.54b)$$

$$\mathbf{H}_z = b \mathbf{B}_x + c \mathbf{B}_y + K_z \mathbf{B}_z \quad (5.54c)$$

TWOSTEP uses a fully symmetric matrix, which effectively means each component from the raw data e.g. B_x contributes an equal proportion of itself, to each of the other two calibrated axes H_y and H_z (via the off-diagonal elements), as the corresponding raw data for each of said calibrated axes contributes as a proportion of themselves to

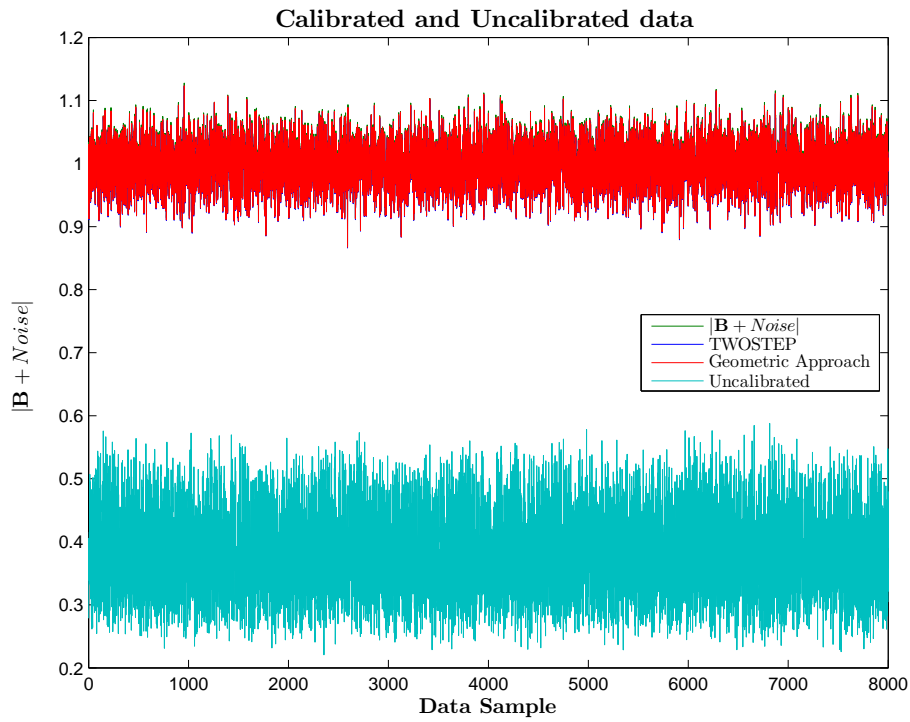


Figure 5.3: Comparison between uncalibrated data with noise (pale blue) and true (known magnetic field data) with noise (green), calibrated (estimated) $|\mathbf{B}_{estimate}|$ using TWOSTEP (blue) and Geometric Approach (red) methods. 8000 Samples.

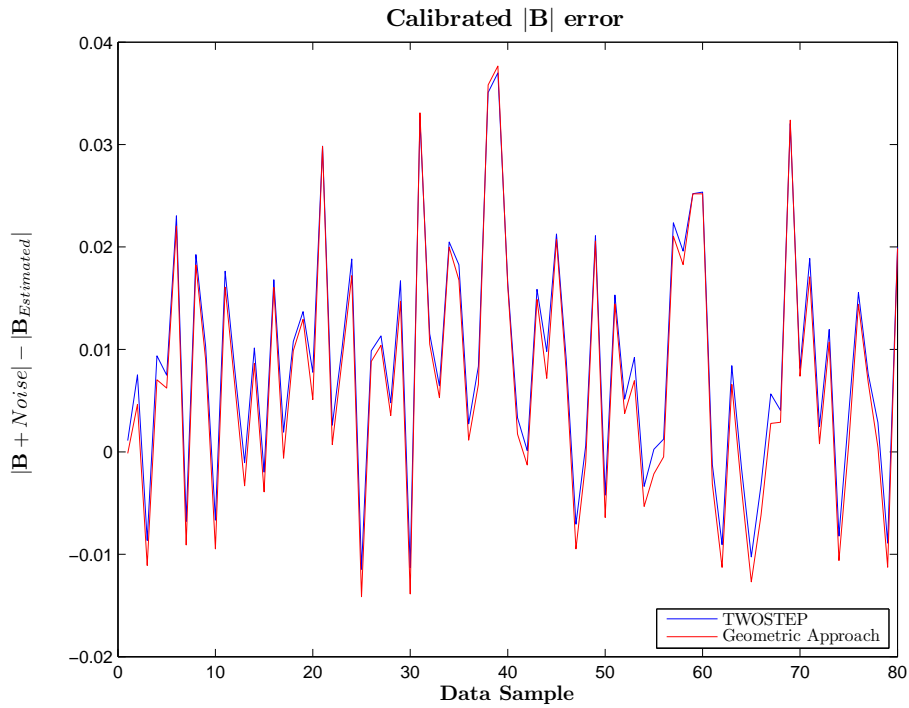


Figure 5.4: TWOSTEP and Geometric Approach $|\mathbf{B} + noise|$ Errors - 80 Samples.

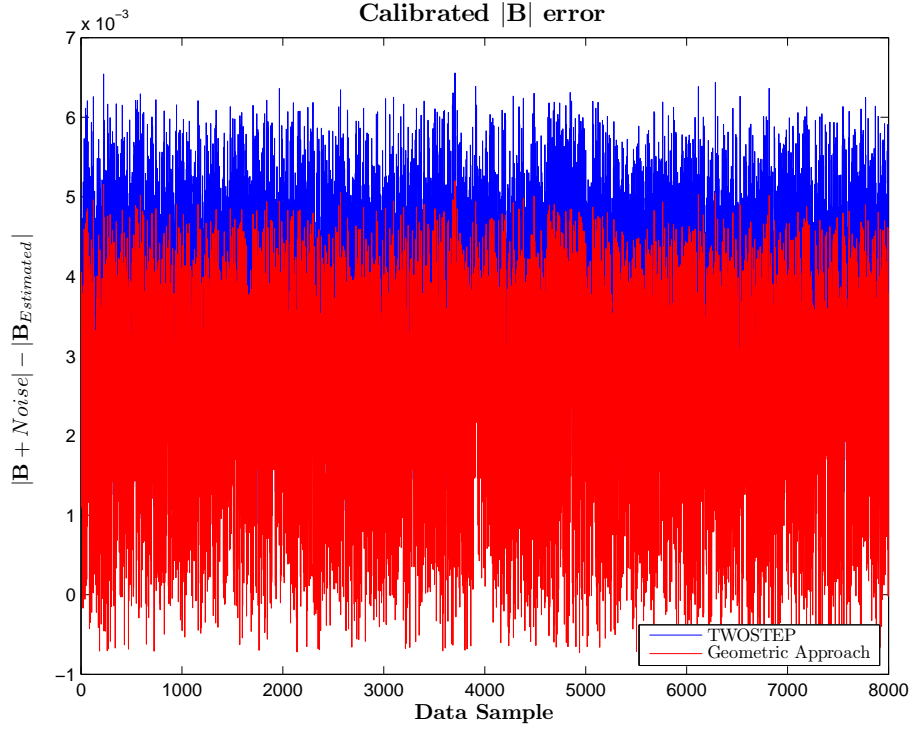


Figure 5.5: TWOSTEP and Geometric Approach $|\mathbf{B} + noise|$ Errors - 8000 Samples.

the original calibrated axis. Equation (5.54) illustrates this, where H_x receives a from B_y and b from B_z , and B_x contributes a to H_y and b to H_z .

The Geometric Approach uses a lower triangular matrix as a first guess, meaning the x -axis is assumed to have no orthogonality error, and the error projected onto the y and z axes; but the final Geometric Approach matrix has no restrictions on it, meaning there are no restrictions on the reference frame of the sensor. To enable the comparison of specific calibration parameters, results must be brought into a single reference frame.

For convenience a lower triangular matrix, was selected as the reference frame (shown in Figure 5.6) for comparing results, this reference frame matches frame used in the first guess in the Geometric Approach. TWOSTEP and Geometric Approach sensitivity and orthogonality matrices are easily brought into the correct frame using QL decomposition, which produces a singular orthogonal matrix Q (a rotation matrix) and a calibration matrix L shown in Equation (5.55), from which sensitivity (K_x , K_y and K_z) and orthogonality (ρ , λ and ϕ) errors can be extracted algebraically. L can be used to transform the ellipsoid (x' , y' , z' axes, Figure 5.6) in Figure 5.1 to the sphere (x , y , z axes,

5.3 Estimator Selection

Figure 5.6) representing the true field, by multiplying the ellipsoid data by L , using the values of K_x , K_y , K_z , ρ , λ , and ϕ from Table 5.2.

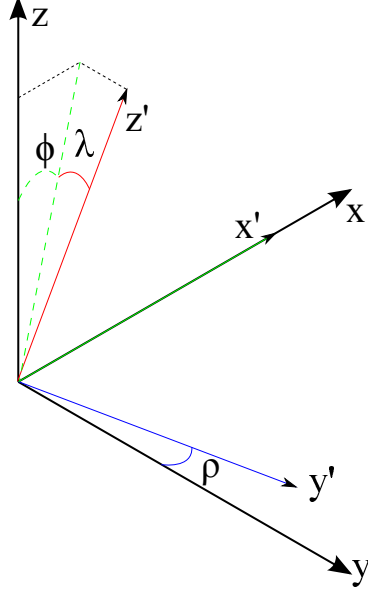


Figure 5.6: Coordinate framework for lower-triangular matrix, where $\begin{pmatrix} x & y & z \end{pmatrix}^T = L \begin{pmatrix} x' & y' & z' \end{pmatrix}^T$ converts the raw measured sensor readings to calibrated readings.

$$L = \begin{bmatrix} K_x & 0 & 0 \\ K_y \sin(\rho) & K_y \cos(\rho) & 0 \\ K_z(\sin(\phi) \cos(\lambda)) & K_z \sin(\lambda) & K_z \cos(\phi) \cos(\lambda) \end{bmatrix} \quad (5.55)$$

5.3.3 Performance for noisy data

The total field strength in the following section is unity with a isotropic noise of variance of 2×10^{-6} to 2×10^{-2} added to the data-set of 2000 samples. Performance characteristics were measured at each data-set and averaged over 30 simulations with the same noise characteristics. Note the spikes in the Geometric Approach curves occur when the calibration algorithm has failed to converge to a solution within acceptable stop conditions¹³. Use of the median of the simulation runs would have removed the spikes and provided a better approximation to the expected performance, but it was

¹³The stop conditions relate to the magnitude of the step size at each iteration.

believed important to retain the anomalies as an illustration of the impact certain datasets can have on the estimator. Estimator stopping conditions were set to the point where solutions just start not being able to converge, to enable a fair comparison of the best achievable solutions for each algorithm.

5.3.3.1 Processing Time and Number of Iterations

Figure 5.7 shows the processing time for the Geometric Approach is slightly dependent on noise variance, with a slight increase in high noise environments, whilst the TWOSTEP algorithm exhibits a minima at 10^{-4} noise variance, rapidly increasing if noise variance is reduced, or slowly increasing if noise is increased. The reason the TWOSTEP processing time increases for low noise is associated with the numerical precision in MATLAB, leading to quasi singular or badly scales matrices, when a small noise variance is used. This is most likely caused by the centring process (Section 5.1.7). Estimation using TWOSTEP is significantly faster than using Geometric Approach.

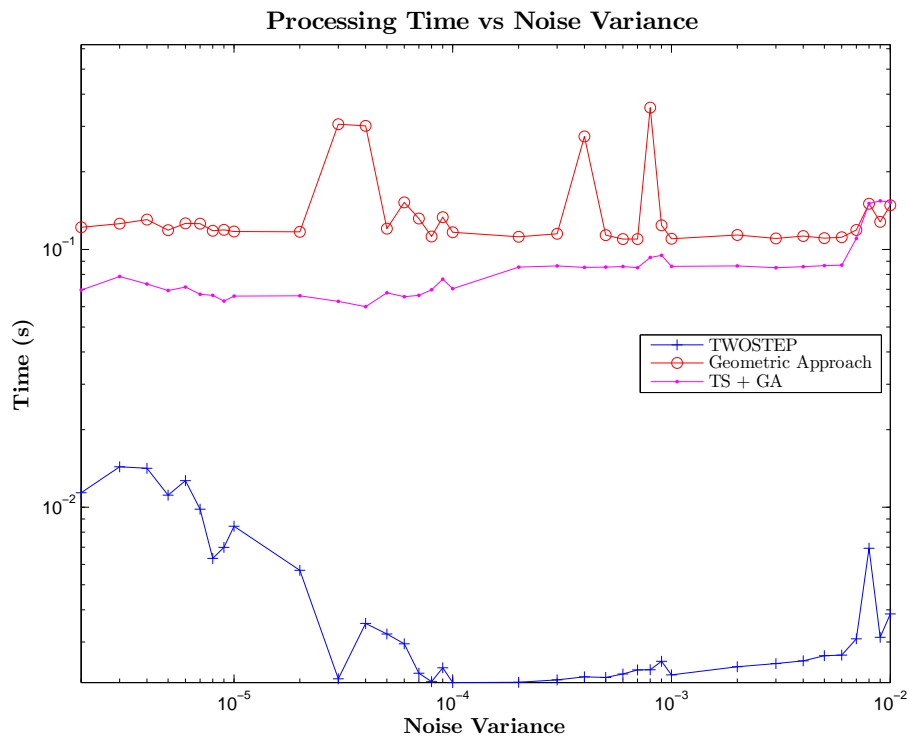


Figure 5.7: TWOSTEP (blue), Geometric Approach (red), and TS + GA (magenta): processing time vs noise.

5.3 Estimator Selection

The reason for the Geometric Approach's close-to-constant processing time becomes apparent from Figure 5.8. The Geometric Approach tends to converge in approximately 5 iterations, unless the data is pre-processed with TWOSTEP, in which case it converges in as little as 3 iterations. TWOSTEP on the other hand takes between 5 and 100 iterations to converge to a solution.

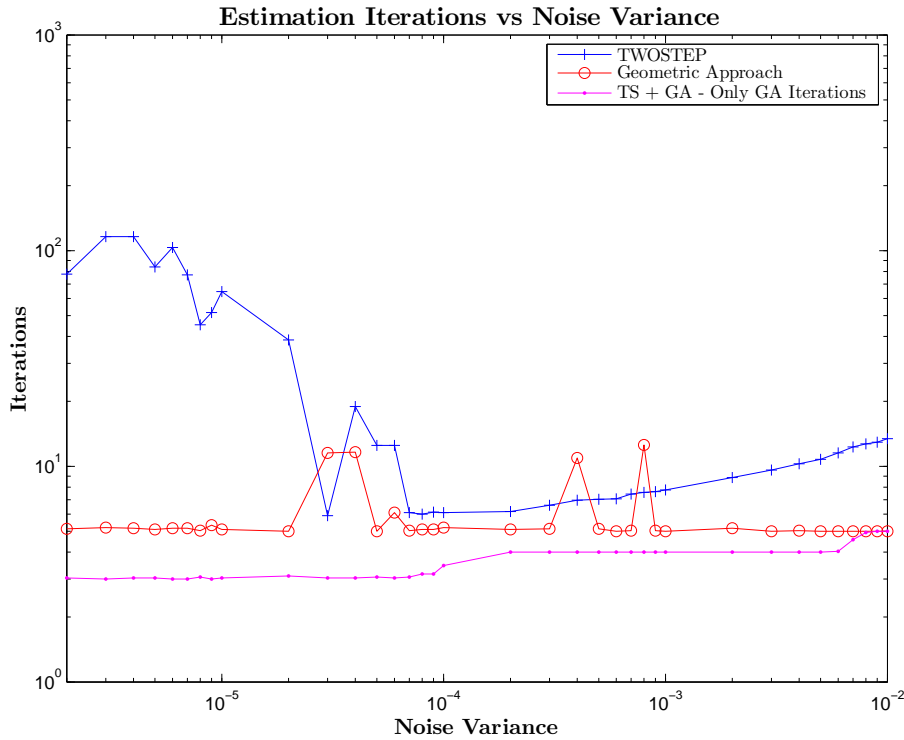


Figure 5.8: Number of TWOSTEP (blue), Geometric Approach (red), and TS + GA (magenta): iterations required for convergence vs noise.

5.3.3.2 $|B + noise|$ RMS error

Figure 5.9 shows the RMS error of the total field for both estimators as noise is increased. TWOSTEP and Geometric Approach are effectively identical in their performance for low noise, but Geometric Approach marginally outperforms TWOSTEP for high noise environments.

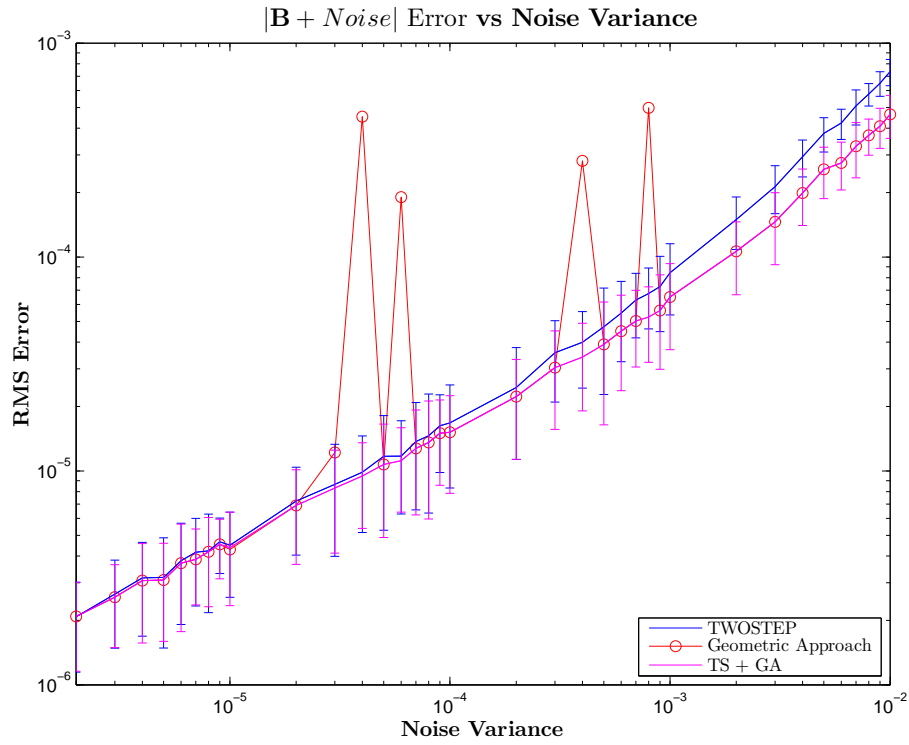


Figure 5.9: TWOSTEP (blue), Geometric Approach (red), and TS + GA (magenta): RMS of $(|\mathbf{B} + \text{noise}| - |\mathbf{B}_{\text{estimate}}|)$ vs noise.

5.3.3.3 Individual parameter errors

For a direct comparison between TWOSTEP and Geometric Approach calibration parameters, both sensitivity and orthogonality estimates were extracted using QL decomposition, as shown in Section 5.3.2.

Figure 5.10 shows that the TWOSTEP and Geometric Approach orthogonality errors increase with increasing noise, Geometric Approach appears to slightly outperform TWOSTEP for high noise environments, but fails to converge more often than TWOSTEP, causing in “spikes” in the simulation results.

Similarly the sensitivity errors shown in 5.11 show good agreement between the two methods, but the Geometric Approach clearly gets slightly better in high noise.

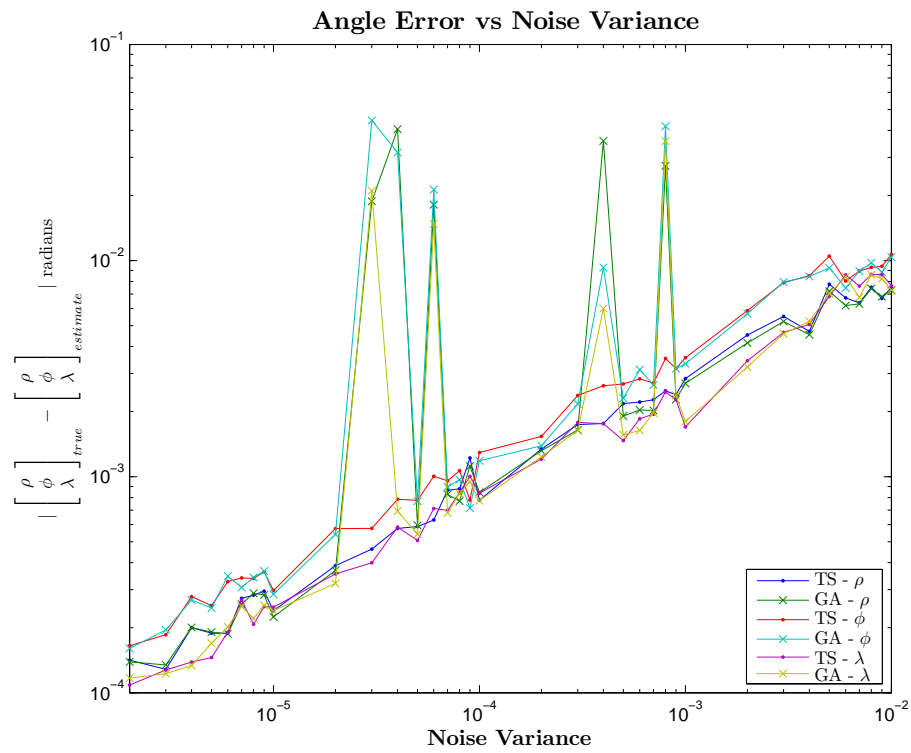


Figure 5.10: TWOSTEP and Geometric Approach: angle errors vs noise.

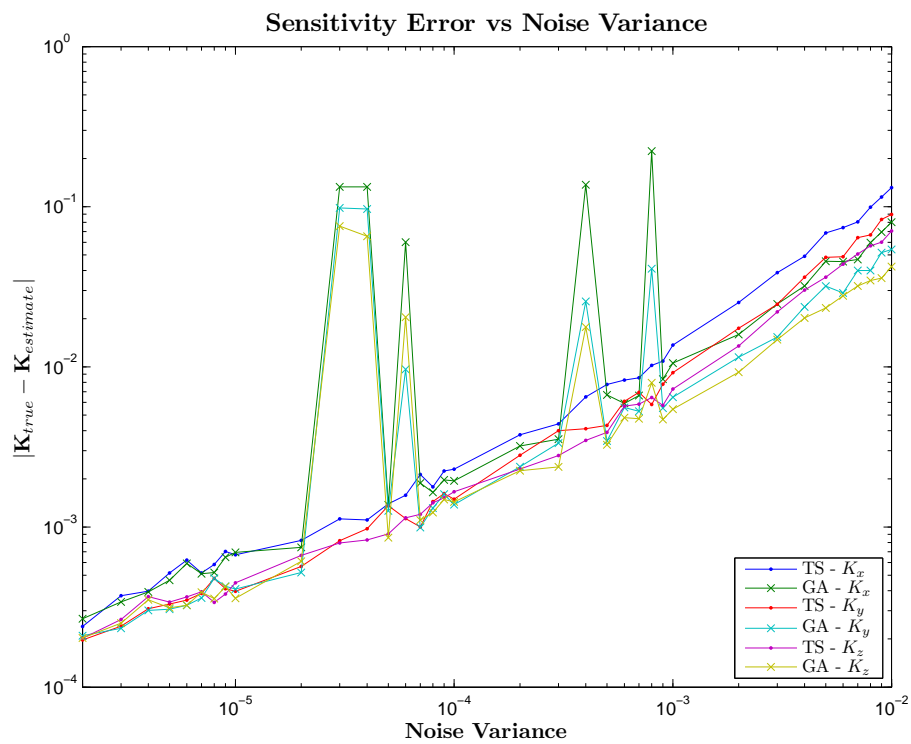


Figure 5.11: TWOSTEP and Geometric Approach: sensitivity errors vs noise.

5.3.4 Performance for large data-sets

The total field strength in the following section is unity with an isotropic noise of variance of 10^{-4} added to the data-sets consisting of 20 to 2×10^5 samples. Performance characteristics (processing time and number of iterations) and estimation errors were recorded for each data-set and averaged over 30 iterations with the same noise characteristics.

5.3.4.1 Processing time and Number of Iterations

Figure 5.12 shows the increase in processing time as sample size is increased. TWOSTEP outperforms Geometric Approach by between one and two orders of magnitude. When optimising the code it was noticed the bulk of the time within Geometric Approach is taken up by Kronecker product (\otimes) operations over k samples and to a lesser extent normal matrix multiplication operations between matrices that are k samples deep¹⁴. This slow-down is caused by the large memory requirements necessary to process all the data concurrently in the matrices, and is likely due to the calibration matrix not being triangular or symmetric, hence not being vectorised to reduce memory usage. Extrapolating from the graph, 10^7 samples (2hours 45min of data sampled at 1kHz) could be processed by TWOSTEP in 10s.

Figure 5.13 indicates processing time is principally dependent on memory usage, since the number of iterations for the Geometric Approach is fundamentally flat. TWOSTEP on the other hand seems to dramatically increase the number of iterations it takes to converge once the sample size increases above 2000 samples.

5.3.4.2 $|B + noise|$ RMS error

Figure 5.14 shows the RMS error for the total field is significantly reduced as the sample size is increased; the Geometric Approach is shown to have a lower error for extremely large datasets.

¹⁴A normal matrix is $m \times n$, but since the estimator uses k samples the fastest implementation tested uses $m \times n \times k$ matrices and dot product operations to reduce time-consuming memory allocation operations.

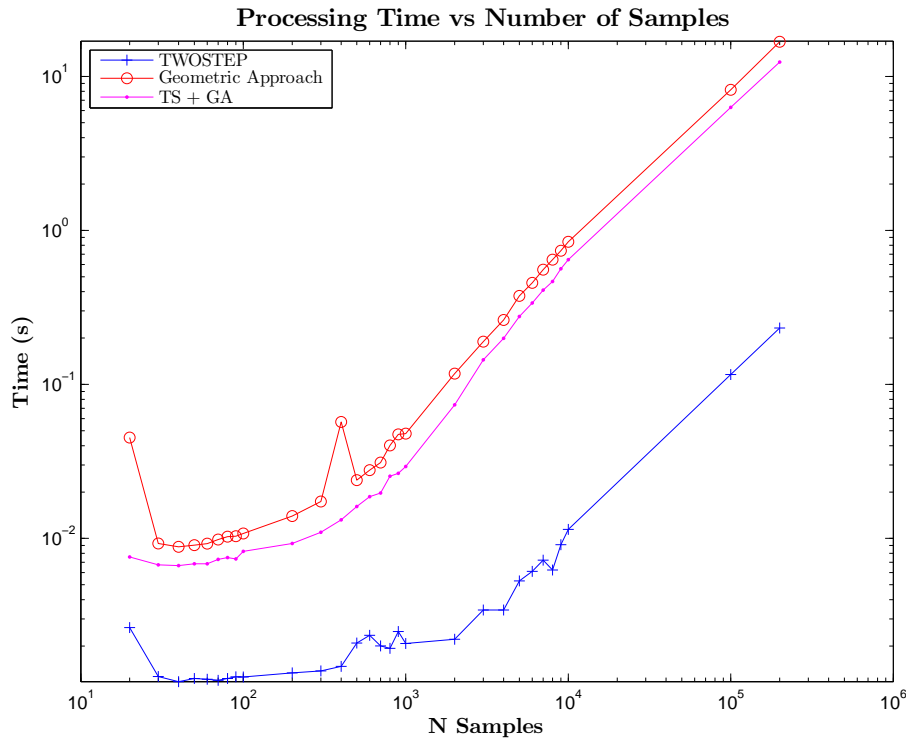


Figure 5.12: TWOSTEP (blue), Geometric Approach (red), and TS + GA (magenta): processing time vs sample size.

5.3.4.3 Individual parameter errors

Similarly to the tests for changing noise variance, Figures 5.15 and 5.16 show the Geometric Approach marginally outperforming TWOSTEP in orthogonality error angle estimation, and clearly outperforming TWOSTEP in sensitivity estimation.

5.3.5 Summary

The Geometric Approach is an elegant approach to the problem and compares very well to TWOSTEP, but suffers from large memory requirements, and excessive processing time due to the calculation of the Kronecker matrix product for each sample, as well as some relatively rare convergence issues. The magnetic calibration facility is intended to run at high sample rates, with relatively low noise, allowing suitable estimation accuracy to be achieved through the use of large datasets processed using the TWOSTEP algorithm.

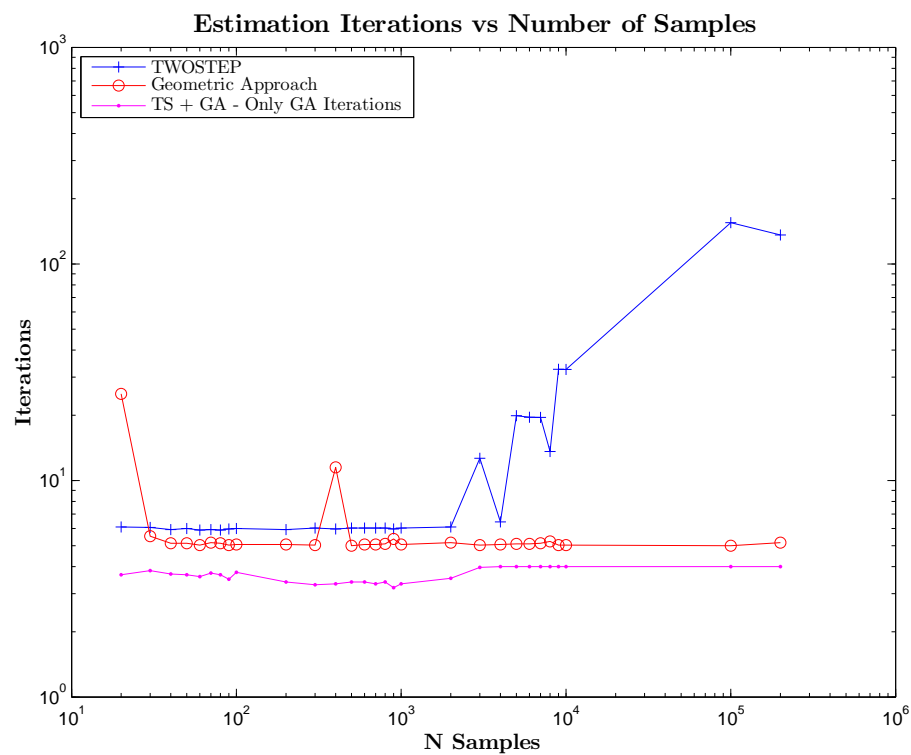


Figure 5.13: Number of TWOSTEP (blue), Geometric Approach (red), and TS + GA (magenta): iterations required for convergence vs sample size.

5.3 Estimator Selection

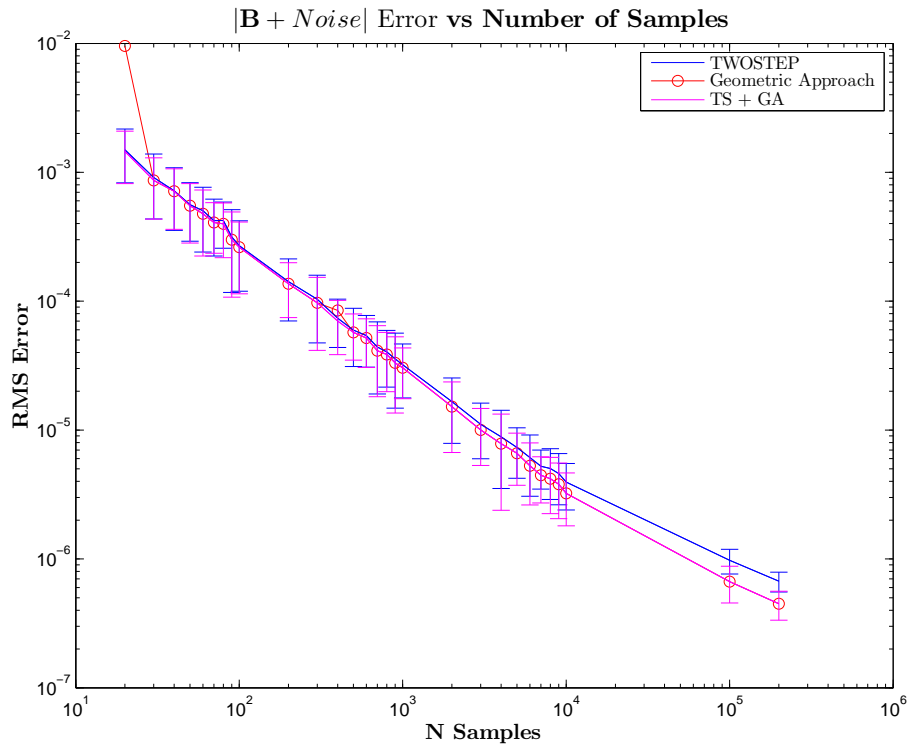


Figure 5.14: TWOSTEP (blue), Geometric Approach (red), and TS + GA (magenta): RMS of $(|\mathbf{B} + \text{noise}| - |\mathbf{B}_{\text{estimate}}|)$ vs sample size.

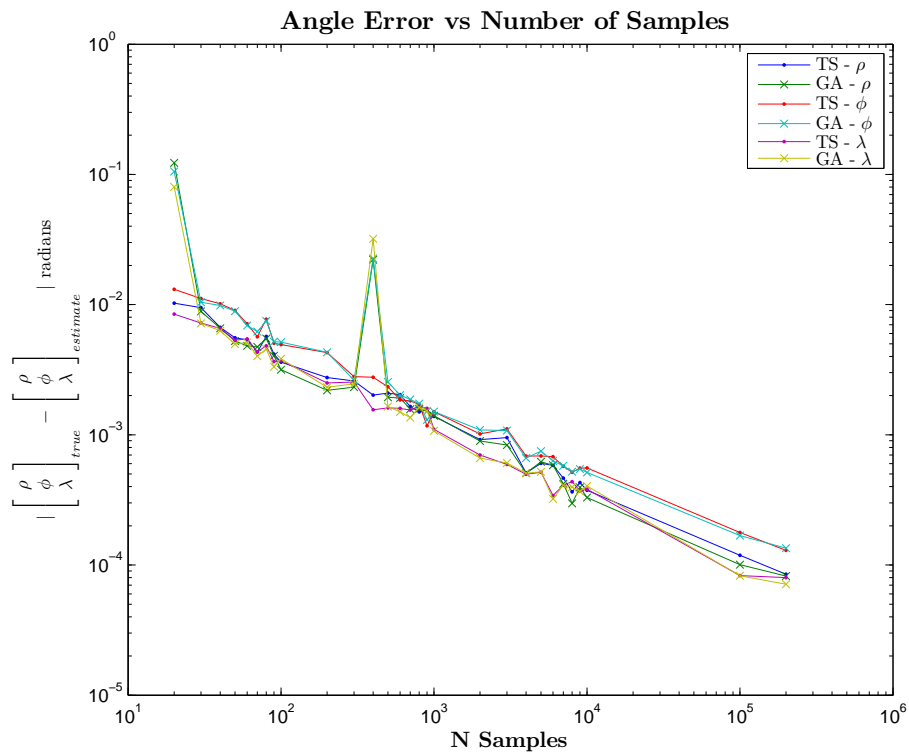


Figure 5.15: TWOSTEP and Geometric Approach: angle errors vs sample size.

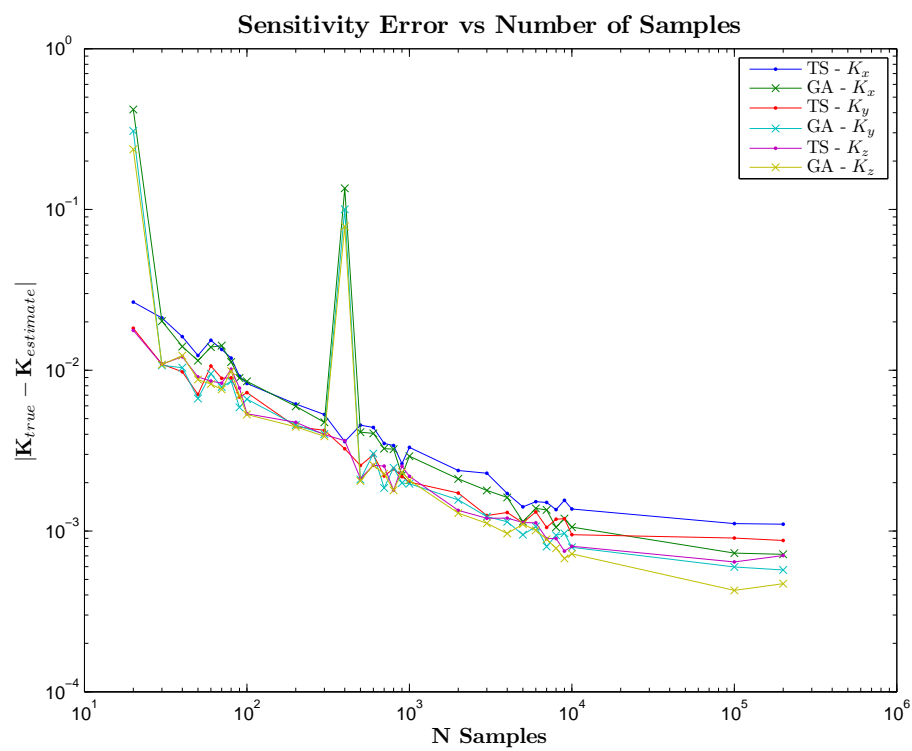


Figure 5.16: TWOSTEP and Geometric Approach: sensitivity errors vs sample size.

Chapter 6

Calibration Methods

In this section the TWOSTEP algorithm's use is extended to encompass the calibration of coils and sensors within coils. Additionally an AC calibration is presented, which provides sensitivity and orthogonality without estimating bias. In the first section (6.1), the coil to be calibrated refers to the relatively large coil (e.g. Ternan coil), into which a calibrated reference sensor is placed. In the second section (6.2), the un-calibrated sensor is calibrated by placing it within the previously calibrated large coil.

6.1 Coil Calibration Estimation

Coil calibration is preferably done with an Overhauser sensor, hence the total field must always remain within the sensor's operating range. This can be performed using earth's field as a "bias" field placing the sensor into its operating range, and applying only signal amplitudes which do not take the Overhauser sensor out of its operating range. Alternatively a calibrated fluxgate vector magnetometer can be used as the reference sensor, at the expense of a lesser precision of results.

6.1.1 Model

We begin by defining the coil model as follows:

$$(I + D)SI_k + A^e(\mathbf{b}^e + \boldsymbol{\varepsilon}_k^e) = \boldsymbol{\vartheta}^T A^s \mathbf{H}_k + \boldsymbol{\varepsilon}_k' \quad (6.1)$$

6.1 Coil Calibration Estimation

where I_k is the k^{th} reading of the current driving the coils¹⁵, and S is a diagonal matrix representing the coil factors. D is a fully populated symmetric matrix representing coil factor and orthogonality errors when added to the identity matrix I . H_k is the reference magnetometer reading, \mathbf{b}^e is the bias magnetic field associated with earth's field, ϵ_k^e is the earth's geo-magnetic noise, and ϵ'_k is reference sensor (e.g. Overhauser) noise. A^e is an attitude correction matrix bringing earth's field into the coil's reference frame, while A^s and ϑ are an attitude correction for the reference sensor and a rotational error within the reference sensor. These terms serve no part in the estimation, but are included to show similarity to the TWOSTEP method. It is assumed the coil produces no magnetic field when there is no current flowing in it, removing the need for a bias variable associated with it.

6.1.2 Manipulation to enable use of TWOSTEP

We combine S and I_k , and combine A^e with \mathbf{b}^e and ϵ_k^e as shown in (6.2), to obtain B_k , \mathbf{b} and ϵ , shown in (6.3).

$$\begin{aligned} B_k &= SI_k \\ \mathbf{b} &= -A^e \mathbf{b}^e \\ \epsilon_k &= -A^e \epsilon_k^e + \epsilon'_k \end{aligned} \tag{6.2}$$

$$(I + D)B_k - \mathbf{b} - \epsilon_k = \vartheta^T A^s H_k \tag{6.3}$$

Rearranging (6.3), gives us (6.4), which is the same as (5.1), enabling the use of the Alonso and Shuster TWOSTEP model re-derived in Section 5.1.

$$B_k = (I + D)^{-1}(\vartheta^T A^s H_k + \mathbf{b} + \epsilon_k) \tag{6.4}$$

\mathbf{b} , which estimates earth's field in the coil's reference frame can be discarded after the estimation is complete, or used as a record of earth's field with respect to the coils.

¹⁵Actual measurement is the voltage across a resistor, which is then converted to current I_i with temperature compensation.

6.1.3 Driving the coil

When driving the coil to stimulate the sensor, we are only truly aware of a desired \mathbf{H}_k , and estimated \mathbf{b} and D . If we assume A^s and ϑ to be known and to be identity matrices then (6.4) can be used for stimulation purposes.

The driving current \mathbf{I}_k is found as $\mathbf{I}_k = S^{-1}\mathbf{B}_k$, which can be used directly as the desired input reference for whenever the system is being driven by a PID (Proportional Integration Differentiation) control system, or in the case of higher frequency work, driving voltage implied where $\mathbf{V}_k = R\mathbf{I}_k$ and where \mathbf{V}_k is a vector representing the voltage driving the coil, R is a diagonal matrix defined by the coil winding resistances, and \mathbf{I}_k is a vector representing the current flowing through the coil.

6.1.4 Implementation issues in TWOSTEP

The initial centred estimate within TWOSTEP requires a “first guess” of $\boldsymbol{\theta}'$, which is generally set to zero. Recall that $\boldsymbol{\theta}' = (\mathbf{cE})^T$ (5.12b) and $\mathbf{c} = (I + D)\mathbf{b}$ (5.6b), i.e. $\boldsymbol{\theta}'$ is in terms of \mathbf{b} and the symmetric matrix D . In the case of coil calibration, \mathbf{b}^e is used to represent the bias introduced by earth’s field. The initial calculation of σ_k^2 using (5.15a), is dependent on \mathbf{B} and \mathbf{b} , and since in the typical sensor calibration case $|\mathbf{B}| \gg |\mathbf{b}|$, setting $\mathbf{b} = \mathbf{0}$ will have little impact on the result. For the typical coil excitation amounts of $B = 28.5 \times 10^{-6}$ T/A (3.7), when $|\mathbf{B}| \approx |\mathbf{b}|$, as is the case with coil calibrations, the x, y, z components of the earth’s magnetic field at DC are superimposed on the relatively weak AC field generated by the coil (e.g. $\cos(\theta)$ Ternan coil), and the errors are no longer negligible, hence \mathbf{b} should be as close to the real value as possible. In this context, an un-calibrated fluxgate sensor should provide a suitable first guess for $(\mathbf{b})^e$.

6.2 Sensor in Coil Estimation

The calibration of sensors in a coil is preferably performed with a reference sensor co-located with the sensor under test. Earth's field cancelation could otherwise be achieved by applying an offset field \mathbf{b}^e , estimated in Section 6.1.

6.2.1 Model

We begin by defining the sensor model as follows:

$$\mathbf{B}_k = (\mathbf{I} + \mathbf{D})^{-1}(\vartheta^T \mathbf{A}^s (\mathbf{A}^e (\mathbf{H}_k^e + \boldsymbol{\varepsilon}_k^{e'}) + \mathbf{H}_k^c) + \mathbf{b} + \boldsymbol{\varepsilon}_k') \quad (6.5)$$

where \mathbf{B}_k is the k^{th} sensor reading, \mathbf{H}_k^e is earth's magnetic field at that reading, \mathbf{H}_k^c is the coil-generated magnetic field at that reading, \mathbf{b} is sensor bias, $\boldsymbol{\varepsilon}_k^{e'}$ and $\boldsymbol{\varepsilon}_k'$ are the measurement noise associated with earth's field and the coil system respectively. \mathbf{D} is a fully populated symmetric matrix representing sensitivity and orthogonality errors when added to the identity matrix \mathbf{I} . \mathbf{A}^e is an attitude correction matrix (rotation), to put \mathbf{H}_k^e in the same reference frame as \mathbf{H}_k^c , while \mathbf{A}^s is an attitude correction matrix (rotation) to put $\mathbf{A}^e \mathbf{H}_k^e$ and \mathbf{H}_k^c in the same reference frame as \mathbf{B}_k . ϑ is a rotational error within the sensor, hence is another rotation matrix.

We zero out earth's field, either by using a reference sensor, or the estimated \mathbf{b}^e from Section 6.1, removing \mathbf{H}_k^e .

$$\mathbf{B}_k = (\mathbf{I} + \mathbf{D})^{-1}(\vartheta^T \mathbf{A}^s (\mathbf{A}^e \boldsymbol{\varepsilon}_k^{e'} + \mathbf{H}_k^c) + \mathbf{b} + \boldsymbol{\varepsilon}_k') \quad (6.6)$$

Assuming isotropic noise and setting $\boldsymbol{\varepsilon}_k^e = \vartheta^T \mathbf{A}^s \mathbf{A}^e \boldsymbol{\varepsilon}_k^{e'}$, and $\boldsymbol{\varepsilon}_k = \boldsymbol{\varepsilon}_k^e + \boldsymbol{\varepsilon}_k'$ gives (6.7), which can be solved using TWOSTEP.

$$\mathbf{B}_k = (\mathbf{I} + \mathbf{D})^{-1}(\vartheta^T \mathbf{A}^s \mathbf{H}_k^c + \mathbf{b} + \boldsymbol{\varepsilon}_k) \quad (6.7)$$

\mathbf{H}_k^c and \mathbf{A}^e are expected to be known during the calibration, but only the $|\mathbf{H}_k^c|$ needed for TWOSTEP, and ϑ is not known or estimated. \mathbf{A}^s is likely to be an identity matrix, depending how the sensor is placed within the coil.

Since the noise has been merged into ε_k , its mean and variance should be calculated, with $\varepsilon_k^{e'} \sim \mathcal{N}(\mathbf{0}, \Sigma_k^{e'})$ and $\varepsilon_k^e \sim \mathcal{N}(\mathbf{0}, \Sigma_k^e)$, showing $\varepsilon_k \sim \mathcal{N}(\mathbf{0}, \Sigma_k)$, where $E(\varepsilon_k^e) = E(\vartheta^T A^s A^e \varepsilon_k^{e'}) = 0$ and $\Sigma_k^e = \Sigma_k^{e'}$

$$\begin{aligned} E(\varepsilon_k) &= E(\varepsilon_k^e) + E(\varepsilon_k^{e'}) \\ &= 0 + 0 \\ &= 0 \end{aligned} \tag{6.8}$$

$$\begin{aligned} \Sigma_k &= E(\varepsilon_k^2) - E(\varepsilon_k) \\ &= E(\varepsilon_k^2) \\ &= \frac{1}{N} \sum_{k=1}^N (\varepsilon_k^{e'} + \varepsilon_k^e)^2 \\ &= \frac{1}{N} \sum_{k=1}^N \varepsilon_k^{e'}{}^2 + \varepsilon_k^e{}^2 + 2\varepsilon_k^{e'}\varepsilon_k^e \end{aligned} \tag{6.9}$$

6.2.2 Bias issues

Due to slow varying geomagnetic noise, perfect zeroing of earth's field cannot be assured, hence the remaining \mathbf{H}_k^e will "bleed through" the estimation to \mathbf{b} , introducing an additional bias error. This bias error can be eliminated if a calibrated reference sensor is collocated with the device under test, providing true total field measurements.

Chapter 7

Experimental Results

7.1 Introduction

This section presents the results of a series of experiments which were conducted in December 2012 and March 2013 to perform the following list of tasks:

- Magnetometer spin calibration - Calibration of Bartington sensors in earth's field.
- Calibration for various sample sizes - Evaluate estimator, and select suitable calibration timeframe.
- Calibration with filters - Investigate the impact of filtering on calibration.
- Calibrated Excitation - Excite the coil using a calibration matrix.
- Transfer function - Measure the frequency response of the Ternan coil.
- Uniformity measurements - Investigate the usable uniform volume in the Ternan coil.

7.1.1 Experimental setup

The overall experimental setup is shown in Figure 7.1.

A laptop running custom LabVIEW control and acquisition software is interfaced to the system via two separate National Instruments acquisition chassis. The first is a cDAQ 9188 chassis containing one 16-bit analog output module to control the system, and two 24-bit differential analog input modules to sample the voltage signals from a

7.1 Introduction

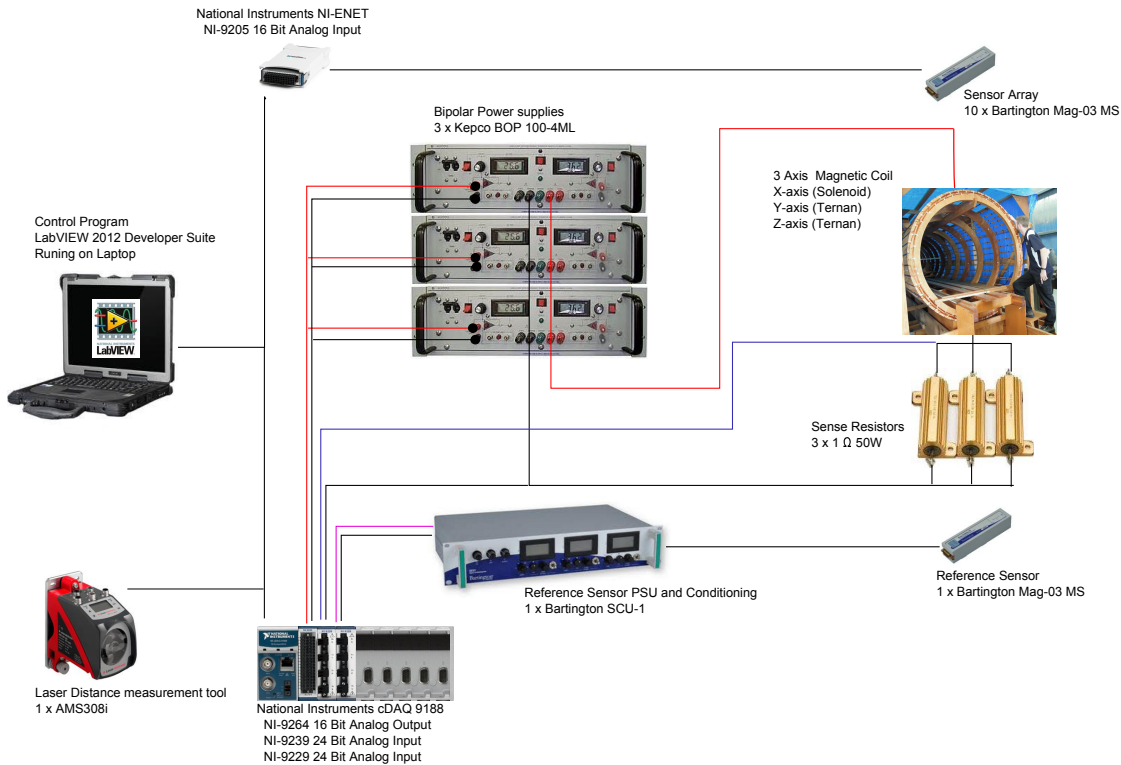


Figure 7.1: Experimental setup used throughout the experiments.

reference sensor and reference 1Ω resistors. The second chassis is a NI-ENET single module chassis, containing a 16-bit 32-channel analog input module, which is used to sample the voltage signals from an array of 10 sensors during the uniformity experiment. All analog input and output modules are sampled at 6.25 kHz, with the acquisition starts synchronised by a hardware trigger.

Three Kepco bipolar BOP-100 amplifiers were used. The two new BOP-100 ML were used to drive the y -axis and z -axis (Ternan design), while an older BOP-100 M was used to drive the x -axis (Solenoidal design). The amplifiers were each connected to the coils in series with a 1Ω 50 W reference resistor respectively. The reference resistors were always on the low-side of the amplifiers for safety reasons.

The reference sensor was powered by a Bartington signal conditioning unit (SCU), but the unconditioned output was used in all experiments except the “Calibration with filters” dataset. The reference sensor was always located at the coil centre $(0, 0, 0)$, the sensor is a Bartington MAG3 - SM, with serial number “386”. The array of sensors was mounted in a purpose built rig, placing the sensors in a line parallel to the y -axis and

at a height $z = 0$ (Table 7.1) and the array was moved along the x -axis using a trolley designed for the purpose. The trolley and sensor array assembly can be seen in Figure 7.2.

Since the earth's magnetic field was of no interest in these measurements, data was pre-processed by removing the mean from each dataset, to reduce the probability of the TWOSTEP estimator detecting a local maxima instead of a global maxima.



Figure 7.2: Array of Bartington MAG3-SM sensors used to measure field uniformity.

7.1.2 Stimulation signals

For accurate TWOSTEP estimate results, the reference sensor needs to be stimulated by a signal of approximately constant “Total field” amplitude, with the field direction uniformly distributed on the surface of a sphere. Failure to sufficiently spread the field direction can cause the TWOSTEP estimator to generate a $D + I$ calibration matrix containing imaginary components, which is incompatible with the known magnetic field properties. Hence the field-generating coils were stimulated using a signal starting from pointing up along the z -axis, spiralling to point downward, and then continuing up to the original direction as illustrated in Figures 7.3 and 7.4.

The MATLAB code for generating a 200 data-point test signal is shown below:

```
N=200;
```

7.1 Introduction

| Sensor Name | Sensor S/N | X Position | Y Position (m) | Z Position (m) |
|-------------|------------|------------|----------------|----------------|
| S1 | 388 | Measured | -0.43 | 0 |
| S2 | 418 | Measured | -0.33 | 0 |
| S3 | 392 | Measured | -0.23 | 0 |
| S4 | 389 | Measured | -0.13 | 0 |
| S5 | 419 | Measured | -0.045 | 0 |
| S6 | 391 | Measured | 0.045 | 0 |
| S7 | 420 | Measured | 0.13 | 0 |
| S8 | 421 | Measured | 0.23 | 0 |
| S9 | 390 | Measured | 0.33 | 0 |
| S10 | 385 | Measured | 0.43 | 0 |

Table 7.1: Sensor array serial numbers (S/N) and placement.

```
theta=[0:1/N:1]*2*pi;  
Ratio=20;  
phi=theta*Ratio;  
Z=cos(theta);  
X=sin(theta).*sin(phi);  
Y=sin(theta).*cos(phi);
```

Ramp-up and ramp-down of the amplifiers were achieved by applying a Tukey window to the whole test signal.

Calibration signal used in experiments

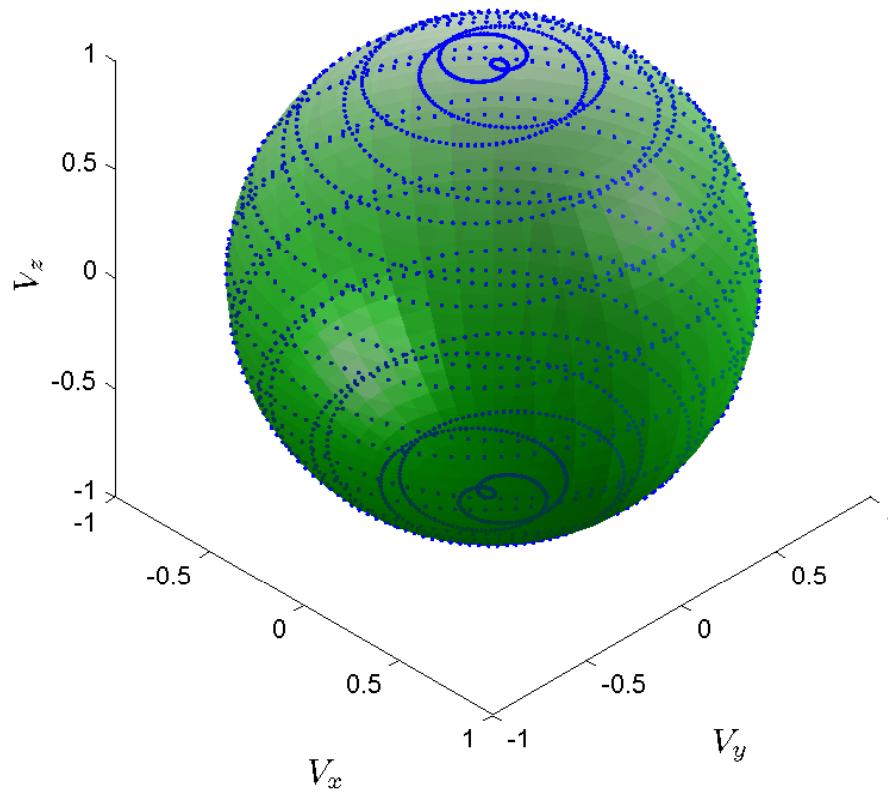


Figure 7.3: Ideal distribution of data-points forming the calibration test signal.

7.2 Magnetometer Spin Calibration

7.2.0.1 Aim

To calibrate sensors in a uniform, low-noise environment, to enable latter use in coil experiments.

7.2.0.2 Method

Magnetometers were taken to a low-noise magnetic facility located at the Defence Establishment, Orchard Hills in Sydney. Sensors were then individually mounted on an approximately 1.5 m long fibre-glass pole, the pole was pointed vertically toward the sky, and rotated such that the sensor remained at a constant height. This procedure was

7.2 Magnetometer Spin Calibration

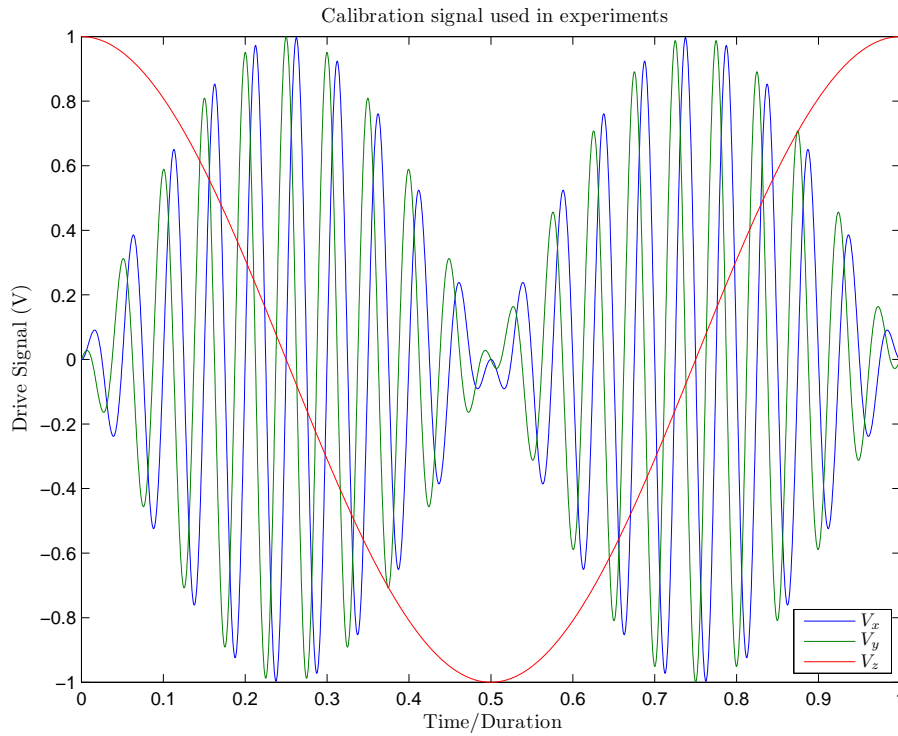


Figure 7.4: Ideal stimulation signals applied to the coils.

repeated for each axis, with a different axis pointing skyward in each iteration. Figure 7.5 shows the measured data superimposed on a sphere of radius equal to the earth's magnetic field scalar magnitude in nanoTesla. Data-sets were concatenated prior to processing using the TWOSTEP algorithm.

The TWOSTEP matrices were reduced using QL decomposition and angular information was recovered from the lower-triangular matrix form. Results are presented below in Tables 7.2, 7.3, and 7.4.

Results proved to be generally within the manufacturer-claimed specifications. Sensor 386 was selected for use as the reference sensor in the coil measurements.

Calibration data - S/N:386 (500 nT)

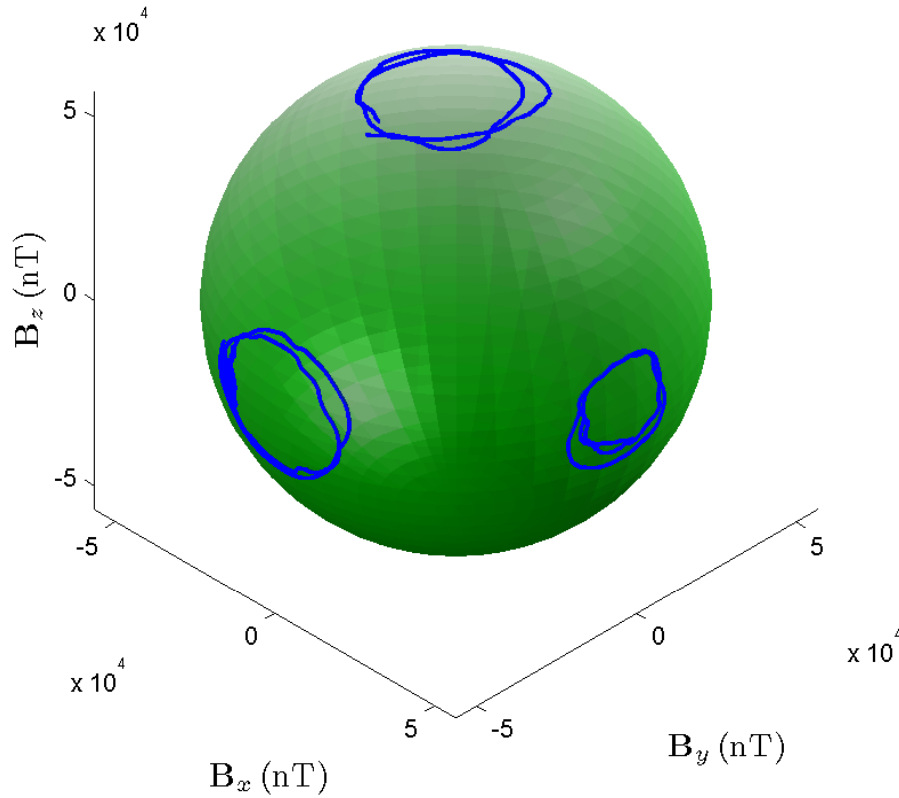


Figure 7.5: Calibration data obtained by spinning the reference sensor about its axes in a uniform magnetic field.

7.3 Calibration Experiments

7.3.1 Coil calibration

7.3.1.1 Aim

To excite the coil with sample sets of increasing length, to investigate convergence of calibration factors to their true values as sample set size is increased.

7.3.1.2 Method

The coil system was connected as detailed in Figure 7.1, with the sensor array placed at the end of the coil. The coil was allowed to warm up for a few minutes by running an

7.3 Calibration Experiments

| $SensorS/N$ | K_x | K_y | K_z |
|-------------|---------|---------|---------|
| 159 | 0.99374 | 0.98745 | 0.99009 |
| 161 | 0.99171 | 0.99171 | 0.98968 |
| 315 | 1.00197 | 0.99913 | 0.99942 |
| 316 | 1.00332 | 0.99979 | 1.00027 |
| 317 | 1.00260 | 1.00210 | 0.99966 |
| 322 | 0.99314 | 0.99148 | 0.99409 |
| 386 | 1.00009 | 1.00565 | 1.00448 |
| 387 | 1.00462 | 1.00379 | 1.00497 |
| 388 | 1.00429 | 1.00558 | 1.00383 |
| 389 | 1.00478 | 1.00286 | 1.00315 |
| 390 | 1.00560 | 1.00493 | 1.00306 |
| 391 | 0.99902 | 0.99842 | 1.00108 |
| 392 | 1.00137 | 0.99966 | 1.00325 |
| 418 | 1.00070 | 1.00109 | 1.00124 |
| 419 | 0.99998 | 0.99928 | 0.99985 |
| 420 | 1.00018 | 1.00030 | 1.00088 |
| 421 | 1.00031 | 0.99919 | 1.00194 |

Table 7.2: Bartington sensor sensitivity errors. Shown to ≈ 5 significant figures consistent with Section 5.3.4 for large sample sets.

offset current before and between measurement runs, and all measurements are made by the reference sensor located at $x = y = z = 0$

Samples sets were taken for the following durations: 1, 2, 3, 4, 5, 6, 7, 8, 9, 10, 15, 20, 30, 40, 50, 60, and 90 seconds.

7.3.1.3 Results & Discussion

Figures 7.6 and 7.7 show the convergence of the estimated coil factors as the sample-set-size is increased from 1 s to 90 s. For short calibration time-frames it is believed the system exhibited nonlinearities associated with the large current gradients required to

| $SensorS/N$ | ρ (deg) | ϕ (deg) | λ (deg) |
|-------------|--------------|--------------|-----------------|
| 159 | -0.34417 | -0.09965 | 0.25455 |
| 161 | -0.01075 | -0.03184 | -0.19319 |
| 315 | -0.78405 | 0.24710 | -0.09915 |
| 316 | -0.79654 | 0.09066 | 0.39563 |
| 317 | -1.29952 | 0.39933 | 0.07478 |
| 322 | -0.28263 | -0.25253 | -0.13953 |
| 386 | -0.28920 | 0.16337 | -0.01491 |
| 387 | -0.35171 | 0.19582 | -0.10789 |
| 388 | -0.12805 | 0.29536 | 0.05781 |
| 389 | -0.17107 | 0.22887 | -0.01739 |
| 390 | -0.17035 | 0.25021 | 0.11852 |
| 391 | -0.22311 | 0.23156 | 0.08445 |
| 392 | -0.25378 | 0.30264 | -0.01593 |
| 418 | -0.27751 | 0.25580 | 0.02654 |
| 419 | -0.20675 | 0.20195 | -0.01028 |
| 420 | -0.27895 | 0.25246 | 0.01144 |
| 421 | -0.23791 | 0.33610 | -0.13507 |

Table 7.3: Bartington sensor orthogonality errors. Shown to ≈ 5 significant figures consistent with Section 5.3.4 for large sample sets.

drive the coils with the calibration signals in a compressed time-frame. For larger data-sets the estimator outputs converged to the results in Figure 7.6, which were within 1% of the theoretically calculated coil factors, validating the modelling in Section 3.1.2.

Figure 7.8 shows the convergence of the orthogonality errors as the sample-set-size is increased. Similarly to the Coil Factors, the Orthogonality estimates converge as the sample-set-size is increased, but not as rapidly as the coil factors. The errors are within the expected fabrication errors of the Ternan coil, and better estimates are believed to be obtainable if larger sample-sizes are taken by either increasing the sampling frequency up to the 50 kHz maximum, or increasing the calibration duration to a few minutes.

7.3 Calibration Experiments

| <i>SensorS/N</i> | b_x (nT) | b_y (nT) | b_z (nT) |
|------------------|------------|------------|------------|
| 159 | 33.57672 | 22.35900 | 0.41812 |
| 161 | 12.03960 | 16.44380 | −4.13686 |
| 315 | −174.50699 | −156.40457 | −178.95622 |
| 316 | −147.12588 | −77.25312 | −126.21145 |
| 317 | −230.59581 | −214.92621 | −306.58141 |
| 322 | −10.28013 | 5.73829 | −2.82243 |
| 386 | −185.77491 | −219.63206 | −197.52151 |
| 387 | −234.02717 | −254.95418 | −229.84132 |
| 388 | −160.93132 | −158.60122 | −208.77428 |
| 389 | −258.03338 | −236.03616 | −199.25907 |
| 390 | −187.44494 | −227.44446 | −201.38858 |
| 391 | −238.83838 | −255.40458 | −221.76330 |
| 392 | −231.59662 | −232.21947 | −223.22166 |
| 418 | −187.21094 | −207.46959 | −206.52609 |
| 419 | −187.64405 | −231.71029 | −221.83179 |
| 420 | −221.85912 | −217.47157 | −211.56249 |
| 421 | −214.83496 | −207.11894 | −220.55367 |

Table 7.4: Bartington sensor bias errors. Shown to ≈ 5 significant figures consistent with Section 5.3.4 for large sample sets.

Out of curiosity a TWOSTEP calibration was performed between the theoretical drive voltage signal at the amplifier output, and the current passing through the coils. It was found the output represented a matrix with diagonal elements equal to the series resistance of the coils and reference resistors, and the non-diagonal elements showing the coupling between the respective coil axes. Similarly to the coil factors these results converged very rapidly, as shown in Figure 7.9.

From the above results it is evident a 10 s calibration converges sufficiently to enable comparison of datasets as other parameters are varied, but for a true coil calibration, a 30 to 90 s duration or greater is recommended.

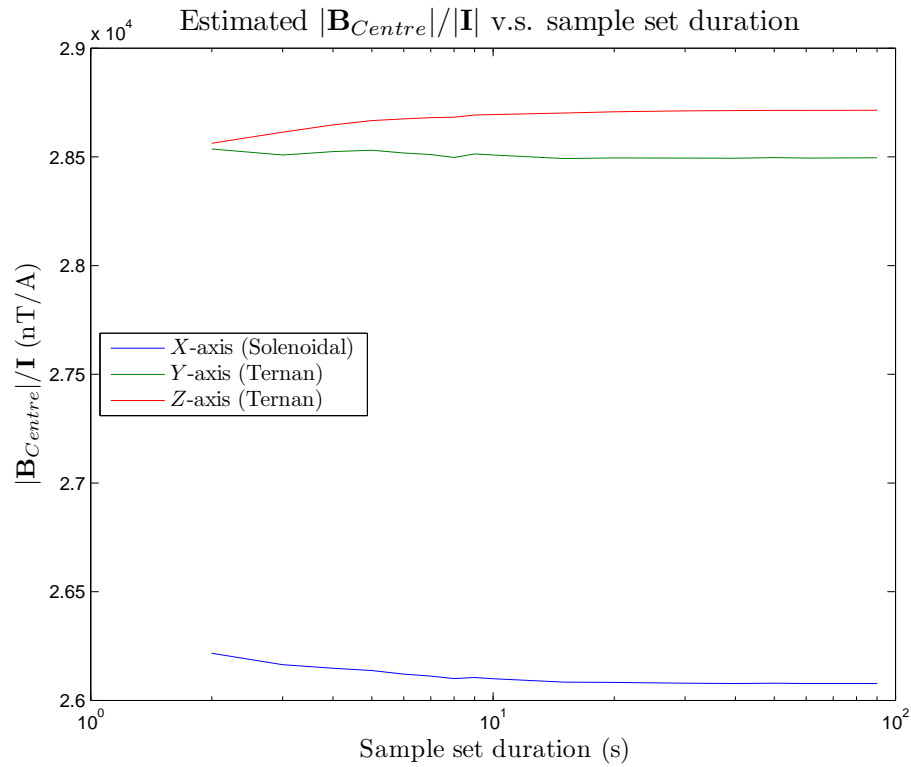


Figure 7.6: Coil factors converging to a stable value as sample-set-size is increased.

7.3.2 B field predictions

7.3.2.1 Aim

To predict the generated field based on the drive signal (voltage or current) and the calibration matrix, using the stimulation signal described in Section 7.1.2 Figures 7.3 and 7.4.

7.3.2.2 Method

The drive signals from the data-sets measured in the coil calibration experiments were re-processed using the calibration matrix ($D + I$) derived from: the 90 second data-set, each individual data-set and the calibration matrix defined by the coil factors theoretically derived in Section 3.1.2.

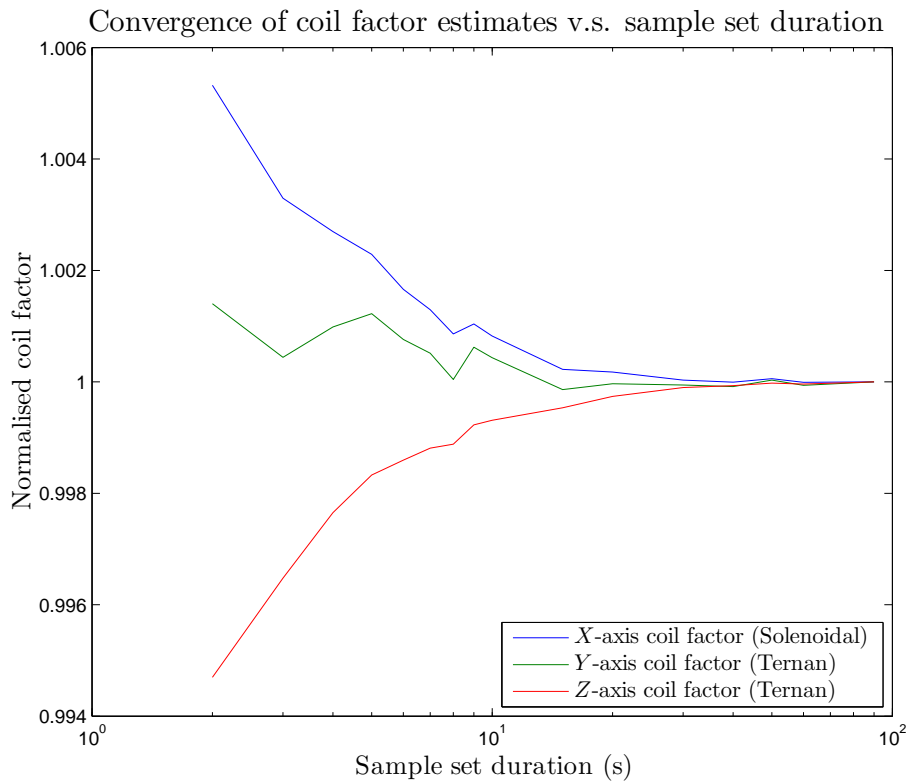


Figure 7.7: Coil factors normalised with respect to the values estimated by the 90 s dataset.

7.3.2.3 Results & Discussion

Figure 7.10 shows the RMS value of the magnetic field measured by the reference sensor (located at the centre of the Ternan coil) taken away from the predicted field based on the theoretically derived coil factors, the calibration matrix derived for the individual data-sets, and the calibration matrix derived using the 90 second data-set. The 90 second data-set calibration matrix outperforms the theoretically derived matrix, and matches the results for the data-set specific matrices at large duration data-sets and outperforms them for shorter time-frames. Figures 7.11 and 7.12 show the error in the predicted fields, for the 4 and 40 second data-sets, they appear to indicate the greatest prediction errors are where there are the greatest magnetic field gradients in the signal. This is likely due to small phase offsets between the signals, being most evident for fast changing signals. Note the large oscillations in the theoretical curves (green) in Figures 7.11 and 7.12, are caused by the theoretical coil factors deviating from reality.

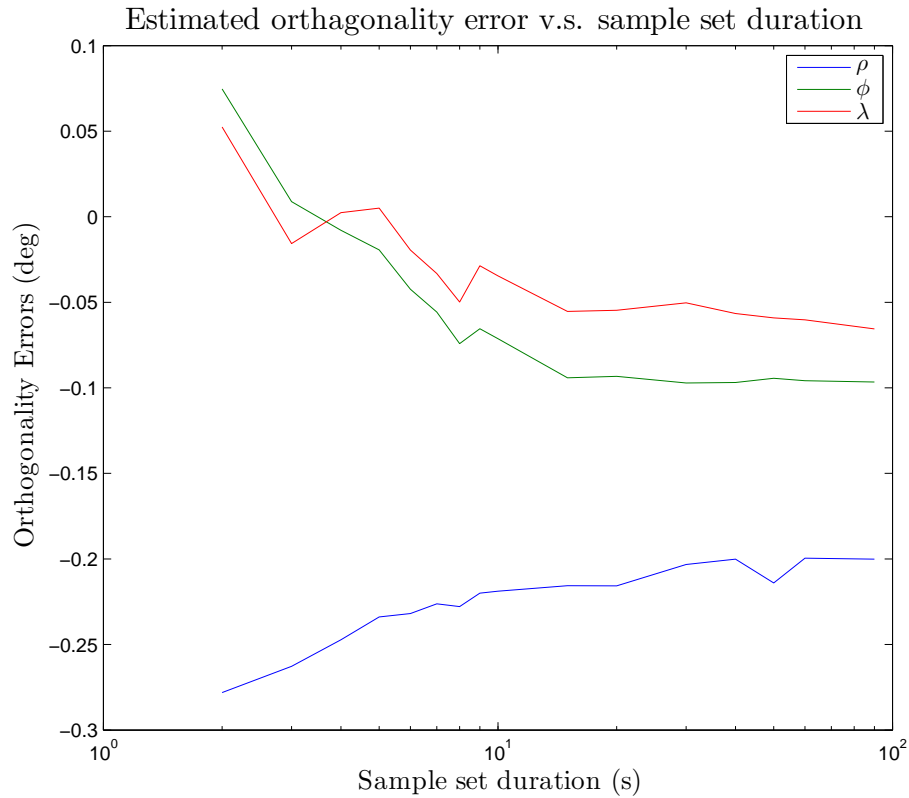


Figure 7.8: Orthogonality errors converging to stable values as set-size is increased. Convergence is not as rapid as that of the coil factors.

Figures 7.13, 7.14 and 7.15 show the output field can be more effectively predicted from the measured current flowing through the coil, than from the voltage driving the signal amplifiers. This is mostly likely due to small fluctuations of either the drive voltage seen by the amplifier, or of the amplifier output. Any voltage fluctuations in the amplifier were captured by the current measurement leading to a more accurate prediction of the generated magnetic field.

This means for high precision magnetic field generation, a feedback system will still be necessary to maintain a desired magnitude, and compensate for minor fluctuations.

Sudden jumps in the magnetic field predictions with respect to voltage shown in Figure 7.15 have been tracked down to originating from the x -axis coil prediction. Figure 7.16 shows a sudden jump in the measured current which coincides with the jumps in the predicted field. This is believed to be an effect of the amplifier not being optimised to drive high inductance loads.

7.3 Calibration Experiments

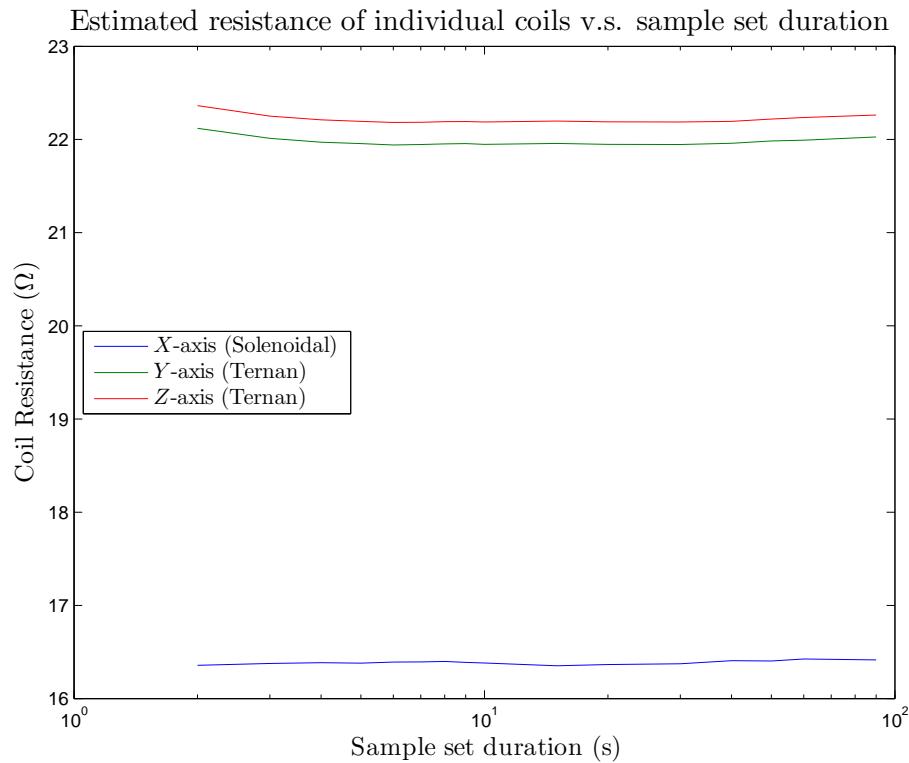


Figure 7.9: Estimated system resistance viewed from the amplifier output as sample-set-size is increased.

The remaining noise appears to be principally 50 Hz noise introduced into the system by un-shielded wires driving the amplifiers. The noise floor within the facility was 17.5 nT peak to peak.

7.3.3 Analog filter impacts

7.3.3.1 Aim

To excite the coil with and without filters, to investigate changes in calibration accuracy if noise is reduced.

7.3.3.2 Method

The coil system was connected as detailed in Figure 7.1, with the sensor array placed at the end of the coil. The coil was allowed to warm up for a few minutes by running

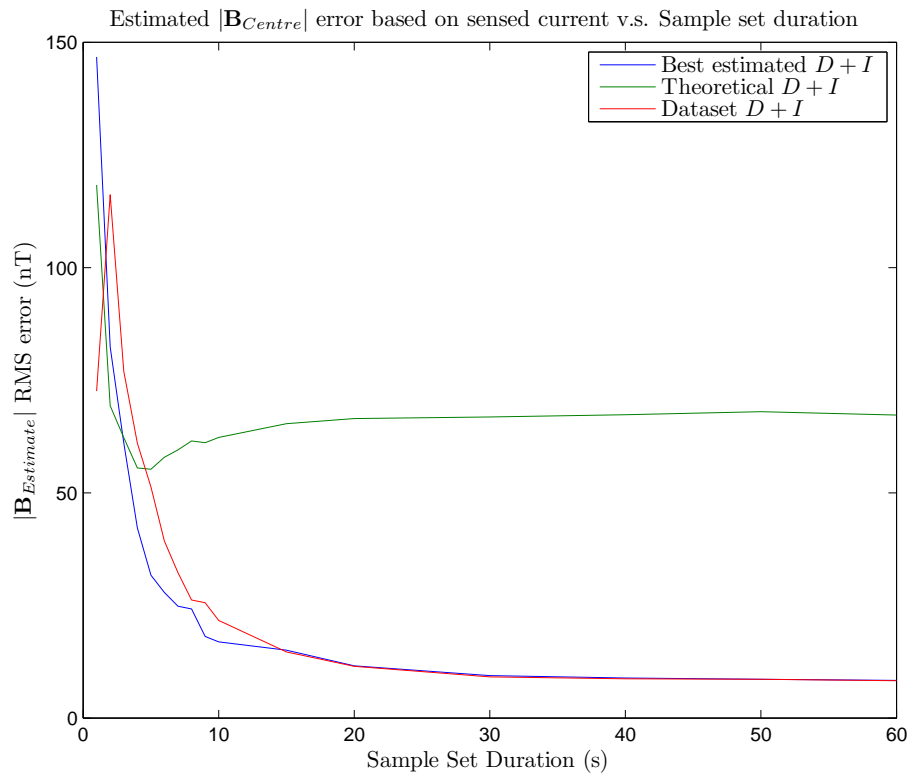


Figure 7.10: RMS error of field prediction using theoretical and estimated calibration matrices.

an offset current before and between measurements. Measurements were taken at the Bartington SCU-1 filter settings shown in Table 7.5.

Note that in this and subsequent measurements sets, the sense resistors for the x -axis and y -axis were shorted due to a loose connection, the resulting coupling changes the resultant coil factors with respect to the drive voltage, since the system resistance is reduced by $\sim 0.5\Omega$, and there is an increase in coupling between the two axes. Hence the subsequent figures are referenced to the system drive voltage, and whilst the coil factors and couplings are slightly different to those measured prior to the reference resistors shorting, the results are not invalidated.

7.3.3.3 Results & Discussion

Figures 7.17 and 7.18 show the estimated orthogonality errors and coil factors for each of the filter settings respectively. It is evident the bandpass filters cause the estimator to generate spurious results, this is likely caused by the oscillations introduced by the

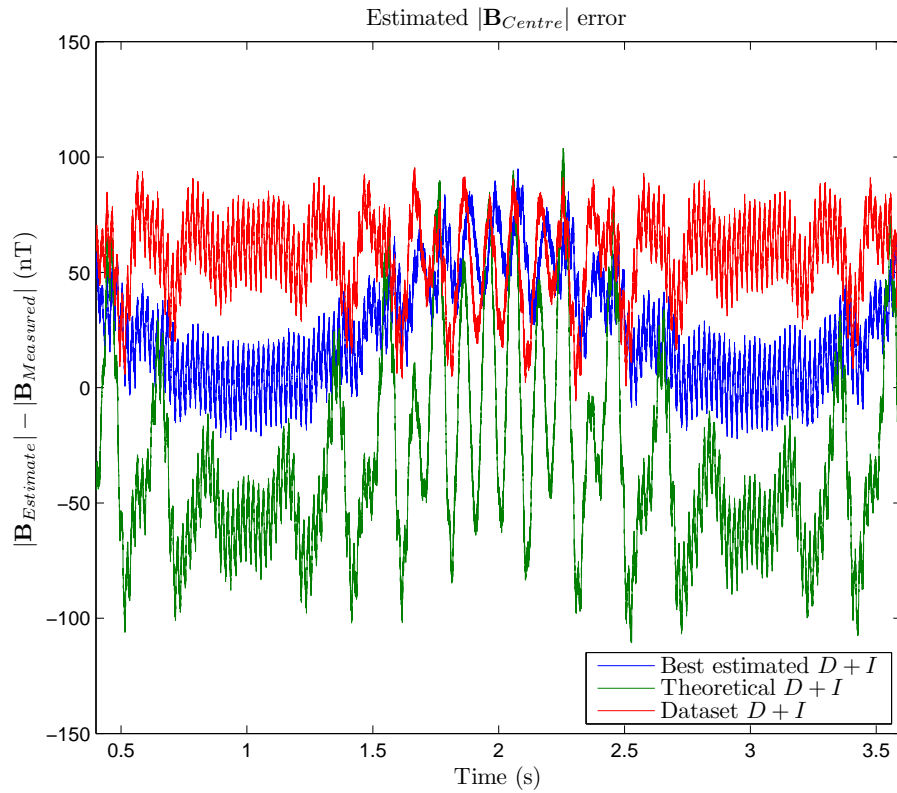


Figure 7.11: $|\mathbf{B}_{centre}| - |\mathbf{B}_{estimated}|$ using theoretical and estimated calibration matrices. 4 second calibration.

| Description | LPF (Hz) | HPF (Hz) |
|-------------|----------|----------|
| APF | N/A | N/A |
| LPF1 | 1000 | 0 |
| LPF2 | 100 | 0 |
| LPF3 | 10 | 0 |
| LPF4 | 1 | 0 |
| BPF1 | 10 | 0.01 |
| BPF2 | 100 | 0.01 |
| BPF3 | 1,000 | 0.01 |
| BPF4 | 10,000 | 0.01 |

Table 7.5: Bartington SCU-1 filter settings (3dB) used in experiment.

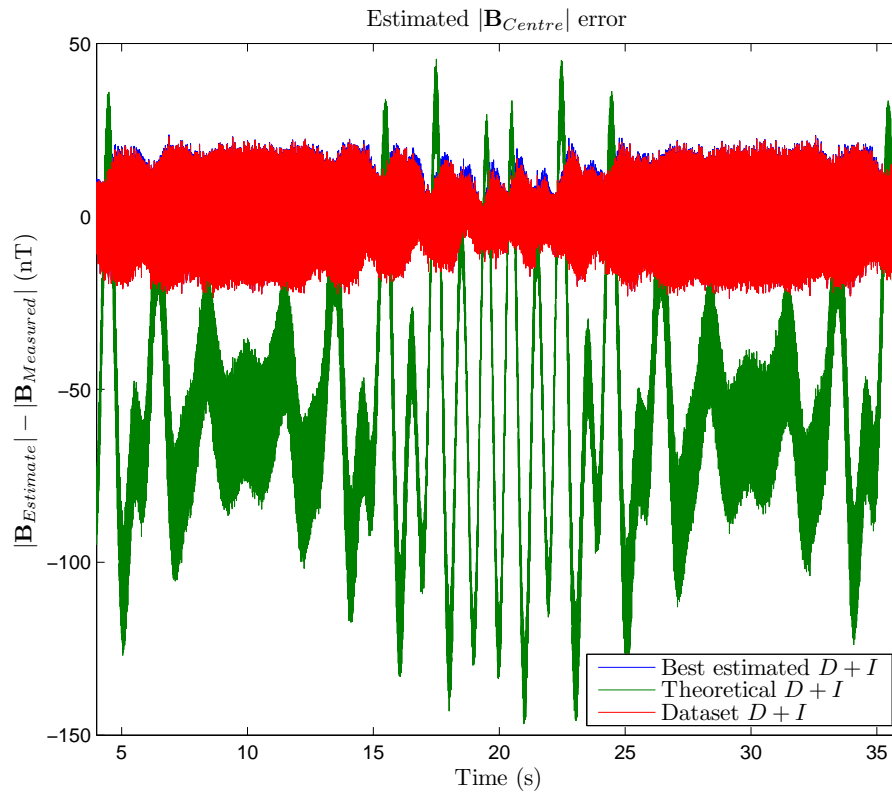


Figure 7.12: $|\mathbf{B}_{centre}| - |\mathbf{B}_{estimated}|$ using theoretical and estimated calibration matrices. 40 second calibration.

bandpass filters whenever there is a large gradient within the field, as shown in Figure 7.19. The LPF4 data-set generated incorrect results due to the filter removing the majority information present in the stimulating field.

Focusing in on data-sets APF, and LPF1-3, Figures 7.20 and 7.21 show the filtering does not have a major impact on the estimation of coil factors, but the angles are affected as the low-pass filter corner frequency is lowered. LPF3, the only filter which eliminates 50 Hz noise also affects the orthogonality error estimation, increasing the estimated errors.

From Figure 7.22, it appears filters LPF1-3 all track the APF extremely well, but if observed close up as shown in Figures 7.23 and 7.24, the filtering causes significant diversions from the true signal at inflection points, and generally a small delay in the signal.

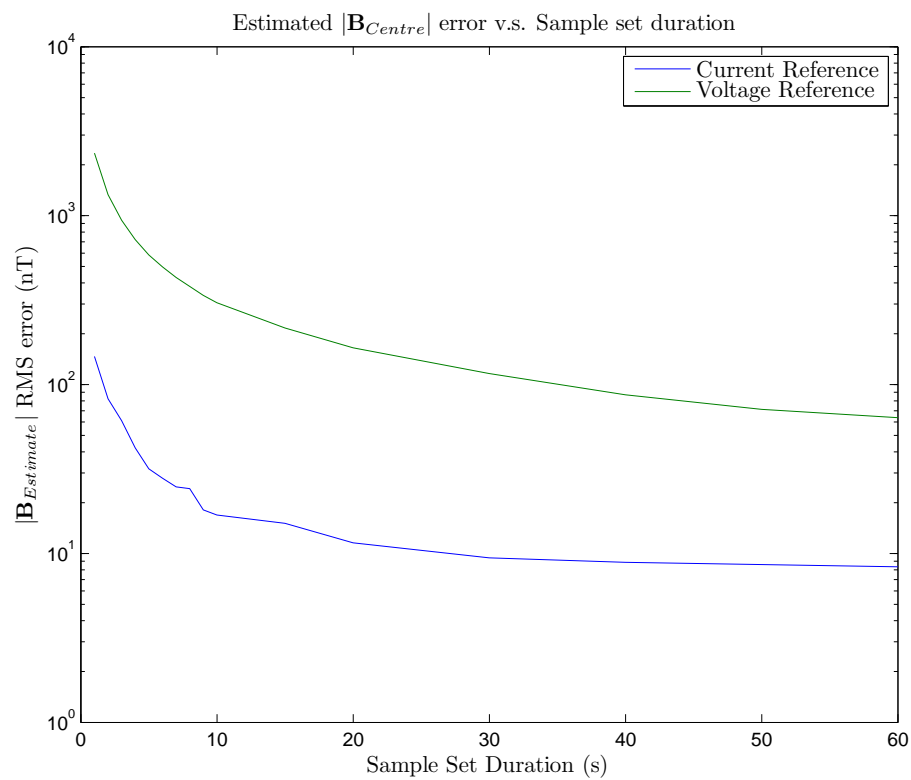


Figure 7.13: RMS error of field prediction using estimated voltage and current referenced calibration matrices.

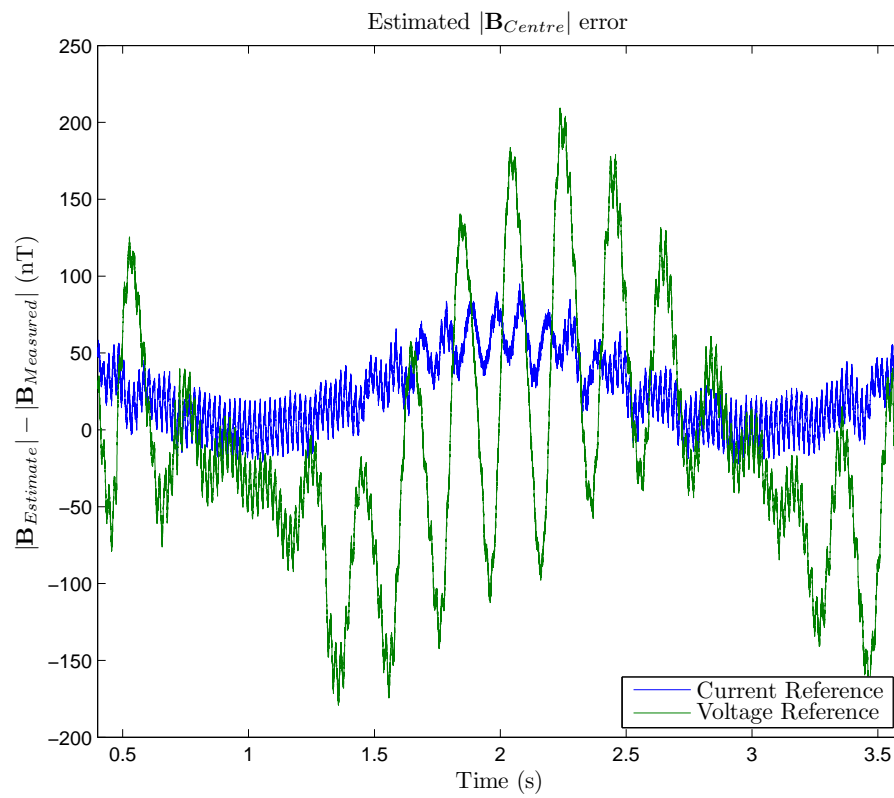


Figure 7.14: $|\mathbf{B}_{centre}| - |\mathbf{B}_{estimated}|$ using voltage and current referenced calibration matrices. 4 second calibration.

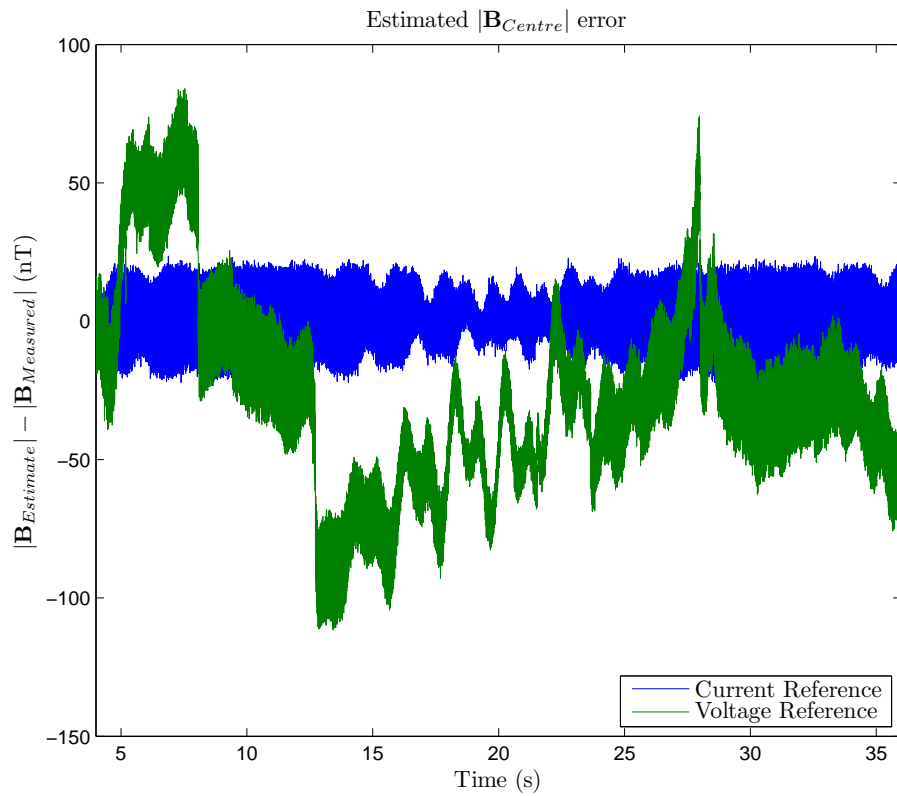


Figure 7.15: $|\mathbf{B}_{centre}| - |\mathbf{B}_{estimated}|$ using voltage and current referenced calibration matrices. 40 second calibration.

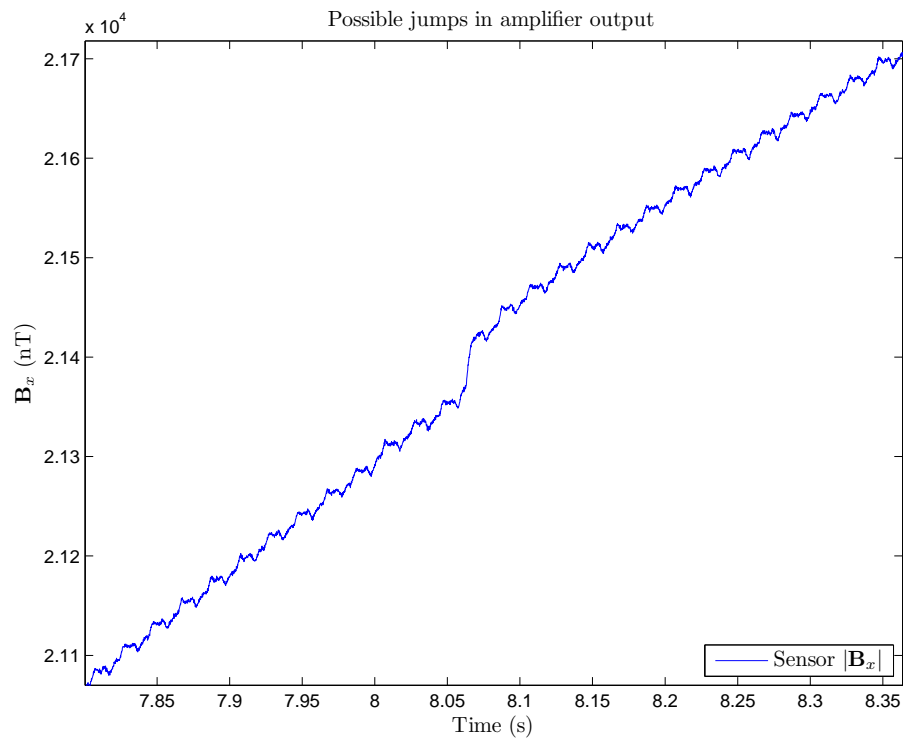


Figure 7.16: Unexpected step increase in the current flowing in the x -axis coil.

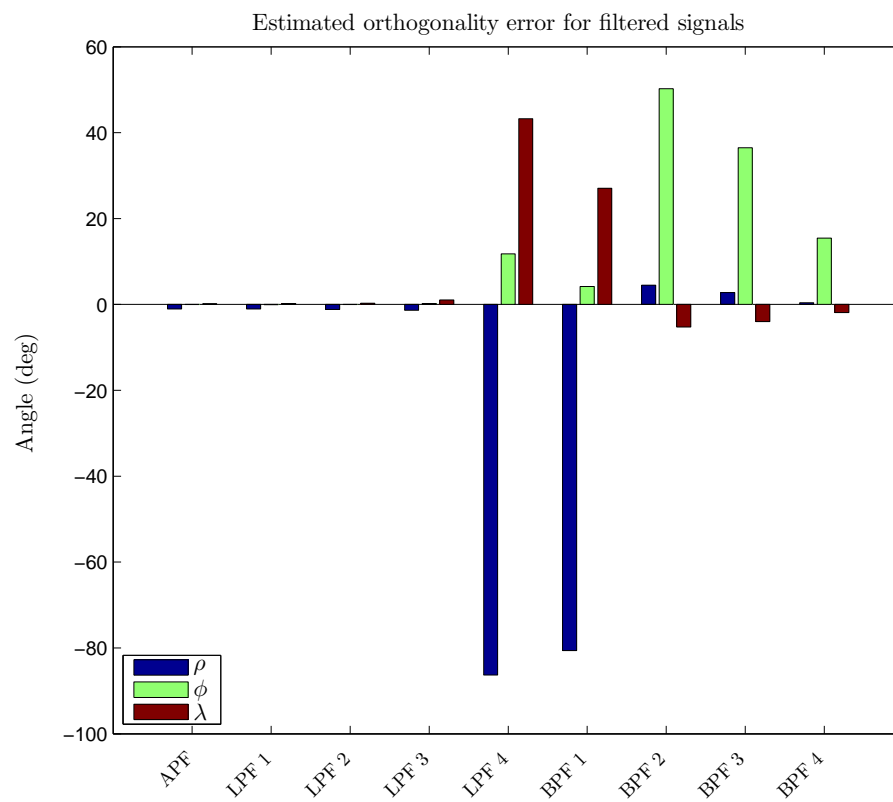


Figure 7.17: Estimated orthogonality errors within the Ternan coil system, using a variety of analog filters.

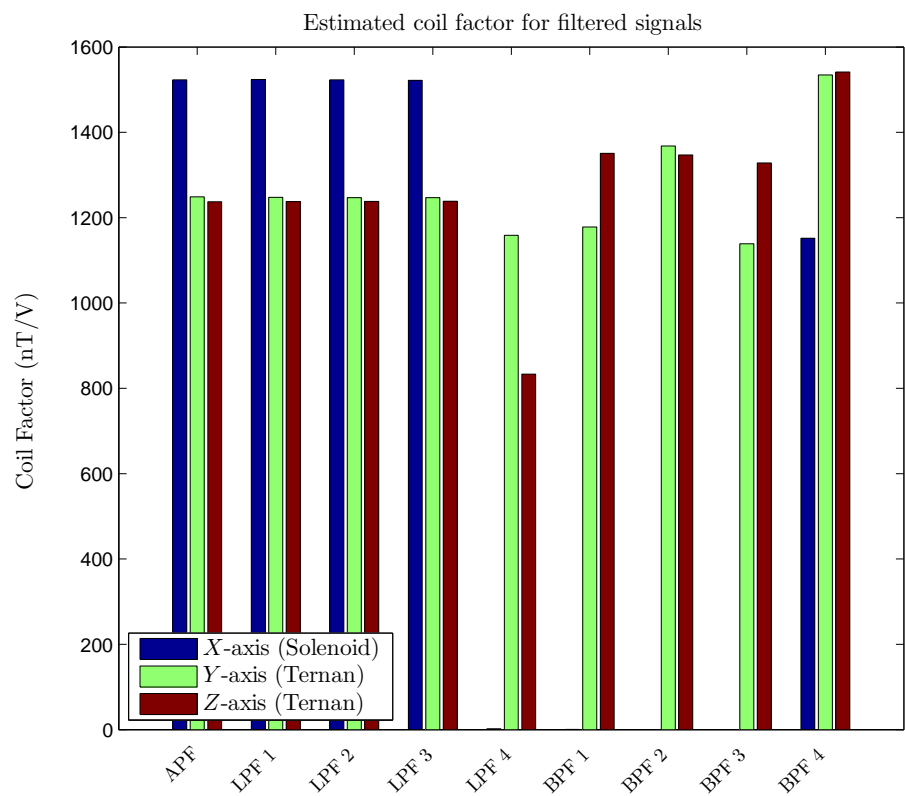


Figure 7.18: Estimated coil factors within the Ternan coil system, using a variety of analog filters.

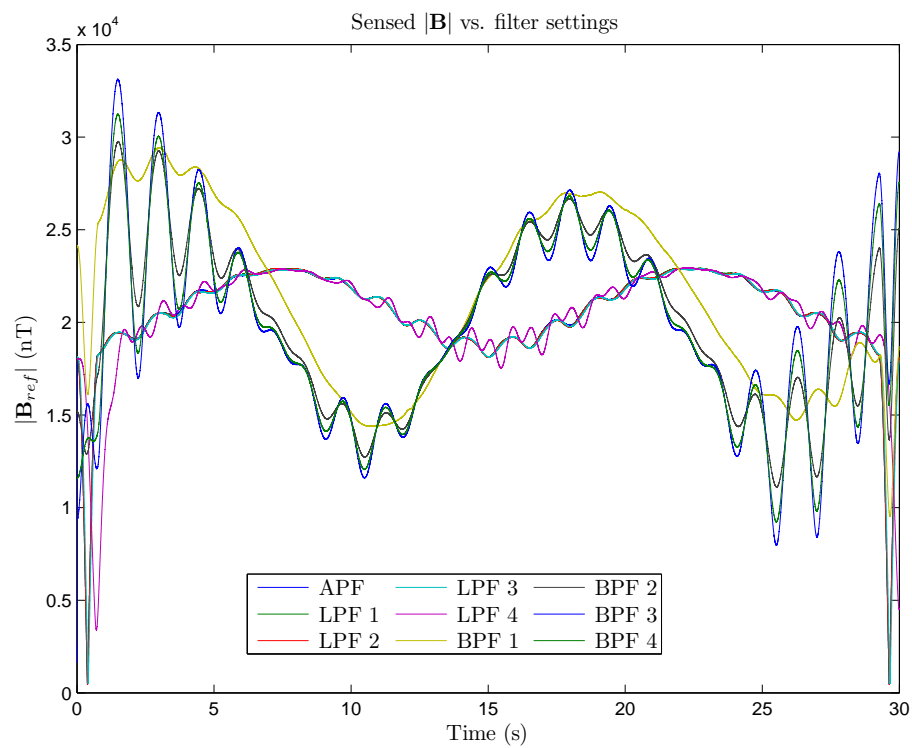


Figure 7.19: Recorded $|B_{centre}|$ data, using a variety of analog filters.

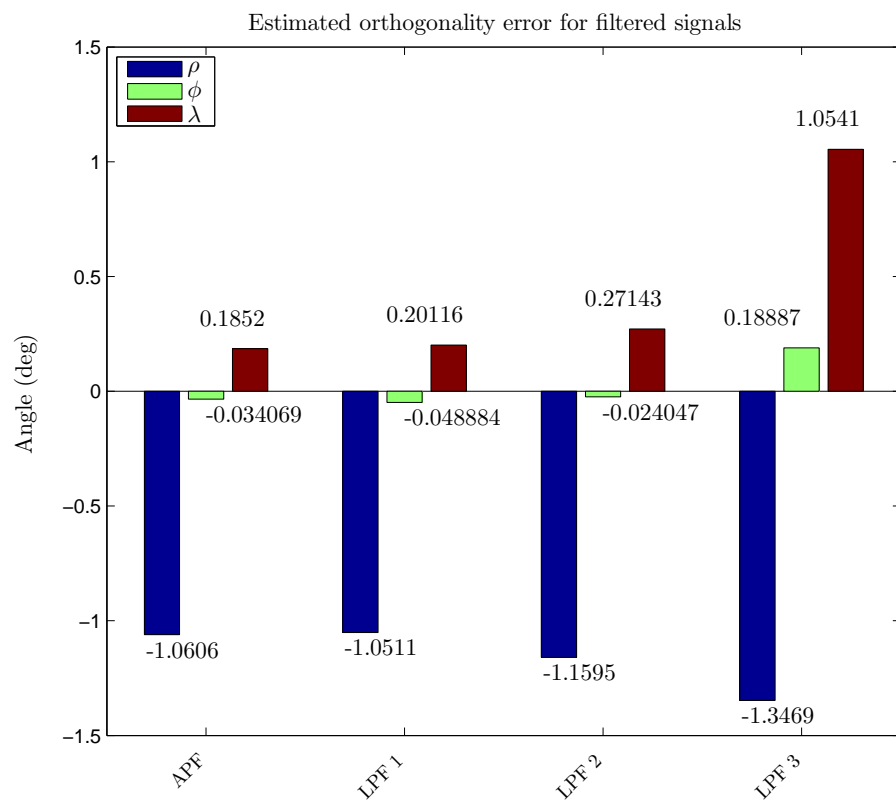


Figure 7.20: Estimated orthogonality errors within the Ternan coil system, using an all-pass-filter and some low-pass-filters.

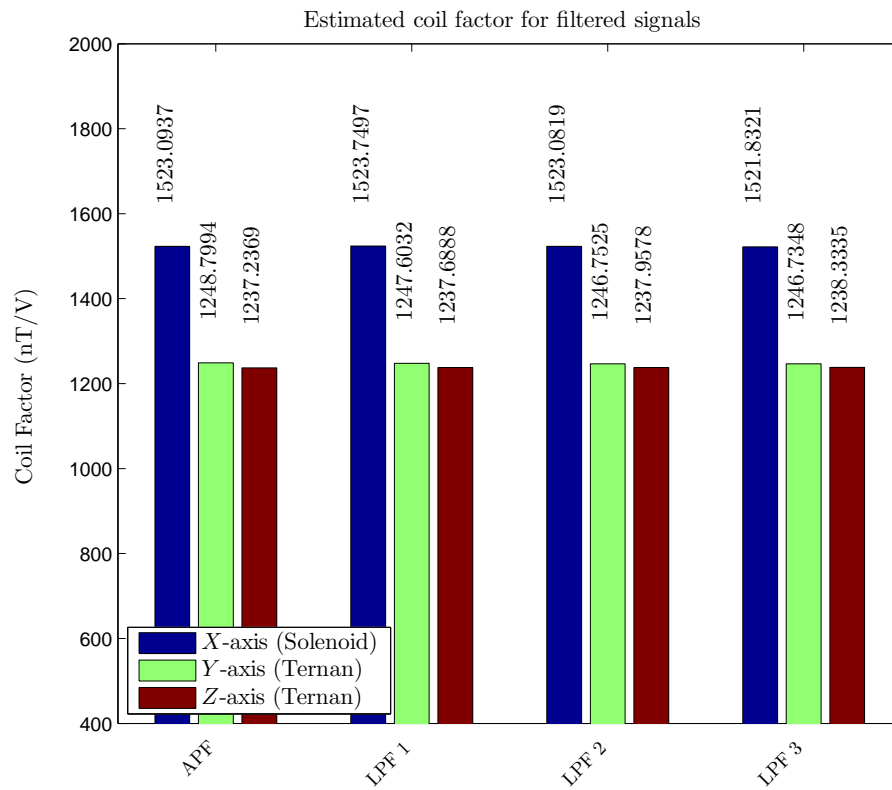


Figure 7.21: Estimated coil factors within the Ternan coil system, using an all-pass-filter and some low-pass-filters.

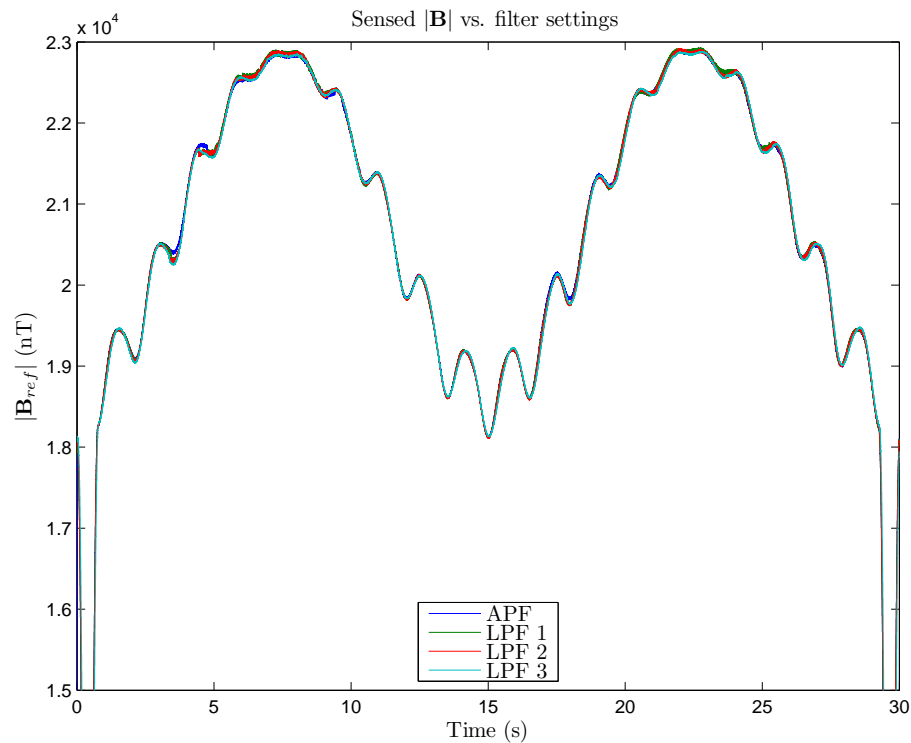


Figure 7.22: Recorded $|\mathbf{B}_{centre}|$ data, using an all-pass-filter and some low-pass-filters.

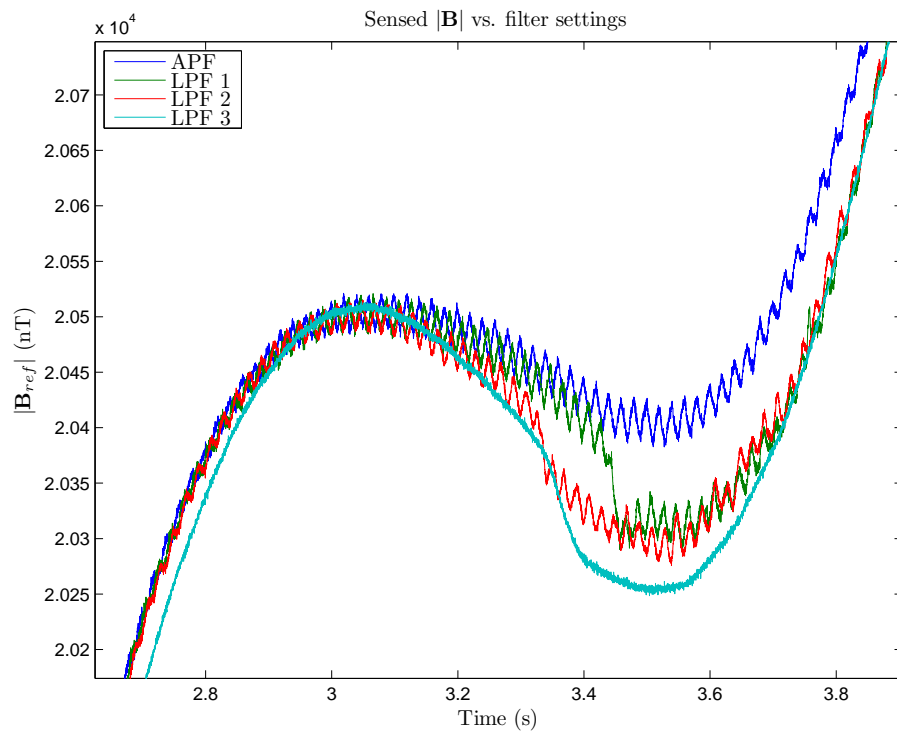


Figure 7.23: Filter-induced deviation from the unfiltered (APF) magnetic signal.

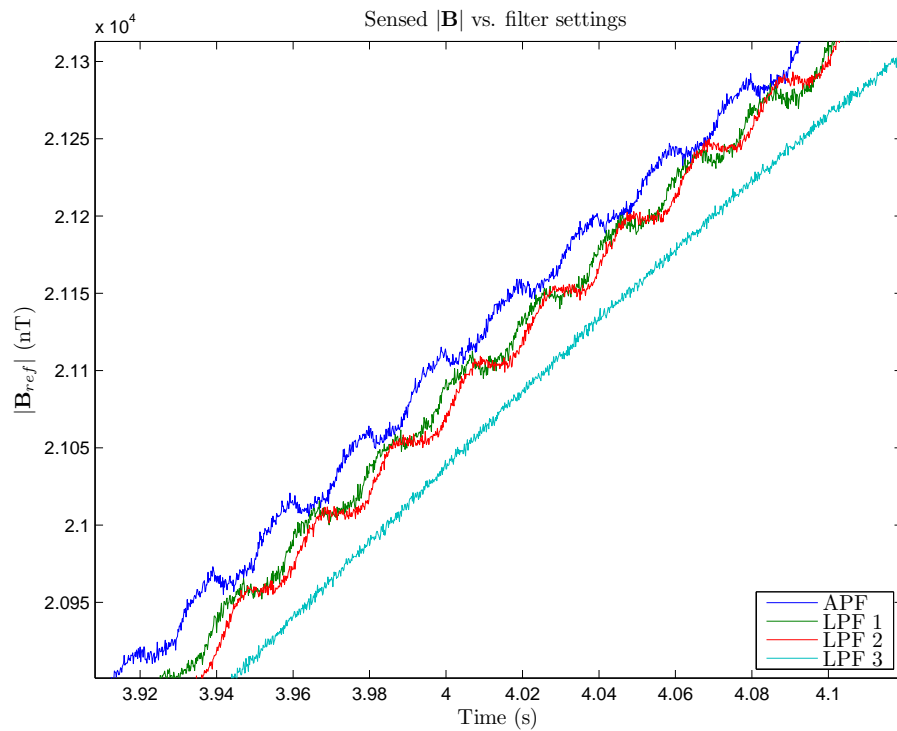


Figure 7.24: Filter-induced temporal delay of signals.

From the above data it is evident filtering has the potential to adversely affect the estimator, but when the cut-off frequency is lowered sufficiently to remove the predominant noise source (50 Hz interference) the calibration signals are also affected. An extension of the calibration signal duration should lower the calibration signal component frequencies sufficiently to be unaffected by the filters, but for such signal durations the estimators will have already converged to stable values due to the sample-set-size.

While it sounds counter-intuitive it would appear the estimator performs better without any filtering, or only sufficient filtering to remove signals above the Nyquist frequency of the sampling system.

7.4 Coil Property Measurements

7.4.1 Coil frequency response

7.4.1.1 Aim

To measure the generated magnetic field with respect to the drive voltage as the frequency is changed.

7.4.1.2 Method

The coil system was connected as detailed in Figure 7.1, with the sensor array placed at the end of the coil. The coil was allowed to warm up for a few minutes by running an offset current before and between measurements. The frequency was changed from 1 to 90 Hz, stimulating each axis coil sequentially, generating independent sets of measurements for each coil.

7.4.1.3 Results & Discussion

Figure 7.25 shows the coil factor with respect to the drive voltage decreases as the drive frequency is increased. Figure 7.26 shows the 3 dB point of the system is 80 Hz. The attenuation observed in Figures 7.25 and 7.26 is due to the amplifier's inability to drive the inductive load at high frequencies.

Figure 7.27 shows the phase response of the system between the drive voltage at the amplifier input, and the reference sensor as the frequency is increased. The phase change is principally attributable to a ~ 8 ms delay introduced by the amplifier.

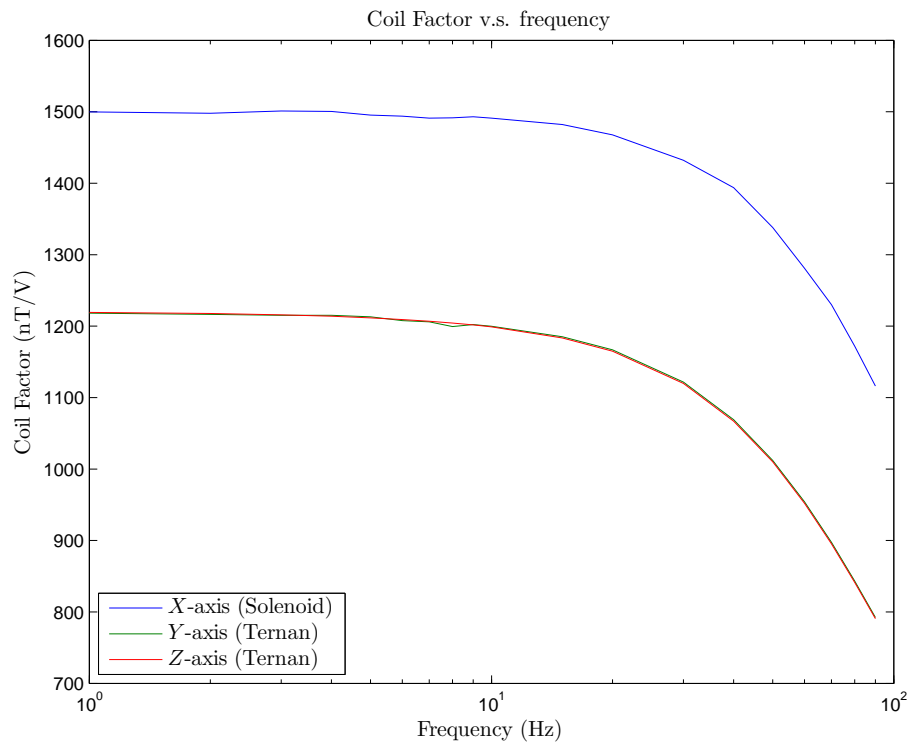


Figure 7.25: Coil factors for Ternan coil system as frequency is increased from 1 Hz to 90 Hz. Coil factors are with respect to the amplifier drive signal.

7.4.2 Uniformity

7.4.2.1 Aim

To measure the uniformity of the magnetic field generated by the magnetic coil system (Coil length of 8 m, and diameter of 2 m).

7.4.2.2 Method

The coil system was connected as detailed in Figure 7.1, with the sensor array placed at the centre of the coil. The coil was allowed to warm up for a few minutes by running an offset current before and between measurements. The frequency of the drive signal was set to 3 Hz, stimulating each axis coil sequentially, generating independent sets of measurements for each coil. After each measurement the array of sensors was moved a small distance (~ 5 cm) along the x -axis toward the end of the coil (shown in Figure 7.28). The reference sensor remained at the centre of the coil, to enable the relative

7.4 Coil Property Measurements

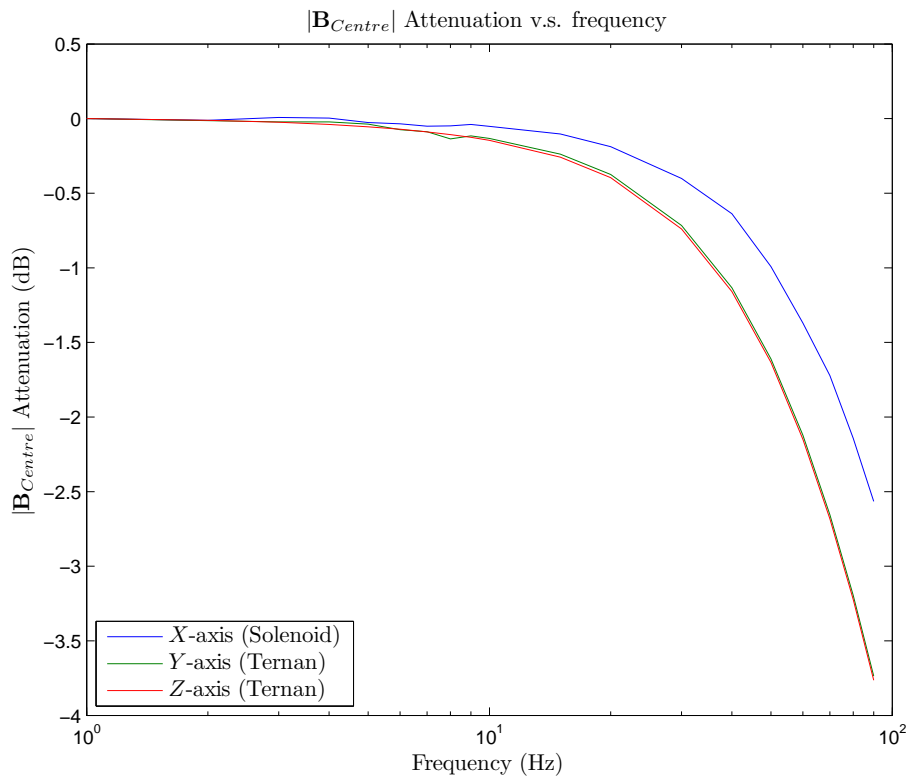


Figure 7.26: Attenuation of generated magnetic field for the Ternan coil system as frequency is increased from 1 Hz to 90 Hz.

variation in field amplitude to be measured as the array of sensors is moved along the x -axis.

7.4.2.3 Results & Discussion

Figure 7.29 shows the x -axis coil has a large ripple on it correlated to the spacing of the coil segments forming the solenoid, with the sensors closest to the boundary showing the ripple most strongly. Figures 7.30 and 7.31 show the y -axis and z -axis coils exhibit smooth uniformity transitions as the sensors are moved along the x -axis, with a large drop-off at ~ 3 m from the coil centre.

Figure 7.32 shows the magnitude of the magnetic field generated by each coil, for situations where only magnetic field amplitude uniformity is necessary, this graph indicates a cylindrical object up to 2.5 m long and 50 cm in diameter can be placed into a 0.5% uniformity field, assuming symmetric field uniformity along the x -axis.

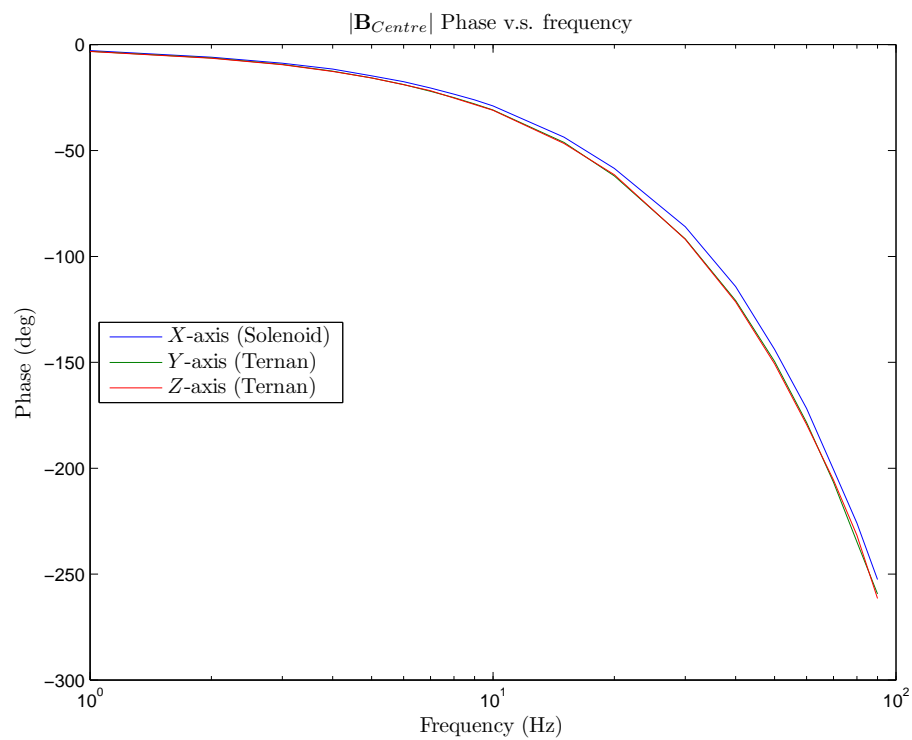


Figure 7.27: Phase delays in the Ternan coil system as frequency is increased from 1 Hz to 90 Hz. Delays are with respect to the amplifier drive signal.



Figure 7.28: Trolley and array of sensors at end of coil.

7.4 Coil Property Measurements

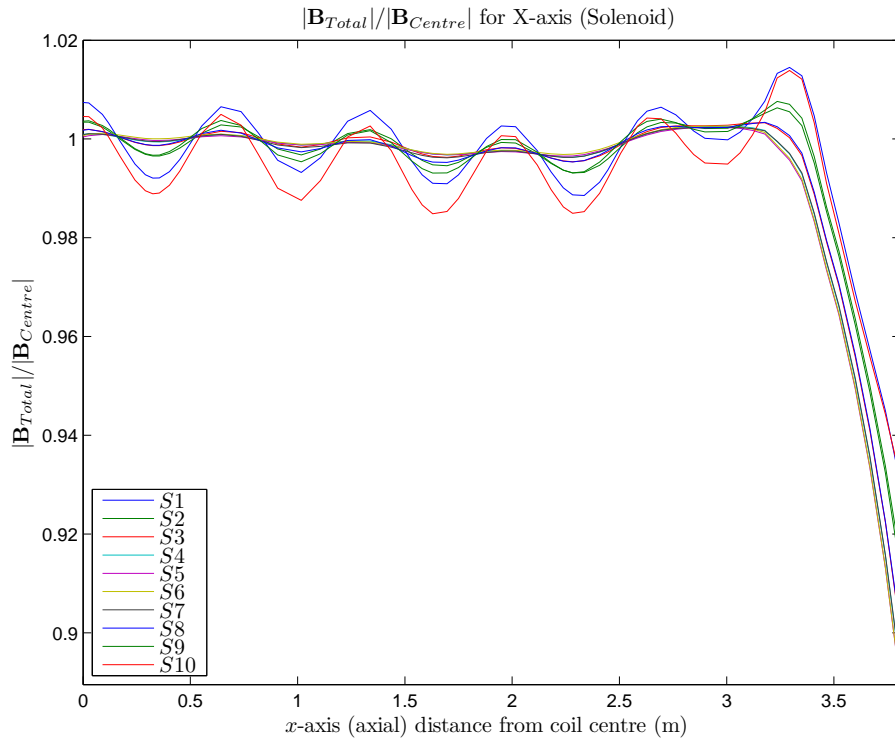


Figure 7.29: Total Field strength for 3Hz \mathbf{B}_x signals, sensors placed parallel to y -axis (Table 7.1) and moved along x -axis.

Figure 7.33 shows a much more stringent definition of magnetic field uniformity, where the variations from the desired signal components are added vectorially, as in equation (3.12). In this case it appears only a $\sim 1\%$ field uniformity can be obtained.

Figure 7.34 shows the \mathbf{B}_x , \mathbf{B}_y and \mathbf{B}_z fields generated when only stimulating the x -axis coil. The \mathbf{B}_y generated appears much closer to zero than the \mathbf{B}_z generated, indicating the non-uniformity is likely caused by a slight error in the sensor alignment with the coils, hence the $\sim 1\%$ uniformity claimed above is likely an overestimate.

Fig. 7.35 and 7.36 show the \mathbf{B}_x , \mathbf{B}_y and \mathbf{B}_z fields generated when only stimulating the y -axis and z -axis coils respectively. Note that the \mathbf{B}_y and \mathbf{B}_z 1% boundary agree with the shape generated by computer modelling in Section ???. The slight asymmetry along the y -axis in Fig. 7.35 (bottom) is believed to be due to a minor error in the placement of the sensors on the trolley.

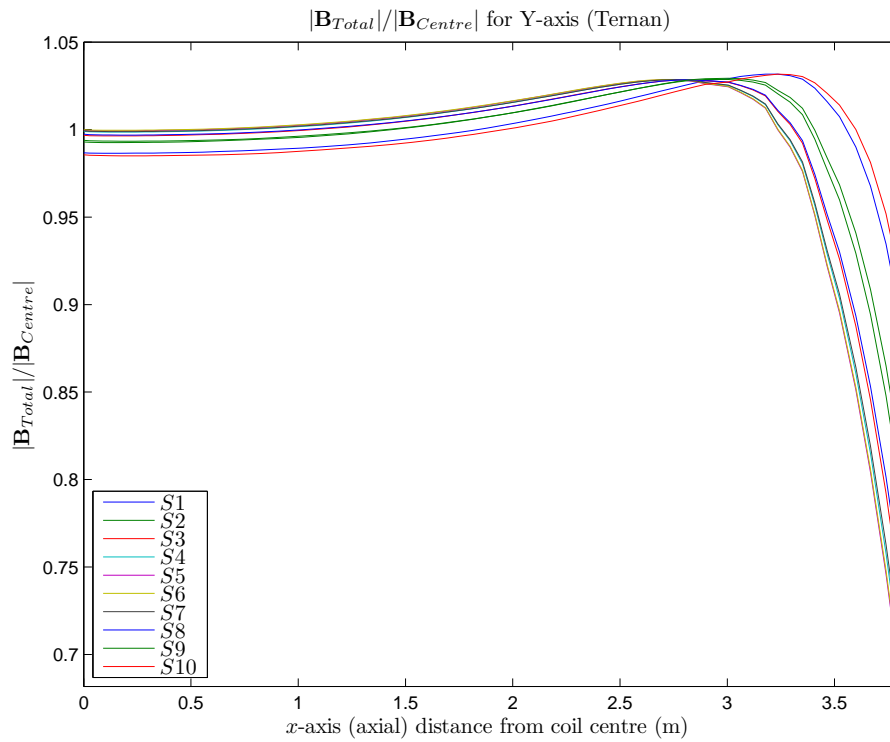


Figure 7.30: Total Field strength for 3Hz \mathbf{B}_y signals, sensors placed parallel to y -axis (Table 7.1) and moved along x -axis.

The Ternan coil has been demonstrated to generate a large long volume of uniformity, and will be suitable for a variety of ranging, calibration and measurement experiments run by DSTO.

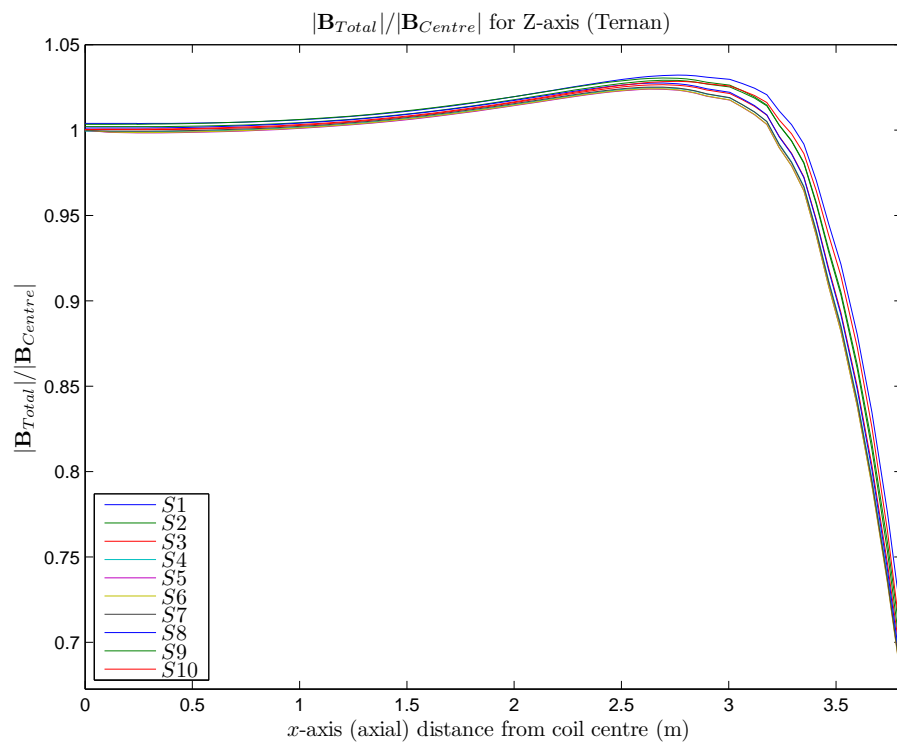


Figure 7.31: Total Field strength for 3Hz B_z signals, sensors placed parallel to y -axis (Table 7.1) and moved along x -axis.

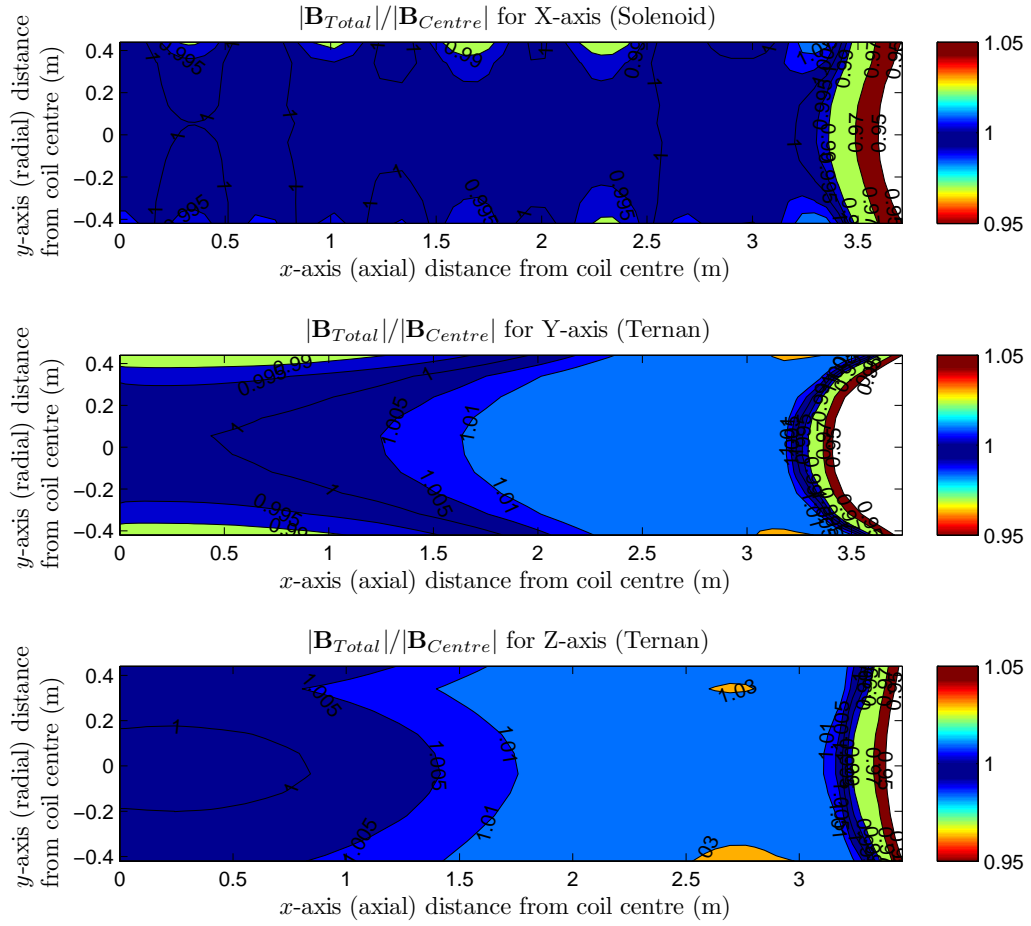


Figure 7.32: Total Field contour plot for 3 Hz B_x , B_y and B_z coil signals. Sensors were placed parallel to y -axis (Table 7.1) and moved along x -axis.

7.4 Coil Property Measurements

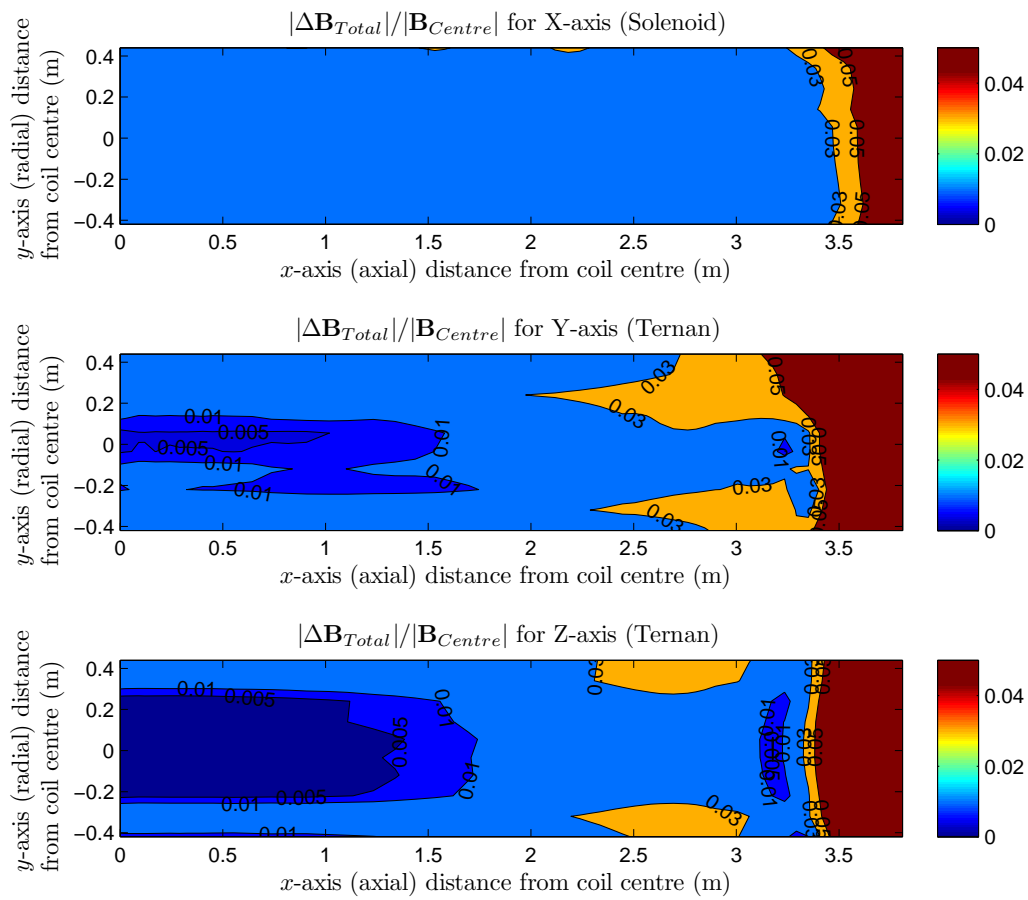


Figure 7.33: Total Field error contour plot for 3 Hz \mathbf{B}_x , \mathbf{B}_y and \mathbf{B}_z coil signals. Sensors were placed parallel to y -axis (Table 7.1) and moved along x -axis.

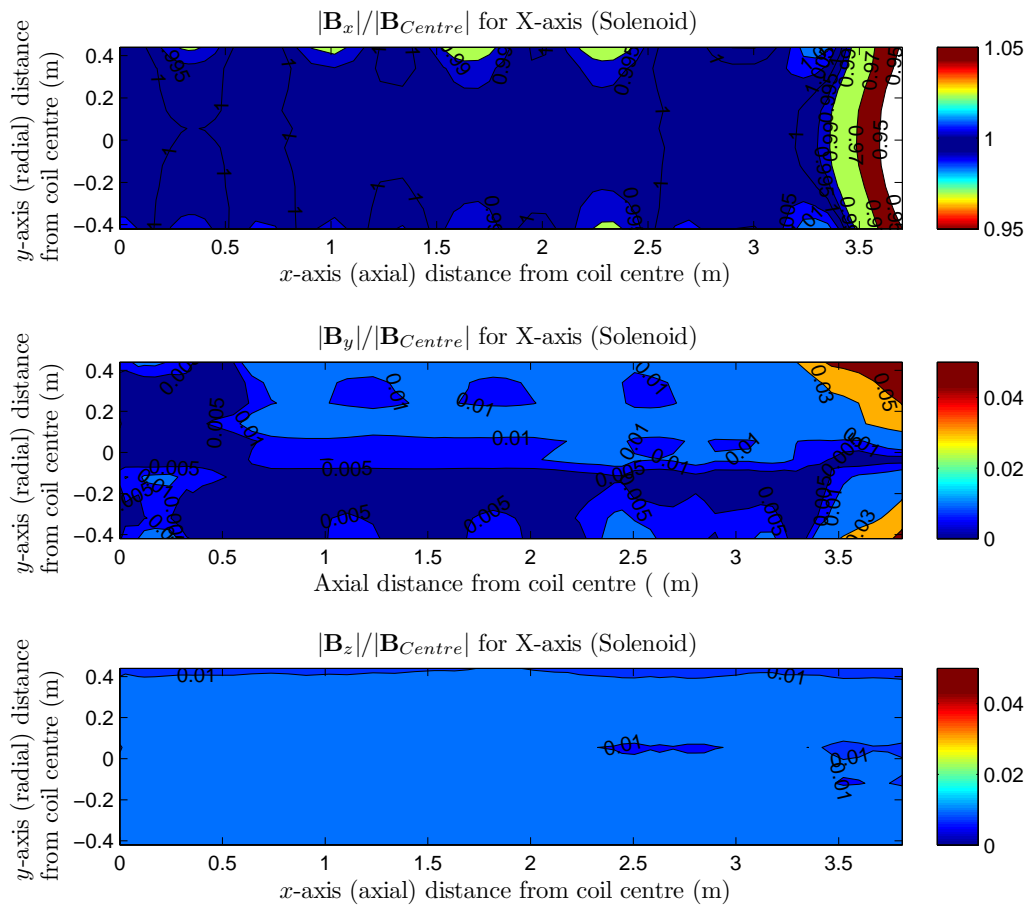


Figure 7.34: B_x , B_y and B_z contour plot for 3 Hz B_x coil signals. Sensors were placed parallel to y -axis (Table 7.1) and moved along x -axis.

7.4 Coil Property Measurements

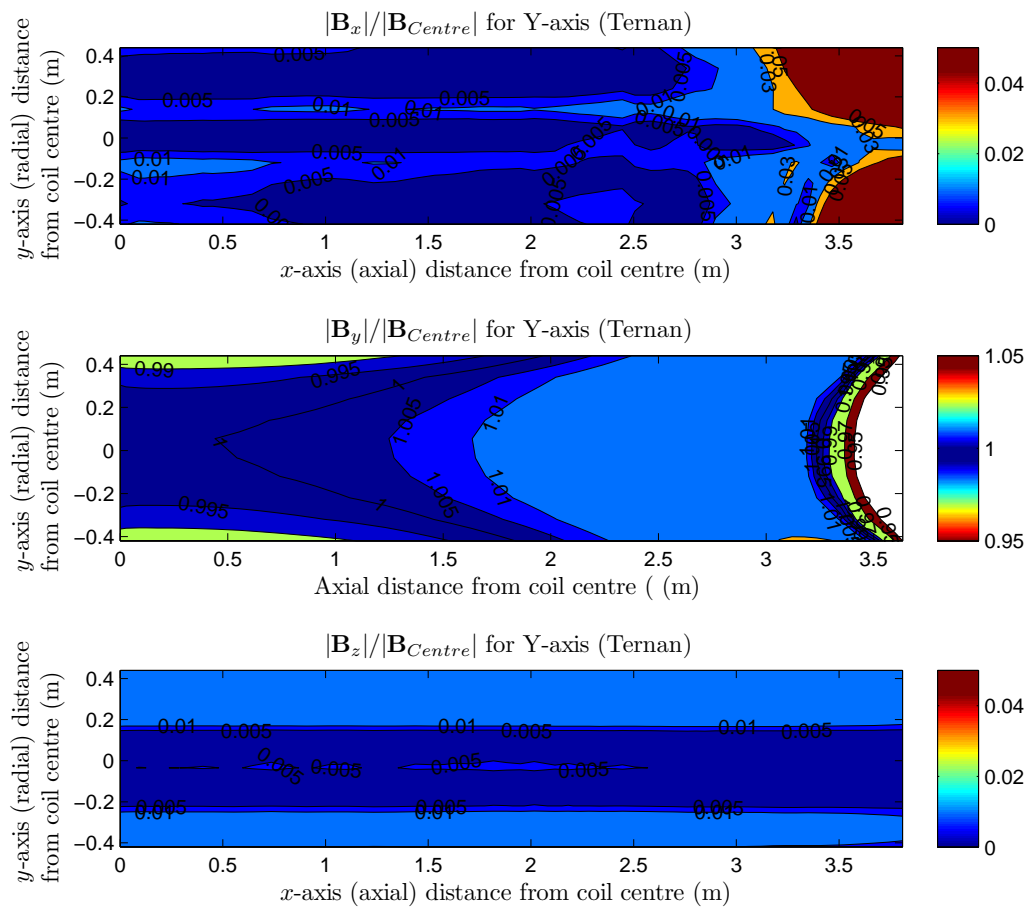


Figure 7.35: B_x , B_y and B_z contour plot for 3 Hz B_y coil signals. Sensors were placed parallel to y -axis (Table 7.1) and moved along x -axis.

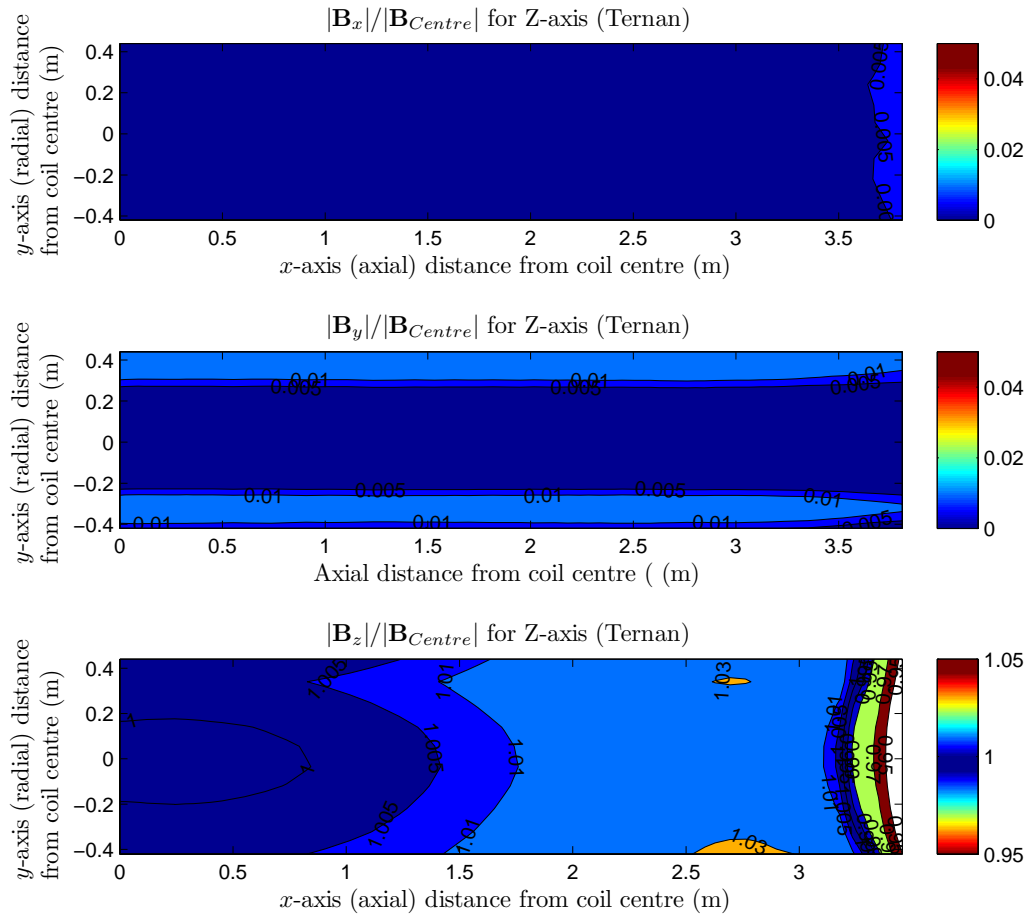


Figure 7.36: B_x , B_y and B_z contour plot for 3 Hz B_z coil signals. Sensors were placed parallel to y -axis (Table 7.1) and moved along x -axis.

Chapter 8

Conclusions

This thesis investigated existing magnetometer calibration estimators, implemented them in MATLAB and bench-marked their performance to select the most computationally fast algorithm. The magnetometer calibration models were extended to enable their use for the calibration of triaxial magnetic coil systems.

The best performing estimator was field tested against both magnetometers, and magnetic coils, in both cases converging to a fixed solution using relatively small datasets. Estimated calibration matrices were shown to improve the prediction of generated magnetic fields when compared to theoretically derived coil factors. Analog filtering was used to reduce interfering noise sources, but was found to introduce phase delays and distortions into the signals, degrading rather than enhancing results.

Additionally this thesis analysed and modelled the design of the previously undocumented Ternan coil, developing an improved magnetic coil design in the process, named the “ELFcage”. Magnetic field uniformity measurements were conducted on the Ternan coil, agreeing with numerical modelling of the coil system. The magnetic uniformity was found to be sufficiently large to house most equipment being magnetically tested by DSTO. The impact of high permeability shielding was also briefly investigated, with modelling showing the magnetic field uniformity can be increased by selecting the appropriate shielding geometry.

8.1 Recommendations

Given the DSTO magnetic test facility is already built and available for use it is recommended that the existing Ternan $\cos(\theta)$ coil configuration be kept, and be used for

8.1 Recommendations

characterisation of ranging system sensors, and measurement of magnetic signatures of bulky equipment. It is also recommended a small 2-axis ELFcage coil be built for y -axis and z -axis field stimulation of small sensors within a shielded laboratory environment, for use in the design and development of future ranging systems, and that an additional removable solenoid be built to stimulate the x -axis field.

Appendix A

Additional Definitions and Derivations

A.1 Moments of a Gaussian random variable

First, second, third and fourth order moments of a Gaussian RV are listed below, as presented in problem sheet 4 of White (2012). Supposing $X \sim N(\mu, \sigma^2)$:

The first order moment is shown in (A.1).

$$E \{X_i\} = E \{X\} \quad (\text{A.1a})$$

$$= \mu \quad (\text{A.1b})$$

Second order moments for differing and matching indices are shown in (A.2) and (A.3) respectively.

$$E \{X_i X_j\} = E \{X\}^2 \quad (\text{A.2a})$$

$$= \mu^2 \quad (\text{A.2b})$$

$$E \{X_i X_i\} = E \{X^2\} \quad (\text{A.3a})$$

$$= \mu^2 + \sigma^2 \quad (\text{A.3b})$$

A.1 Moments of a Gaussian random variable

Third order moments for three differing indices is shown in (A.4), two matching indices are shown in (A.5), and all three matching indices are shown in (A.6).

$$E \{X_i X_j X_k\} = E \{X\}^3 \quad (\text{A.4a})$$

$$= \mu^3 \quad (\text{A.4b})$$

$$E \{X_i X_i X_j\} = E \{X^2\} E \{X\} \quad (\text{A.5a})$$

$$= (\mu^2 + \sigma^2) \mu \quad (\text{A.5b})$$

$$= \mu^3 + \sigma^2 \mu \quad (\text{A.5c})$$

$$E \{X_i X_i X_i\} = E \{X\}^3 \quad (\text{A.6a})$$

$$= (\mu^3 + 3\sigma^2 \mu) \quad (\text{A.6b})$$

Third order moments for four differing indices is shown in (A.7), two matching indices are shown in (A.8), two pairs of matching indices are shown in (A.9), three matching indices are shown in (A.10), and all four indices matching are shown in (A.11).

$$E \{X_i X_j X_k X_l\} = E \{X\}^4 \quad (\text{A.7a})$$

$$= \mu^4 \quad (\text{A.7b})$$

$$E \{X_i X_i X_j X_k\} = E \{X^2\} E \{X\}^2 \quad (\text{A.8a})$$

$$= (\mu^2 + \sigma^2) \mu^2 \quad (\text{A.8b})$$

$$= \mu^4 + \sigma^2 \mu^2 \quad (\text{A.8c})$$

$$E \{X_i X_i X_j X_j\} = E \{X^2\}^2 \quad (\text{A.9a})$$

$$= (\mu^2 + \sigma^2)^2 \quad (\text{A.9b})$$

$$= \mu^4 + 2\sigma^2 \mu^2 + \sigma^4 \quad (\text{A.9c})$$

$$E \{X_i X_i X_i X_j\} = E \{X\}^3 E \{X\} \quad (\text{A.10a})$$

$$= (\mu^3 + 3\sigma^2\mu)\mu \quad (\text{A.10b})$$

$$= \mu^4 + 3\sigma^2\mu^2 \quad (\text{A.10c})$$

$$E \{X_i X_i X_i X_i\} = E \{X^4\} \quad (\text{A.11a})$$

$$= \mu^4 + 6\sigma^2\mu^2 + 3\sigma^4 \quad (\text{A.11b})$$

A.1.1 Fourth moment of noise amplitude

Equation (5.15a) in Section B.1.4 contains the estimate of the fourth power of noise sample ε_k . $E(\varepsilon_k) = \mu = 0$, and $E(\varepsilon_k^2) - E(\varepsilon_k) = \Sigma_k$. This estimate is not straightforward, so will be derived below:

$$E \{|\varepsilon_k|^4\} = E \{(\sqrt{\varepsilon_k \cdot \varepsilon_k})^4\} \quad (\text{A.12a})$$

$$= E \{(\varepsilon_k \cdot \varepsilon_k)^2\} \quad (\text{A.12b})$$

$$= E \{(\varepsilon_{k_1}^2 + \varepsilon_{k_2}^2 + \varepsilon_{k_3}^2)^2\} \quad (\text{A.12c})$$

$$= E \{ \varepsilon_{k_1}^4 + \varepsilon_{k_2}^4 + \varepsilon_{k_3}^4 + 2(\varepsilon_{k_1}^2 \varepsilon_{k_2}^2 + \varepsilon_{k_1}^2 \varepsilon_{k_3}^2 + \varepsilon_{k_2}^2 \varepsilon_{k_3}^2) \} \quad (\text{A.12d})$$

$$= \left(\sum_{i=1}^3 \mu_i^4 + 6\sigma_i^2 \mu_i^2 + 3\sigma_i^4 \right) + 2 \left(\sum_{i=1}^3 \mu_i^4 + 2\sigma_i^2 \mu_i^2 + \sigma_i^4 \right) \quad (\text{A.12e})$$

$$= 3tr(\Sigma_k^2) + 2tr(\Sigma_k^2) \quad (\text{A.12f})$$

$$= 5tr(\Sigma_k^2) \quad (\text{A.12g})$$

Assuming noise is isotropic, we can say $|\varepsilon_{k_1}| \equiv |\varepsilon_{k_2}| \equiv |\varepsilon_{k_3}|$:

$$E \{v_k\}^2 = (-tr(\Sigma_k))^2 \quad (\text{A.13a})$$

$$= (\varepsilon_{k_1}^2 + \varepsilon_{k_2}^2 + \varepsilon_{k_3}^2)^2 \quad (\text{A.13b})$$

$$= \varepsilon_{k_1}^4 + \varepsilon_{k_2}^4 + \varepsilon_{k_3}^4 + 2(\varepsilon_{k_1}^2 \varepsilon_{k_2}^2 + \varepsilon_{k_1}^2 \varepsilon_{k_3}^2 + \varepsilon_{k_2}^2 \varepsilon_{k_3}^2) \quad (\text{A.13c})$$

$$= 3(\varepsilon_{k_1}^4 + \varepsilon_{k_2}^4 + \varepsilon_{k_3}^4) \quad (\text{A.13d})$$

$$= 3tr(\Sigma_k^2) \quad (\text{A.13e})$$

A.2 Sum of centre and centred pseudo-covariance

Equation (5.21) from 5.1.7 relies on a summation over the product of centred and centre variable to equal zero. The derivation is shown below.

$$\sum_{k=1}^N \frac{1}{\sigma_k^2} (\tilde{v}_k - \tilde{\mu}_k)(\bar{v} - \bar{\mu}) = \sum_{k=1}^N \frac{1}{\sigma_k^2} (v_k - \bar{v} - \mu_k + \bar{\mu})(\bar{v} - \bar{\mu}) \quad (\text{A.14a})$$

$$= \sum_{k=1}^N \frac{1}{\sigma_k^2} (v_k - \mu_k)(\bar{v} - \bar{\mu}) - \sum_{k=1}^N \frac{1}{\sigma_k^2} (\bar{v} - \bar{\mu})^2 \quad (\text{A.14b})$$

$$= (\bar{v} - \bar{\mu}) \sum_{k=1}^N \frac{1}{\sigma_k^2} (v_k - \mu_k) - (\bar{v} - \bar{\mu})^2 \sum_{k=1}^N \frac{1}{\sigma_k^2} \quad (\text{A.14c})$$

$$= (\bar{v} - \bar{\mu}) \frac{1}{\bar{\sigma}^2} (\bar{v} - \bar{\mu}) - (\bar{v} - \bar{\mu})^2 \frac{1}{\bar{\sigma}^2} \quad (\text{A.14d})$$

$$= 0 \quad (\text{A.14e})$$

A.3 Expectations of centre and centred variables

$E\{x\} = \mu = \int_{-\infty}^{\infty} xg(x)dx$. For $E\{\mu\}$, the probability distribution $g(x)$ is a delta function, so $E\{\mu_k\} = \mu_k$. The same applies for σ_k^2 .

$$E\{(\nu_k - \mu_k)^2\} = E\{(\nu_k^2 - 2\nu_k\mu_k + \mu_k^2)\} \quad (\text{A.15a})$$

$$= E\{\nu_k^2\} - E\{2\nu_k\mu_k\} + E\{\mu_k^2\} \quad (\text{A.15b})$$

$$= \sigma_k^2 + \mu_k^2 - 2\mu_k E\{\nu_k\} + \mu_k^2 \quad (\text{A.15c})$$

$$= \sigma_k^2 + 2\mu_k^2 - 2\mu_k^2 \quad (\text{A.15d})$$

$$= \sigma_k^2 \quad (\text{A.15e})$$

A.3.1 Centre variables

$$E\{\bar{\sigma}^2\} = E\left\{\frac{1}{\sum_{k=1}^N \frac{1}{\sigma_k^2}}\right\} = \frac{1}{E\left\{\sum_{k=1}^N \frac{1}{\sigma_k^2}\right\}} \quad (\text{A.16a})$$

$$= \frac{1}{\sum_{k=1}^N \frac{1}{E\{\sigma_k^2\}}} = \frac{1}{\sum_{k=1}^N \frac{1}{\sigma_k^2}} \quad (\text{A.16b})$$

$$= \bar{\sigma}^2 \quad (\text{A.16c})$$

$$E\{\bar{\mu}_k\} = \bar{\mu}_k \quad (\text{A.17a})$$

$$E \{ \bar{v} \} = E \left\{ \bar{\sigma}^2 \sum_{k=1}^N \frac{1}{\sigma_k^2} v_k \right\} \quad (\text{A.18a})$$

$$= \bar{\sigma}^2 E \left\{ \sum_{k=1}^N \frac{1}{\sigma_k^2} v_k \right\} \quad (\text{A.18b})$$

$$= \bar{\sigma}^2 \sum_{k=1}^N \frac{1}{\sigma_k^2} E \{ v_k \} \quad (\text{A.18c})$$

$$= \bar{\sigma}^2 \sum_{k=1}^N \frac{1}{\sigma_k^2} \mu_k \quad (\text{A.18d})$$

$$= \bar{\mu} \quad (\text{A.18e})$$

$$E \{ \bar{v} - \bar{\mu} \} = E \{ \bar{v} \} - E \{ \bar{\mu} \} \quad (\text{A.19a})$$

$$= \bar{\mu} - \bar{\mu} \quad (\text{A.19b})$$

$$= 0 \quad (\text{A.19c})$$

$$E \{ (\bar{v} - \bar{\mu})^2 \} = E \{ \bar{v}^2 \} - 2E \{ \bar{v} \bar{\mu} \} + E \{ \bar{\mu}^2 \} \quad (\text{A.20a})$$

$$= \bar{\mu}^2 + \bar{\sigma}^2 - 2\bar{\mu} E \{ \bar{v} \} + \bar{\mu}^2 \quad (\text{A.20b})$$

$$= \bar{\sigma}^2 \quad (\text{A.20c})$$

A.3.2 Centered variables

$$E \{ \tilde{v}_k \} = E \{ v_k - \bar{v} \} \quad (\text{A.21a})$$

$$= E \{ v_k \} - E \{ \bar{v} \} \quad (\text{A.21b})$$

$$= \mu_k - \bar{\mu} \quad (\text{A.21c})$$

$$= \tilde{\mu}_k \quad (\text{A.21d})$$

$$E \{ \tilde{\mu}_k \} = E \{ \mu_k - \bar{\mu} \} \quad (\text{A.22a})$$

$$= E \{ \mu_k \} - E \{ \bar{\mu} \} \quad (\text{A.22b})$$

$$= \mu_k - \bar{\mu} \quad (\text{A.22c})$$

$$= \tilde{\mu}_k \quad (\text{A.22d})$$

$$E \{ \tilde{v}_k - \tilde{\mu}_k \} = E \{ \tilde{v}_k \} - E \{ \tilde{\mu}_k \} \quad (\text{A.23a})$$

$$= \tilde{\mu}_k - \tilde{\mu}_k \quad (\text{A.23b})$$

$$= 0 \quad (\text{A.23c})$$

A.4 Geometric Approach Auxiliary Formulae

This section contains the Auxiliary variables taken directly from Vasconcelos *et al.* (2011).

A.4.1 Least squares estimate

Scaling an misalignment parameters are described in Vasconcelos *et al.* (2011) as:

$$a = \frac{1}{2\alpha_1} (-(4D + E^2)\alpha_2)^{1/2} \quad (\text{A.24a})$$

$$b = \frac{1}{2\alpha_1} (-(4A + C^2)\alpha_2)^{1/2} \quad (\text{A.24b})$$

$$c = \frac{1}{2\alpha_1} ((4DA - B^2)\alpha_2)^{1/2} \quad (\text{A.24c})$$

$$\tan(\rho) = -\frac{1}{2}(2B + EC)(\alpha_1)^{-1/2} \quad (\text{A.24d})$$

$$\tan(\phi) = (BE - 2CD)(\alpha_1)^{-1/2} \quad (\text{A.24e})$$

$$\tan(\lambda) = E(-\alpha_1\alpha_3^{-1})^{1/2} \quad (\text{A.24f})$$

A.4 Geometric Approach Auxiliary Formulae

Auxiliary variables are defined as:

$$\beta_1 = 2BH + BEI - 2CDI - 4DG + ECH - E^2G \quad (\text{A.25a})$$

$$\beta_2 = -2AEI + 4AH - BCI - 2BG + C^2H - CEG \quad (\text{A.25b})$$

$$\beta_3 = 4DIA - 2DGC + EGB - IB^2 - 2EHA + CBH \quad (\text{A.25c})$$

$$\alpha_1 = -B^2 + DC^2 + 4DA + AE^2 - BEC \quad (\text{A.25d})$$

$$\begin{aligned} \alpha_2 = & 4AE^2J - E^2G^2 - 4BECJ + 2ECHG \\ & + 2BEIG - 4EHAI - 4DICG - C^2H^2 \\ & + 4DAI^2 + 2CBHI - 4DG^2 + 4DC^2J \\ & + 4BHG - 4AH^2 - B^2I^2 - 4B^2J + 16DAJ \end{aligned} \quad (\text{A.25e})$$

$$\begin{aligned} \alpha_3 = & E^4A - CBE^3 + E^2C^2D - 2B^2E^2 \\ & + 8DAE^2 - 4DB^2 + 16D^2A \end{aligned} \quad (\text{A.25f})$$

The error matrix, which is the inverse of T_k is expressed below:

$$C = \frac{1}{\|E\mathbf{h}\|} \begin{bmatrix} a & 0 & 0 \\ b \sin(\rho) & b \cos(\rho) & 0 \\ c(\sin(\phi) \cos(\lambda)) & c \sin(\lambda) & c \cos(\phi) \cos(\lambda) \end{bmatrix} \quad (\text{A.26})$$

A.4.2 Maximum likelihood estimate

Vasconcelos *et al.* (2011) derived the log-likelihood function to be:

$$f(\mathbf{T}, \mathbf{b}) = \sum_{i=1}^n \left(\frac{\|\mathbf{T}(\mathbf{h}_{ri} - \mathbf{b})\| - 1}{\sigma_{mi}} \right)^2 \quad (\text{A.27})$$

If we let $\mathbf{u}_i = \mathbf{h}_{ri} - \mathbf{b}$, gradient $\nabla f|_x$ is split into two sub-matrices $\nabla f|_x = [\nabla f|_T \nabla f|_b]$

where $\mathbf{x}_k = \begin{bmatrix} \mathbf{T}_k \\ \mathbf{b}_k \end{bmatrix}$.

$$\nabla f|_T = \sum_{i=1}^n \frac{2c_T}{\sigma_{mi}^2} \mathbf{u}_i \otimes \mathbf{T} \mathbf{u}_i \quad (\text{A.28a})$$

$$\nabla f|_b = \sum_{i=1}^n \frac{-2c_T}{\sigma_{mi}^2} \mathbf{T}^T \mathbf{T} \mathbf{u}_i \quad (\text{A.28b})$$

where $c_T = 1 - \|\mathbf{T}\mathbf{u}_i\|^{-1}$ and \otimes is the Kronecker product¹⁶.

The Hessian $\nabla^2 f|_x$ can be expressed as:

$$\nabla^2 f|_x = \begin{bmatrix} H_{T,T} & H_{T,b} \\ H_{T,b}^T & H_{b,b} \end{bmatrix} \quad (\text{A.29})$$

with sub-matrices:

$$H_{T,T} = \sum_{i=1}^n \frac{2}{\sigma_{mi}^2} \left[\frac{(\mathbf{u}_i \mathbf{u}_i^T) \otimes (\mathbf{T} \mathbf{u}_i \mathbf{u}_i^T \mathbf{T}^T)}{\|\mathbf{T} \mathbf{u}_i\|^3} + c_T [(\mathbf{u}_i \mathbf{u}_i^T) \otimes I_3] \right] \quad (\text{A.30a})$$

$$H_{T,b} = \sum_{i=1}^n \frac{-2}{\sigma_{mi}^2} \left[\frac{(\mathbf{u}_i \otimes \mathbf{T} \mathbf{u}_i) \mathbf{u}_i^T \mathbf{T}^T \mathbf{T}}{\|\mathbf{T} \mathbf{u}_i\|^3} + c_T [\mathbf{u}_i \otimes \mathbf{T} + I_3 \otimes \mathbf{T} \mathbf{u}_i] \right] \quad (\text{A.30b})$$

$$H_{b,b} = \sum_{i=1}^n \frac{2}{\sigma_{mi}^2} \left[\frac{\mathbf{T}^T \mathbf{T} \mathbf{u}_i \mathbf{u}_i^T \mathbf{T}^T \mathbf{T}}{\|\mathbf{T} \mathbf{u}_i\|^3} + c_T \mathbf{T}^T \mathbf{T} \right] \quad (\text{A.30c})$$

¹⁶A fast implementation for the Kronecker product can be found in C.2.5

Appendix B

Ancillary Results

B.1 AC calibration

Section 6.1 alludes to the coil inherently having zero bias error associated with it. The only manufacture errors present are related to coil factors and orthogonality, hence \mathbf{b} does not need to be estimated for coil calibration purposes, and the bias due to earth's field and the reference sensor would need to be removed from \mathbf{B}_k and \mathbf{H}_k measurements. This could be achieved by the use of a filtering, or the use of FFTs as mentioned in Section 2.3. The following estimator is effectively a special case of TWOSTEP in which $\mathbf{b} = \mathbf{0}$.

B.1.1 Model

The simplified coil calibration model is:

$$(I + D)S\mathbf{I}_k + A^e \boldsymbol{\varepsilon}_k^e = \boldsymbol{\vartheta}^T A^s \mathbf{H}_k + \boldsymbol{\varepsilon}_k' \quad (\text{B.1})$$

Following the same steps as shown in section Section 6.1.2 gives:

$$\mathbf{B}_k = (I + D)^{-1}(\boldsymbol{\vartheta}^T A^s \mathbf{H}_k + \boldsymbol{\varepsilon}_k) \quad (\text{B.2})$$

B.1 AC calibration

Although \mathbf{H}_k is expected to be known during the calibration, A_k and ϑ are not known or estimated, so (B.2) is manipulated to eliminate the rotations (which are orthogonal), hence only magnitude data is used. Section 5.1.2 included the same step, but for different reasons.

$$|\mathbf{H}_k|^2 = ((I + D)\mathbf{B}_k - \boldsymbol{\varepsilon}_k)^T((I + D)\mathbf{B}_k - \boldsymbol{\varepsilon}_k) \quad (\text{B.3a})$$

$$= \mathbf{B}_k^T(I + D)^T(I + D)\mathbf{B}_k - 2\mathbf{B}_k^T(I + D)^T\boldsymbol{\varepsilon}_k + |\boldsymbol{\varepsilon}_k|^2 \quad (\text{B.3b})$$

If a scalar sensor were used to measure $|\mathbf{H}_k|$, filtering could not be applied to individual components of \mathbf{H}_k , meaning the vector sum would distort the AC signal, introducing harmonics.

B.1.2 Parameter re-definition

$|\mathbf{H}_k|^2$ is re-arranged and a better set of basis functions is selected for improved model stability (Barker *et al.* 2007), hence:

$$|\mathbf{H}_k|^2 = \mathbf{B}_k^T(I + 2D + D^2)\mathbf{B}_k - 2\mathbf{B}_k^T(I + D)^T\boldsymbol{\varepsilon}_k + |\boldsymbol{\varepsilon}_k|^2 \quad (\text{B.4a})$$

$$= |\mathbf{B}_k|^2 + \mathbf{B}_k^T E \mathbf{B}_k - (2[(I + D)\mathbf{B}_k] \cdot \boldsymbol{\varepsilon}_k - |\boldsymbol{\varepsilon}_k|^2) \quad (\text{B.4b})$$

$$= |\mathbf{B}_k|^2 + \mathbf{B}_k^T E \mathbf{B}_k - \nu_k \quad (\text{B.4c})$$

ν_k is defined later in (B.6b). For ease of estimation we removed the non-linear dependence on parameter D , defining matrix E as shown in (B.5).

$$E = 2D + D^2 \quad (\text{B.5})$$

B.1.3 Sensor error measurement & sensor error measurement noise

As shown in (B.4), ν_k holds all the $\boldsymbol{\varepsilon}_k$ noise elements present in $|\mathbf{H}_k|^2$, and z_k could be considered a scalar measurement of the sensors errors we are trying to estimate. z_k and ν_k are defined in (B.6).

$$z_k = |\mathbf{B}_k|^2 - |\mathbf{H}_k|^2 \quad (\text{B.6a})$$

$$\nu_k = [(I + D)\mathbf{B}_k] \cdot \boldsymbol{\varepsilon}_k - |\boldsymbol{\varepsilon}_k|^2 \quad (\text{B.6b})$$

Using (B.4) the scalar measurement z_k is expressed as follows:

$$z_k = |\mathbf{B}_k|^2 - |\mathbf{H}_k|^2 \quad (\text{B.7a})$$

$$= -\mathbf{B}_k^T \mathbf{E} \mathbf{B}_k + \nu_k \quad (\text{B.7b})$$

For ease of derivation and coding E is vectorised, rearranging to remove the symmetric 3×3 matrix E and to use 6×1 vector \mathbf{E} instead, as was done in (5.9), obtaining $\mathbf{B}_k^T \mathbf{E} \mathbf{B}_k = \mathbf{K}_k \mathbf{E}$. Where \mathbf{K}_k and \mathbf{E} are defined as follows:

$$\mathbf{E} = \begin{pmatrix} E_{11} & E_{22} & E_{33} & E_{12} & E_{13} & E_{23} \end{pmatrix}^T \quad (\text{B.8a})$$

$$\mathbf{K}_k = \begin{pmatrix} B_{1k}^2 & B_{2k}^2 & B_{3k}^2 & 2B_{1k}B_{2k} & 2B_{1k}B_{3k} & 2B_{2k}B_{3k} \end{pmatrix} \quad (\text{B.8b})$$

Applying the simplification, z_k is expressed in terms of variables \mathbf{K}_k and \mathbf{E} .

$$z_k = -\mathbf{B}_k^T \mathbf{E} \mathbf{B}_k + \nu_k \quad (\text{B.9a})$$

$$= -\mathbf{K}_k \mathbf{E} + \nu_k \quad (\text{B.9b})$$

A re-arrangement of (B.9) represents ν_k in terms of \mathbf{K}_k and \mathbf{E} as shown in (B.10).

$$\nu_k = z_k + \mathbf{K}_k \mathbf{E} \quad (\text{B.10})$$

B.1.4 Noise distribution

As part of the MLE process the noise in the system needs to be characterised. As earlier $\boldsymbol{\varepsilon}_k$ is assumed to be white and Gaussian distributed with zero mean. Since $\boldsymbol{\varepsilon}_k \sim \mathcal{N}(\mathbf{0}, \Sigma_k)$ then $\nu_k \sim \mathcal{N}(\mu_k, \sigma_k^2)$ as shown in (B.11a) and (B.12a).

B.1 AC calibration

Calculation of μ_k is shown below:

$$\mu_k \equiv E \{ \nu_k \} \quad (\text{B.11a})$$

$$= E \{ 2[(I + D)\mathbf{B}_k] \cdot \boldsymbol{\varepsilon}_k \} - E \{ |\boldsymbol{\varepsilon}_k|^2 \} \quad (\text{B.11b})$$

$$= 0 - E \{ (\sqrt{\boldsymbol{\varepsilon}_k \cdot \boldsymbol{\varepsilon}_k})^2 \} \quad (\text{B.11c})$$

$$= -tr(\boldsymbol{\Sigma}_k) \quad (\text{B.11d})$$

Once again, calculation of σ_k^2 requires the use of Gaussian random variable moments presented in Appendix A.1.

$$\sigma_k^2 \equiv E \{ \nu_k^2 \} - \mu_k^2 \quad (\text{B.12a})$$

$$= 4E \{ [(I + D)\mathbf{B}_k]^T \boldsymbol{\varepsilon}_k \}^2 + 2E \{ [(I + D)\mathbf{B}_k]^T \boldsymbol{\varepsilon}_k |\boldsymbol{\varepsilon}_k|^2 \} + E \{ |\boldsymbol{\varepsilon}_k|^4 \} - tr(\boldsymbol{\Sigma}_k)^2 \quad (\text{B.12b})$$

$$= 4E \{ [(I + D)\mathbf{B}_k]^T \boldsymbol{\varepsilon}_k \boldsymbol{\varepsilon}_k^T [(I + D)\mathbf{B}_k] \} + E \{ |\boldsymbol{\varepsilon}_k|^4 \} - tr(\boldsymbol{\Sigma}_k)^2 \quad (\text{B.12c})$$

$$= 4[(I + D)\mathbf{B}_k]^T \boldsymbol{\Sigma}_k [(I + D)\mathbf{B}_k] + 5tr(\boldsymbol{\Sigma}_k^2) - 3tr(\boldsymbol{\Sigma}_k^2) \quad (\text{B.12d})$$

$$= 4[(I + D)\mathbf{B}_k]^T \boldsymbol{\Sigma}_k [(I + D)\mathbf{B}_k] + 2tr(\boldsymbol{\Sigma}_k^2) \quad (\text{B.12e})$$

B.1.5 Likelihood function

Having characterised the noise, the likelihood (B.13a) and negative log-likelihood (B.14a) functions are obtained:

$$f_{N|\boldsymbol{\Theta}'=\mathbf{E}'}(\mathbf{E}') = \prod_{k=1}^N \frac{1}{\sqrt{2\pi\sigma_k^2}} e^{-(\nu_k - \mu_k)^2 / 2\sigma_k^2} \quad (\text{B.13a})$$

$$= \prod_{k=1}^N \frac{1}{\sqrt{2\pi\sigma_k^2}} e^{-(z_k + \mathbf{K}_k \mathbf{E} - \mu_k)^2 / 2\sigma_k^2} \quad (\text{B.13b})$$

$$J(\mathbf{E}') = -\ln f_{N|\Theta'=\mathbf{E}'}(\mathbf{E}') \quad (\text{B.14a})$$

$$= \sum_{k=1}^N \left[(z_k + \mathbf{K}_k \mathbf{E} - \mu_k)^2 / 2\sigma_k^2 + \frac{1}{2} \ln(2\pi\sigma_k^2) \right] \quad (\text{B.14b})$$

$$= \frac{1}{2} \sum_{k=1}^N \left[\frac{1}{\sigma_k^2} (z_k + \mathbf{K}_k \mathbf{E} - \mu_k)^2 + \ln(2\pi\sigma_k^2) \right] \quad (\text{B.14c})$$

B.1.5.1 Estimator

The estimator for the measurement is found by setting $\frac{\partial}{\partial \mathbf{E}'} J = 0$.

$$\frac{\partial}{\partial \mathbf{E}'} J = \frac{\partial}{\partial \mathbf{E}'} \frac{1}{2} \sum_{k=1}^N \frac{1}{\sigma_k^2} (z_k + \mathbf{K}_k \mathbf{E} - \mu_k)^2 \quad (\text{B.15a})$$

$$+ \text{terms independent of } \mathbf{E}) \quad (\text{B.15b})$$

$$= \frac{1}{2} \sum_{k=1}^N \frac{2\mathbf{K}_k^T}{\sigma_k^2} (z_k + \mathbf{K}_k \mathbf{E} - \mu_k) \quad (\text{B.15c})$$

$$= \sum_{k=1}^N \frac{1}{\sigma_k^2} (z_k - \mu_k) \mathbf{K}_k^T + \sum_{k=1}^N \frac{\mathbf{K}_k^T \mathbf{K}_k}{\sigma_k^2} \mathbf{E} = 0 \quad (\text{B.15d})$$

$$\therefore \sum_{k=1}^N \frac{\mathbf{K}_k^T \mathbf{K}_k}{\sigma_k^2} \mathbf{E} = \sum_{k=1}^N \frac{-1}{\sigma_k^2} (z_k - \mu_k) \mathbf{K}_k^T \quad (\text{B.15e})$$

We multiply both sides by the inverse of $\sum_{k=1}^N \frac{\mathbf{K}_k^T \mathbf{K}_k}{\sigma_k^2}$ to obtain the estimate \mathbf{E}^* , where $*$ indicates the value is an estimate. $\mathfrak{J}(\mathbf{E})$ is the Fisher Information Matrix and is derived in Section [B.1.6](#)

$$\therefore \mathbf{E}^* = \left(\sum_{k=1}^N \frac{\mathbf{K}_k^T \mathbf{K}_k}{\sigma_k^2} \right)^{-1} \sum_{k=1}^N \frac{-1}{\sigma_k^2} (z_k - \mu_k) \mathbf{K}_k^T \quad (\text{B.16a})$$

$$= [\mathfrak{J}(\mathbf{E})]^{-1} \sum_{k=1}^N \frac{-1}{\sigma_k^2} (z_k - \mu_k) \mathbf{K}_k^T \quad (\text{B.16b})$$

B.1.6 Fisher information matrix

The Fisher Information Matrix \mathfrak{J} is the expectation of the Hessian matrix - the square matrix of the second order partial derivatives of the negative log likelihood function $J(\mathbf{E})$. The fisher matrix is defined by Poor (1994) as presented in [\(5.26\)](#):

B.1 AC calibration

Using (5.27) the Fisher Information Matrix for $J(E)$ is derived¹⁷, as shown in (B.17).

$$\mathfrak{J}(E) = E\left\{\left(\frac{\partial^2 J(E)}{\partial E^2}\right)\right\} \quad (\text{B.17a})$$

$$= E\left\{\left(\frac{\partial^2}{\partial E^2} \sum_{k=1}^N \frac{1}{\sigma_k^2} (z_k + \mathbf{K}_k E - \mu_k)^T (z_k + \mathbf{K}_k E - \mu_k)\right)\right\} \quad (\text{B.17b})$$

$$= E\left\{\frac{\partial}{\partial E} \sum_{k=1}^N \frac{1}{\sigma_k^2} \mathbf{K}_k^T (z_k + \mathbf{K}_k E - \mu_k)\right\} \quad (\text{B.17c})$$

$$= E\left\{\sum_{k=1}^N \frac{1}{\sigma_k^2} \mathbf{K}_k^T \mathbf{K}_k\right\} \quad (\text{B.17d})$$

$$= \sum_{k=1}^N \frac{1}{\sigma_k^2} \mathbf{K}_k^T \mathbf{K}_k \quad (\text{B.17e})$$

B.1.7 Converting to D

Estimate E^* is not in the desired form D^* , but E^* can be changed back into matrix form E^* by using its definition in (B.8a). To compute D^* we write:

$$E^* = USU^T \quad (\text{B.18})$$

where U is orthogonal and S is a 3×3 diagonal matrix with elements s_i , and both matrices are obtained by the Eigen-decomposition of symmetric matrix E^* .

We define diagonal matrix W , satisfying $S = 2W + W^2$, hence using the quadratic formula the elements are¹⁸:

$$w_j = -1 + \sqrt{1 + s_j} \quad (\text{B.19})$$

The maximum likelihood estimate for D can hence be calculated by:

$$D^* = UWU^T \quad (\text{B.20})$$

¹⁷Due to the differentiation $\mathfrak{J}(E)$ is no longer dependent on E .

¹⁸ $w_j = -1 - \sqrt{1 + s_j}$, is not used as it would give negative sensitivity values, implying the sensor was facing the wrong way. This is not possible since it would have been accounted for by attitude rotations, and manufacture quality control is expected to capture such major sensitivity errors

B.1.7.1 Covariance Matrix

To obtain the covariance matrix need to transform $\mathfrak{I}(\mathbf{E})$ to $\mathfrak{I}(\mathbf{D})$, where \mathbf{D} is defined with respect to \mathbf{D} the same way as \mathbf{E} was defined in (B.8a). Explicit derivation of this process is not shown.

$$\mathfrak{I}(\mathbf{D})^{-1} = \left(\frac{\partial \mathbf{D}}{\partial \mathbf{E}} \right) \mathfrak{I}(\mathbf{E})^{-1} \left(\frac{\partial \mathbf{D}}{\partial \mathbf{E}} \right)^T \quad (\text{B.21a})$$

Element by element differentiation of $\left(\frac{\partial \mathbf{D}}{\partial \mathbf{E}} \right)$ can be represented as $\left(\frac{\partial \mathbf{D}}{\partial \mathbf{E}} \right)_{i,j} = \frac{\partial E_j}{\partial D_i}$

$$\left(\frac{\partial \mathbf{D}}{\partial \mathbf{E}} \right) = \left(\frac{\partial \mathbf{E}}{\partial \mathbf{D}} \right)^{-1} \quad (\text{B.22a})$$

$$= [\mathbf{M}_{ED}(\mathbf{D})]^{-1} \quad (\text{B.22b})$$

where

$$\mathbf{M}_{ED}(\mathbf{D}) = \begin{pmatrix} 2 + 2D_1 & 0 & 0 & 2D_4 & 2D_5 & 0 \\ 0 & 2 + 2D_2 & 0 & 2D_4 & 0 & 2D_6 \\ 0 & 0 & 2 + 2D_3 & 0 & 2D_5 & 2D_6 \\ D_4 & D_4 & 0 & 2 + D_1 + D_2 & D_6 & D_5 \\ D_5 & 0 & D_5 & D_6 & 2 + D_1 + D_3 & D_4 \\ 0 & D_6 & D_6 & D_5 & D_4 & 2 + D_2 + D_3 \end{pmatrix} \quad (\text{B.23})$$

B.1.8 Implementation

Begin by assuming \mathbf{H}_k , \mathbf{B}_k , and Σ_k are known.

- Remove unwanted signals from \mathbf{H}_k , and calculate filtered $|\mathbf{H}_k|$
- Calculate $\mu_k = -tr(\Sigma_k)$
- Calculate z_k using (B.6a).

B.2 Amplifier linearity

- Calculate K_k using (B.8b)
- Set $E = \mathbf{0}$, and calculate σ_k^2 using (B.12a).
- Calculate Fisher Information Matrix $\mathfrak{J}(E^*)$ using (B.17).
- Estimate \tilde{E}^* using (B.16).
- Recover desired values D as shown in Sections B.1.7 and B.1.7.1.

An implementation of the code can be found in Appendix C.3.

Since the TWOSTEP estimator performed extremely well, it was decided the AC Calibration would be unnecessary, due to the large amount of time required to generate a suitable data-set. Instead the 3 Hz frequency bin values of an FFT of the reference sensor data-sets from the uniformity measurements in Section 7.4.2 were used to generate a 60 point data-set for the AC Calibration, the results of which are shown in Figures B.1 and B.2. As we can see the coil factors were very close to those estimated using TWOSTEP; the orthogonality errors are close to those estimated by TWOSTEP, but in one case of the wrong sign. The AC calibration appears to work as expected, and may in future be used for measurements in high noise environments, where noise is too high for TWOSTEP to handle with the current limitations on computer memory.

B.2 Amplifier linearity

During the measurement of the coil transfer functions, concerns were raised about the linearity of the coil system. Figures B.3, B.4 and B.5 were generated using the reference sensor, and Figures B.6, B.7 and B.8 were generated using the reference resistor voltages¹⁹. It is apparent that for each drive frequency several higher order harmonics were generated, with power ~ -80 dB that of the fundamental.

¹⁹Since only one coil was being stimulated at a time, the frequency distribution measured in the resistor will match that present in the coil, even though there was a short between the x -axis and y -axis coils.

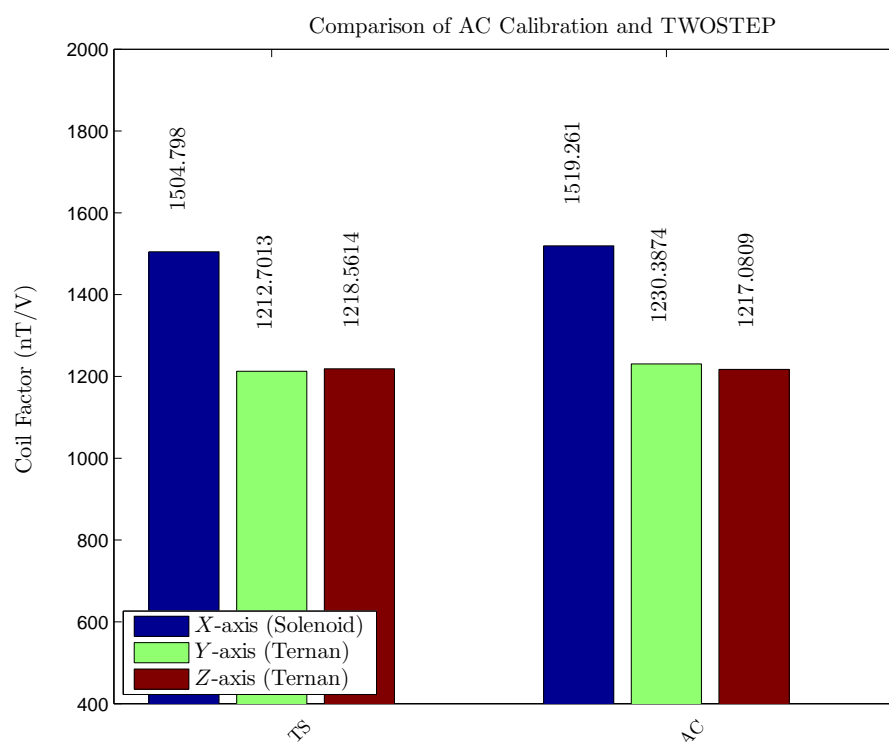


Figure B.1: Coil factors estimated by the AC Calibration algorithm compared to the coil factors estimated by the TWOSTEP algorithm.

To identify the source of the harmonics the amplifiers were tested within the lab. Figure B.9 shows the power spectral density of the amplifiers with a 60 Hz signal applied. It is apparent the amplifiers are the source of the harmonics, but their amplitude is within the amplifier specifications, hence whilst there is a definite non-linearity to the amplifiers it is unlikely to have a significant impact on the system.

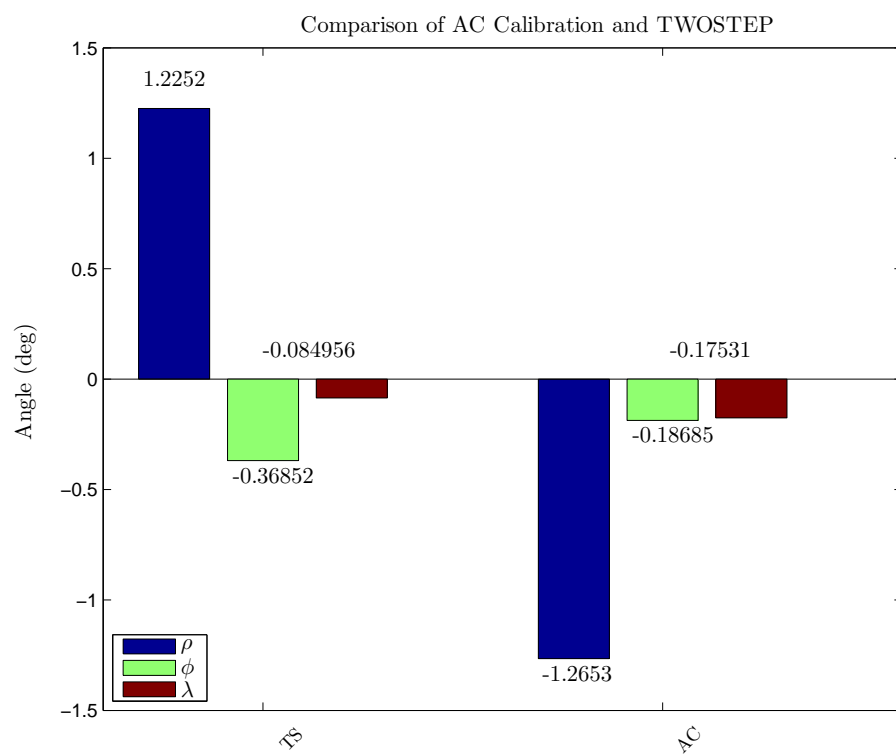


Figure B.2: Orthogonality errors estimated by the AC Calibration algorithm compared to the orthogonality errors estimated by the TWOSTEP algorithm.

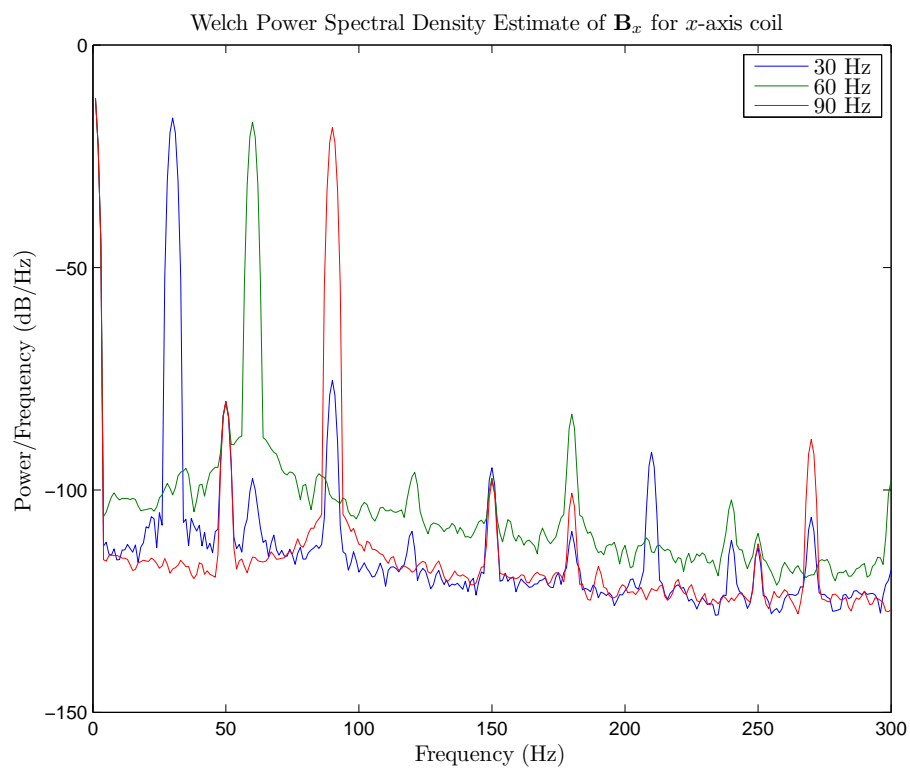


Figure B.3: Measured Welch power spectral density of the reference sensor x -axis when the coil x -axis is energised.

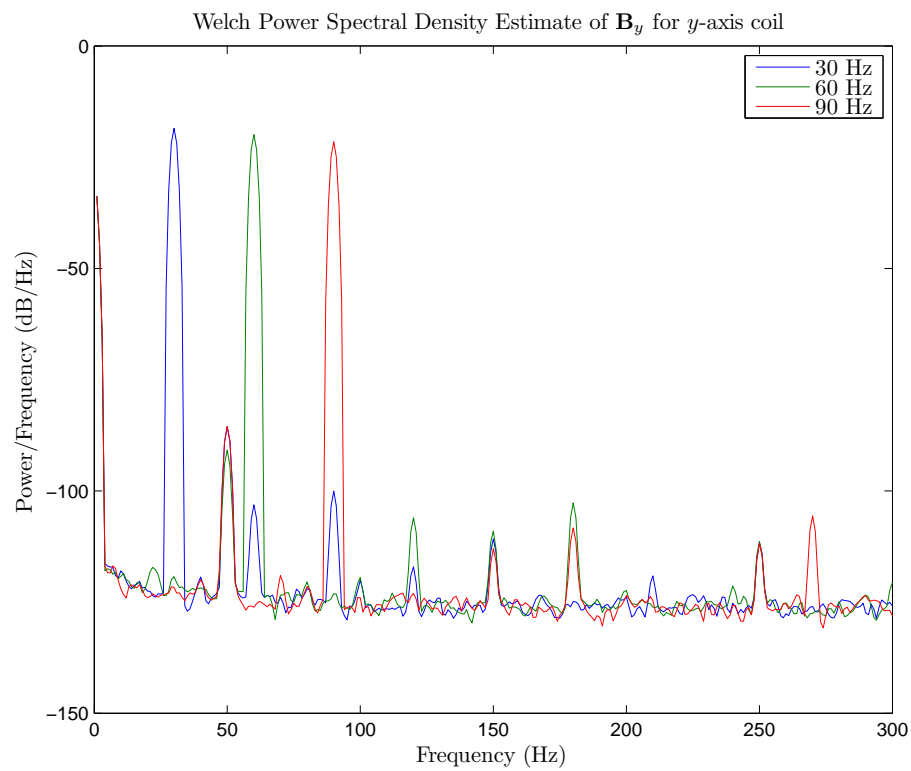


Figure B.4: Measured Welch power spectral density of the reference sensor y -axis when the coil y -axis is energised.

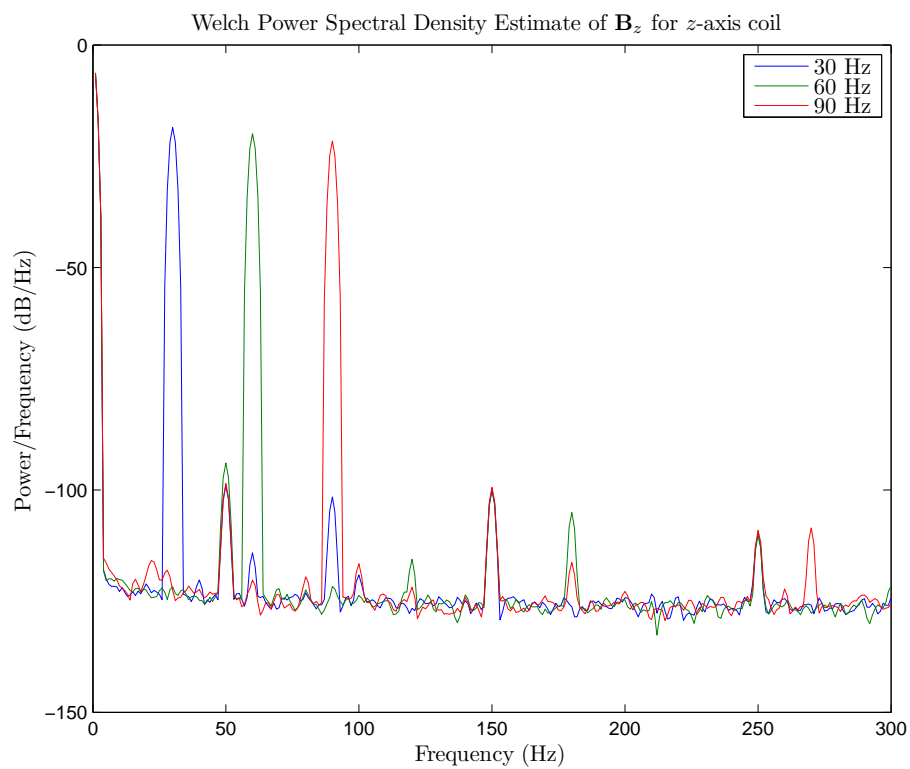


Figure B.5: Measured Welch power spectral density of the reference sensor z -axis when the coil z -axis is energised.

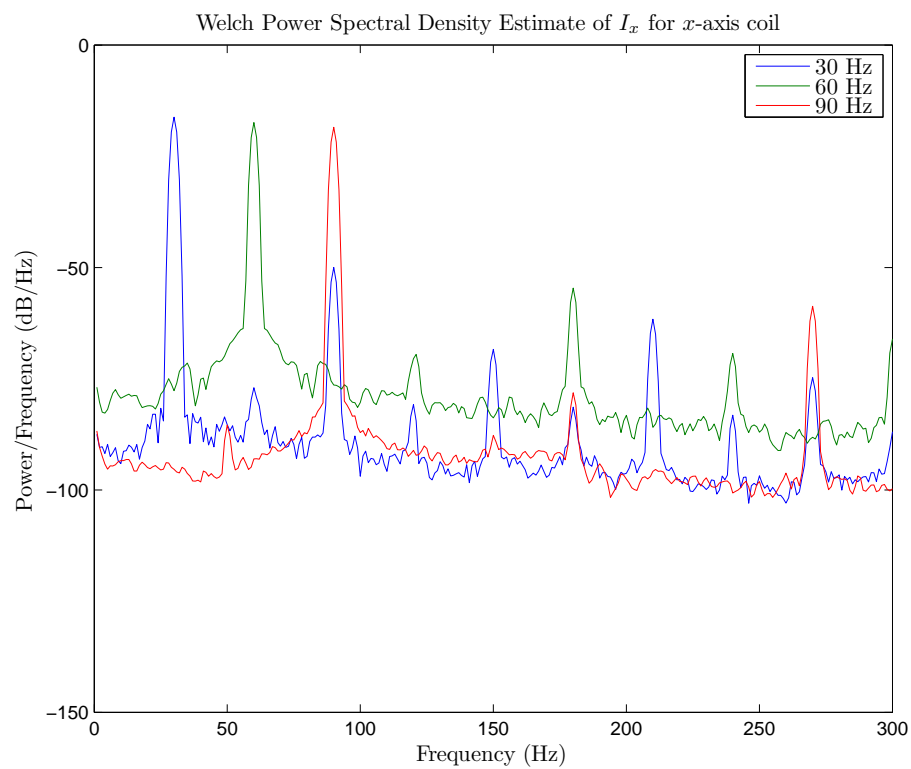


Figure B.6: Measured Welch power spectral density of current flowing in the x -axis coil.

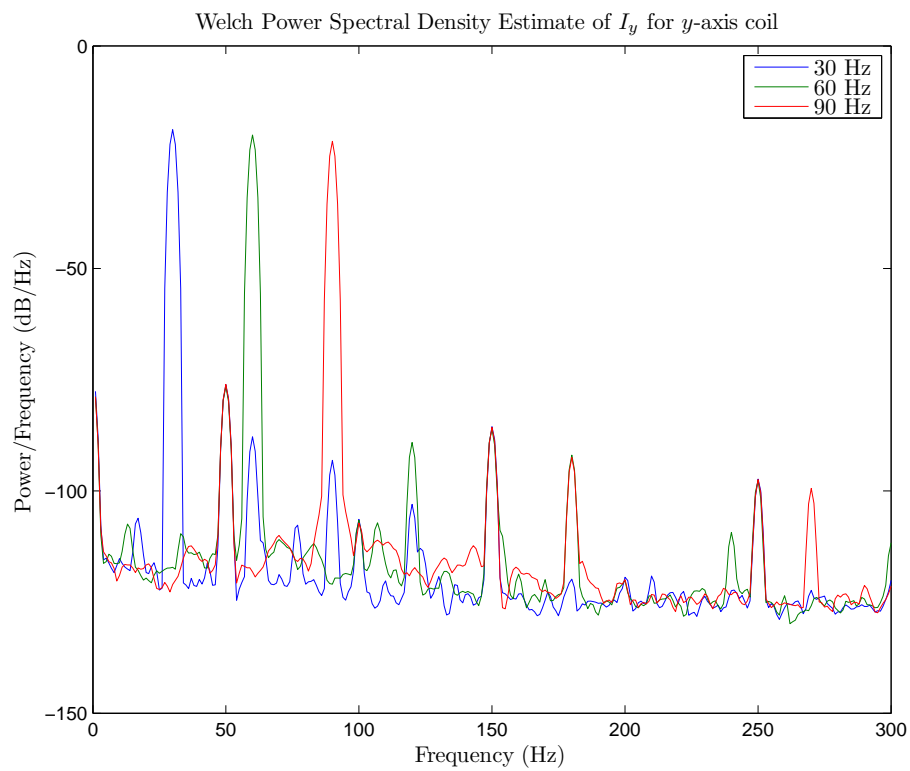


Figure B.7: Measured Welch power spectral density of current flowing in the y -axis coil.

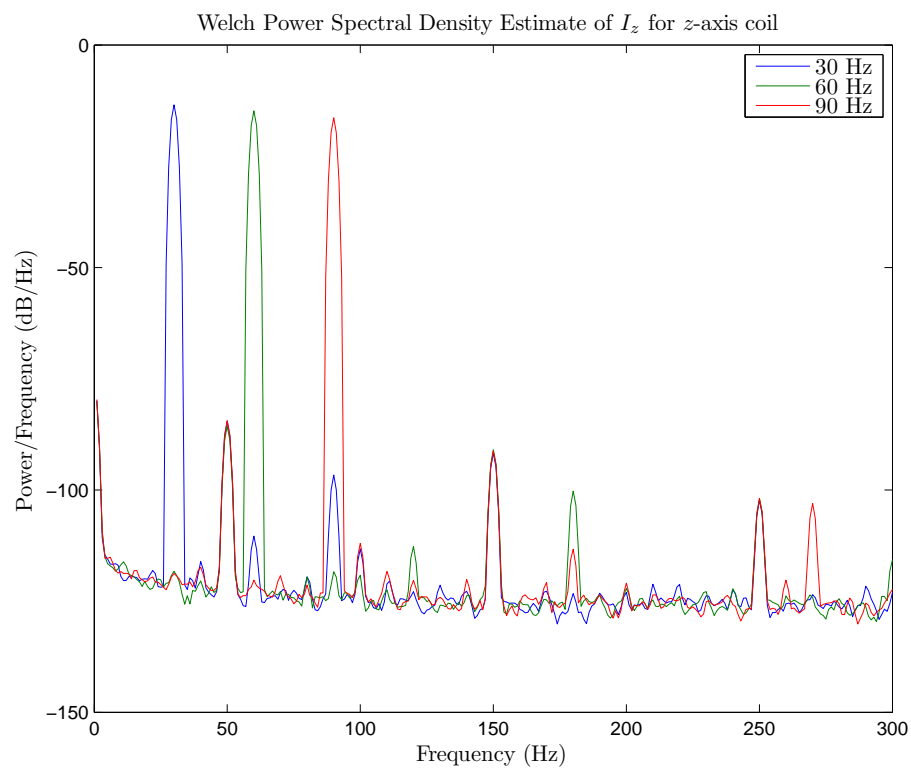


Figure B.8: Measured Welch power spectral density of current flowing in the z -axis coil.

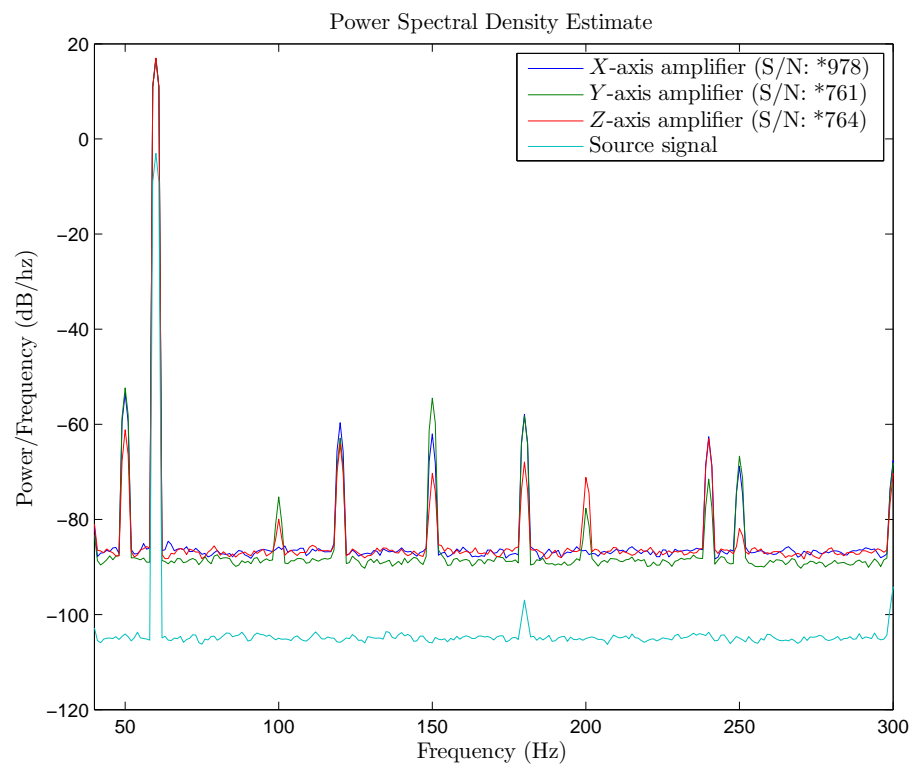


Figure B.9: Measured power spectral density of the Kepco amplifiers used to drive the Ternan coil system.

Appendix C

Code

C.1 TWOSTEP estimator

C.1.1 'TWOSTEP_estimate.m'

```
function [D_est,b_est,n,Cov_est]=TWOSTEP_estimate(B,H,Sigma_noise)
%TWOSTEP_ESTIMATE estimation of magnetometer errors.
% [D_est,b_est,n,Cov_est]=TWOSTEP_estimate(B,H,Sigma_noise)
% B - 3xN matrix, where N is the number of signal samples
% H - Earth's magnetic field in Earth frame coordinates
% Sigma_noise - 3xN noise covariance array, where each column is a
% diagonal of the noise covariance matrix.
%
% Implemented based on the work presented in:
% "Complete Linear Attitude-Independent Magnetometer Calibration"
% by R.Alonso and M. Shuster
% in "The Journal of the Astronautical Sciences" Vol. 50 No.4
% October-December 2002.
%
% Sections of code and optimisation adapted from the TWOSTEP code written
% by J.F.Vasconcelos for the validation of geometric calibration presented
% in "A geometric approach to strapdown magnetometer calibration in sensor
% frame" by J.F. Vasconcelos et al. in Aerospace and Electronic Systems,
% IEEE Transactions 47(2) 2011. Many thanks go to Dr. Jos Vasconcelos for
% his assistance.
%
% Slight variation in the calculation of the centered J function, was used
% for clarity in derivations.
```

C.1 TWOSTEP estimator

```
%  
  
% Justin Dinale, DSTO Department of Defence, Australia  
% $Revision: 1.0.0 $ $Date: 2012/11/05$  
%%%%%%%%%%%%%%%%%%%%%%%%%%%%%%%%%%%%%%%%%%%%%%%%%%%%%%%%%%%%%%%%%%%%%%%%  
  
% Define stop condition and perform housekeeping  
stop_tol=1e-24; % Stop Condition from Alonso paper  
max_n=200; % Max number of iterations  
k_samples=size(B,2); % Number of signal samples  
  
%% TWOSTEP Centered estimate  
% Set initial guess for b and D.  
b0=[0 0 0]';  
D0=zeros(3);  
  
% Calculate L  
L_k=[2*B;...  
      -(B.^2);...  
      -2*B(1,:).*B(2,:);...  
      -2*B(1,:).*B(3,:);...  
      -2*B(2,:).*B(3,:)];  
  
% Calculate scalar measurement z  
z_k=total_field(B).^2-total_field(H).^2;  
  
% Calculate mean and variance of noise  
mu_k=-sum(Sigma_noise,1); % Mean  
sigma_sq_k=4*sum(((eye(3)+D0)*B-b0*ones(1,k_samples)).*...  
                (Sigma_noise.*((eye(3)+D0)*B-b0*ones(1,k_samples)))),1)...  
          +5*(sum(Sigma_noise.^2,1)-(sum(Sigma_noise,1).^2);  
  
% Calculate centered sigma squared  
sigma_sq_bar=1/sum(1./sigma_sq_k);  
  
% Center the data  
[mu_bar,mu_k_tilde]=center_data(mu_k,sigma_sq_k,sigma_sq_bar);
```



```

[z_bar,z_k_tilde]=center_data(z_k,sigma_sq.k,sigma_sq.bar);
[L_bar,L_k_tilde]=center_data(L_k,sigma_sq.k,sigma_sq.bar);

% Calculate fisher information matrix
[I_fisher_tilde,I_fishinv_tilde]=TS_fisher_centered(sigma_sq.k,L_k_tilde);
% Calculate centered estimate
theta_0_tilde=...
    I_fishinv_tilde*(L_k_tilde*((z_k_tilde-mu_k_tilde)'/sigma_sq.k));

%% TWOSTEP Center correction
theta_n=theta_0_tilde; % Initiate theta for first iteration
n=0; % Initialise iteration counter
TS_err=Inf; %Initial condition for error.

% ABC is used to remove intensive calculations out of for loop.
ABC=-(((z_k_tilde-mu_k_tilde)'/sigma_sq.k)*L_k_tilde)';

while (TS_err>stop_tol && n<max_n)
    if (n~=0) % If we are not in the first iteration
        theta_n=theta_npl;
    end;

    % Extract c and E components
    [c,E]=theta_to_c_E(theta_n);

    % Calculate second derivative of b^2 wrt theta
    tmp=((eye(3)+E)\c)*((eye(3)+E)\c)';
    dbsq_dtheta_p=[2*((eye(3)+E)\c); -diag(tmp);...
        -2*tmp(1,2); -2*tmp(1,3); -2*tmp(2,3)]';

    %Calculate gradient of J
    dJdThetap_tilde=ABC + I_fisher_tilde*theta_n;
    dJdThetap_bar=(-(1/sigma_sq_bar)*(L_bar' - dbsq_dtheta_p)*...
        (z_bar -L_bar'*theta_n +c'*((eye(3)+E)\c) - mu_bar))';
    dJdTheta=dJdThetap_tilde+dJdThetap_bar;

    % Calculate Fisher matrix

```

C.1 TWOSTEP estimator

```
[I_fisher_bar] =TS.fisher_center(sigma_sq_bar,L_bar,dbsqdtheta_p);

% Update theta
theta_npl=theta_n-(I_fisher_tilde+I_fisher_bar)\dJdTheta;

% Calculate Error
TS_err=(theta_npl-theta_n) '*...
        (I_fisher_tilde+I_fisher_bar)*...
        (theta_npl-theta_n);
n=n+1; %Increase counter
end;

[b_est,D_est]=theta_to_b.D(theta_npl);

% Extract covariance matrix
b=b_est;
D=D_est;
M_cD=[b(1) 0 0 b(2) b(3) 0; ...
       0 b(2) 0 b(1) 0 b(3); ...
       0 0 b(3) 0 b(1) b(2)];

M_ED=[2*D(1), 0, 0, 2*D(4), 2*D(5), 0; ...
       0, 2*D(2), 0, 2*D(4), 0, 2*D(6); ...
       0, 0, 2*D(3), 0, 2*D(5), 2*D(6); ...
       D(4), D(4), 0, D(1)+D(2), D(6), D(5); ...
       D(5), 0, D(5), D(6), D(1)+D(3), D(4); ...
       0, D(6), D(6), D(5), D(4), D(6)+D(5)]; ...

dbD_dcE=([eye(3)+D), M_cD; zeros(6,3), M_ED)\eye(9);
Cov_est=dbD_dcE*(I_fisher_tilde+I_fisher_bar)\dbD_dcE';
%END TWOSTEP

function [B_total]=total_field(B_in)
% Calculates total field of B_in (3xn matrix).
B_total=sum(B_in.^2,1).^0.5;

function [X_bar,X_tilde]=center_data(X,sigma_sq_k,sigma_sq_bar)
```

```

% Calculates the centered and center components of X
% Center component
X_bar = sigma_sq_bar*(X*(1./sigma_sq_k)');
% Centered component
X_tilde = X - X_bar*ones(1,size(X,2));

function [I_fisher_tilde,I_fishinv_tilde] =...
    TS_fisher_centered(sigma_sq,L_tilde)
% Calculates the fisher information matrix for the centered estimate, when
% given variance sigma_sq and centered vectors of L_tilde
% Calculate fisher information matrix
I_fisher_tilde=...
    ((L_tilde.*(ones(size(L_tilde,1),1)*(1./sigma_sq)))*L_tilde');
% Calculate inverse
I_fishinv_tilde=(I_fisher_tilde)\eye(9);

function [I_fisher_bar] =...
    TS_fisher_center(sigma_sq_bar,L_bar,dbsqdtheta_p)
% Calculates center information matrix. Used for readability
I_fisher_bar=((L_bar'-dbsqdtheta_p)'*(L_bar'-dbsqdtheta_p))/sigma_sq_bar;

function [b,D]= theta_to_b_D(theta)
% Converts a value of theta to usable physical values
[c,E]=theta_to_c_E(theta);
[U,S]=eig(E);
W=eye(3)+(eye(3)+S).^(0.5);
D=U*W*U';
% Calculate b using the inverse of (I+D)
b=(eye(3)+D)\c;

function [c,E]=theta_to_c_E(theta)
% Extracts c and E elements from theta as per Alonso paper.
c=theta(1:3);
E=[theta(4), theta(7), theta(8);...
    theta(7), theta(5), theta(9);...
    theta(8), theta(9), theta(6)];

```

C.2 Geometric Approach estimator

C.2.1 'ellipsoid_estimate.m'

```
function [T,b,n]=ellipsoid_estimate(h_r,sigma_sq,B_e)
%ELLIPSOID_ESTIMATE estimation of magnetometer errors.
% [T,b,n]=ellipsoid_estimate(h_r,sigma_sq,B_e)
% h_r - 3xN matrix, where N is the number of signal samples
% sigma_sq - 1xN noise covariance array, where each column is a
% diagonal of the noise covariance matrix. Note single row since noise
% assumed to be isotropic.
% B_e total earth field. 1xN vector.
%
%
% Implemented based on the work presented in:
% "Geometric approach to strapdown magnetometer calibration
% in sensor frame"
% by J.F. Vasconcelos et al. in Aerospace and Electronic Systems,
% IEEE Transactions 47(2) 2011.
%
% Justin Dinale, DSTO Department of Defence, Australia
% $Revision: 1.0.0 $ $Date: 2012/11/05$
%%%%%%%%%%%%%%%%%%%%%%%%%%%%%%%%%%%%%%%%%%%%%%%%%%%%%%%%%%%%%%%%%%%%%%%%

% Define stop condition and perform housekeeping
stop_tol=1e-5; % Stop Condition from Alonso paper
max_n=200; % Max number of iterations
k_samples=size(h_r,2); % Number of samples

%% Make first-guess estimation of T and b
[T0,b0]=ellipsoid_first_estimate(h_r);

%% Iterative corrections in estimate
T=T0;
b=b0;
GC_error=Inf;
```

```

n=1;
while (abs(GC_error)>stop_tol && n<max_n)
X=[T(:,1) ; T(:,2) ; T(:,3); b];
% If sigma^2 is constant, convert it to an array of samples
if (length(size(sigma_sq))==1)
    sigma_sq(1,1,:)=sigma_sq*ones(1,k_samples);
else
    tmp_sigma(1,1,:)=squeeze(sigma_sq);
    sigma_sq=tmp_sigma;
    clear tmp_sigma
end

%% Calculate u_{i} The measurement without bias
% Calculate temporary vector
u_t=h_r-[b(1)*ones(1,k_samples);...
        b(2)*ones(1,k_samples);...
        b(3)*ones(1,k_samples)];
% Put vector in 3D matrix accountign for samples, also store transpose
u(:,1,:)=u_t;
u_p(1,,:)=u_t;

%% Calculate regularly used elements
% Calcualte Tu
Tu(:,1,:)=T*squeeze(u);

% Calculate magnitude of Tu -> |Tu|
ITuI(1,1,:)=sqrt(sum(squeeze(Tu).^2,1));

% Calcucalte c_T
c_T(1,1,:)=ones(k_samples,1)-1./squeeze(ITuI);

%% Calculate First order Derivative with respect to T
tmp1=kron_k(u,Tu);
two_c_T_on_sigma(1,1,:)=2*(c_T./sigma_sq);
tmp2(:,1,:)=kron_k(ones(9,1),two_c_T_on_sigma);
Δ_f_dT=sum(tmp2.*tmp1,3);
clear tmp1 tmp2

```

C.2 Geometric Approach estimator

```
%% Calculate First order Derivative with respect to b
% Calcualte T'Tu
TpTu(:,1,:)=T'*squeeze(Tu);
tmp2(:,1,:)=kron_k(ones(3,1),two_c_T_on_sigma);
Δ_f_db=sum(-tmp2.*TpTu,3);
clear tmp1 tmp2

%% First order Derivative
Δ_f_dx=[Δ_f_dT ; Δ_f_db];

%% Second Order Derivatives
% Hessian Matrix Element H.TT
uu_p=kron_k(u,u_p);
b=kron_k(c_T,kron_k(uu_p,eye(3)));
TuupTp=mult_k(T,mult_k(uu_p,T'));
one_over_Tu_cube(1,1,:)=1./(ITuI.^3);
a=kron_k(one_over_Tu_cube,kron_k(uu_p,TuupTp));
two_on_sigma(1,1,:)=2*(1./sigma_sq);
H.TT=sum(kron_k(two_on_sigma,(a+b)),3);
clear a b

% Hessian Matrix Element H.Tb
b=kron_k(c_T,kron_k(u,T)+kron_k(eye(3),Tu));
a=kron_k(one_over_Tu_cube, mult_k(kron_k(u,Tu),mult_k(u_p,T'*T)));
H.Tb=sum(kron_k(-two_on_sigma,(a+b)),3);

% Hessian Matrix Element H.bb
TpTuupTpT=mult_k(T'*T,mult_k(uu_p,T'*T));
b=kron_k(c_T,T'*T);
a=kron_k(one_over_Tu_cube,TpTuupTpT);
H.bb=sum(kron_k(two_on_sigma,(a+b)),3);

% Merge Hessians
H=[H.TT H.Tb; H.Tb' H.bb];

%% T and b estimation
```

```

% Calculate new estimate
X_old=X;
X= X-H\Δ-f-dx;
% Calculate error for stop condition
GC_error=(X-X_old)'*H*(X-X_old); % Error for stop condition from Alonso

% Extract T= reshape(X(1:9),3,3)
T=[X(1) X(4) X(7);...
    X(2) X(5) X(8);...
    X(3) X(6) X(9)];
% Extract b
b= X(10:12);
n=n+1; %Increase counter
end

```

C.2.2 'ellipsoid_first_estimate.m'

```

function [T0,b0]=ellipsoid_first_estimate(h_r)
% ELLIPSOID-FIRST-ESTIMATE estimation of magnetometer errors.
% [T0,b0]=ellipsoid_first_estimate(h_r)
% h_r - 3xN matrix, where N is the number of signal samples
% Noise is irrelevant, and total-field is assumed to be constant.
%
% Implemented based on the work presented in:
% "Geometric approach to strapdown magnetometer calibration
% in sensor frame"
% by J.F. Vasconcelos et al. in Aerospace and Electronic Systems,
% IEEE Transactions 47(2) 2011.
%
% This is a Vasconcelos et al. implementation of:
% "Extension of a two-step calibration methodology to include
% nonorthogonal sensor axes"
% by Elkaïm & Forster in Aerospace and Electronic Systems,
% IEEE Transactions 44(3) 2008.
%

```

C.2 Geometric Approach estimator

```
% Note a correction to T0 , where the second column in the second row was
% chanced to +(1/b)*sec(rho) instead if -(1/b)*sec(rho) as in the paper.
%
% Justin Dinale, DSTO Department of Defence, Australia
% $Revision: 1.0.0 $ $Date: 2012/11/05$
%%%%%%%%%%%%%%%%%%%%%%%%%%%%%%%%%%%%%%%%%%%%%%%%%%%%%%%%%%%%%%%%%%%%%%%%
h_z_sq=h_r(3,:)'.^2;
X=[h_r(1,:)'.^2, h_r(1,:)'.*h_r(2,:) ', h_r(1,:)'.*h_r(3,:) ', ...
   h_r(2,:)'.^2 , h_r(2,:)'.*h_r(3,:) ', ...
   h_r(1,:) ', h_r(2,:) ', h_r(3,:) ' ones(size(h_r,2),1)];
p=X\h_z_sq;
A=p(1);
B=p(2);
C=p(3);
D=p(4);
E=p(5);
G=p(6);
H=p(7);
I=p(8);
J=p(9);
beta_1=2*B*H + B*E*I - 2*C*D*I - 4*D*G + E*C*H - E^2*G;
beta_2=-2*A*E*I + 4*A*H - B*C*I - 2*B*G + C^2*H - C*E*G;
beta_3=4*D*I*A - 2*D*G*C + E*G*B - I*B^2 - 2*E*H*A + C*B*H;
alpha_1 = -B^2 + D*C^2 + 4*D*A + A*E^2 - B*E*C;
alpha_2 = 4*A*(E^2)*J - E^2*G^2 - 4*B*E*C*J + 2*E*C*H*G ...
          + 2*B*E*I*G - 4*E*H*A*I - 4*D*I*C*G - C^2*H^2 ...
          + 4*D*A*I^2 + 2*C*B*H*I - 4*D*G^2 + 4*D*C^2*J ...
          + 4*B*H*G - 4*A*H^2 - B^2*I^2 - 4*B^2*J + 16*D*A*J;
alpha_3 = E^4*A - C*B*E^3 + E^2*C^2*D - 2*B^2*E^2 ...
          + 8*D*A*E^2 - 4*D*B^2 + 16*D^2*A;

a=1/(2*alpha_1)*sqrt(-(4*D+E^2)*alpha_2);
b=1/(2*alpha_1)*sqrt(-(4*A+C^2)*alpha_2);
c=1/(2*alpha_1)*sqrt((4*D*A-B^2)*alpha_2);

tan_rho=-0.5*(2*B+E*C)/sqrt(alpha_1);
tan_phi=(B*E-2*C*D)/sqrt(alpha_1);
```



```

tan_lambda=E*sqrt(-alpha_1/alpha_3);
rho=atan(tan_rho);
phi=atan(tan_phi);
lambda=atan(tan_lambda);
T0=[1/a, 0, 0; ...
    -(1/a)*tan_rho, +(1/b)*sec(rho), 0; ...
    (1/a)*(tan_rho*tan_lambda*sec(phi)-tan_phi), ...
    -(1/b)*(sec(rho)*tan_lambda*sec(phi)), ...
    (1/c)*(sec(lambda)*sec(phi))];
b0=(1/(2*alpha_1))*[beta_1 ; beta_2; beta_3];

```

C.2.3 'normcol.m'

```

function out=normcol(A)
%NORMCOL    Columnwise norm.
%
% normcol(A) returns a vector with dimension size(A,2) containing
% the norm of the columns of A.the skew symmetric matrix defined by the
%
% Example: A=[a1 a2]
% normcol(A)=[||a1|| ||a2||];
%
% 2008-10-16 J. F. Vasconcelos    DSOR SVN repository version.

out=sqrt(sum(A.^2,1));

```

C.2.4 'mult_k.m'

```

function M = mult_k(A,B)
%MULT_K    Matrix product, for i samples
% MULT_K(X,Y) is the matrix product of X and Y.
% The result is a large matrix formed products between the samples of X
% and those of Y at each index i

```

C.2 Geometric Approach estimator

```
%  
%  
%   Help text adapted from Mathworks KRON function.  
%   Copyright 2012 Justin Dinale, DSTO Department of Defence, Australia  
%   $Revision: 1.0.0 $ $Date: 2012/11/05$  
%%%%%%%%%%%%%%%%%%%%%%%%%%%%%%%%%%%%%%%%%%%%%%%%%%%%%%%%%%%%%%%%%%%%%%%%  
  
sA=size(A); % Get size of array A  
sB=size(B); % Get size of array B  
sA_l=length(sA); % Get number of dimensions for A  
sB_l=length(sB); % Get number of dimensions for B  
  
nDim=max(sA_l,sB_l); % Check what number of dimension are used.  
if nDim>3 % Only up to 3D are acceptable  
    error('KRON.K operates with at most 3 dimensions');  
elseif nDim<3 % Is the multiplication a single sample?  
    M=A*B;  
else % 3D matrix (2D with multiple samples)  
  
% Fix up dimension issues if there are any  
    if sA_l<nDim  
        sA=[sA ones(1,nDim-sA_l)];  
        k=sB(3);  
        A=repmat(A,[1 1 k]);  
    elseif sB_l<nDim  
        sB=[sB ones(1,nDim-sB_l)];  
        k=sA(3);  
        B=repmat(B,[1 1 k]);  
    else  
        k=sA(3);  
        if (sA(3)~= sB(3))  
            error('Uneven number of sampled in A and B');  
        end  
    end  
  
% Get transpose of A.
```

```
A=permute(A,[2 1,3]);  
%Expand out A for dot product  
A=A(:,sort(mod((1:sA(1))*sB(2))-1,sA(1))+1,:);  
% Prepare matrix B  
B=B(:,mod((1:sB(2))*sA(1))-1,sB(2))+1,:);  
% Perform the multiplication of A and B elements.  
M=A.*B;  
M=sum(M,1);  
M=reshape(M,sB(2),[],k);  
M=permute(M,[2 1,3]);  
end
```

C.2.5 'kron_k.m'

```
function K = kron_k_new(A,B)

%KRON_K    Kronecker tensor product, for i samples

%    KRON_K(X,Y) is the Kronecker tensor product of X and Y.
%    The result is a large matrix formed by taking all possible
%    products between the elements of X and those of Y at each index k
%    For example, if X is 2 by 3 by k, then KRON_K(X,Y) is
%
%    [ X(1,1,:).*Y  X(1,2,:).*Y  X(1,3,:).*Y
%      X(2,1,:).*Y  X(2,2,:).*Y  X(2,3,:).*Y ]
%
%    No optimisation is made for sparse matrices since intended use is for
%    matrices up to 9x9xN
%
%
%    Help text adapted from Mathworks KRON function.
%    Copyright 2012 Justin Dinale, DSTO Department of Defence, Australia
%    $Revision: 1.0.0 $ $Date: 2012/11/05$

%%%%%%%%%%%%%%%%%%%%%%%%%%%%%%%%%%%%%%%%%%%%%%%%%%%%%%%%%%%%%%%%%%%%%%%%

sA=size(A); % Get size of array A
sB=size(B); % Get size of array B
```

C.2 Geometric Approach estimator

```
sA_l=length(sA); % Get number of dimensions for A
sB_l=length(sB); % Get number of dimensions for B

nDim=max(sA_l,sB_l); % Check what number of dimension are used.
if nDim>3 % Only up to 3D are acceptable
    error('KRON.K operates with at most 3 dimensions');
elseif nDim<3 % Is the multiplication a single sample?
    K=kron(A,B);
else % 3D matrix (2D with multiple samples)

% Fix up dimension issues if there are any
    if sA_l<nDim
        sA=[sA ones(1,nDim-sA_l)];
        k=sB(3);
        A=repmat(A,[1 1 k]);
    elseif sB_l<nDim
        sB=[sB ones(1,nDim-sB_l)];
        k=sA(3);
        B=repmat(B,[1 1 k]);
    else
        k=sA(3);
        if (sA(3)~= sB(3))
            error('Uneven number of sampled in A and B');
        end
    end
end

% Prepare matrix A for multiplication. Increase each element of A top be
% sB(1) by sB(2) matrix
A=A(sort(mod((1:sA(1)*sB(1))-1,sA(1))+1),...
    sort(mod((1:sA(2)*sB(2))-1,sA(2))+1),:);
% Prepare matrix B using indexing to perfopr same task as repmat
% B=repmat(B,[sA(1),sA(2),1]);
B=B(mod((1:sB(1)*sA(1))-1,sB(1))+1,mod((1:sB(2)*sA(2))-1,sB(2))+1,:);
% Perform the multiplication of A and B elements.
K=A.*B;
end
```

C.3 AC calibration estimator

C.3.1 'AC_estimate.m'

```
function [D_est,Cov_est]=AC_estimate(B,H,Sigma_noise)
%AC_ESTIMATE estimation of magnetometer errors.
% [D_est,n,Cov_est]=AC_estimate(B,H,Sigma_noise)
% B - 3xN matrix, where N is the number of signal samples
% H - Earth's magnetic field in Earth frame coordinates
% Sigma_noise - 3xN noise covariance array, where each column is a
% diagonal of the noise covariance matrix.
%
% Implemented based on special case of the work presented in:
% "Complete Linear Attitude-Independent Magnetometer Calibration"
% by R.Alonso and M. Shuster
% in "The Journal of the Astronautical Sciences" Vol. 50 No.4
% October-December 2002.
%
% Justin Dinale, DSTO Department of Defence, Australia
% $Revision: 1.0.0 $ $Date: 2013/03/19$
%%%%%%%%%%%%%%%%%%%%%%%%%%%%%%%%%%%%%%%%%%%%%%%%%%%%%%%%%%%%%%%%%%%%%%%%

%% AC estimate
% Set initial guess for b and D.
D0=zeros(3);

% Calculate K
K_k=[(B.^2);...
      +2*B(1,:).*B(2,:);...
      +2*B(1,:).*B(3,:);...
      +2*B(2,:).*B(3,:)];

% Calculate scalar measurement z
z_k=total_field(B).^2-total_field(H).^2;

% Calculate mean and variance of noise
```

C.3 AC calibration estimator

```
mu_k=-sum(Sigma_noise,1); % Mean
sigma_sq_k=4*sum((eye(3)+D0)*B).*...
    (Sigma_noise.*(eye(3)+D0)*B),1)...
    +5*(sum(Sigma_noise.^2,1)-(sum(Sigma_noise,1).^2);

% Calculate fisher information matrix
[I_fisher,I_fishinv]=AC_fisher(sigma_sq_k,K_k);
% Calculate AC estimate
theta_0=...
    I_fishinv*(-K_k*((z_k-mu_k)'./sigma_sq_k'));

[D_est]=theta_to_D(theta_0);

% Extract covariance matrix
D=D_est;

M_ED=[2*D(1), 0, 0, 2*D(4), 2*D(5), 0; ...
    0, 2*D(2), 0, 2*D(4), 0, 2*D(6); ...
    0, 0, 2*D(3), 0, 2*D(5), 2*D(6); ...
    D(4), D(4), 0, D(1)+D(2), D(6), D(5); ...
    D(5), 0, D(5), D(6), D(1)+D(3), D(4); ...
    0, D(6), D(6), D(5), D(4), D(6)+D(5)]; ...

dD_dE=(2*eye(6)+M_ED)\eye(6);
Cov_est=dD_dE*(I_fisher)\dD_dE';
%END TWOSTEP

function [B_total]=total_field(B_in)
% Calculates total field of B_in (3xn matrix).
B_total=sum(B_in.^2,1).^0.5;

function [I_fisher,I_fishinv] =...
    AC_fisher(sigma_sq,K)
% Calculates the fisher information matrix for the centered estimate, when
% given variance sigma_sq and centered vectors of K
% Calculate fisher information matrix
I_fisher=...
```

```

        ((K.*(ones(size(K,1),1)*(1./sigma_sq)))*K');
% Calculate inverse
I_fishinv=(I_fisher)\eye(6);

function [D]= theta_to_D(theta)
% Converts a value of theta to usable physical values
[E]=theta_to_E(theta);
[U,S]=eig(E);
W=-eye(3)+(eye(3)+S).^ (0.5);
D=U*W*U';

function [E]=theta_to_E(theta)
% Extracts E elements from theta as per Alonso paper.
E=[theta(1), theta(4), theta(5);...
    theta(4), theta(2), theta(6);...
    theta(5), theta(6), theta(3)];

```

C.4 Parameter recovery

C.4.1 'recover_angles.m'

```

function [S,rho,phi,lambda]=recover_angles(Dj)
% Convert to Diagonal Matrix for comparison of estimators
[Q1,L1]=ql(eye(3)+Dj);
D = diag(sign(diag(L1)));
L = D*L1;
Q = Q1*D;

S(1)=L(1,1);
rho=atan(L(2,1)/L(2,2));
S(2)=L(2,1)/sin(rho);
phi=atan(L(3,1)/L(3,3));
lambda=atan(L(3,2)/(L(3,3)/cos(phi)));
S(3)=L(3,2)/sin(lambda);

```

C.4.2 'ql.m'

```
function [Q,L]=ql(A)
tmp1=zeros(size(A));
tmp2=tmp1;
tmp1(:)=1:numel(A);
tmp2(:)=numel(A):-1:1;
J=tmp1'==tmp2;
[JQJ,JLJ]=qr(J*A*J);
Q=J*JQJ*J;
L=J*JLJ*J;
```


Bibliography

- AAROE-M., MONACO-R., KOSHELETS-V. P., AND MYGIND-J. (2009). A quantitative investigation of the effect of a close-fitting superconducting shield on the coil factor of a solenoid, *Superconductor Science Technology*, **22**(9), p. 095017.
- ALONSO-R., AND SHUSTER-M. D. (2002a). Twostep: A fast robust algorithm for attitude-independent magnetometer-bias determination, *The Journal of the astronautical sciences*, **50**(4), pp. 433–451. eng.
- ALONSO-R., AND SHUSTER-M. D. (2002c). Complete linear attitude-independent magnetometer calibration, *The Journal of the astronautical sciences*, **50**(4), pp. 477–490. eng.
- ALONSO-R., AND SHUSTER-M. D. (2003). Centering and observability in attitude-independent magnetometer-bias determination, *The Journal of the astronautical sciences*, **51**(2), pp. 133–141. eng.
- AUSTER-H. U., FORNACON-K. H., GEORGESCU-E., GLASSMEIER-K. H., AND MOTSCHMANN-U. (2002). Calibration of flux-gate magnetometers using relative motion, *Measurement Science and Technology*, **13**(7), p. 1124.
- BARKER-J. R. (1949). New coil systems for the production of uniform magnetic fields, *Journal of Scientific Instruments*, **26**(8), p. 273.
- BARKER-R., COX-M., FORBES-A., AND HARRIS-P. (2007). Software support for metrology best practice guide no. 4 - Discrete modelling and experimental data analysis, *Technical report*, National Physical Laboratory, Teddington, Middlesex.
- BOYVATN-M., AND HAFNER-C. V. (2012). Molding the flow of magnetic field with metamaterials: magnetic field shielding , *Electromagnetics Research, Progress In*, **126**, pp. 303–316.
- BRACKEN-R., SMITH-D., AND BROWN-P. (2005). Calibrating a tensor magnetic gradiometer using spin data, *Technical report*, U.S. Geological Survey, Reston, Virginia.
- BRONAUGH-E. (1995). Helmholtz coils for calibration of probes and sensors: limits of magnetic field accuracy and uniformity, *Electromagnetic Compatibility, 1995. Symposium Record. 1995 IEEE International Symposium on*, pp. 72 –76.
- CAMPS-F., HARASSE-S., AND MONIN-A. (2009). Numerical calibration for 3-axis accelerometers and magnetometers, *Electro/Information Technology, 2009. eit '09. IEEE International Conference on*, pp. 217 –221.

- CAPRARI-R. S. (1995). Optimal current loop systems for producing uniform magnetic fields, *Measurement Science and Technology*, **6**(5), p. 593.
- CARTER-R. (1976). Coil-system design for production of uniform magnetic fields, *Electrical Engineers, Proceedings of the Institution of*, **123**(11), pp. 1279 –1283.
- CHENG-D. (1989). *Field and wave electromagnetics*, Addison-Wesley series in electrical engineering, Addison-Wesley.
- CLARKE-D. (2011). Re: Ternan coils, Personal communication.
- CLAYCOMB-J., AND MILLER-H. (2006). Superconducting and high-permeability shields modeled for biomagnetism and nondestructive testing, *Magnetics, IEEE Transactions on*, **42**(6), pp. 1694 –1702.
- CROTTI-G., AND GIORDANO-D. (2004). Evaluation of frequency behaviour of coils for reference magnetic field generation, *Precision Electromagnetic Measurements Digest, 2004 Conference on*, pp. 28 –29.
- CROTTI-G., CHIAMPI-M., AND GIORDANO-D. (2006). Estimation of stray parameters of coils for reference magnetic field generation, *Magnetics, IEEE Transactions on*, **42**(4), pp. 1439 –1442.
- DONLEY-E. A., HODBY-E., HOLLBERG-L., AND KITCHING-J. (2007). Demonstration of high-performance compact magnetic shields for chip-scale atomic devices, *Scientific Instruments, Review of*, **78**(8), p. 7.
- DRAKE-A. (1994). Traceability for low level low frequency magnetic field measurements, *Low Level Low Frequency Magnetic Fields, IEE Colloquium on*, pp. 3/1 –3/2.
- EVERETT-J., AND OSEMEIKHIAN-J. (1966). Spherical coils for uniform magnetic fields, *Journal of Scientific Instruments*, **43**(7), p. 470.
- Fleet Command - RAN Ranges and Assessing Unit* (2009). Commonwealth of Australia.
- FRIX-W., KARADY-G., AND VENETZ-B. (1994). Comparison of calibration systems for magnetic field measurement equipment, *Power Delivery, IEEE Transactions on*, **9**(1), pp. 100 –108.
- GRIFFITHS-D. (1999). *Introduction to electrodynamics*, Prentice Hall.
- HARTMANN-G. K. (1979). *Weapons that wait : mine warfare in the U.S. Navy* / Gregory K. Hartmann, Naval Institute Press, Annapolis, Md. .:
- HAYES-C., EDELSTEIN-W., SCHENCK-J., MUELLER-O., AND EASH-M. (1985). An efficient, highly homogeneous radiofrequency coil for whole-body nmr imaging at 1.5t, *Journal of Magnetic Resonance*, **63**, p. 622 to 628.
- HUANG-L., AND JING-W. (2008). Attitude-independent geomagnetic navigation using onboard complete three-axis magnetometer calibration, *Aerospace Conference, 2008 IEEE*, pp. 1 –7.

- KIM-E., AND BANG-H.-C. (2007). Bias estimation of magnetometer using genetic algorithm, *Control, Automation and Systems, 2007. ICCAS '07. International Conference on*, pp. 195–198.
- KIM-W.-S., KIM-Y. B., KIM-M.-S., KIM-K.-T., CHONG-Y., PARK-P. G., AND KIM-Y. G. (2007). Optimizing the shielding effectiveness of a shielding cabinet via FEM simulation, *Journal of Magnetism and Magnetic Materials*.
- KIRSCHVINK-J. L. (1992). Uniform magnetic fields and double-wrapped coil systems: Improved techniques for the design of bioelectromagnetic experiments, *Bioelectromagnetics*, **13**, pp. 401–411.
- KLYMOVYCH-Y., AND PAJUNPAA-K. (2004). Precise calibration system for dc vector magnetometers and approach to its accrediting, *Precision Electromagnetic Measurements Digest, 2004 Conference on*, pp. 506–507.
- KUBERRY-R. (1967). Absolute calibration of the magnetic field generated by a small coil, *Geoscience Electronics, IEEE Transactions on*, **5**(3), pp. 94–96.
- LASSAHN-M., AND TRENKLER-G. (1995). Vectorial calibration of 3d magnetic field sensor arrays, *Instrumentation and Measurement, IEEE Transactions on*, **44**(2), pp. 360–362.
- LEE-S.-K., AND ROMALIS-M. V. (2008). Calculation of magnetic field noise from high-permeability magnetic shields and conducting objects with simple geometry, *Journal of Applied Physics*, **103**(8), pp. 084904–084904–10.
- LENZ-J., AND EDELSTEIN-S. (2006). Magnetic sensors and their applications, *Sensors Journal, IEEE*, **6**(3), pp. 631–649.
- LIAO-Y. (2011). *Phase and frequency estimation: High-accuracy and low-complexity techniques*, Master's thesis.
- MAGER-A. (1968). Magnetic shielding efficiencies of cylindrical shells with axis parallel to the field, *Journal of Applied Physics*, **39**(3), p. 1914.
- MAGER-A. (1970). Magnetic shields, *Magnetics, IEEE Transactions on*, **6**(1), pp. 67–75.
- MATHWORKS. (2012). Mathworks Australia - Procrustes Analysis @ONLINE.
- MEEKER-D. (2010). Finite Element Method Magnetics Version 4.2 Users Manual@ONLINE.
- MENGCHUN-P., HONGFENG-P., SHITU-L., QI-Z., AND RUIFANG-X. (2010). Calibration improvement of three-axis magnetometer in disturbing magnetic circumstance based on fir digital filter, *Signal Processing (ICSP), 2010 IEEE 10th International Conference on*, pp. 247–250.
- MERAYO-J., BRAUER-P., PRIMDAHL-F., J.R.-P., AND O.V.-N. (2000). Scalar calibration of vector magnetometers, *Measurement Science and Technology*, **11**, pp. 120–132.
- MIRZAEVA-G., SUMMERS-T., AND BETZ-R. (2012). A laboratory system to produce a highly accurate and uniform magnetic field for sensor calibration, *Industrial Technology (ICIT), 2012 IEEE International Conference on*, pp. 1020–1025.

- NISSEN-J., AND PAULSSON-L.-E. (1996). Influence of field inhomogeneity in magnetic calibration coils, *Instrumentation and Measurement, IEEE Transactions on*, **45**(1), pp. 304 –306.
- OLSEN-N., RISBO-T., BRAUER-P., MERAYO-J., PRIMDAHL-F., AND SABAKA-T. (2001). *In-Flight Calibration Methods Used For The rsted Mission*.
- PETRUCHA-V., AND KASPAR-P. (2009). Calibration of a triaxial fluxgate magnetometer and accelerometer with an automated non-magnetic calibration system, *Sensors, 2009 IEEE*, pp. 1510 –1513.
- PIERGENTILI-F., CANDINI-G., AND ZANNONI-M. (2011). Design, manufacturing, and test of a real-time, three-axis magnetic field simulator, *Aerospace and Electronic Systems, IEEE Transactions on*, **47**(2), pp. 1369 –1379.
- POOR-H. V. (1994). *An Introduction to Signal Detection and Estimation*, Springer.
- SCHAAD-T. P. (2009). Nano-resolution: Oceanic, atmospheric and seismic sensors with parts-per-billion resolution, *Technical report*, Paroscientific Inc., Redmons, Washington.
- SCHILL-R. A., AND HOFF-K. (2001). Characterizing and calibrating a large helmholtz coil at low ac magnetic field levels with peak magnitudes below the earth's magnetic field, *Review of Scientific Instruments*, **72**(6), pp. 2769 –2776.
- SHIFRIN-V., ALEXANDROV-E., CHIKVADZE-T., KALABIN-V., YAKOBSON-N., KHOREV-V., AND PARK-P. (2000). A standard calibration system for geomagnetometers, *Precision Electromagnetic Measurements Digest, 2000 Conference on*, pp. 236 –237.
- SOKEN-H., AND HAJIYEV-C. (2011). In flight magnetometer calibration via unscented kalman filter, *Recent Advances in Space Technologies (RAST), 2011 5th International Conference on*, pp. 885 –890.
- STANSFIELD-D. (1991). *Underwater Electroacoustin Transducers*, Bath University Press and Institute of Acoustics.
- TASHIRO-K., WAKIWAKA-H., MATSUMURA-K., AND OKANO-K. (2011). Desktop magnetic shielding system for the calibration of high-sensitivity magnetometers, *Magnetics, IEEE Transactions on*, **47**(10), pp. 4270 –4273.
- T. OETIKER, H. PARTL-I. H., AND SCHLEGL-E. (2000). *The Not So Short Introduction to LATEX 2e*, Tobias Oetiker and all Contributors to LShort.
- TUMANSKI-S. (2007). Induction coil sensors a review, *Measurement Science and Technology*, **18**(3), p. R31.
- VASCONCELOS-J., ELKAIM-G., SILVESTRE-C., OLIVEIRA-P., AND CARDEIRA-B. (2011). Geometric approach to strapdown magnetometer calibration in sensor frame, *Aerospace and Electronic Systems, IEEE Transactions on*, **47**(2), pp. 1293 –1306.

- VCELAK-J. (2006). Calibration of triaxial fluxgate gradiometer, *Journal of Applied Physics*, **99**(8), pp. 08D913 –08D913–3.
- WANG-X. (2008). Automatic and adaptive correction of diversionary errors in tri-axial magnetometer using neural networks, *Knowledge Acquisition and Modeling Workshop, 2008. KAM Workshop 2008. IEEE International Symposium on*, pp. 271 –274.
- WHITE-L. B. (2012). Detection, estimation and classification 2012, Lecture Notes, Adelaide University.
- YODA-K. (1990). Analytical design method of self-shielded planar coils, *Journal of Applied Physics*, **67**(9), pp. 4349 –4353.
- YOUGUANG-G., JIANGUO-Z., ZHIWEI-L., JINJIANG-Z., LU-H., AND SHUHONG-W. (2006). Calibration of sensing coils of a three-dimensional magnetic property tester, *Magnetics, IEEE Transactions on*, **42**(10), pp. 3243 –3245.
- ZHANG-X., AND GAO-L. (2009). A novel auto-calibration method of the vector magnetometer, *Electronic Measurement Instruments, 2009. ICEMI '09. 9th International Conference on*, pp. 1–145 –1–150.
- ZLOBIN-A., AMBROSIO-G., ANDREEV-N., BARZI-E., CHICHILI-D., KASHIKHIN-V., LIMON-P., TERECHKINE-I., YADAV-S., AND YAMADA-R. (2001). Development of cos-theta nb3sn dipole magnets for vlhc, *Particle Accelerator Conference, 2001. PAC 2001. Proceedings of the 2001*, Vol. 5, pp. 3427 –3429 vol.5.

| DEFENCE SCIENCE AND TECHNOLOGY ORGANISATION DOCUMENT CONTROL DATA | | | | | | | |
|---|-----------------------|-----------------------------|---|---|--|---------------------------------|--|
| | | | | 1. PRIVACY MARKING/CAVEAT (OF DOCUMENT) | | | |
| 2. TITLE Magnetic Test Facility - Sensor and Coil Calibrations | | | 3. SECURITY CLASSIFICATION (FOR UNCLASSIFIED REPORTS THAT ARE LIMITED RELEASE USE (L) NEXT TO DOCUMENT CLASSIFICATION) Document (U) Title (U) Abstract (U) | | | | |
| 4. AUTHOR(S) Justin Peter Dinale | | | 5. CORPORATE AUTHOR DSTO Defence Science and Technology Organisation 506 Lorimer St Fishermans Bend Victoria 3207 Australia | | | | |
| 6a. DSTO NUMBER DSTO-RR-0396 | | 6b. AR NUMBER AR-015-690 | | 6c. TYPE OF REPORT Research Report | | 7. DOCUMENT DATE August 2013 | |
| 8. FILE NUMBER U-490-6-477-1 | 9. TASK NUMBER CEI | 10. TASK SPONSOR CEI | | 11. NO. OF PAGES 221 | | 12. NO. OF REFERENCES 65 | |
| 13. DSTO Publications Repository http://dspace.dsto.defence.gov.au/dspace/ | | | 14. RELEASE AUTHORITY Chief, Maritime Division | | | | |
| 15. SECONDARY RELEASE STATEMENT OF THIS DOCUMENT <i>Approved for public release</i> | | | | | | | |
| OVERSEAS ENQUIRIES OUTSIDE STATED LIMITATIONS SHOULD BE REFERRED THROUGH DOCUMENT EXCHANGE, PO BOX 1500, EDINBURGH, SA 5111 | | | | | | | |
| 16. DELIBERATE ANNOUNCEMENT No Limitations | | | | | | | |
| 17. CITATION IN OTHER DOCUMENTS | | | | Yes | | | |
| 18. DSTO RESEARCH LIBRARY THESAURUS Ternan, ELFcage, TWOSTEP, Calibration, Magnetic, Coil, Estimation | | | | | | | |
| 19. ABSTRACT This report details the areas in which signal processing techniques have enabled DSTO Sydney to enhance its existing magnetic testing capability, and present viable data processing options for their implementation. This entails not only accurate sensor calibration, but also calibration of the excitation coils used within the magnetic test system. Reduction of external noise influences through the use of high permeability shielding and filtering are detailed, presenting modelling of coil-shield interactions, and experimental tests for various filter characteristics. Various magnetic coil designs, including DSTO's previously undocumented "Ternan" coil, are also investigated, leading to the design of a new magnetic coil, the "ELFcage" coil, being developed. Field uniformity measurements for the "Ternan" magnetic coil are also presented. | | | | | | | |